# CONDUCTIVE THIN FILM-COATED FLEXIBLE POLYMERS

## A NEW MATERIALS APPROACH FOR DESIGNING BIOMEDICAL ELECTRODES

Paulo Eduardo Teixeira Batista Pedrosa

DISSERTAÇÃO PARA A OBTENÇÃO DO GRAU DE DOUTOR EM ENGENHARIA BIOMÉDICA PELA
FACULDADE DE ENGENHARIA DA UNIVERSIDADE DO PORTO

U.PORTO
FEUP FACULDADE DE ENGENHARIA
UNIVERSIDADE DO PORTO

TESE REALIZADA SOB A ORIENTAÇÃO DE:

**Professor Doutor José Carlos Magalhães Duque da Fonseca**

Professor Auxiliar do Departamento de Engenharia Metalúrgica e de Materiais da Faculdade de Engenharia da Universidade do Porto

**Professor Doutor José Filipe Vilela Vaz**

Professor Associado com Agregação do Departamento de Física da Escola de Ciências da Universidade do Minho

## ACKNOWLEDGEMENTS

The present work would not be possible without the direct and indirect participation of several people, institutions and funding agencies.

First of all, the author would like to express his gratitude to the supervisors of this thesis – Professor José Carlos Magalhães Duque da Fonseca and Professor José Filipe Vilela Vaz – for the always accurate scientific guidance and also for the constant availability and support in all steps that ultimately led to the successful completion of the present manuscript. To Professor Nicolas Martin from the FEMTO-ST Institute in Besançon, France for the always warm welcome and for allowing an unrestricted used of all the necessary facilities and equipment involving the Glancing Angle Deposition technique.

To my PhD colleagues and (above all) friends Cláudia Lopes, Diana Morais, João Coelho, Joel Borges and Miguel Rodrigues for the relentless daily motivation and support. Also to Patrique Fiedler from the BMTI Institute, Technische Universität Ilmenau, Germany for the many warm welcomes and assistance in all matters concerning the electroencephalographic (EEG) signal monitoring and processing. To Diogo Machado for the invaluable help on the production and characterization of the coatings. To Beatriz Vasconcelos for being a valuable subject on the EEG trials.

The author acknowledges FCT for the Ph.D. grant SFRH/BD/70035/2010 and Programa Pessoa 2012/2013 Cooperação Portugal/França, the FP7-People Marie Curie IAPP project 610950 (ANDREA) and the German Academic Exchange Services for the Germany/Portugal bi-lateral project – D/57036536.

To my mother.

To Ema.

## ABSTRACT

The present thesis focuses on the development of new thin film systems and technological approaches for attaining a novel class of flexible dry biopotential electrodes. These electrodes, in opposition to the commercially used wet Ag/AgCl ones, neither rely on the application of a conductive gel nor on an extensive skin preparation (for which trained personnel is often needed), thus being able to be used in applications where a simple and fast montage is needed.

For this purpose, several titanium nitride (TiN)-based thin film systems were optimized in traditional substrates (glass and silicon) and later sputtered onto flexible polyurethane substrates, including the final multipin bioelectrode design, which was used for the electroencephalographic (EEG) biosignal monitoring. This study started by investigating the pure $TiN_x$ system with different N/Ti atomic ratios. Despite the encouraging morphological, structural and electrochemical results, this thin film system was not suitable for the EEG trials, since the coatings often failed after only one measurement due to the brittle nature of this ceramic material. Consequently, in order to increase the in-service stability of the coatings and also to tailor its elasticity, electrical response and bactericide character, silver (Ag) was added (up to 50 at.%) to a stoichiometric TiN matrix – $Ag_x$:TiN system. However, extensive Ag particle segregation was found in the as-deposited TiN stoichiometric-like films (N/Ti atomic ratio close to 1) coatings, which translated into a long-term poor structural stability of the $Ag_x$:TiN films. Hence, with the objective of depleting the undesired Ag segregation, a new under-stoichiometric-like $Ag_y$:$TiN_x$ system was studied ($x < 1$). These coatings were sputtered with decreasing N/Ti atomic ratios (towards under-stoichiometric conditions) and different Ag contents (from 8 to 32 at.%). No significant Ag particle segregation was visible in this system due to the possible formation of TiAg intermetallics.

Then, the architecture of the coatings was firstly optimized and then finally sputtered into flexible polyurethane substrates, using the Glancing Angle Deposition (GLAD) technique. A Ag:TiN system with a N/Ti atomic ratio of 0.7 and 10 at.% Ag was GLAD sputtered with incidence angles of 0º, 40º and 80º and with inclined columnar and zigzag architectures and its electrochemical behaviour was investigated. The porous (80º columnar and zigzag) coatings exhibited the best set of properties to be used as bioelectrodes.

To finalize the present study, the adhesion of the optimized Ag:TiN coating to the polyurethane substrates was evaluated by performing a set of plasma activation treatments with different powers, times and gases. In combination with bipolar EEG monitoring (Ag:TiN-coated polyurethane dry multipin electrode vs. wet Ag/AgCl commercial electrode), it was possible to determine the best plasma treatment conditions (100 W, 15 min., regardless of the used gas – Ar, $O_2$ and $N_2$) to be used in order to effectively activate the surface of the polyurethane multipins prior to the Ag:TiN functionalization. Furthermore, no significant EEG signal differences were found between the wet and dry multipin electrodes, thus making them promising candidates to substitute the standard wet Ag/AgCl electrodes in specific clinical and ambulatory procedures.

## RESUMO

A presente tese foca-se no desenvolvimento de novos sistemas de filmes finos e abordagens tecnológicas com o intuito de obter uma nova classe de eléctrodos secos de biopotencial. Estes eléctrodos, ao contrário dos eléctrodos húmidos de Ag/AgCl usados comercialmente, dispensam a aplicação de um gel condutor, bem como uma extensiva preparação da pele (para a qual, muita das vezes, é necessária a presença de técnicos qualificados). São, portanto, ideais para o uso em aplicações onde uma montagem simples e rápida é necessária.

Tendo em conta este propósito, vários sistemas de filmes finos baseados em nitreto de titânio (TiN) foram optimizados em substratos clássicos (vidro e silício), sendo depois depositados em substratos flexíveis de poliuretano, incluindo o design final em forma de multipino, que foi usado na aquisição de sinais electroencefalográficos (EEG). Este estudo começou por investigar o sistema $TiN_x$ com vários rácios atómicos N/Ti. Apesar dos resultados encorajadores em termos morfológicos, estruturais e electroquímicos, este sistema não se revelou adequado durante os ensaios de EEG, uma vez que os revestimentos falharam consistentemente após somente uma medição, devido á natureza frágil deste material cerâmico.

Consequentemente, de modo a aumentar a estabilidade dos revestimentos em condições de serviço e melhorar a sua resposta eléctrica, elasticidade e carácter bactericida, foi adicionada prata (Ag, até um máximo de 50 at.%) à matriz estequiométrica de TiN – sistema $Ag_x$:TiN. No entanto, foi observado um extenso fenómeno de segregação de partículas de Ag, o que se traduziu numa fraca estabilidade estrutural a longo prazo dos filmes finos estequiométricos de $Ag_x$:TiN. Posto isto, com o objectivo de eliminar a indesejada segregação de Ag, foi estudado um novo sistema $Ag_y$:$TiN_x$. Estes revestimentos foram depositados com rácios atómicos N/Ti decrescentes (condições sub-estequiométricas) e diferentes teores de Ag (de 8 até 32 at.%). Não foram encontradas evidências significativas de segregração de Ag neste sistema, devido à possível formação de compostos intermetálicos TiAg. De seguida, a arquitectura dos revestimentos foi primeiramente optimizada e finalmente depositada em substratos flexíveis de poliuretano, usando a técnica Glancing Angle Deposition (GLAD). Foi então investigado um sistema Ag:TiN com um rácio atómico N/Ti de 0.7 e um teor em Ag de 10 at.%, depositado com ângulos de incidência de 0º, 40º e 80º colunares e com arquitectura em ziguezague, sendo o seu comportamento electroquímico estudado posteriormente. Os filmes porosos (80º colunares e ziguezague) exibiram o conjunto de propriedades mais apropriadas para serem usados como bioeléctrodos.

Para finalizar o presente estudo, a adesão dos revestimentos optimizados de Ag:TiN aos substratos de poliuretano foi estudada após a realização de vários tratamentos de plasma com diferentes potências, tempos e gases. Em combinação com a aquisição bipolar de EEG (eléctrodo seco multipino revestido com Ag:TiN versus eléctrodo comercial húmido de Ag/AgCl), foi possível determinar quais as condições optimizadas (100 W, 15 min. independentemente do gás utilizado – Ar, $O_2$ e $N_2$) que promovem o tratamento de plasma mais eficaz na activação superficial dos multipinos de poliuretano. Paralelamente, não foram detectadas diferenças significativas na qualidade dos sinais de EEG adquiridos com os eléctrodos, tornando-os, por isso, candidatos promissores à substituição dos tradicionais eléctrodos húmidos de Ag/AgCl em procedimentos clínicos e ambulatórios específicos.

# TABLE OF CONTENTS

## LIST OF PUBLICATIONS

### International peer-reviewed journal papers:

P. Fiedler, L.T. Cunha, **P. Pedrosa**, S. Brodkorb, C. Fonseca, F. Vaz, J. Haueisen, "*Novel $TiN_x$-based biosignal electrodes for electroencephalography*", Measurement Science and Technology 22 (2011) 124007.

P. Fiedler, **P. Pedrosa**, S. Griebel, C. Fonseca, F. Vaz, F. Zanow, J. Haueisen, "*Novel Flexible Dry PU/TiN-Multipin Electrodes: First Application in EEG Measurements*", Proceedings of the 33rd Annual International Conference of the IEEE EMBS (2011) 55-58.

**P. Pedrosa**, E. Alves, N.P. Barradas, P. Fiedler, J. Haueisen, F. Vaz, C. Fonseca, "*$TiN_x$ coated polycarbonate for bio-electrode applications*", Corrosion Science 56 (2012) 49-57.

P. Fiedler, C. Fonseca, **P. Pedrosa**, A. Martins, F. Vaz, S. Griebel, J. Haueisen, "*Novel Flexible Dry Multipin Electrodes for EEG: Signal Quality and Interfacial Impedance of the Ti and TiN Coatings*" Proceedings of the 35th Annual Conference of the IEEE EMBS (2013) 547-550.

D. Machado, **P. Pedrosa**, C. Fonseca, N. Martin, F. Vaz, "*Structural and Morphological Changes in Ag:TiN Nanocomposite Films promoted by in-vacuum annealing*" Journal of Nano Research 25 (2013) 67-76.

C. Lopes, C. Gonçalves, **P. Pedrosa**, F. Macedo, E. Alves, N.P. Barradas, N. Martin, C. Fonseca, F. Vaz, "*$TiAg_x$ thin films for lower limb prosthesis pressure sensors: Effect of composition and structural changes on the electrical and thermal response of the films*", Applied Surface Science 285P (2013) 10-18.

**P. Pedrosa**, D. Machado, C. Lopes, E. Alves, N.P. Barradas, N. Martin, F. Macedo, C. Fonseca, F. Vaz, "*Nanocomposite Ag:TiN thin films for dry biopotential electrodes*", Applied Surface Science 285P (2013) 40-48.

**P. Pedrosa**, D. Machado, M. Evaristo, A. Cavaleiro, C. Fonseca, F. Vaz, "*Ag:TiN nanocomposite thin films for bioelectrodes: The effect of annealing treatments on the electrical and mechanical behavior*", Journal of Vacuum Science and Technology A 32 (2014) 031515.

**P. Pedrosa**, C. Lopes, N. Martin, C. Fonseca, F. Vaz, "*Electrical characterization of Ag:TiN thin films produced by glancing angle deposition*", Materials Letters 115 (2014) 136-139.

**P. Pedrosa**, E. Alves, N.P. Barradas, N. Martin, P. Fiedler, J. Haueisen, F. Vaz, C. Fonseca, "*Electrochemical behaviour of nanocomposite* $Ag_x$*:TiN thin films for dry biopotential electrodes*", Electrochimica Acta 125 (2014) 48-57.

P. Fiedler, S. Griebel, **P. Pedrosa**, C. Fonseca, F. Vaz, L. Zentner, F. Zanow, J. Haueisen, "*Multichannel EEG with novel Ti/TiN dry electrodes*", Sensors and Actuators A 221 (2015) 139-147.

**P. Pedrosa**, D. Machado, E. Alves, N.P. Barradas, F. Vaz, C. Fonseca, "*Electrochemical evaluation of nanocomposite* $Ag_y:TiN_x$ *thin films for dry biopotential electrodes: the effect of the N/Ti ratio and Ag content*", Electrochimica Acta 153 (2015) 602–611.

**P. Pedrosa**, D. Machado, J. Borges, M.S. Rodrigues, E. Alves, N.P. Barradas, N. Martin, M. Evaristo, A. Cavaleiro, C. Fonseca, F. Vaz, "$Ag_y:TiN_x$ *thin films for dry biopotential electrodes: the effect of composition and structural changes on the electrical and mechanical behaviours*", Applied Physics A: Materials Science and Processing, in press, accepted manuscript, DOI: 10.1007/s00339-014-8943-9.

**P. Pedrosa**, D. Machado, E. Alves, N.P. Barradas, N. Martin, F. Vaz, C. Fonseca, "*Ag:TiN-coated polyurethane for dry biopotential electrodes produced by Glancing Angle Deposition*", submitted to Plasma Processes and Polymers, under review.

**P. Pedrosa**, C. Lopes, P. Fiedler, E. Alves, N.P. Barradas, J. Haueisen, A.V. Machado, C. Fonseca, F. Vaz, "*Ag:TiN-coated polyurethane for dry biopotential electrodes: from polymer plasma activation to the first EEG measurements*", submitted to Applied Materials and Interfaces, under review.

**International conferences:**

P. Fiedler, **P. Pedrosa**, S. Griebel, C. Fonseca, F. Vaz, F. Zanow, J. Haueisen, "*Novel flexible dry PU/TiN-Multipin electrodes: First application in EEG measurements*", Engineering in Medicine and Biology Society (EMBC), 2011 Annual International Conference of the IEEE, Boston, United States of America.

**P. Pedrosa**, C. Lopes, F. Vaz, A. Ferreira, S. Lanceros-Mendez, E. Alves, N.P. Barradas, N. Martin, C. Fonseca, "*Silver-doped* $TiN_x$ *nanocomposites: Effect of composition and structural changes in the electrical response of the films*", 13th International Conference on Plasma Surface Engineering – PSE 2012, Garmisch-Partenkirchen, Germany.

B. Branco, P. Chaves, G. Vieira, P. Almeida, D. Rodrigues, **P. Pedrosa**, F. Barbosa, C. Fonseca, "*Development of Novel Dry Multi-Pin Electrodes for Electroencephalographic Recording*", IJUP 2012 - Investigação Jovem na Universidade do Porto, Porto, Portugal.

P. Fiedler, C. Fonseca, **P. Pedrosa**, A.C. Martins, F. Vaz, S. Griebel, J. Haueisen, "*Novel Flexible Dry Multipin Electrodes for EEG: Signal Quality and Interfacial Impedance of Ti and TiN Coatings*", 35th Annual International Conference of the IEEE Engineering in Medicine and Biology Society (EMBC '13), Osaka, Japan.

C. Lopes, F. Macedo, A. Ferreira, S. Lanceros-Mendez, **P. Pedrosa**, C. Fonseca, F. Vaz, "$TiAg_x$ *coated pressure sensors for lower limb prosthesis: effect of composition and structural changes in the electrical response of the films*", 8th International Conference on Materials Science and Engineering – BRAMAT 2013, Brasov, Romania.

**P. Pedrosa**, C. Lopes, F. Macedo, C. Fonseca, F. Vaz, "*Silver-doped* $TiN_x$ *nanocomposite thin films for biosignals (EEG and ECG) acquisition*", 8th International Conference on Materials Science and Engineering – BRAMAT 2013, Brasov, Romania.

**P. Pedrosa**, D. Machado, C. Lopes, E. Alves, N.P. Barradas, N. Martin, C. Fonseca, F. Vaz, "*Growth and Characterization of Nanocomposite Ag:TiN Thin Films Produced by Glancing Angle Deposition for Biopotential Electrodes*", Materiais 2013, Coimbra, Portugal.

C. Lopes, C. Gonçalves, **P. Pedrosa**, A. Ferreira, S. Lanceros-Mendez, E. Alves, N.P. Barradas, N. Martin, C. Fonseca, F. Vaz, "*Effect of Thermal Treatments on the Properties of* $TiAg_x$ *Thin Films Prepared by Sputtering*", Materiais 2013, Coimbra, Portugal.

**P. Pedrosa**, N. Martin, F. Vaz, C. Fonseca, "*Ag:TiN nanocomposite thin films produced by Glancing Angle Deposition for flexible dry biopotential electrodes*", Materials Science and Engineering 2014, Darmstadt, Germany.

# CHAPTER 1

## GENERAL INTRODUCTION

*EEG electrode cap composed of 97 individual polyurethane dry multipin electrodes. Copyright: P. Fiedler, TU Ilmenau*

## 1.1. Thesis outline

The present document is a scientific article-based thesis. As such, the manuscript was divided into seven chapters, according to nine main publications, which refer to the three thin film systems studied.

Chapter 1 comprises the introductory part of the present study. This section is divided into three sub-chapters, which include the outline of the document, as well as the motivations and background of the present work. No extensive state-of-the-art or theoretical background will be performed in chapter 1, since most of the bibliographic review and theory concepts were already widely focused on the introduction section of the scientific papers that comprise the manuscript.

Regarding the results obtained in the present study, chapter 2 is dedicated to the initially investigated $TiN_x$ thin film system and how the encountered drawbacks gave rise to an alteration of the initial approach by adding silver to a stoichiometric TiN matrix. Hence, chapter 3 takes account of the optimization of the silver content that should be added to the stoichiometric TiN matrix in terms of the obtained morphological, structural, electrical, mechanical and electrochemical properties (sections 3.1. to 3.3.). Since an unwanted silver segregation phenomenon was found in the stoichiometric $Ag_x$:TiN system, chapter 4 reports on the tailoring of the TiN matrix stoichiometry towards under-stoichiometric conditions. Similarly to the previous chapter, the influence of the stoichiometry tailoring on several $Ag_y$:$TiN_x$ system properties are exhibited in sections 4.1. and 4.2. The thin film architecture was investigated in chapter 5, namely in terms of the optimization of the GLAD sputtering parameters (section 5.1.) and subsequent sputtering onto polyurethane substrates, on which the electrochemical properties were studied (section 5.2.). Finally, the in-service validation of all optimization performed throughout the present thesis is patent in chapter 6, namely the thin film/polyurethane adhesion and subsequent electroencephalographic signal monitoring in human volunteers.

The final chapter 7 comprehends the general discussion, main conclusions and future work.

## 1.2. Motivation

The ultimate goal of the present thesis is to optimize conductive thin film-coated flexible polymers, aiming at the development of novel dry biomedical electrodes for electroencephalographic (EEG) applications. This new class of dry electrodes should be able to replace the wet commercial silver/silver chloride ones (Ag/AgCl) in applications where a fast and easy montage is needed. The wet Ag/AgCl electrodes need to be applied in combination with electrolyte gels or pastes, involving uncomfortable and time-consuming procedures, for which trained personnel is often needed. They are also commonly quite rigid, which can give rise to an incorrect and uncomfortable skin contact. In opposition, the thin film-coated flexible dry multipin electrode proposed in the present study should not rely on the application of the referred conductive gel, thus significantly reducing the preparation times and associated costs. Moreover, due to its flexibility and design, the proposed electrode should promote higher patient comfort and hair interfusion.

The new thin film systems, whose development is proposed in this thesis, are essential to ensure the functionality of such electrodes. Consequently, different TiN-based PVD coatings should be optimized according to the several requirements of the proposed dry electrodes. The proposed coating systems ($TiN_x$, $Ag_x$:TiN and $Ag_y$:$TiN_x$) should then be characterized in terms of the influence of the Ag content, $TiN_x$ matrix stoichiometry (N/Ti atomic ratios) and thin film architecture on (i) the morphological and structural stability (avoiding long-term Ag segregation), as well as on (ii) the mechanical (the coatings should comply with the substrate deformations) and (iii) electrochemical behaviour (in contact with synthetic sweat) of the sputtered composites.

Furthermore, since the optimized coatings were to be sputtered onto flexible polyurethane substrates, a thorough adhesion characterization should also be performed in order to prevent in-service failure of the coatings. At the end, the dry multipin electrodes should be coated with the optimized thin film system and tested for EEG biosignal monitoring.

## 1.3. Background

For the past few decades, modern medicine has relied on non-invasive, high resolution monitoring of biopotentials produced by the human body, such as electroencephalography (EEG, brain activity), electrocardiography (ECG, heart activity) and electromyography (EMG, muscular activity), in order to accurately comprehend several pathologies and physiological conditions of human patients, Fig. 1.1.

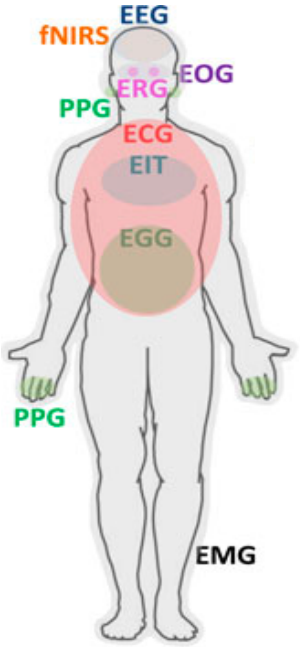

**Figure 1.1.** Examples of non-invasive physiological monitoring (adapted from [1]).

In particular, the human electroencephalogram (originally published in 1929 by the German psychiatrist Hans Berger [2]) is still a powerful tool for detecting acute brain disorders, such as epileptic seizures, acute encephalitis, head trauma, coma and strokes [3-7]. More recently, EEG has been applied in the study of brain-computer interfaces (BCI), enabling a direct communication between the human brain and external devices [8]. The conventional biopotential acquisition set-up relies on the use of the standard silver/silver chloride (Ag/AgCl) wet electrodes [9-11]. These are considered the gold standard electrodes [3,8,12], as they are non-polarizable and reveal excellent reliability, displaying low and almost frequency independent skin-contact impedance values, in the order of a few tens of kΩ.cm$^2$ [10,11].

However, a preliminary skin preparation and a gel paste application are needed before the exam, in order to lower the skin/electrode impedance. This preparation is time consuming, uncomfortable to the patient and requires trained staff. Furthermore, some patients have developed severe allergic reactions to the common used gel pastes [11] and the risk of short-circuiting adjacent electrodes due to gel running can be relatively high. Susceptibility to motion artefacts is also widely reported [10,11] and a known difficulty that hampers a wider use of EEG in promising fields such as sports science [13]. Nevertheless, with proper skin preparation and correct conductive gel application, the wet Ag/AgCl electrodes exhibit excellent biopotential signal quality [8], although at the expense of increased amounts of preparation times. All the aforementioned drawbacks inhibit the use of EEG in clinical applications where an easy and fast montage is needed, such as in emergency medical settings or in ambulatory conditions. It is important to note that the presence of EEG monitoring systems is still seldom in intensive care units (long-term EEG monitoring) or in the standard equipment of most paramedic units (mobile EEG applications) [3].

Eliminating the need to use the conductive gel paste would, in fact, reduce most of the above-referred disadvantages of the standard Ag/AgCl electrode system. Consequently, a new class of biopotential electrodes is being widely investigated, which are commonly called dry electrodes, in order to obtain an easier, faster and unobtrusive biopotential monitoring process. These electrodes do not require any previous skin preparation or gel application and are commonly based on inert-like materials, either metallic-like or insulator-coated metals [11,14], Fig. 1.2. However, these electrodes still maintain some important drawbacks that have also been reported in other similar dry systems [15,16], such as incorrect and/or uncomfortable skin contact due to its intrinsic stiffness nature that do not allow them to conform to the human body. Moreover, focusing on the typical EEG acquisition setup, the use of lighter, cheaper and more comfortable electrodes would translate in numerous advantages to the patients in comparison with the standard Ag/AgCl ones, once the use of 128 or even 256 electrodes in a single exam is becoming an increasingly common practice.

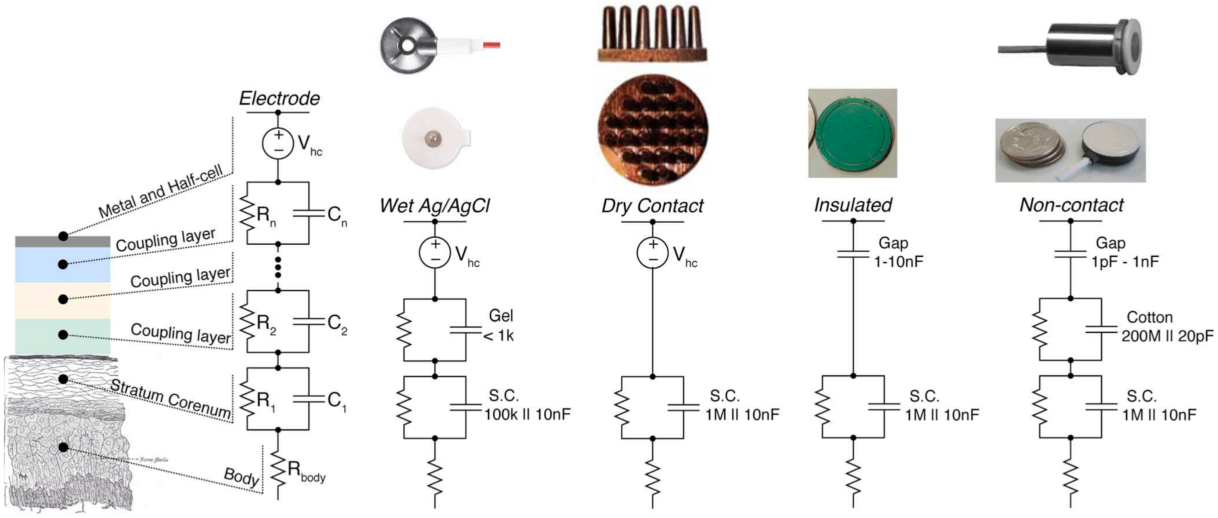

**Figure 1.2.** Different technological approaches for biopotential electrodes, including the standard Ag/AgCl wet, dry multipin, thin film insulated metal plate and non-contact electrodes (adapted from [12]).

The electrically conductive materials initially used in dry electrodes were metals such as stainless steel [17] and aluminium [11], but their low corrosion resistance when in contact with the human sweat made them inappropriate. Subsequently, gold [18], metal oxide and nitride coatings like $TiO_2$ or TiN, which are much more resistant to corrosion, have been proposed [16,19-23]. Materials such as graphite [24], conductive silicone or rubber [15] have also been suggested, but these materials also display too high electrical impedances (> 500 $k\Omega.cm^2$). Resistive and capacitive electrode materials were also investigated but the fabrication costs and patient discomfort have been reported as drawbacks often encountered for these types of electrodes [8,25].

In terms of design, Fig. 1.3., the dry electrodes also exhibit concept-specific fundamental problems. Many dry electrode systems [16] display an incorrect and/or uncomfortable skin contact due to the intrinsic stiff nature of the base materials [25] or even because of conceptual problems (rigid planar plates/disks unable to interfuse the hair layer [23,26]). Micro-electromechanical system (MEMS) sensors that use microneedles to penetrate the *stratum corneum* have been studied [27]. However, the microneedles are often able to penetrate live skin layers, which translated into patient pain and induced infections [8]. Consequently, several authors have recently focused on the development of textile and polymer-based flexible dry electrodes [15,28-31], since they should be able to promote a more reliable and comfortable skin contact, thus reducing some of the stated drawbacks. However, the textile-based electrode design still needs improvements since the contact area of the skin/electrode interface is significantly reduced when extensive hairlines are present [8]. With the objective of eliminating the comfort drawback, non-contact electrodes have also been proposed but are highly susceptible to the type of insulator material used and also to environmental conditions such as humidity [1].

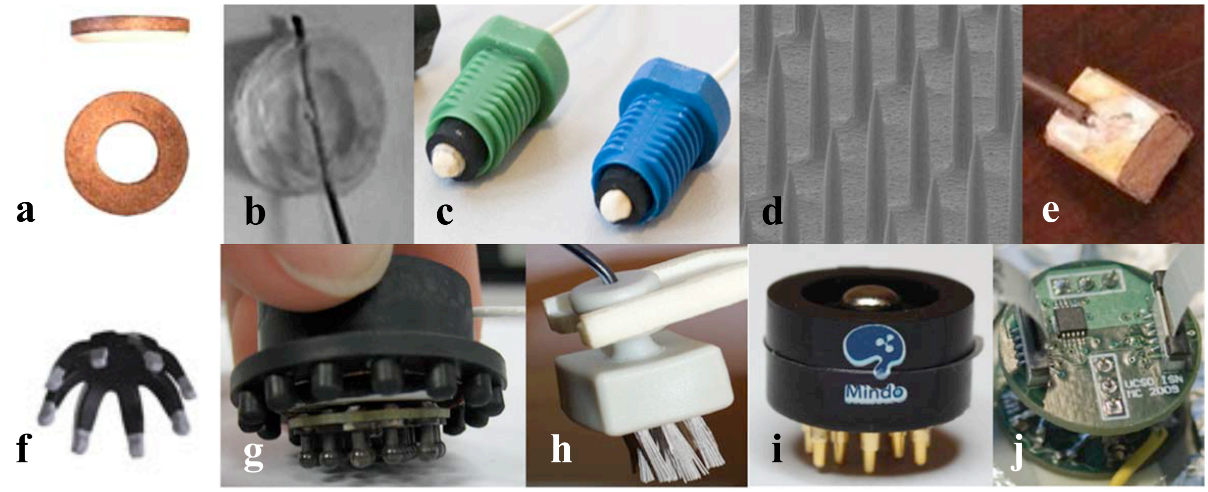

**Figure 1.3.** Comparison between several designs of biopotential electrodes: (a) wet Ag/AgCl ring electrodes, (b) polyacrylate wet electrode [32], (c) water-based sensors [33], (d) MEMS [27], (e) foam electrodes and (f-j) dry fingered/multipin electrodes [34-39] and (j) non-contact sensor (adapted from [1,8]).

Therefore, the present thesis focuses on the polymeric multipin design, since it displays the desired set of advantages over the other aforementioned designs and technologies (inexpensive, lightweight, patient comfort and hair interfusion ability) and can be easily functionalized with several conductive thin film systems.

Reactive DC magnetron sputtering is commonly accepted as one of the most versatile and less expensive coating techniques, being widely assumed as able to produce fairly high deposition rates and compact coatings, when compared to other techniques. It also allows the coating of several base materials, Fig. 1.4. Regarding the chosen thin film materials, TiN is an electrically conductive coating, with an excellent chemical stability in most media and outstanding mechanical properties, which led to a very broad range of applications, including those in the biomedical area [26,40]. Furthermore, TiN is biocompatible, but it is also a relatively hard and high Young's modulus material, thus unable to withstand large deformations (in fact, most metallic films tolerate less than 10% of deformation [41-48]). It gives rise to mechanical failure of the coatings, which, in turn, is highly undesirable when the objective is to produce flexible electrodes that are supposed to adapt to the human skin. The inclusion of silver, due to its intrinsic characteristics, particularly the low Young's modulus and high conductivity [49], within the TiN films may offer the possibility to tailor the elasticity of the coating [50], opening a wide range of possible applications, namely those related to the coating of flexible devices such as polymers. Furthermore, silver addition may also allow the tailoring of the electrical conductivity [51], which may be of crucial importance in any electrode-based application. Finally, silver is inherently antimicrobial [52-56], particularly in its nanocrystalline form [53,54] and also an excellent biosensor material [57], which is of major importance in any application that may involve electrophysiological signal monitoring.

Thermoplastic polyurethanes (TPU) have been extensively applied in several fields that range from technical coatings to biomedical applications [58-60], due to their excellent balance between mechanical properties (high flexibility), excellent chemical barrier behaviour, soft tact and biocompatibility [61,62], thus being appropriate to be used as biopotential electrode base material. However, as most polymers, the PU surface displays low surface energies, with evident effects in future polymer/coating interfacial adhesion. Consequently, the PU surfaces must be activated in order to promote the grafting of reactive groups, as well as to increase the surface roughness [63-66].

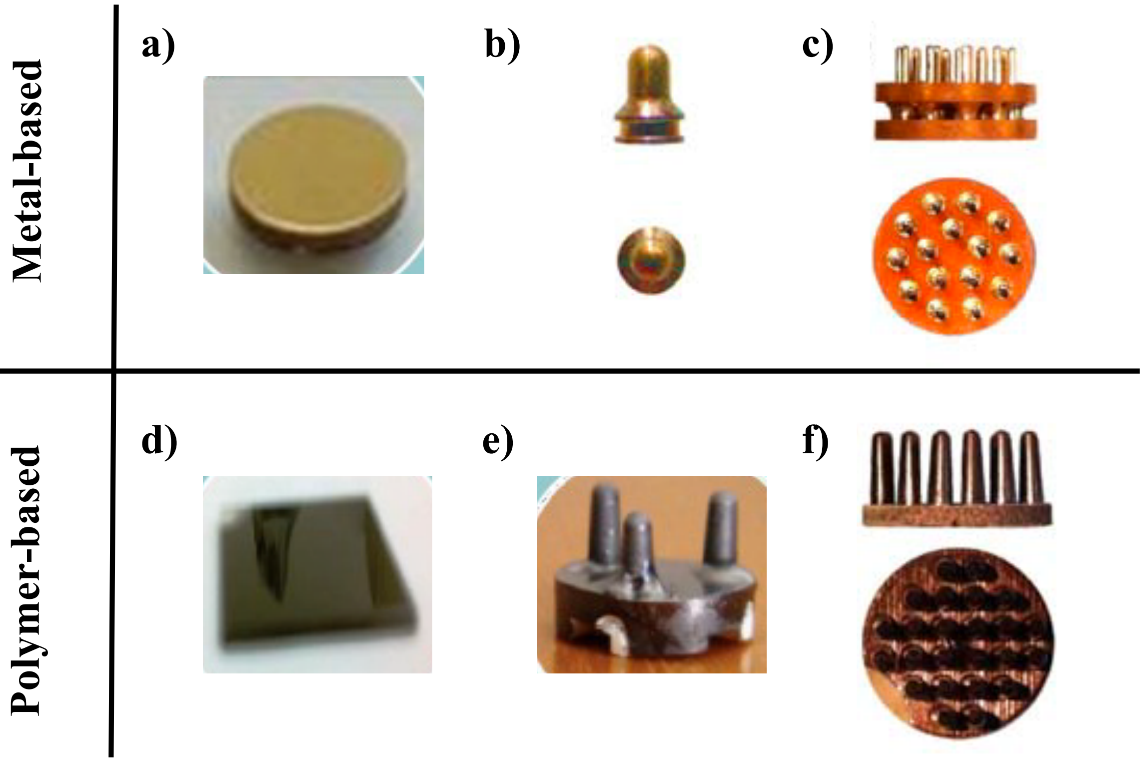

**Figure 1.4.** Dry electrode designs and technological approaches developed within the research group: (a) TiN-coated titanium disks, (b) TiN-coated single pin (bullet), (c) gold multipin electrode (built with commercial parts), (d) TiN-coated polycarbonate sheet, (e) TiN-coated ABS multipin and (f) Ag:TiN-coated polyurethane multipin (optimized in the current work).

Henceforth, the ultimate goal of the present study is to develop and optimize a new generation of flexible polyurethane multipin dry biopotential electrodes that should be able to surpass most of the stated drawbacks that refer to the standard wet Ag/AgCl electrodes in terms of the materials and design points of view, thus allowing the use of EEG monitoring in clinical, ambulatory and emergent situations, where a rapid and easy montage is needed. The development of a dry electrode cap, see Fig. 1.5., is also contemplated and is currently underway, with most of the design and assemblage work being performed at the Institute of Biomedical Engineering and Informatics, Technische Universität Ilmenau.

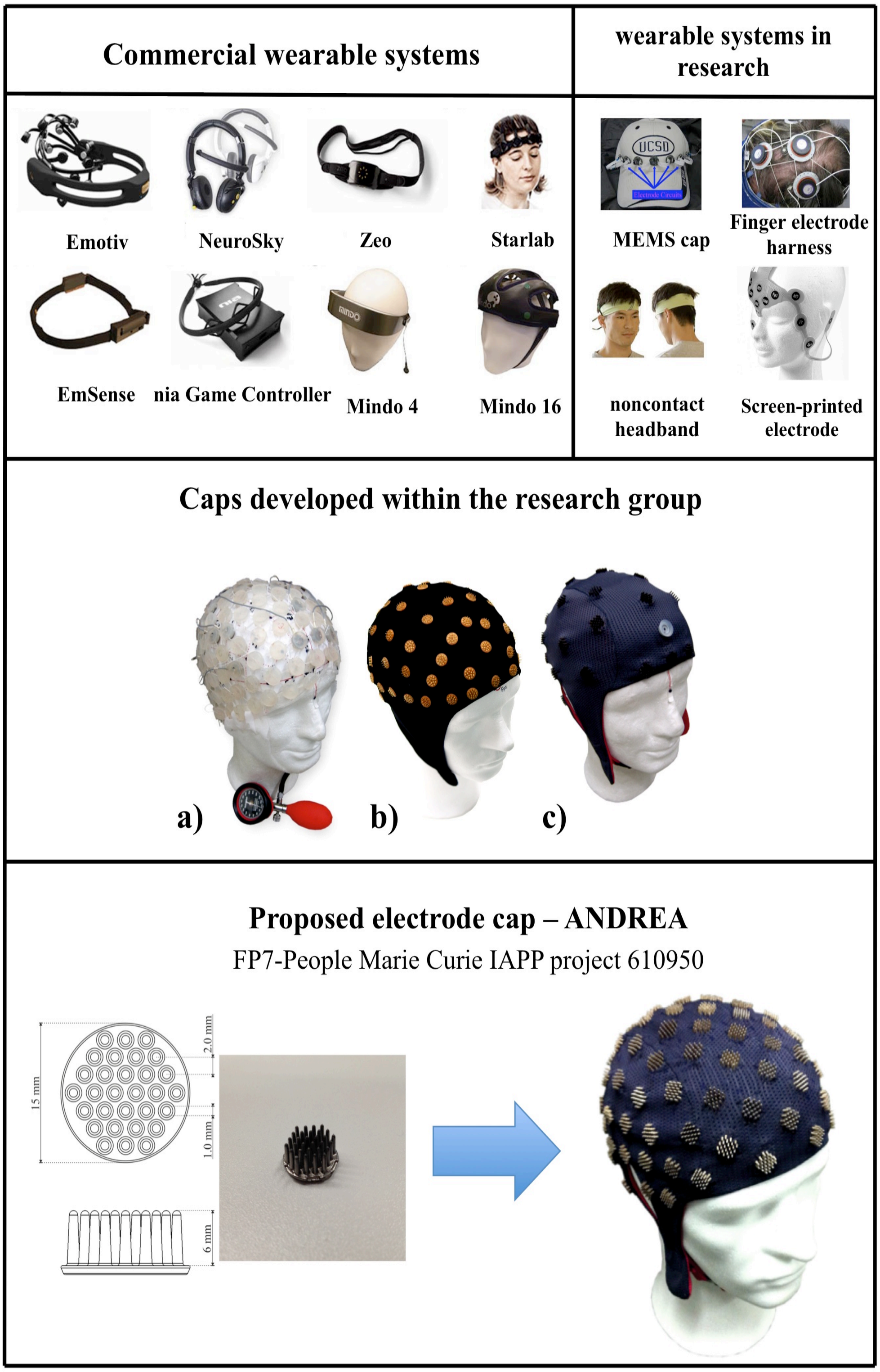

**Figure 1.5.** Commercial and research wearable EEG systems (adapted from [8]) in comparison with the caps developed within the research group (a) silicone-based cap with pressure-driven adduction actuators and TiN-coated single pin electrodes, b) textile cap with gold pin electrodes and c) textile cap with TiN-coated multipin electrodes) and the system proposed in the current work. All photos from caps a-c, as well as the ANDREA cap, Copyright: P. Fiedler, TU Ilmenau.

## 1.4. References

1. S. Ha, C. Kim, Y.M. Chi, A. Akinin, C. Maier, A. Ueno, G. Cauwenberghs, "*Integrated circuits and electrode interfaces for non-invasive physiological monitoring*", IEEE Trans. Biomed. Eng. 61 (2014) 1522-1537.
2. H. Berger, "*Über das Elektrenkephalogramm des Menschen [I. Mitteilung]*", Arch. Psychiatr. 87 (1929) 527–570.
3. P. Lepola, S. Myllymaa, J. Töyräs, A. Muraja-Murro, E. Mervaala, R. Lappalainen, K. Myllymaa, "*Screen-printed EEG electrode set for emergency use*", Sens. Act. A 213 (2014) 19-26.
4. P.N. Varelas, M.V. Spanaki, L. Hacein-Bey, T. Hether, B. Terranova, "*EEG. Emergent, Indications and diagnostic yield*", Neurology 61 (2003) 702-704.
5. S.F. Khan, R. Ashalatha, S.V. Thomas, P.S. Sarma, "*Emergent EEG is helpful in neurology critical care practice*", Clin. Neurophysiol. 116 (2005) 2454-2459.
6. J. Praline, J. Grujic, P. Corcia, B. Lucas, C. Hommet, A. Autret, B. de Toffol, "*Emergent EEG in clinical practice*", Clin. Neurophysiol., 118 (2007) 2149-2155.
7. S. Noachtar, J. Rémi, "*The role of EEG in epilepsy: a critical review*", Epilepsy Behav. 15 (2009) 22-33.
8. L.-D. Liao, C.-T. Lin, K. McDowell, A.E. Wickenden, K. Gramann, T.-P. Jung, L.-W. Ko, J.-Y. Chang, "*Biosensor technologies for Augmented Brain-Computer Interfaces in the next decades*", Proc. IEEE 100 (2012) 1553-1566.
9. M. Teplan, "*Fundamentals of EEG measurement*", Meas. Sci. Rev. 2 (2002) 1-11.
10. E. McAdams, "*Bioelectrodes*", in Encyclopaedia of Medical Devices and Instrumentation, Webster J. G. Ed., New York, Wiley, (1988) 120-166.
11. A. Searle, L. Kirkup, "*A direct comparison of wet, dry and insulating bioelectric recording electrodes*", Physiol. Meas. 22 (2000) 271-283.
12. Y. M. Chi, T.-P. Jung, G. Cauwenberghs, "*Dry-contact and noncontact biopotential electrodes: methodological review*", IEEE Rev. Biomed. Eng. 3 (2010) 106-119.
13. T. Thompson, T. Steffert, T. Ros, J. Leach, J. Gruzelier, "*EEG applications for sport and performance*", Methods 45 (2008) 279–288.
14. W.K. Ko, J. Hynecek, "*Dry electrodes and electrode amplifiers*", in H.A. Miller and D.C. Harrison (Eds), Biomedical Electrode Technology, Academic Press, New York (1974).

15. G. Gargiulo, R.A. Calvo, P. Bifulco, M. Cesarelli, C. Jin, A. Mohamed, A. van Schaik, "*A new EEG recording system for passive dry electrodes*", Clin. Neurophysiol. 121 (5) (2010) 686-693.
16. C. Fonseca, J.P. Silva Cunha, R.E. Martins, V. Ferreira, J.P. Marques de Sá, M.A. Barbosa, A. Martins Silva, "*A novel dry active electrode for EEG recording*", IEEE Trans. Biomed. Eng. 54 (1) (2007) 162-165.
17. E.S. Valchinov, N.E. Pallikarakis, "*An active electrode for biopotential recording from small localized bio-sources*", Biomed. Eng. OnLine 3 (2004) 25-39.
18. A.C. Metting Van Rijn, A.P. Kuiper, T.E. Dankers, C.A. Grimbergen, "*Low-cost active electrode improves the resolution in biopotential recordings*", Proc. IEEE EMBC, 18 (1996) 101-102.
19. B.A.-Taheri, R.T Knight, R.L Smith, "*A dry electrode for EEG recording*", Electroen. Clin. Neuro, 90 (1994) 376-383.
20. B.A.-Taheri, R.T. Knight, R.L. Smith, "*An active, microfabricated, scalp electrode array for EEG recording*", Sens. Actuat. A, 54 (1996) 606-611.
21. N.S. Dias, J.P. Carmo, A.F. da Silva, P.M. Mendes, J.H. Correia, "*New dry electrodes based on iridium oxide (IrO) for non-invasive biopotential recordings and stimulation*", Sens. Actuat. A, 164 (2010) 28-34.
22. P. Fiedler, L.T. Cunha, P. Pedrosa, S. Brodkorb, C. Fonseca, F. Vaz, J. Haueisen, "*Novel TiNx-based biosignal electrodes for electroencephalography*", Meas. Sci. Technol., 22 (2011) 124007.
23. L.T. Cunha, P. Pedrosa, C.J. Tavares, E. Alves, F. Vaz, C. Fonseca, "*The role of composition, morphology and crystalline structure in the electrochemical behaviour of* $TiN_x$ *thin films for dry electrode sensor materials*", Electrochim. Acta 55 (1) (2009) 59–67.
24. M. Negishi, M. Abildgaard, I. Laufer, T. Nixon, R.T. Constable, "*An EEG (electroencephalogram) recording system with carbon wire electrodes for simultaneous EEG-fMRI (functional magnetic resonance imaging) recording*", J. Neurosci. Meth., 173 (2008) 99-107.
25. R. Matthews, P.J. Turner, N.J. McDonald, K. Ermolaev, T.M. Manus, R.A. Shelby, M. Steindorf, "*Real time workload classification from an ambulatory wireless EEG system using hybrid EEG electrodes*", Proc. IEEE 30th Annu. Int. Conf., Eng. Med. Biol. Soc., EMBS 2008, 2008, 5871–5875.
26. P. Pedrosa, E. Alves, N.P. Barradas, P. Fiedler, J. Haueisen, F. Vaz, C. Fonseca, "$TiN_x$

*coated polycarbonate for bio-electrode applications*", Corros. Sci. 56 (2012) 49–57.

27. P. Griss, P. Enoksson, H.K. Tolvanen-Laakso, P. Merilainen, S. Ollmar, G. Stemme, "*Micromachined electrodes for biopotential measurement*", IEEE J. Microelectromech. Syst. 10 (2001) 10–15.
28. K.-P. Hoffmann and R. Ruff, "*Flexible Dry Surface-electrodes for ECG Long-term Monitoring*", Proceedings of the 29th Annual International Conference of the IEEE EMBS, Lyon, France, August, (2007) 23-26.
29. J. Baek, J. An, J. Choi, K. Park, S. Lee, "*Flexible polymeric dry electrodes for the long-term monitoring of ECG*", Sens. Actuators A 143 (2008) 423–429.
30. A. Gruetzmann, S. Hansen, J. Muller, "*Novel dry electrodes for ECG monitoring*", Physiol. Meas. 28 (2007) 1375–1390.
31. V. Marozas, A. Petrenas, S. Daukantas, A Lukosevicius, "*A comparison of conductive textile-based and silver/silver chloride gel electrodes in exercise electrocardiogram recordings*", J. Electrocardiology 44 (2011) 189–194.
32. N.A. Alba, R.J. Sclabassi, M. Sun, X.T. Cui, "*Novel hydrogel-based preparation-free EEG electrode*", IEEE Trans. Neural Syst. Rehab. Eng. 18 (2010) 415–423.
33. I. Volosyak, D. Valbuena, T. Malechka, J. Peuscher, A. Graser, "*Brain-computer interface using water-based electrodes*", J. Neural Eng. 7 (2010) 066007.
34. C.T. Lin, L.D. Liao, Y.H. Liu, I.J. Wang, B.S. Lin, J.Y. Chang, "*Novel dry polymer foam electrodes for long-term EEG measurement*", IEEE Trans. Biomed. Eng. 58 (2011) 1200–1207.
35. Cognionics Inc., "*High density dry EEG headset system spec sheet.*" [Online]. Available: http://www.cognionics.com
36. Y.Wang, K. Guo, W.-H. Pei, Q. Gui, X.-Q. Li, H.-D. Chen, J.-H. Yang, "*Fabrication of dry electrode for recording bio-potentials*", Chinese Phys. Lett. 28 (2011) 010701.
37. L.-D. Liao, I.J. Wang, S.-F. Chen, J.-Y. Chang, C.-T. Lin, "*Design, fabrication and experimental validation of a novel dry-contact sensor for measuring electroencephalography signals without skin preparation*", Sensors 11 (2011) 5819–5834.
38. R. Matthews, N.J. McDonald, H. Anumula, J. Woodward, P.J. Turner, M.A. Steindorf, K. Chang, J.M. Pendleton, "*Novel hybrid bioelectrodes for ambulatory zero-prep EEG measurements using multi-channel wireless EEG system*", Lecture Notes in Computer Science 4565 (2007) 137–146.
39. G. Cristian, C.D. Voinescu, S. Fazli, "*Bristle-sensors-low-cost flexible passive dry EEG*

*electrodes for neurofeedback and BCI applications*", J. Neural Eng. 8 (2011) 025008.

40. S. Piscanec, L. Ciacchi, E. Vesselli, G. Comelli, O. Sbaizero, S. Meriani, A. De Vita, "*Bioactivity of TiN-coated titanium implants*", Acta Mater. 52 (2004) 1237.
41. S.L. Chui, J. Leu, P.S. Ho, "*Fracture of metal-polymer line structures. I. Semiflexible polyimide*", J. Appl. Phys. 76 (1994) 5136.
42. O. Kraft, M. Hommel, E. Arzt, "*X-ray diffraction as a tool to study the mechanical behaviour of thin films*", Mater. Sci. Eng., A 288 (2000) 209.
43. M. Hommel, O. Kraft, "*Deformation behavior of thin copper films on deformable substrates*", Acta Mater. 49 (2001) 3935.
44. B.E. Alaca, M.T.A. Saif, H. Sehitoglu, "*On the interface debond at the edge of a thin film on a thick substrate*", Acta Mater. 50 (2002) 1197.
45. D.Y.W. Yu, F. Spaepen, "*The yield strength of thin copper films on Kapton*", J. Appl. Phys. 95 (2003) 2991.
46. S.P. Lacour, S. Wagner, Z. Huang, Z. Suo, "*Stretchable gold conductors on elastomeric substrates*", Appl. Phys. Lett. 82 (2003) 2404.
47. Y. Xiang, T. Li, Z. Suo, J. Vlassak, "*High ductility of a metal film adherent on a polymer substrate*", Appl. Phys. Lett. 87 (2005) 161910.
48. R.M. Niu, G. Liu, C. Wang, G. Zhang, X.D. Ding, J. Sun, "*Thickness dependent critical strain in submicron Cu films adherent to polymer substrate*", Appl. Phys. Lett. 90 (2007) 161907.
49. R.X. Wang, X.M. Tao, Y. Wang, G.F. Wang, S.M. Shang, "*Microstructures and electrical conductance of silver nanocrystalline thin films on flexible polymer substrates*", Surf. Coat. Technol. 204 (2010) 1206–1210.
50. R.C. Adochite, D. Munteanu, M. Torrell, L. Cunha, E. Alves, N.P. Barradas, A. Cavaleiro, J.P. Riviere, E. Le Bourhis, D. Eyidi, F. Vaz, "*The influence of annealing treatments on the properties of Ag:TiO2 nanocomposite films prepared by magnetron sputtering*", Appl. Surf. Sci. 258 (2012) 4028–4034.
51. H. Chiriac, M. Urse, F. Rusu, C Hison, M. Neagu, "*Ni–Ag thin films as strain-sensitive materials for piezoresistive sensors*", Sens. Actuators, A 76 (1999) 376-380.
52. K.-H. Liao, K.-L. Ou, H.-C. Cheng, C.-T. Lin, P.-W. Peng, "*Effect of silver on antibacterial properties of stainless steel*", Appl. Surf. Sci. 256 (2010) 3642-3646.
53. M. Fiori, M. Paula, A. Bernardin, H. Riella, E. Angioletto, "*Bactericide glasses developed by $Na^+/Ag^+$ ionic exchange*", Mater. Sci. Eng., C 29 (2009) 1569–1573.

54. M. Santos, C. Oliveira, C. Tachinski, M. Fernandes, C. Pich, E. Angioletto, H.G. Riella, M. Fiori, "*Bactericidal properties of bentonite treated with Ag+ and acid*", Int. J. Miner. Process. 100 (2011) 51–53.

55. P.J. Kelly, H. Li, K.A. Whitehead, J. Verran, R.D. Arnell, I. Iordanova, "*A study of the antimicrobial and tribological properties of TiN/Ag nanocomposite coatings*", Surf. Coat. Technol. 204 (2009) 1137–1140.

56. P.J. Kelly, H. Li, P.S. Benson, K.A. Whitehead, J. Verran, R.D. Arnell, I. Iordanova, "*Comparison of the tribological and antimicrobial properties of CrN/Ag, ZrN/Ag, TiN/Ag, and TiN/Cu nanocomposite coatings*", Surf. Coat. Technol. 205 (2010) 1606–1610.

57. L.A. Geddes, L.E. Baker, A.G. Moore, "*Optimum electrolytic chloriding of silver electrodes*", Med. Biol. Eng. 7 (1969) 49-56.

58. R.J. Zdrahala, I.J. Zdrahala, "*Biomedical applications of polyurethanes: a review of past promises, present realities, and a vibrant future*", J. Biomater. Appl., 14 (1999) 67–90.

59. K. Stokes, A. Coury, P. Urbanski, "*Autooxidative degradation of implanted polyether polyurethane devices*", J. Biomater. Appl., 1 (1986), 411–448.

60. A. Tiwari, H. Salacinski, A.M. Seifalian, G. Hamilton, "*New prostheses for use in bypass grafts with special emphasis on polyurethanes*", Cardiovasc. Surg., 10 (2002), 191–197.

61. M.R. Sanchis, O. Calvo, O. Fenollar, D. Garcia, R. Balart, "*Characterization of the surface changes and the aging effects of low-pressure nitrogen plasma treatment in a polyurethane film*", Polym. Test. 27 (2008) 75–83.

62. C. Zandén, M. Voinova, J. Gold, D. Mörsdorf, I. Bernhardt, J. Liu, "*Surface characterisation of oxygen plasma treated electrospun polyurethane fibres and their interaction with red blood cells*", Eur. Polym. J. 48 (2012) 472–482.

63. M. Noeske, J. Degenhardt, S. Strudthoff, U. Lommatzsch, "*Plasma jet treatment of five polymers at atmospheric pressure: surface modifications and the relevance for adhesion*", Int. J. Adhes., 24 (2004), 171-177.

64. C. Oehr, "*Plasma surface modification of polymers for biomedical use*", Nucl. Instr. and Meth. in Phys. Res. B, 208 (2003), 40–47.

65. D. Hegemann, H. Brunner, C. Oehr, "*Plasma treatment of polymers for surface and adhesion improvement*", Nucl. Instr. and Meth. B, 208 (2003), 281-286.

66. E.M. Liston, L. Martinu, M.R. Wertheimer, “Plasma surface modification of polymers for improved adhesion: a critical review”, J. Adhes. Sci, 7 (1993), 1091-1127.

# CHAPTER 2

# THE TiN$_X$ SYSTEM*

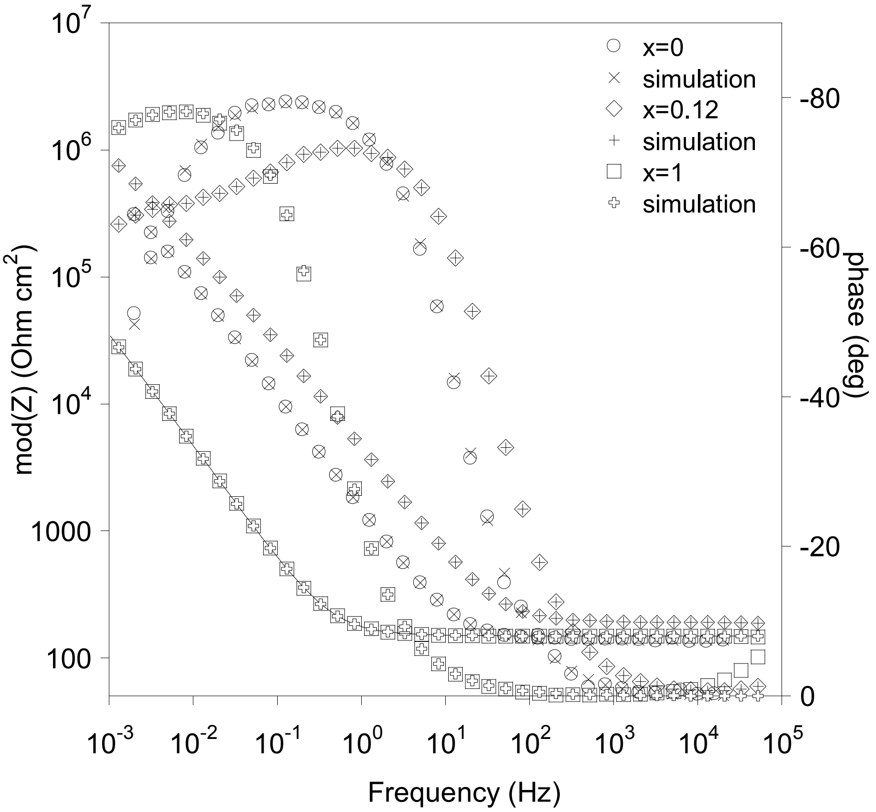

"*The impedance modulus is clearly lower for the zone II TiN$_x$ sample...*"

---

[*] This chapter is based on the following publication:

P. Pedrosa, E. Alves, N.P. Barradas, P. Fiedler, J. Haueisen, F. Vaz, C. Fonseca, "*TiN$_x$ coated polycarbonate for bio-electrode applications*", Corrosion Science 56 (2012) 49-57.

The following chapter refers to the state-of-the-art within the group at the beginning of the present thesis. The $TiN_x$ system had already been previously studied to be used as bioelectrodes in titanium disk substrates[1]. The results were promising, namely the excellent chemical resistance of the N-rich coatings in the presence of synthetic sweat, which led to the conclusion that the $TiN_x$ system was, in fact, a suitable candidate to be further studied. Hence, the same $TiN_x$-coated titanium disk electrodes were tested by recording EEG signals in parallel with the commercially used wet Ag/AgCl ones[2]. Once more, encouraging results were obtained in terms of signal quality. However, dependences between the electrode shape (planar disks) and the obtained results could not be ruled out, thus it was decided that a new electrode design (flexible polymeric multipin) should be explored. The new design should be able to allow an effective hair interfusion in order to minimize the electrode-skin impedance.

Consequently, in order to establish correlations with the previously results obtained in titanium disks and to assess the low-temperature sputtering viability on polymeric substrates (in terms of adhesion, morphological and structural stability of the coatings), the $TiN_x$ system was sputtered onto polycarbonate disks. In opposition to what was done when using the titanium disks, no temperature or bias voltage could be used, in order not to damage the polycarbonate substrates. In this way, using a simple planar shape, the optimization of the sputtering conditions and subsequent characterization should be simplified. The obtained results are then patent in the following chapter.

The main results that raised from the work performed in this chapter indicated that a stoichiometric $TiN_x$ matrix appeared to be the most suitable to be used as bioelectrodes, since lower passive dissolution currents, as well as lower impedance values (cover figure) and electrochemical noise and drift values comparable to the wet Ag/AgCl commercial electrodes

---

[1] L.T. Cunha, P. Pedrosa, C.J. Tavares E. Alves, F. Vaz, C. Fonseca, "*The role of composition, morphology and crystalline structure in the electrochemical behaviour of $TiN_x$ thin films for dry electrode sensor materials*", Electrochimica Acta 55 (2009) 59-67.

[2] P. Fiedler, L.T. Cunha, P. Pedrosa, S. Brodkorb, C. Fonseca, F. Vaz, J. Haueisen, "*Novel $TiN_x$-based biosignal electrodes for electroencephalography*", Measurement Science and Technology 22 (2011) 1-7.

were found. In addition, the stoichiometric TiN$_x$ films showed the best adhesion to the PC disk substrates, as it can be seen in Fig. 2.1.

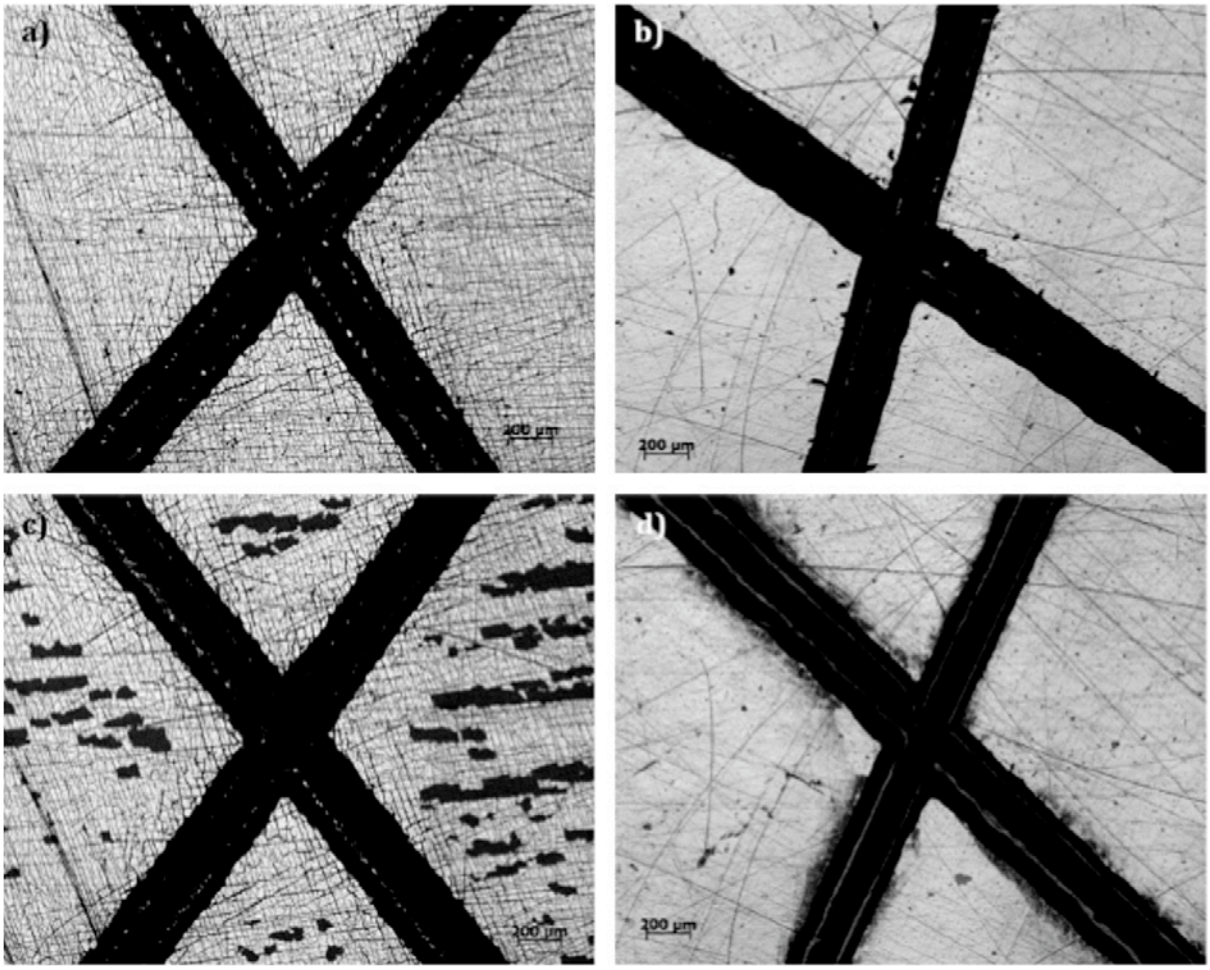

**Figure 2.1.** x-cut tape test performed on the surface of representative samples of the TiN$_x$ thin film system. (a) under-stoichiometric sample before removal of the tape, (b) stoichiometric sample before removal of the tape, (c) under-stoichiometric sample after removal of the tape and (d) stoichiometric sample after removal of the tape.

Consequently, the stoichiometric TiN$_x$ coatings were selected for further investigations (Ag doping, chapter 3) due to the aforementioned set of characteristics that make them, *a priori*, the most suitable ones for bioelectrode applications.

Corrosion Science 56 (2012) 49–57

Contents lists available at SciVerse ScienceDirect

Corrosion Science

journal homepage: www.elsevier.com/locate/corsci

# TiN$_x$ coated polycarbonate for bio-electrode applications

P. Pedrosa [a,b,e], E. Alves [c], N.P. Barradas [c], P. Fiedler [d], J. Haueisen [d], F. Vaz [e], C. Fonseca [a,b,f,*]

[a] Universidade do Porto, Faculdade de Engenharia, Departamento de Engenharia Metalúrgica e de Materiais, Rua Roberto Frias, s/n, 4200-465 Porto, Portugal
[b] SEG-CEMUC – Department of Mechanical Engineering, University of Coimbra, Rua Luís Reis Santos, 3030-788 Coimbra, Portugal
[c] Instituto Tecnológico Nuclear, Dept. Física, E.N. 10, 2686-953 Sacavém, Portugal
[d] Institute of Biomedical Engineering and Informatics, Ilmenau University of Technology, Ilmenau, Germany
[e] Centro de Física, Universidade do Minho, 4710-057 Braga, Portugal
[f] INEB – Instituto de Engenharia Biomédica, Divisão de Biomateriais, Universidade do Porto, Rua do Campo Alegre, 823, 4150-180 Porto, Portugal

## ARTICLE INFO

*Article history:*
Received 8 September 2011
Accepted 25 November 2011
Available online 3 December 2011

*Keywords:*
A. Sputtered films
B. EIS
B. Cyclic voltammetry
B. XRD
C. Passivity

## ABSTRACT

Titanium nitride (TiN$_x$) thin films were deposited by PVD, in a wide range of compositions ($0 < x < 0.99$), on polycarbonate (PC) substrates, aiming at studying their potential application as bio-electrodes. The electrochemical study of the TiN$_x$ films, performed in an isotonic sodium chloride solution, proved the very good chemical stability of all films in salt solution conditions. On the other hand, the electrochemical noise analysis showed that the electrical noise generated at the stoichiometric TiN/electrolyte interface is of the same magnitude as that generated by the traditional Ag/AgCl electrodes.

## 1. Introduction

Electroencephalography (EEG) is the recording of the brain electrical activity along the scalp [1]. EEG is nowadays the most widely used brain imaging technique. It provides very good time-resolution of brain activity, and it offers significant advantages over competing state of the art technologies, such as MRI (magnetic resonance imaging) and CT (computerized tomography), both in terms of cost and space requirements. The conventional recording set-up generally involves the use of silver/silver chloride electrodes (Ag/AgCl) for signal transduction [1]. These are very reliable non-polarizable electrodes, with low skin-contact impedance values of the order of a few tens of k$\Omega$ cm$^2$ which are almost frequency independent [2]. However, skin preparation and gel paste application are needed before the exam in order to lower the skin/electrode impedance. This preparation is time consuming, uncomfortable to the patient and requires trained staff.

In order to overcome the drawbacks of the Ag/AgCl electrodes, a new class of devices is being investigated, for which no skin preparation or gel application are needed, the so-called “dry” electrodes. In these electrodes, the sensors are inert materials, either a metal or an insulator [3,4]. In a previous work [5] the authors investigated a dry electrode sensor, based in a titanium nitride (TiN) thin film deposited on a titanium substrate. TiN is an electrically conductive material, with a good chemical stability in most media and outstanding mechanical properties, used in a very broad range of applications, including in the biomedical area [6]. The influence of the N/Ti ratio on the structural, morphological and electrochemical properties of the TiN film in contact with synthetic sweat was studied, and it was concluded that the stoichiometric and slightly over-stoichiometric composition (N/Ti $\geqslant$ 1) were the most adequate for the applications envisioned [5].

In this work the titanium substrate was replaced by polycarbonate (PC), resulting in a potentially much cheaper and lighter electrode. These are two important advantages, particularly if 128 or even 256 electrodes are to be used for a single exam.

However, there are two important differences between using titanium or PC as substrates for the TiN PVD thin film deposition: (i) there is no chemical affinity between TiN and PC, so the PC surface must be activated before deposition in order to achieve good adhesion of the film to the polymeric substrate, and (ii) the deposition on PC cannot be performed at the high temperatures usual for metals [5], which limits the kinetic energy available to enhance interfacial adhesion and structural arrangements that help the film to reach a stable thermodynamic state.

In this work the structural, mechanical and electrochemical behaviour of titanium nitride (TiN$_x$) thin-film coated polycarbonate (PC) was studied in order to optimize the deposition conditions for bio-electrode applications. A comparison with commercial silver/silver chloride (Ag/AgCl) electrodes was performed.

---

* Corresponding author at: Universidade do Porto, Faculdade de Engenharia, Departamento de Engenharia Metalúrgica e de Materiais, Rua Roberto Frias, s/n, 4200-465 Porto, Portugal. Tel.: +351 22 508 1995; fax: +351 22 508 1447.
*E-mail address:* cfonseca@fe.up.pt (C. Fonseca).

0010-938X/$ - see front matter © 2011 Elsevier Ltd. All rights reserved.
doi:10.1016/j.corsci.2011.11.008

## 2. Experimental details

$TiN_x$ films were deposited on PC (disks), on glass and on silicon (100) substrates, in a laboratory-sized reactive DC magnetron sputtering system. The PC disks, 20 mm in diameter and 4 mm thick, were press moulded from standard PC pellets (250 °C, 20 tons). The discs were: (i) wet abraded with SiC paper of decreasing grain sizes, (ii) polished with diamond pastes of 6 and 1 μm, (iii) cleaned in a sonicator with isopropanol (5 min) and (iv) distilled water (5 min) just before each deposition. Processes (iii) and (iv) were also used for the glass and Si substrates.

The films were prepared with the substrate holder positioned at 70 mm from the target, using a DC current density of 100 A $m^{-2}$ on the titanium target (99.96 at. % purity). A gas atmosphere composed of argon + nitrogen was used. The argon flow was kept constant at 60 sccm (Standard Cubic Centimetres per Minute, corresponding to $1 \times 10^{-6}$ $m^3/s$), which resulted in a partial pressure of 0.3 Pa for all depositions. The nitrogen flow varied from 0 to 5.5 sccm (corresponding to a partial pressure variation between 0 and $3.6 \times 10^{-2}$ Pa). The working pressure was approximately constant during the depositions, varying only slightly between 0.3 and 0.4 Pa. No bias voltage or external heating were used in order to avoid the polymeric substrates degradation. A thermocouple was placed close to the surface of the "substrate holder" on the plasma side (not in direct contact, since depositions were done in rotation mode), and the temperature was monitored during the entire film deposition time. A delay time of 5 min was used before positioning the surface of the samples in front of the Ti target in order to avoid film contamination resulting from previous depositions (which may have resulted in some target poisoning), and also to assure a practically constant deposition temperature during film growth.

The atomic composition of the as-deposited samples was measured by Rutherford Backscattering Spectroscopy (RBS) using (1.4, 1.75) MeV and 2 MeV for the proton and $^4He$ beams, respectively. Two detectors were used, located at scattering angles 140 and 180° (annular detector). Measurements were made for two sample tilt angles, 0 and 30°. Composition profiles for the as-deposited samples were determined using the software NDF [7]. For the $^{14}N$, $^{16}O$ and $^{28}Si$ data, the cross-sections given by Gurbich were used [8]. The area analyzed was about $0.5 \times 0.5$ $mm^2$. The uncertainty in the N concentrations is around 5 at. %.

The structure and phase distribution of the coatings were assessed by X-ray diffraction (XRD), using a Bruker AXS Discover D8 diffractometer, operating with Cu $K_\alpha$ radiation and in a Bragg–Brentano configuration. The XRD patterns were deconvoluted and fitted with a Voigt function to determine the structural characteristics of the films, such as the peak position ($2\theta$), the full width at half maximum (FWHM) and the crystallite size.

Morphological features of the samples were probed by scanning electron microscopy (SEM), carried out in a Jeol JSM 6301F microscope operating at 10 keV. The adhesion level of the as-deposited $TiN_x$ coatings to the polymeric substrates was assessed by the X-cut tape test, according to the ASTM D3359 standard. The samples were then analysed by optical microscopy before and after test.

In the voltammetric experiments, the potential was scanned from −0.6 to 2.5 V at 1 mV/s (linear voltammetry), and from −0.4 to 0.4 V at 0.1 to 5 V/s (cyclic voltammetry). The experimental set-up consisted of a EG&G PAR 273A potentiostat, driven by the CorrWare/CorrView@ software from Scribner. The three-electrode configuration was used with a saturated calomel electrode (SCE) and a Platinum wire as the reference and auxiliary electrodes, respectively. A 0.9% sodium chloride solution was used in all electrochemical studies, in order to simulate the sweat effect. Electrochemical impedance spectra (EIS) were acquired daily for a week, using a Solartron 1250 frequency response analyser and a EG&G PAR 273 potentiostat, driven by the Zplot/Zview@ software from Scribner. The frequency was scanned from 20 kHz to 1 mHz, with a 7 mV (rms) amplitude ac signal. The Zview software was used for the simulations of the experimental spectra.

The electric noise measurements were performed with a Gamry G300 potentiostat driven by the ESA410 software. Several couples of similar samples, either Ag/AgCl (Easycap@ sintered disc electrodes, 12 mm in diameter) or PC coated with TiN, were immersed in the sodium chloride solution and the open circuit potential difference acquired with a 500 Hz sampling rate for periods of 10 min. The electrochemical cell was kept inside a Faraday cage. Data analysis was performed by first applying a 20th order Buttherworth bandpass filter (0.5–100 Hz). The first 10 s of each filtered data set were neglected to avoid including considerable filter artefact in subsequent evaluations. Then, successive segments of 30 s were considered for the calculation of the RMS values of noise and drift rate, over the total acquisition times. The power spectral density (Welch estimation) was calculated for 10 min segments, representative of all the Ag/AgCl commercial electrodes and $TiN_x$ sample couples.

## 3. Results and discussion

### 3.1. Composition of the as-deposited samples

The evolution of the composition ratio (N/Ti) as a function of the nitrogen partial pressure is plotted in Fig. 1. The partial pressure of nitrogen, $P_{N_2}$, was monitored by the nitrogen flow rate, $\phi_{N_2}$. No argon was detected by RBS analysis in the as-deposited samples, which means that its content should be less than ~3–5 at. %.

As it can be seen from Fig. 1, the increase of the nitrogen partial pressure strongly influences the atomic concentration of the chemical elements in the layers. Initially, from 0 to $2 \times 10^{-2}$ Pa, the evolution of the N/Ti atomic ratio is very smooth. At higher nitrogen partial pressures, from $2 \times 10^{-2}$ to $3.6 \times 10^{-2}$ Pa, a small increase in the nitrogen partial pressure leads to an abrupt and almost linear evolution of the N/Ti atomic ratio. At the highest $N_2$ partial pressures, nearly stoichiometric films were formed. No over-stoichiometric films were obtained, otherwise a third zone should appear, where the N/Ti atomic ratio evolution would stabilize [5].

The high amounts of Ti atoms that are sputtered from the target and the low nitrogen pressures inside the reactor up to ~$2 \times 10^{-2}$

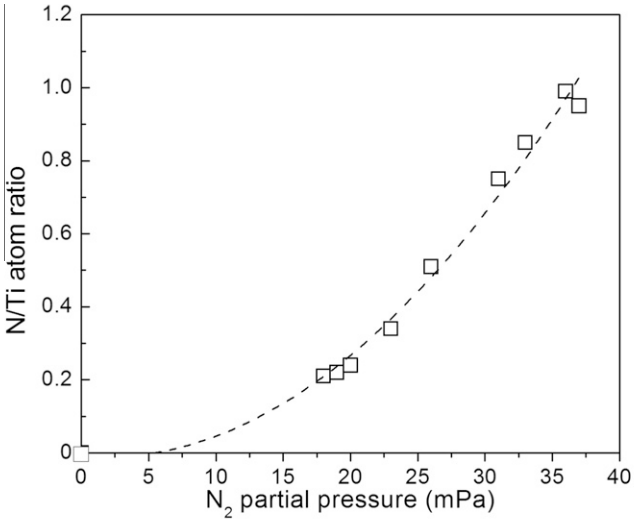

**Fig. 1.** Plot of the nitrogen content in the films ($x$ = N/Ti atomic ratio) as a function of the nitrogen partial pressure inside the sputtering chamber.

Pa create a high mean-free path for the Ti atoms. As no substrate bias voltage or external heating were used during the sputtering process, the low amount of nitrogen available cannot be easily absorbed in the growing films due to mobility constraints. As the amount of available nitrogen increases (with the increase of its partial pressure), its incorporation in the film is facilitated, thus explaining the rapid increase of the N/Ti ratio in this zone. When the nitrogen partial pressure is relatively high, the mean-free path starts to decrease, as well as the sputtering rate, due to a higher degree of nitrogen coverage of the cathode (target) and increasing secondary electron coefficient [5]. This may explain why the $TiN_x$ film produced with the highest nitrogen partial pressure ($3.7 \times 10^{-2}$ Pa) has a very similar value of the N/Ti atomic ratio to that of the film obtained at $3.6 \times 10^{-2}$ Pa.

### 3.2. Structural and morphological characterization of the samples

Previous studies of sputtered $TiN_x$ coatings on metallic substrates show that as N is added to Ti, the atomic lattice progressively changes from the hcp α-Ti phase to the fcc δ-TiN phase. This is due to the progressive increase of lattice distortions, as a result of the lattice size increment coming from N insertions [5].

Analysing the XRD diffraction patterns shown in Fig. 2, the overall tendency seems similar to what is observed for films deposited on metallic substrates [5]. However, a closer look reveals that the diffraction patterns can be clearly divided into distinct zones. Zone I comprehends the films prepared with the lowest nitrogen partial pressures, corresponding to highly sub-stoichiometric films, with N/Ti ratios up to 0.24. The films prepared within this zone revealed a set of diffraction patterns which are not easily indexed, since their angular position is situated between those of δ-TiN (fcc – ICDD card no. 00-038-1420) and α-Ti (hcp – ICDD card no. 00-038-1420). Nevertheless, and due to the low mobility and low $N_2$ partial pressures some nitrogen is expected to be incorporated in interstitial positions within the Ti lattice, forming a kind of Ti(N) metastable solution. The nitrogen incorporation leads to the expansion of the Ti lattice observed in this first zone, demonstrated by the lower angular positions of the diffraction peaks when compared to the position of the (1 0 1) peak from the Ti lattice.

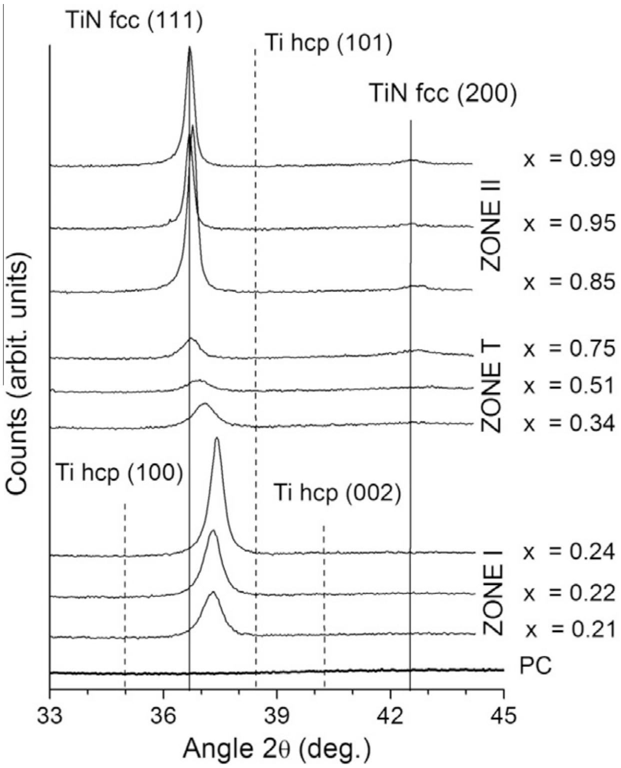

**Fig. 2.** Evolution of the XRD patterns of the films as a function of N/Ti atomic ratio (*x*).

The titanium–nitrogen phase diagram is complex, but basically the Ti crystal is considered to be an "interstitial" crystal where N atoms fit into the gaps of the Ti structure. This structure evolves from hexagonal α-Ti (space group P63/mmc), to face-centred-cubic δ-TiN (space group Fm-3 m) as the amount of nitrogen is increased. The α-Ti lattice can accept small amounts of nitrogen at octahedral sites [9], but since PVD is a thermodynamically non-equilibrium process, the α-Ti lattice may be forced to accept more nitrogen atoms due to hindered mobility of the deposited particles [10]. Therefore, an oversaturated metastable solution of nitrogen in titanium is formed for the lower N contents. The shift in the diffraction lines revealed by Fig. 2 is thus a consequence of the N interstitials in octahedral α-Ti sites, which causes lattice distortion. The fact that no significant variations are observed in peak positions is also consistent with the similar composition of the three films prepared within this zone.

A second major zone, zone II, can be indexed to the films prepared with the higher nitrogen partial pressures, corresponding to roughly stoichiometric films, with N/Ti ratios ranging from 0.85 up to 0.99. As one would expect from its particular close-stoichiometric condition, the films develop a fcc-type structure characteristic of stoichiometric-like TiN films. The fcc (1 1 1) peak is clearly visible and is placed in its expected angular position. An important note is that within this second zone the crystallinity of the films is particularly evident, as demonstrated by the sharpening of the diffraction peaks and their increased intensity. There is still a slight shift of the diffraction peaks, towards lower diffraction angles, which can be understood by the already mentioned stoichiometric or closely stoichiometric conditions of the films within this zone.

Between these two major zones, one can define a transition zone, zone T, comprehending the films that exhibit intermediate N/Ti ratios – from 0.34 to 0.75. The diffraction patterns of this zone T suggest the existence of a transition between the results obtained for the films indexed to the previous two major zones, evidenced by the progressive shift towards lower diffraction angles, consistent with the change from the two previous crystalline phases (hcp Ti and fcc TiN).

While in the films from zone I a growing crystallinity was observed (increasing peak definition and intensity), in zone T the films are quasi-amorphous, as demonstrated by the significant peak broadening and low intensity of the diffraction pattern. This behaviour is not surprising due to the particular composition of the samples: relatively high amounts of N if regarded from a hcp, α-Ti like structure in which they would occupy interstitial positions, but relatively low from a TiN-like phase, in which a significant amount of N vacancies would be developed. The exact nature of the poor crystallinity is difficult to ascertain unequivocally, but it seems to be rather close to that of fcc-TiN. In fact, the correspondent phase diagram [11–13] shows that the δ-TiN phase can occur already for atomic concentrations of N as low as 30 at. % which is the case of the samples prepared within this transition zone. Moreover, the large lattice deformations that result from the formation of the cubic lattice in these high sub-stoichiometric conditions (resulting from extensive N vacancies), leads to the development of crystalline structures with extensive lattice defects, and thus to the poor crystallinity observed in these films. As the N/Ti atomic ratio increases, the higher amounts of $N_2$can compensate the lack of mobility in the system, thus being inserted within the lattice of TiN (fcc), giving rise to a less vacant lattice. As a result, the diffraction peak shifts continuously towards lower diffraction angles, approaching the expected position of the (1 1 1) peak from TiN. This explains the observed behaviour of the films indexed to this zone. For $x = 0.75$, the (2 0 0) diffraction peak of δ-TiN can also be found, as a broad and low intensity peak around $2\theta$–42.5°, reinforcing the assignment of these films to the fcc TiN-type structure.

Further evidence of these different groups of samples within the whole set of prepared films can be seen in Fig. 3, where the grain sizes were obtained after the XRD peaks deconvolution. The values of grain size within the transition zone should be seen with care since the diffraction patterns are difficult to deconvolute. It is important to note that the results correlate very well with the diffraction patterns, given that the films crystallinity is clearly higher in zones I and II.

The films from zones I and T give rise to grains (values around ∼15 nm) that seem to be predominantly smaller than those of zone II (above 25 nm). This tendency towards smaller grain sizes is typical of highly saturated metal–metalloid compounds, and can be described by the Gibbs–Thomson equation [14]. Looking closely into zone I, there seems to be a tendency to have a small increase of grain size with increasing N/Ti atomic ratios, which may be due to the increase of the films crystallinity, as shown above in Fig. 2.

When the transition zone is reached, there is a large peak shift towards lower diffraction angles, which suggests that nitrogen is being inserted in the Ti lattice, thus exhibiting small grain size predominance. It is known that the introduction of nitrogen into Ti lattices implies that the grain growth is inhibited, causing the formation of more grain boundaries and distortion of the lattices (large micro strains are developed) with the nitrogen interstitial sites [5].

In zone II, the small grain size tendency is changed, as the growth is highly (1 1 1) textured and a high level of crystallinity is attained, which is usually associated with a grain growth phenomena [15]. These results of grain size evolution induce, again, the existence of two major types of films, where the first two zones have lower grain sizes when compared to the samples indexed to zone II, where the films present relatively larger grains.

Fig. 4 shows the SEM micrographs of the main types of morphologies observed for the set of $TiN_x$ films that were prepared. The plan view is shown on the micrographs of Fig. 4. Two main types of morphological arrangements are revealed, showing a good correlation with the compositional and structural analysis. The films from both zones I and T display dense, rough and granular-like structures (Fig. 4a and b), where the discontinuities observed are related with the initial polishing features. On the other hand, the films from zone II display grains with a pyramidal shape and a

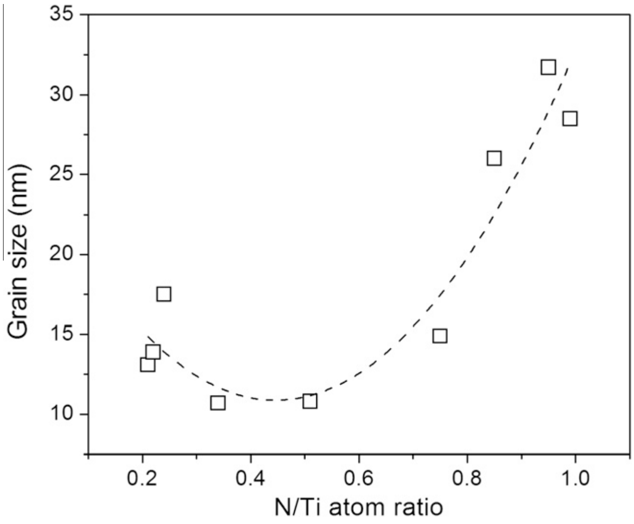

**Fig. 3.** Plot of the titanium nitride grain size calculated from the XRD spectra as a function of the N/Ti atomic ratio ($x$).

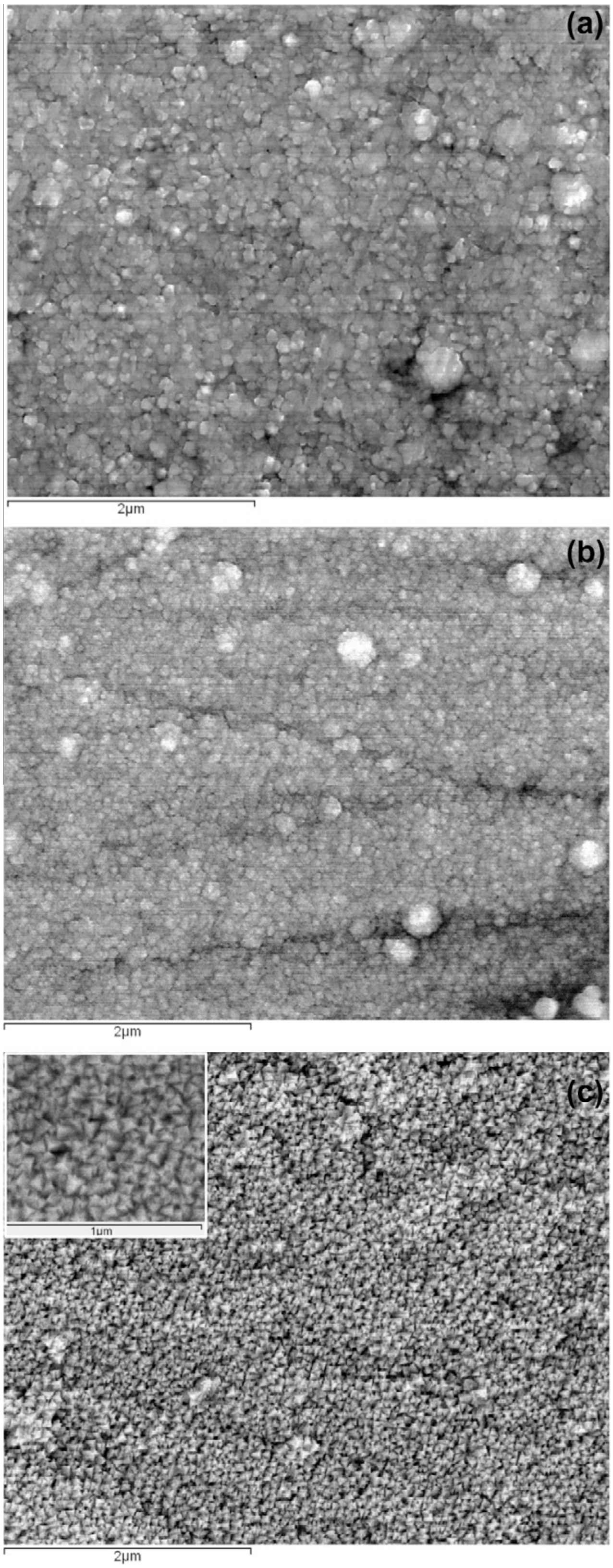

**Fig. 4.** SEM surface images of the $TiN_x$ coatings depoited on PC, taken from films in zone I (a), zone T (b) and zone II (c).

porous structure. The existence of porous films when high N/Ti ratios are used was already observed for $TiN_x$ films deposited on titanium and silicon [5,15] and it is related with the strong internal stresses generated on passing from the α-Ti to the δ-TiN lattice [16,17]. According with our previous studies on titanium, a columnar growth of the films is expected, with the pyramidal grain shape corresponding to the column tops and the pores are ascribed as intercolumnar spacing [5].

When compared with the $TiN_x$ films grown at higher temperatures on metallic substrates [5], some significant differences exist. In fact, although both the high (deposited on titanium) and low temperature (deposited on PC substrates) films show the same structural evolution with the nitrogen content, such evolution is clearly delayed in terms of composition for the low-temperature films. For example, for N/Ti = 0.7 the high temperature film already displays a well-defined δ-TiN structure [5], whereas for the film with the approximately same composition deposited on PC (N/Ti = 0.75) the structure is still essentially amorphous. Also, the columnar structure of the δ-TiN phase is better defined in the case of the high temperature films.

### 3.3. $TiN_x$ adhesion behaviour to PC

In order to test the adhesion level of the as-deposited $TiN_x$ coatings to the PC substrate, the X-cut tape test (ASTM standard D3359-08) was performed on samples from zone I (N/Ti = 0.24) and zone II (N/Ti = 0.95). Samples from zone T were not tested because they have morphology similar to the zone I samples.

Fig. 5 presents the surface aspect of the $TiN_x$ coated PC samples from zones I and II before removal of the tape (a and b), and zones I and II after the removal of the tape (c and d). Major differences in terms of adhesion are apparent from the after test photos, (Fig. 5c and d), where a much stronger delamination is apparent in the under-stoichiometric sample. The distorted lattice with strong internal stresses of zone I samples leads to an as-deposited coating that is already severely cracked due to the cutting procedure (Fig. 5a), giving rise to a very poor adhesion level, rated as 0A – *removal beyond the area of the X* (Fig. 5c). On the other hand, the as-deposited sample from zone II (Fig. 5b) presents only some initial scratches due to the polishing procedure and no further cracking of the coating is visible. Consequently, the adhesion behaviour of the sample from zone II is much better than the one from zone I, being rated as 4A – *trace peeling or removal along incisions or at their intersection.* In conclusion, zone I samples seem unsuitable for electrode application, where repeated skin contact and cleaning would most likely lead to a rapid damaging of the coatings.

### 3.4. Electrochemical studies in sodium chloride solutions

#### 3.4.1. Open circuit potential

The open circuit potentials (OCP) for the $TiN_x$ samples are shown in Fig. 6. The results indicate that there is a stabilization period of about 10–15 min, common to all samples, after which a continuous and smooth potential decrease takes place, tending to a plateau. The Ti-rich samples consistently display less noble OCP values. This lower thermodynamic stability may be related with the fact that, as described in section 3.2, these samples display either amorphous or highly distorted and metastable structures, and therefore higher reactivity than the stoichiometric, well-crystallized ones. Also, the Ti-rich films have non-oxidized free titanium within their structures, which is much more reactive towards oxygen than stoichiometric or close-stoichiometric titanium nitride. Finally, a different surface charge contribution effect also cannot be discarded to help explaining the observed differences.

#### 3.4.2. Potentiodynamic analysis

The cyclic voltammetry (CV) curves show a capacitive behaviour extending from about −0.25 to –0.25 V for films from zone I and zone II at low sweep rates, see Fig. 7. However, for zone II films, at the highest sweep rates, the behaviour tends to incorporate a resistive component, as shown in Fig. 7B. This behaviour is characteristic of a porous electrode [15], which corroborates the SEM results

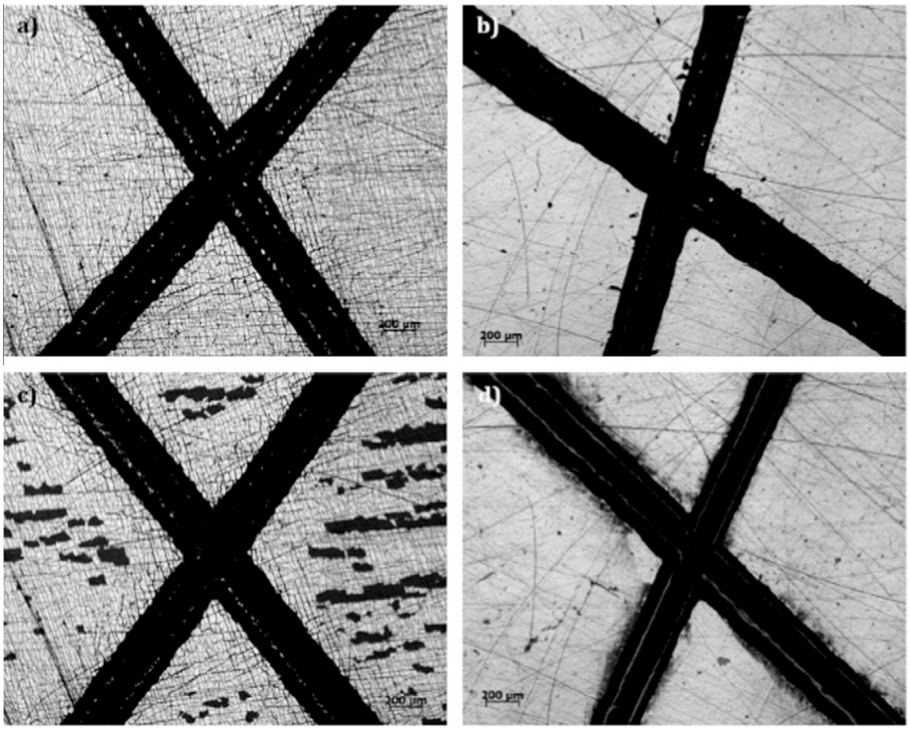

**Fig. 5.** Surface aspect of the $TiN_x$ coated PC samples from (a) zone I before removal of the tape, (b) zone II before removal of the tape, (c) zone I after removal of the tape and (d) zone II after removal of the tape.

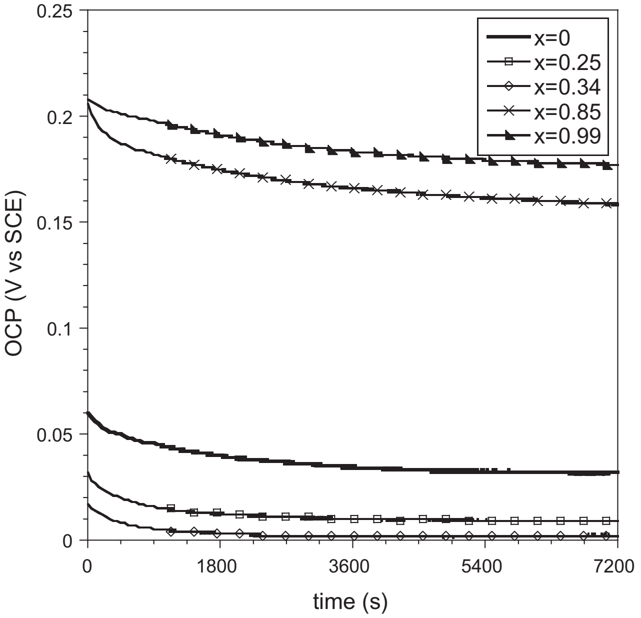

**Fig. 6.** Open circuit potential (OCP) vs time for TiN films representative of all compositions. The compositions are indicated as $x$ = N/Ti atomic ratio.

displayed in Fig. 4c. Similar behaviour was previously observed by the authors for stoichiometric TiN films deposited on titanium substrates at high temperatures [5].

The double layer capacitances were calculated for all film stoichiometries from the slope of the line defined by the capacitive current at 0 V (well within the double charging region) vs sweep rate. Only the sweep rates where the capacitive behaviour was observed were considered for the calculations. In these conditions, the evolution of the double layer capacitance values reflects the evolution of the real area of the samples, thus showing how the morphologies of the films change with the N/Ti ratio, Fig. 8. The same three regions already identified in the XRD spectra, Fig. 2, can be seen, showing that the transition from zone I to zone T films takes place with only a slight area increase, whereas the transition from zone T to zone II films involved an important area increase that should be essentially ascribed to the development of the porous structure, following the thin film crystallization in the δ-TiN structure.

The electrochemical potential was also swept at low speed (1 mV/s) in a much wider potential range (−0.75–2.5 V), Fig. 9. Similar curves are displayed by all films, with a small plateau ranging from 0.07 to 0.2 V corresponding to the formation of oxynitrides, and a current peak around 1.5 V ascribed to further oxidation of the oxynitrides, with the formation of titanium oxide and of nitrogen gas [5]. These curves also show that all $TiN_x$ films are chemically stable around their OCP's, as their dissolution currents are in the sub-micro A/cm$^2$. The higher passivation currents observed for titanium and the Ti-rich films are most likely related with the titanium oxidation. We note that the real area of the films was taken into account in the curves, according with the double layer calculations of Fig. 8.

### 3.4.3. Electrochemical impedance spectroscopy

The Bode spectra for three samples representative of all stoichiometries are shown in Fig. 10. The impedance modulus is clearly lower for the zone II TiN sample, as expected from the associated morphologic changes seen in Fig. 4. The phase vs frequency plot for titanium and the zone II films display a quite simple structure that is indicative of a single time constant. On the other hand, the spectrum for the zone I films seems to indicate the presence of more than one time constant.

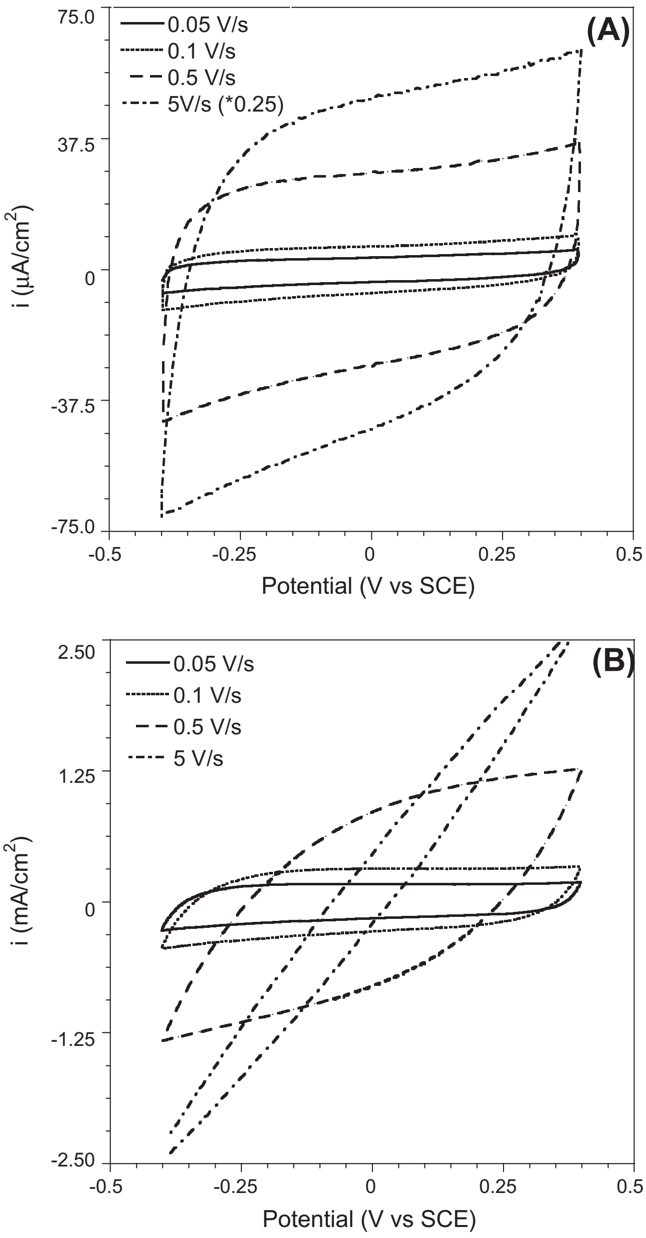

**Fig. 7.** Cyclic voltammograms for TiN films representative of the two behaviours observed for the films: (A) N/Ti = 0.25 (non-porous film) and (B) N/Ti = 0.99 (porous film).

Based on these observations, and taking into account the well-known self-passivating behaviour of titanium, the electrical circuit displayed in Fig. 11 was chosen to describe the interfacial behaviour of the thin films. All capacitive elements were first replaced by constant phase elements (CPE), in order to account for roughness and other surface inhomogeneities or relaxation processes. Following the simulations one of the capacitive elements showed "$p$" values consistently around 1, so a simple capacitor was finally used. The impedance of a CPE can be defined by Eq. (1):

$$Z_{CPE} = 1/[T(j\omega)^p] \qquad (1)$$

where "$T$" and "$p$" are the CPE parameters and $\omega$ stands for the angular frequency [18].

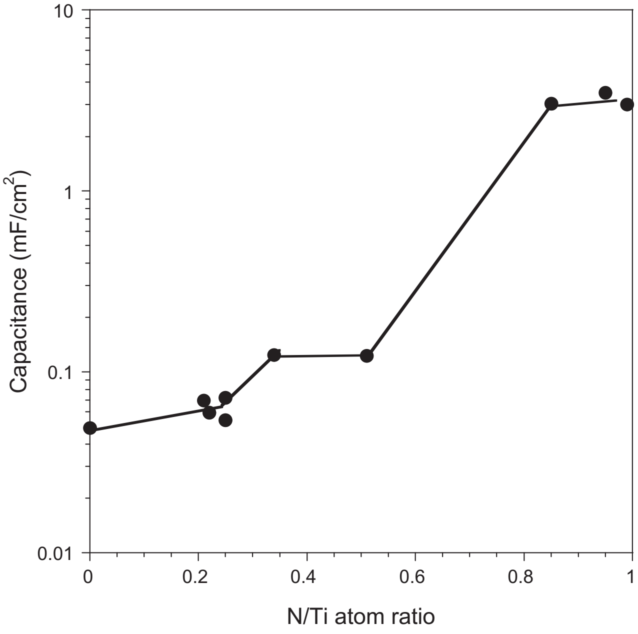

**Fig. 8.** Capacitance of the double charging region vs N/Ti thin film composition. The capacitance values were calculated for each thin film composition from the slope of the current (taken at 0 V vs SCE) vs sweep rate lines.

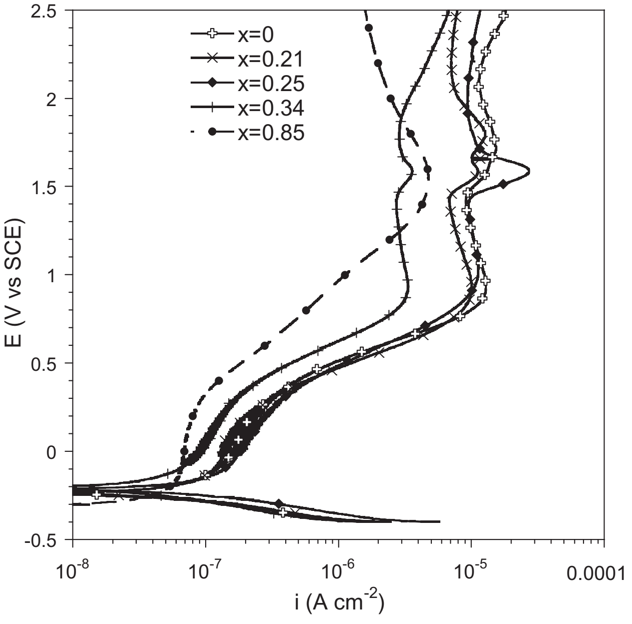

**Fig. 9.** Linear voltammograms as a function of the $x$ = N/Ti film atomic composition. Sweep rate: 1 mV/s.

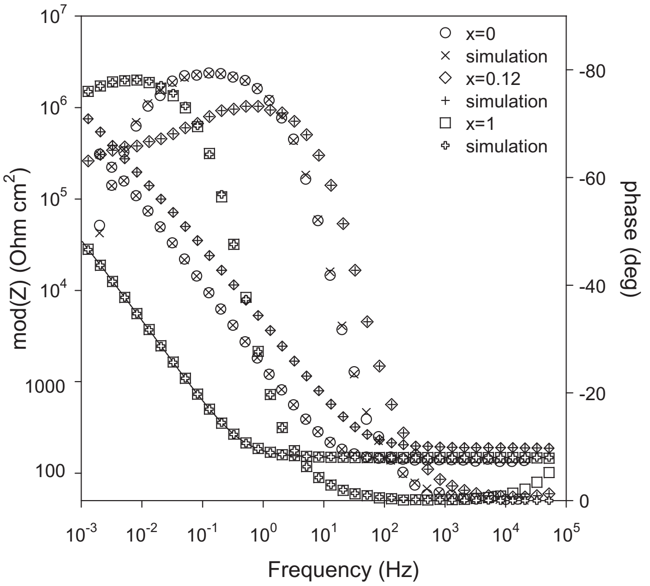

**Fig. 10.** Bode spectra for titanium and samples representative of regions I and II. The crosses correspond to the simulated spectra according with the circuit of Fig. 11.

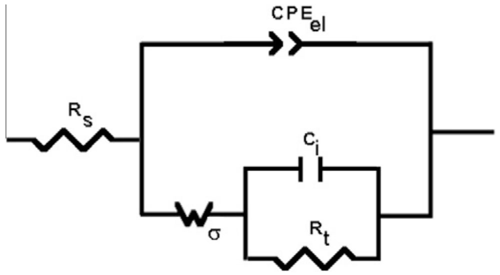

**Fig. 11.** Equivalent circuit used for the simulation of the Ti/electrolyte and stoichiometric TiN/electrolyte interfaces.

In the electric circuit of Fig. 11, $R_s$ stands for the electrolyte resistance and the upper and lower branches of the parallel circuit account for the non-Faradic and Faradic interfacial processes respectively. $CPE_{el}$ simulates the double-layer capacitive behaviour of the TiN/electrolyte interface; the resistance to electronic charge transfer (that should be in parallel with $CPE_{el}$) was considered infinite as no redox reactions are supposed to take place, given the OCP of the interface (see Fig. 6).

In the lower branch, $W_\sigma$ stands for the ionic diffusion through the oxide/oxynitride, which was simulated with a semi-infinite Warburg diffusion element ($p = 0.5$ in Eq. (1)). The Warburg diffusion coefficient, "$\sigma$", relates with "$T_w$" value through Eq. (2) [5]:

$$\sigma = 1/(\sqrt{2}T_w) \tag{2}$$

In fact, TiN is often used in electronics for its atomic diffusion blocking effects. The terms ($CPE_i$, $R_t$) stand for the interfacial capacitance and charge transfer resistance due to the titanium oxide/oxynitride related electrochemical processes.

The simulations are in very good agreement with the experimental spectra, as shown in Fig. 10 and Table I. Titanium displays a "$p$" for the $CPE_{el}$ not far from 1, an indication of an essentially capacitive behaviour of the titanium oxide film, which was formed in contact with atmospheric oxygen. The high "$T_w$" value should be ascribed to a very thin and hydrated oxide film, thus with poor blocking ability. After the insertion of a small amount of nitrogen the blocking character of the film increases (lower $T_w$) and the charge transfer resistance increases. On the other hand, the high $CPE$ calculated for the stoichiometric TiN is an area effect related to porosity and was also observed by Norlin et al. [15]. In the case of the stoichiometric film both the high roughness and porosity should be responsible for the deviation from the ideal capacitor behaviour ($p = 0.82$). The charge transfer resistance is high for all films, corroborating the results of the very low dissolution currents observed in the neighbourhood of the OCP, Fig. 9. They are of the same order of magnitude as those obtained for the high temperature TiN films [5], meaning that the deposition temperature plays an important role on the structure of the films but not in their chemistry.

The "$R_t$" and the Warburg diffusion parameter ($\sigma$) vs composition obtained from the EIS spectra simulations are reported in Fig. 12. The

**Table I**
Electric circuit parameters calculated from the EIS simulated spectra of Fig. 10, according with the equivalent circuits of Fig. 11.

| N/Ti (at.) | $CPE_{el}$-$T$ ($\Omega^{-1}$ cm$^2$ s$^n$) | $CPE_{el}$-$P$ | $CPE_i$-$T_W$ ($\Omega^{-1}$ cm$^2$ s$^n$) | $CPE_i$-$T$ ($\Omega^{-1}$ cm$^2$ s$^n$) | $R_t$ ($\Omega$ cm$^2$) | $\chi^2$ |
|---|---|---|---|---|---|---|
| 0 | $1.2 \times 10^{-4}$ | 0.90 | $1.6 \times 10^{-4}$ | $6 \times 10^{-6}$ | $5.4 \times 10^5$ | $7 \times 10^{-4}$ |
| 0.12 | $3.1 \times 10^{-5}$ | 0.88 | $1.2 \times 10^{-5}$ | $4 \times 10^{-4}$ | $1.4 \times 10^4$ | $1 \times 10^{-4}$ |
| 0.99 | 0.0012 | 0.82 | 0.021 | 0.0015 | $5.1 \times 10^6$ | $5 \times 10^{-4}$ |

evolution of $\sigma$ with composition shows that ionic diffusion is important only for zone I films and the steep $\sigma$ decrease roughly accompanies the transition from zone I to zone T films. As stated before, it should be related with the decrease of crystalinity of the titanium lattice and the formation of a large number of vacancies that provide the necessary paths for ionic diffusion. We note that such high "$\sigma$" drop cannot be explained by simple area change effects. The $R_t$ values, which are related with the Faradic dissolution processes taking place at the interface, increase with the N/Ti ratio, in agreement with the higher reactivity of titanium that exists in the non-combined form in the Ti-rich films. As long as it combines with nitrogen, its reactivity decreases with the consequent increase of $R_t$. This trend is in good agreement with the voltammograms shown in Fig. 9.

The evolution of the electrical behaviour of the $TiN_x$ films with the immersion time was also assessed. All films displayed a very stable behaviour and no significant evolution was observed in the EIS curves except for a slight tendency for $R_t$ to increase.

### 3.4.4. Electrical noise measurements

A main requirement for a material to be used as a bio-electrode is its transparency to the bio-signal, meaning that it should not generate any noise that would mask the signal to be recorded. Thus, if one imagines that a layer of sweat forms between the electrode and skin, the electric noise developed at such an interface should be significantly lower than the ECG signal (~1 mV) or the EEG signal (~50 μV) being recorded.

The power spectral density (PSD) of noise for a stoichiometric TiN/TiN couple is reported in Fig. 13, together with the same plot for a Ag/AgCl/Ag/AgCl, commercial electrode couple. It is apparent that the noise generated by both couples is very similar over all the EEG frequency range as well as the corresponding RMS noise values: 3.23 ± 0.03 μV (TiN) and 2.80 ± 0.02 μV (Ag/AgCl) (vs SCE). There is an increase of the noise for lower frequencies, a typical behaviour already reported by other authors [19].

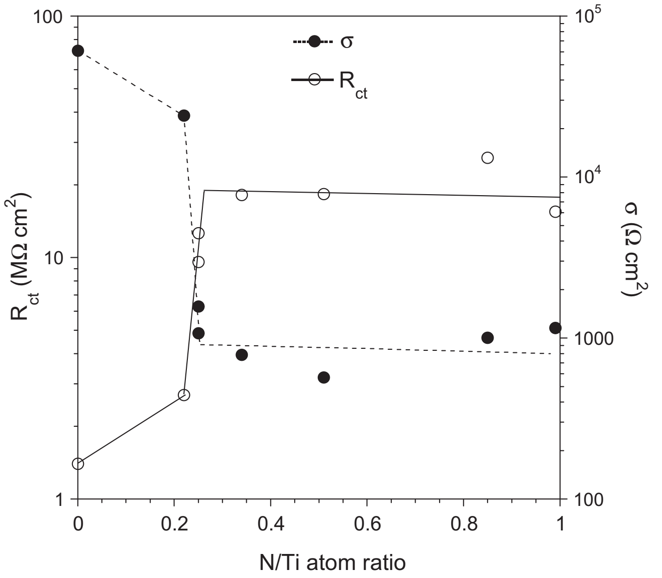

**Fig. 12.** Charge transfer resistance ($R_t$) and Warburg coefficient ($\sigma$) vs thin film composition, as calculated from the simulations of the EIS spectra.

The electrochemical potential drift rate and stabilization time are also important parameters to take into account, particularly when dealing with low frequency and/or small amplitude signals that may easily be masked if important drift rates are present. Concerning the Ag/AgCl electrodes, drift is practically inexistent and potential stabilization is almost instantaneous, as shown in Fig. 14. A much higher electrochemical potential irreproducibility exists among TiN couples. This was expected given that there is not a well-defined electrochemical process taking place at the interface to "lock" the electrochemical potential. However, the drift rate

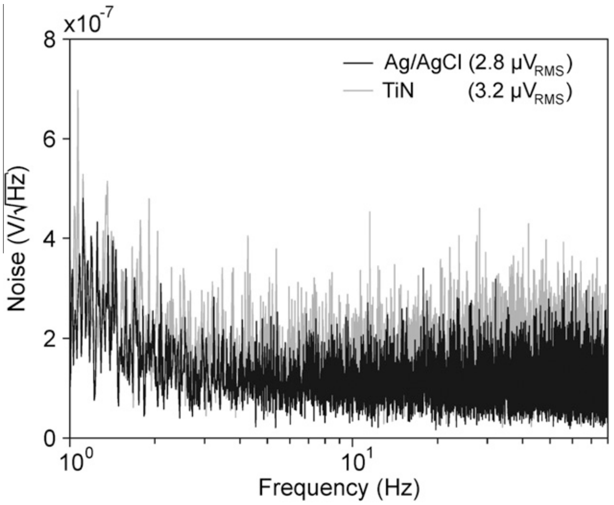

**Fig. 13.** Noise power spectral density (PSD) spectra for commercial Ag/AgCl and stoichiometric TiN electrode couples immersed in isotonic NaCl solution and RMS values of electric noise (SCE).

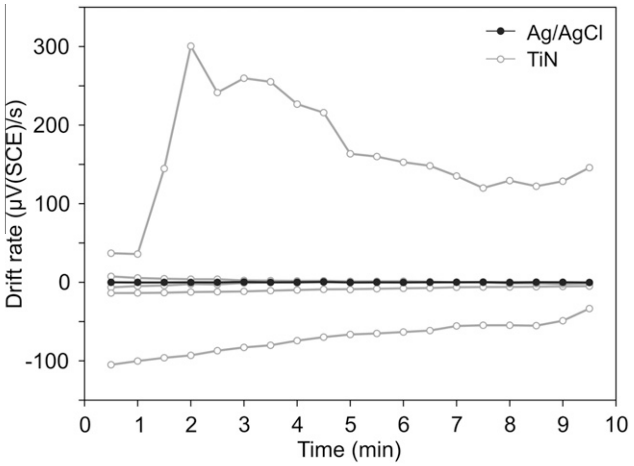

**Fig. 14.** Electrochemical potential drift rates (vs SCE) for commercial Ag/AgCl and stoichiometric TiN electrode couples immersed in isotonic NaCl solution.

decreases to acceptable values within 5–10 min, ensuring that low bio-potential values will be able to be measured.

## 4. Conclusions

In this work, $TiN_x$ thin film coated PC samples were studied in a wide range of compositions, aiming at selecting the best coating composition on PC for dry electrode applications. XRD analysis showed three different zones for the diffraction patterns of $TiN_x$, namely a distorted $\alpha$-Ti lattice for $N/Ti < 0.24$ (zone I), a well crystallized $\delta$-TiN structure for $N/Ti > 0.85$ (zone II) and a transition zone (zone T) between the two mentioned compositions, characterized by an essentially amorphous structure. The films in zones I and T are granular and compact whilst the films formed in zone II display granules with a pyramidal shape and a porous morphology.

All films proved to have a good chemical resistance in the presence of isotonic sodium chloride, independently of their composition. Passive dissolution currents densities below 1 $\mu A/cm^2$ were found in all cases, decreasing for higher N/Ti values. The EIS data showed significantly lower impedance values for the zone II films, what will facilitate bio-signal transfer in the presence of a sweat layer.

The adhesion tests proved that the coatings in zone II exhibit a clearly better adhesion than those from zone I, which was ascribed to a more stable and stress-free lattice.

Finally, electrochemical noise tests carried out in sodium chloride solution showed that zone II $TiN_x$ films display RMS noise values of the order of those measured for the classic Ag/AgCl electrodes but higher drift rates and potential irreproducibility. However, electrochemical potential reaches acceptable values within 5–10 min, making zone II $TiN_x$ films on PC suitable for dry electrode applications.

## Acknowledgements

This research is sponsored by FEDER funds through the program COMPETE-Programa Operacional Factores de Competitividade and by national funds through FCT-Fundação para a Ciência e a Tecnologia, under the project PTDC/CTM-NAN/112574/2009. Authors also aknowledge Eemagine GmbH, the CRUP (Conselho de Reitores das Universidades Portuguesas), through the Germany-Portugal bilateral exchange program, action A-31/11, the CEMUP for SEM analysis and A.V. Nóbrega from Minho University for supplying the polycarbonate samples. One of the authors (C. Fonseca) acknowledges sabbatical leave grants from FCT (SFRH/BSAB/1096/2010) and the Research Training Group Lorenz Force (GK 1567), Technical University of Ilmenau, Germany. P. Pedrosa acknowledges FCT for the Ph.D grant SFRH/BD/70035/2010.

## References

[1] M. Teplan, Fundamentals of EEG measurement, Meas. Sci. Rev. 2 (2) (2002).
[2] E. McAdams, “Bioelectrodes”, in: J.G. Webster (Ed.), Encyclopedia of Medical Devices and Instrumentation, Wiley, NewYork, 1988.
[3] A. Searle, L. Kirkup, Physiol. Meas. 21 (2000) 271–283.
[4] W.K. Ko, J. Hynecek, Dry electrodes and electrode amplifiers, in: H.A. Miller, D.C. Harrison (Eds.), Biomedical Electrode Technology, Academic Press, NY, 1974.
[5] L.T. Cunha, P. Pedrosa, C.J. Tavares, E. Alves, F. Vaz, C. Fonseca, Electrochim. Acta 55 (1) (2009) 59–67.
[6] S. Piscanec, L. Ciacchi, E. Vesselli, G. Comelli, O. Sbaizero, S. Meriani, A. De Vita, Acta Mater. 52 (5) (2004) 1237–1245.
[7] N.P. Barradas, C. Jeynes, R.P. Webb, Appl. Phys. Lett. 71 (2) (1997) 291–293.
[8] A.F. Gurbich, Nucl. Instr. and Meth. B 268 (2011) 1703–1710.
[9] H.A. Wriedt, J.L. Murray, Bull. Alloy Phase Diagram. 8/4 (1987) 378.
[10] Z. Han, J. Tian, Q. Lai, X. Yu, G. Li, Surf. Coat. Technol. 162 (2003) 189–193.
[11] I. Gusev, Phys. Usp. 43 (1) (2000) 1–39.
[12] G.V. Samsonov, Handbook of Refractory Compounds, Plenum, New York, 1980A.
[13] J. Kohlscheen, H. -R. Stock, P. Mayr, Surf. Coat. Technol 120–121 (1999) 740–745.
[14] K. Lu, M.L. Sui, R. Lück, Nanostruct. Mat. 4/4 (1994) 465–473.
[15] A. Norlin, J. Pan, C. Leygraf, J. Electrochem. Soc. 152 (2) (2005) J7–J15.
[16] F. Vaz, P. Machado, L. Rebouta, P. Cerqueira, Ph. Goudeau, J.P. Rivière, E. Alves, K. Pischow, J. de Rijk, Surf. Coat. Technol. 174–175 (2003) 375–382.
[17] F. Vaz, J. Ferreira, E. Ribeiro, L. Rebouta, S. Lanceros-Méndez, J.A. Mendes, E. Alves, Ph. Goudeau, J.P. Rivière, F. Ribeiro, I. Moutinho, K. Pischow, J. de Rijk, Surf. Coat. Technol. 191 (2005) 317–323.
[18] M. Orazem, B. Tribollet, Electrochemical Impedance Spectroscopy, John Wiley & Sons, 2008.
[19] E. Huigen, A. Peper, C. Grimbergen, Med. Biol. Eng. Comput. 40 (3) (2002) 332–338.

# CHAPTER 3

## THE STOICHIOMETRIC $Ag_X$:TiN SYSTEM[*]

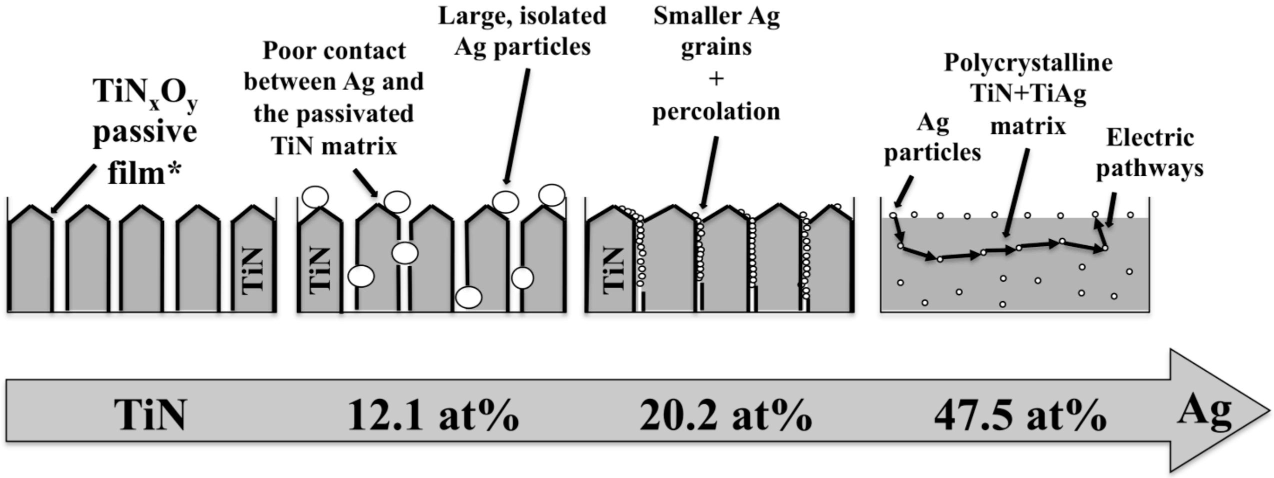

*"...large Ag aggregates can be identified sitting on the TiN matrix surface, as a result of Ag segregation."*

---

[*] This chapter is based on the following publications:

P. Pedrosa, D. Machado, C. Lopes, E. Alves, N.P. Barradas, N. Martin, F. Macedo, C. Fonseca, F. Vaz, "*Nanocomposite Ag:TiN thin films for dry biopotential electrodes*", Applied Surface Science 285P (2013) 40-48.

P. Pedrosa, D. Machado, M. Evaristo, A. Cavaleiro, C. Fonseca, F. Vaz, "*Ag:TiN nanocomposite thin films for bioelectrodes: The effect of annealing treatments on the electrical and mechanical behavior*", Journal of Vacuum Science and Technology A 32 (2014) 031515.

P. Pedrosa, E. Alves, N.P. Barradas, N. Martin, P. Fiedler, J. Haueisen, F. Vaz, C. Fonseca, "*Electrochemical behaviour of nanocomposite Agx:TiN thin films for dry biopotential electrodes*", Electrochimica Acta 125 (2014) 48-57.

The study performed on the previous chapter, Chapter 2, allowed an effective optimization of the sputtering conditions for polymeric-based substrates. Besides the good thin film/substrate adhesion that was obtained, the stoichiometric $TiN_x$ coatings exhibited significantly lower impedance values than the N-deficient ones.

Based on these promising results, the transition to the already referred multipin design was made. Hence, the polyurethane (chosen due to its biocompatibility and wide range of available hardness values, which should translate into increased patient comfort when comparing to polycarbonate) multipin electrodes were sputtered with the optimized $TiN_x$ stoichiometric coating (N/Ti atomic ratio = 1). In a similar way to what had been already performed with the planar disk design, the signal quality and interfacial impedance of the dry $TiN_x$-coated multipin electrode was assessed by performing several EEG trials in human volunteers, using the wet commercial Ag/AgCl electrodes as comparison[1]. The recorded signals revealed good reproducibility, when using the dry $TiN_x$-coated multipin electrodes, with root mean square (RMSD) values between the wet/wet and wet/dry electrode couples that were in the same order of magnitude. However, the coated multipin electrodes often delaminated after only one EEG trial (completely loosing its conductivity), which was ascribed to the high pressure applied on the pin tips (related with the small footprint of the pin tip) and the low elasticity of the stoichiometric $TiN_x$ film, thus not being able to cope with the flexible polyurethane pin deformation. Also, the exhibited impedance values were still two to three orders of magnitude higher than those of the wet electrodes.

Consequently, silver was chosen to be added to the stoichiometric $TiN_x$ matrix, since it should be able to tailor the electrical, morphological, structural, mechanical and electrochemical properties of the final $Ag_X$:TiN coating system. The effect of increasing Ag

---

[1] P. Fiedler, C. Fonseca, P. Pedrosa, A. Martins, F. Vaz, S. Griebel, J. Haueisen, "*Novel Flexible Dry Multipin Electrodes for EEG: Signal Quality and Interfacial Impedance of the Ti and TiN Coatings*" Proceedings of the 35th Annual Conference of the IEEE EMBS (2013) 547-550.

additions (up to 50 at.%) to a stoichiometric $TiN_x$ matrix on the above referred properties in patent in the following chapter.

After the completion of the performed characterization, it was found that the stoichiometric $Ag_x$:TiN system displayed poor morphological and structural stability due to the observed extensive Ag segregation phenomenon (see figure 3.1.).

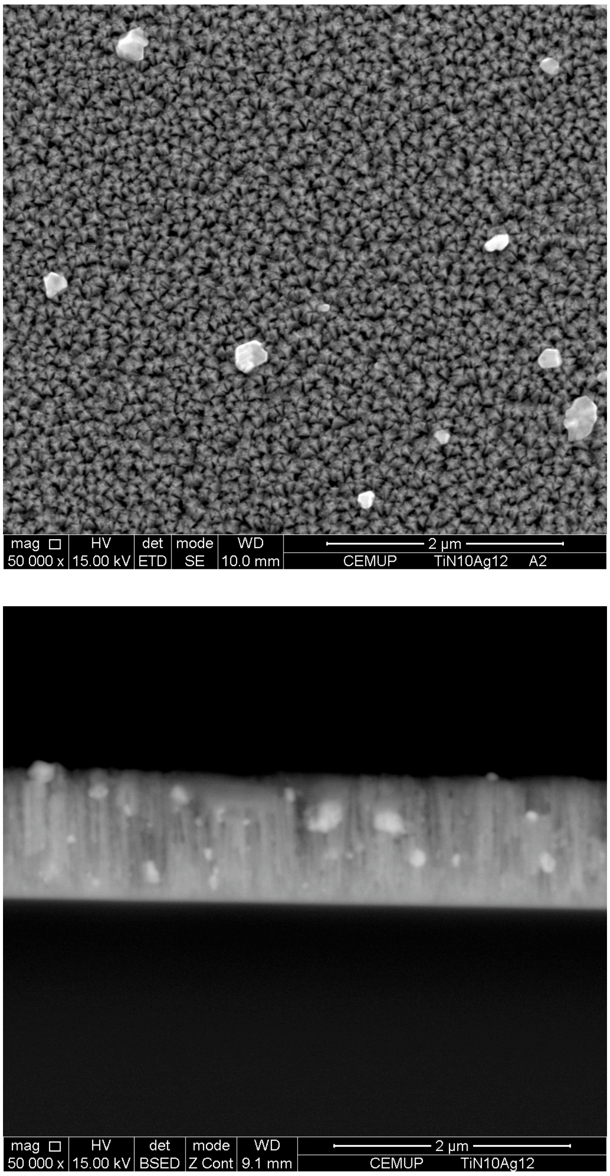

**Figure 3.1.** Evidences of Ag segregation found in the stoichiometric $Ag_x$:TiN thin film system. Secondary electrons (left) and backscattered (right) SEM images.

The occurrence of such extensive Ag segregation phenomenon is not desirable if the coatings are to be used as bioelectrodes, since it originates an unstable skin/electrode interface due to the poor structural stability of the coatings.

Applied Surface Science 285P (2013) 40–48

Contents lists available at ScienceDirect

Applied Surface Science

journal homepage: www.elsevier.com/locate/apsusc

# Nanocomposite Ag:TiN thin films for dry biopotential electrodes

P. Pedrosa[a,b,c], D. Machado[c], C. Lopes[c], E. Alves[d], N.P. Barradas[e], N. Martin[f], F. Macedo[c], C. Fonseca[a,b], F. Vaz[c,*]

[a] *SEG-CEMUC–Department of Mechanical Engineering, University of Coimbra, Portugal*
[b] *Universidade do Porto, Faculdade de Engenharia, Departamento de Engenharia Metalúrgica e de Materiais, Rua Dr. Roberto Frias, s/n, 4200-465 Porto, Portugal*
[c] *Centro de Física, Universidade do Minho, 4710-057 Braga, Portugal*
[d] *Associação Euratom/IST, Instituto de Plasmas e Fusão Nuclear, Instituto Superior Técnico, Universidade Técnica de Lisboa, Av. Rovisco Pais, 1049-001, Lisboa, Portugal*
[e] *Campus Tecnológico Nuclear, Instituto Superior Técnico, Universidade Técnica de Lisboa, E.N. 10, 2686-953 Sacavém, Portugal*
[f] *Institut FEMTO-ST, UMR 6174, Université de Franche-Comté, CNRS, ENSMM, UTBM, 32, Avenue de l'observatoire, 25044 Besançon Cedex, France*

## ARTICLE INFO

*Article history:*
Received 3 April 2013
Received in revised form 30 July 2013
Accepted 30 July 2013
Available online 7 August 2013

*Keywords:*
TiN
Ag addition
Biopotential electrodes
EEG
ECG
Dry electrodes
RBS
XRD
Electrical resistivity, Thermal properties

## ABSTRACT

Silver-added titanium nitride (Ag:TiN) thin films were deposited by DC reactive sputtering with Ag contents ranging from 0 to ∼50 at.% on silicon and glass substrates, aiming at studying their potential application as bio-electrodes. The coatings were characterised regarding their composition, morphology and structure, and their influence on the variation of the electrical resistivity and thermal properties. The sputtered films' behaviour was consistently divided into three main zones, defined mainly by the amount of Ag incorporated and the corresponding changes in the structural and morphological features, which affected both the electrical and thermal response of the films. With increasing Ag concentration, the coatings evolve from a nitride/compound-like behaviour to a metallic-like one. Resistivity values suffer a strong decrease due to the increase of compactness of the coatings and the formation of highly conductive Ag phases, counterbalancing the grain size decrease effects promoted by the hindered growth of the crystalline TiN phases. In good agreement with the electrical resistivity evolution, a similar trend was found in the effusivity values, reflecting a significant degradation of the heat conduction mechanisms in the films as the silver content was increased.

## 1. Introduction

For the past few decades, modern medicine has relied on high resolution monitoring of biopotentials produced by the human body, such as electroencephalography (EEG, brain activity), electrocardiography (ECG, heart activity) and electromyography (EMG, muscular activity), in order to accurately comprehend several pathologies and physiological conditions of human patients. The conventional biopotential acquisition set-up relies on the use of the well-known silver/silver chloride (Ag/AgCl) wet electrodes [1–3]. These are considered the "gold standard" electrodes, as they are non-polarisable and reveal excellent reliability, displaying low and almost frequency independent skin-contact impedance values, in the order of a few tens of kΩ . cm$^2$ [2,3]. However, a preliminary skin preparation and a gel paste application are needed before the exam, in order to lower the skin/electrode impedance. This preparation is time consuming, uncomfortable to the patient and requires trained staff. Furthermore, some patients have developed severe allergic reactions to the common used gel pastes [3] and the risk of short-circuiting adjacent electrodes due to gel running can be, in some cases, relatively high. Susceptibility to motion artefacts and inability to record biopotentials in long-term clinical monitoring (ambulatory) have also been reported [2,3].

Table 1

In order to avoid these and other related drawbacks of the conventional Ag/AgCl electrodes, a new class of devices is being investigated in the group, for which no previous skin preparation or gel application is needed, the so-called "dry" electrodes. In these electrodes, the sensors are based on inert-like materials, either metallic-like or even of insulating type [3,4]. In a previous work [5], the authors investigated a type of dry electrode sensor, based on a titanium nitride (TiN) thin film, deposited on a titanium substrate. Despite the promising results, these electrodes, as well as other similar dry electrodes [6,7], are quite rigid, which can give rise to an incorrect and uncomfortable skin contact, due to the inherent irregular nature of the human skin. In addition, taking into account

---

* Corresponding author. Tel.: +351 253510471; fax: +351 253510461.
*E-mail address:* fvaz@fisica.uminho.pt (F. Vaz).

0169-4332/$ – see front matter © 2013 Elsevier B.V. All rights reserved.
http://dx.doi.org/10.1016/j.apsusc.2013.07.154

**Table 1**
Experimental parameters used in all depositions.

| Deposition parameters | |
|---|---|
| Ar (Pa) | $3 \times 10^{-1}$ |
| $N_2$ (Pa) | $3.4 \times 10^{-2}$ |
| t (s) | 3600 |
| I ($A\,cm^{-2}$) | $1 \times 10^{-2}$ |
| T (°C) | 100 |
| Bias (V) | GND |
| $P_{work}$ (Pa) | $3.5–3.8 \times 10^{-1}$ |
| $P_{base}$ (Pa) | $\sim 10^{-4}$ |

the particular case of an EEG recording set-up, which may involve the use of 128 or even 256 electrodes in a single exam, the use of lighter, cheaper and more comfortable electrodes would translate in numerous advantages in comparison with the standard Ag/AgCl ones.

The use of polymer-based electrodes, namely the flexible ones, would fill in this gap, as they would surpass most of the problems stated above. Recently, several authors have focussed on the development of flexible dry electrodes [8–11]. However, there are still some drawbacks inherent to these electrodes, namely higher impedances at low frequencies and they are also more susceptible to movement artefacts than the standard wet Ag/AgCl ones [1,3,7]. In fact, the absence of conductive gel has a key influence on the exhibited higher impedances and movement artefacts susceptibility, once the gel can act as a "pillow", increasing and stabilizing the contact area (higher and well-defined contact areas are of paramount importance to achieve low contact impedances [10]). This is particularly important in ambulatory applications, where the patient must be able to move freely. Consequently, and in opposition to most common approaches (where authors rely on rigid metal plates or composite materials – foams/conductive polymers), the present work aims at studying Ag:TiN nanocomposite thin films, and assessing their suitability to be sputtered on flexible polymers (to better adapt to the skin and mitigate some of the drawbacks stated above), so that they could be used as flexible dry biopotential electrodes.

Reactive DC magnetron sputtering is commonly accepted as one of the most versatile and less expensive techniques, being widely assumed as able to produce fairly high deposition rates and compact coatings, when compared to other techniques. TiN is an electrically conductive coating, with an excellent chemical stability in most media and outstanding mechanical properties, which led to a very broad range of applications, including those in the biomedical area [12,13]. Furthermore, TiN is biocompatible, but it is also a relatively hard and high Young's modulus material, thus unable to withstand large deformations (in fact, most metallic films tolerate less than 10% of deformation [14–21]). It gives rise to mechanical failure of the coatings, which, in turn, is highly undesirable when the objective is to produce flexible electrodes that are supposed to adapt to the human skin. The inclusion of silver, due to its intrinsic characteristics, particularly the low Young's modulus and high conductivity [22], within the TiN films may offer the possibility to tailor the Young's modulus of the coating [23], opening a wide range of possible applications, namely those related to the coating of flexible devices such as polymers. Furthermore, silver addition may also allow the tailoring of the materials' electrical conductivity [24], which may be of crucial importance in any electrode-based application. Finally, silver is inherently antimicrobial [25–27], particularly in its nanocrystalline form [28,29] and has the ability to stabilise the electrochemical potential [30], which is of major importance in any application that may involve electrophysiological signal monitoring.

Starting with both TiN and silver characteristics, the main goal of the present work is to provide a detailed study on the influence of silver addition to titanium nitride, optimising the deposition conditions in order to obtain conductive and mechanically suitable films to coat flexible polymeric-type substrates and with enough bactericide character that may give the as-prepared thin films a set of characteristics to be used in biopotential electrodes.

## 2. Experimental details

Ag:TiN films were deposited on glass and (1 0 0) silicon substrates by reactive DC magnetron sputtering, in a laboratory-sized deposition system. All substrates were sonicated and cleaned with ethanol 96% (vol.) just before each deposition. The films were prepared with the substrate holder positioned at 70 mm from the Ti/Ag composite target. A DC current density of $100\,A\,m^{-2}$ was applied to the composite target, composed of titanium (99.96 at.% purity/$200 \times 100 \times 6\,mm^3$) and silver pellets ($0.8 \times 0.8\,cm^2$/1 mm thick pellets glued on the surface of the target) distributed symmetrically along the erosion area. The total surface area of the silver pallets varied between 0.75 and $8.3\,cm^2$. A gas atmosphere composed of argon + nitrogen was used. The argon flow was kept constant at 60 sccm for all depositions, as well as the nitrogen flow rate, which was set at 5 sccm (corresponding to a partial pressure of $3.4 \times 10^{-2}$ Pa). The working pressure was approximately constant during the depositions, varying only slightly between 0.35 and 0.38 Pa. No bias voltage was used, and the deposition temperature was maintained approximately constant at 100 °C during the films' growth. A thermocouple was placed close to the surface of the "substrate holder" on the plasma side (not in direct contact, since all depositions were done in rotation mode), and the temperature was monitored during the entire films' deposition time. A delay time of 5 min was used before positioning the surface of the samples in front of the Ti/Ag target in order to avoid films' contamination resulting from previous depositions (which may have resulted in some target poisoning), and also to assure a practically constant deposition temperature during the films' growth.

The atomic composition of the as-deposited samples was measured by Rutherford Backscattering Spectroscopy (RBS) using (1.4, 2.3) MeV and (1.4, 2) MeV for the proton and $^4$He beams, respectively. Three detectors were used. One located at a scattering angle of 140° and two pin-diode detectors located symmetrical to each other, both at 165°. Measurements were made for two sample tilt angles, 0° and 30°. Composition profiles for the as-deposited samples were determined using the software NDF [31]. For the $^{14}$N, $^{16}$O and $^{28}$Si data, the cross-sections given by Gurbich were used [32]. The area analysed was about $0.5 \times 0.5\,mm^2$. The uncertainty in the N concentrations was around 5 at.%. The structure and phase distribution of the coatings were assessed by X-ray diffraction (XRD), using a Bruker AXS Discover D8 diffractometer, operating with Cu $K_\alpha$ radiation and in a Bragg–Brentano configuration. The XRD patterns were deconvoluted and fitted with a Voigt function to determine the structural characteristics of the films, such as the peak position ($2\theta$), the full width at half maximum (FWHM) and the crystallite size. Morphological features of the samples were probed by scanning electron microscopy (SEM), carried out in an FEI Quanta 400FEG ESEM microscope operating at 15 keV. The resistivity measurements were done using the four-probe van der Pauw method [33]. The thermal characteristics of the coatings were accessed by IR radiometry. The measurement system used is externally controlled by software and consists basically of three main parts: excitation, detection and amplification. The amplification is controlled by a pre-amplifier and a two-phase lock-in amplifier (SR 830 DSP). The amplitude and phase lag relative to the modulated excitation, as a function of the heating modulation frequency, giving information on the thermal wave's properties, are recorded by the lock-in and stored in the main computer. Further details on the technique can be found elsewhere [34].

## 3. Results and discussion

### 3.1. Discharge characteristics: target potential and deposition rate

In order to study the kinetics and the deposition-related features, the evolution of the target potential during the films' growth, as well as the final growth rates were firstly characterised. Fig. 1 shows the evolution of these two characteristics as a function of the area of the Ag pellets placed on the target. It is worth noting that the amount of silver in the target (illustrated by the increasing area/number of the pellets placed in the target erosion zone) results in a three-fold variation type, which will be further noted as films prepared within zones I, II and III. Within zone I, the prepared thin films can be described as within a TiN-like zone, where both target potential and deposition rates are somewhat similar to the single TiN sputtering conditions due to the small area of Ag exposed (i.e. below 1 $cm^2$). However, a small change in the behaviour of the studied parameters can be seen with further small additions of Ag. Within zone II, which can be indexed to the incorporation of intermediate amounts of Ag in the target erosion zone, from 1 to 5 $cm^2$, a small increase of discharge voltage is observed, while growth rate values remain somewhat constant. However, the exhibited values are not very different from the values within zone I. As for zone III, where larger fractions of Ag are available for sputtering (> 5 $cm^2$), the increasing of the studied parameters already perceivable in zone II becomes significant. Thus, it is possible to state that both deposition rate and target potential exhibit an overall increasing tendency with increasing areas of Ag exposed in the Ti target. This expected behaviour was explained by Depla et al. [35–37], where the authors studied the effect of several parameters in the ion induced secondary electron emission coefficient (ISEE). One of the referred parameters is the target material dependency of the discharge voltage. At constant current and pressure – corresponding to the conditions used in this work for the preparation of the Ag:TiN coatings – the average ISEE coefficients of the used target materials (Ti and Ag) are rather close, 0.114 and 0.110, respectively. However, based on the Thornton relation [38], it is known that the discharge voltage is inversely proportional to the ISEE coefficient of the target material. Furthermore, one must take into account some poisoning of the Ti fraction of the target during the sputtering process, leading to the formation of nitrides at its surface with a lower ISEE coefficient (0.049 for TiN) [39–42]. This means that the ISEE coefficient of the poisoned fraction of the target will be lower than those stated above for the metallic mode condition (as a result of the TiN poisoning of the Ti fraction of the composite target), while the Ag ISEE coefficient should remain constant, since the formation of AgN is highly improbable thermodynamically, due to the fact that the sputtering of Ag in the presence of nitrogen has an extremely low reactivity [43]. Since the Ag area in the Ti/Ag target is being continuously increased, the Ti poisoning effect is supposed to be gradually reduced, thus a decrease of the target potential values is expected, due to the explained inverse proportionality. However, the opposite behaviour is observed: a slight ~50 V increase of the target potential values is perceivable from ~360 V (low Ag fraction) to ~410 V (high Ag fraction). This effect can probably be ascribed to a gradual covering of the Ti poisoned fraction with Ag, due to strong differences between their sputtering yield values [37], hence altering the discharge characteristics. Note that late zone II and zone III coatings were sputtered with Ag pellets glued (with silver paint) to the target's erosion track, which may also alter the target and plasma properties, namely its impedance, giving rise to higher potentials as more Ag pellets are placed.

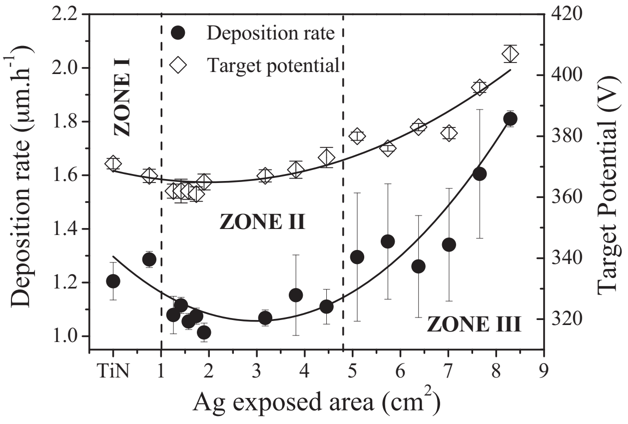

**Fig. 1.** Evolution of the deposition rate and target potential with increasing Ag exposed area in the target.

Since the amount of material that is deposited on the substrate per unit of time is correlated with the amount of atoms sputtered from the target, the explanations given above can also, in part, justify the evolution of the sputtering rate, as the decrease of the poisoned Ti fraction of the compound Ti/Ag target should increase the sputtering rate. In fact, zone I and zone II coatings exhibit rather low deposition rates, indicating that the compound target conditions predominate, while the zone III ones were obtained with higher deposition rates. This must be due to the fact that the Ag fraction in the Ti/Ag target is high enough to somewhat deplete the poisoning effect of the Ti fraction responsible for the low sputtering rates present in both zones I and II.

In a review paper, Smentkowski [44] explained the theoretical concept of sputtering yield, which can be defined by:

$$Y = \Lambda Fd_{(Eo)} \tag{1}$$

where $\Lambda$ contains all of the material properties such as the surface binding energies (which is lower for Ag 3d than that of Ti 2p [45]) and $Fd_{(Eo)}$ is the density of energy deposited at the surface, depending on the mass, energy, and direction of the incident ion, as well as the composition of the target. As the other deposition parameters were maintained constant during all depositions in the present work, the composition of the target is of paramount importance to explain the influence of the sputtering yield on the evolution of the sputtering rate. Furthermore, and since the surface binding energy of Ag is lower than that of Ti, the sputtering yield follows the inverse relation. Smentkowski data [44] show experimental and calculated Ag sputtering yields almost seven times higher than Ti (~2.5 and ~0.35, respectively for 400 eV Xe ion bombardment). Consequently, with increasing Ag fraction in the Ti/Ag target, an increase of the deposition rate is expected, once the TiN thin layer poisoning effect is depleted and Ag sputtering yield (and binding energy) is higher than that of Ti.

### 3.2. Composition of the as-deposited samples

The evolution of the deposition rate and target potential, as well as the increase of Ag fraction in the target will also be correlated with changes in the composition of the films. Fig. 2(a) shows that the Ag chemical composition (at.%) results and the Ag/(Ti + N) ratio of the Ag:TiN coatings obtained from RBS spectra analysis, while Fig. 2(b) exhibits the ternary phase diagram of the deposited samples. Once again, the same three distinct zones are perceivable. Due to the very low area of Ag available for sputtering, the Ag content in the films from zone I is also very low. Besides the TiN reference coating (N/Ti ratio ~1), only one more sample (~0.1 at.% Ag) is ascribed to this zone. Both deposition rate and target potential

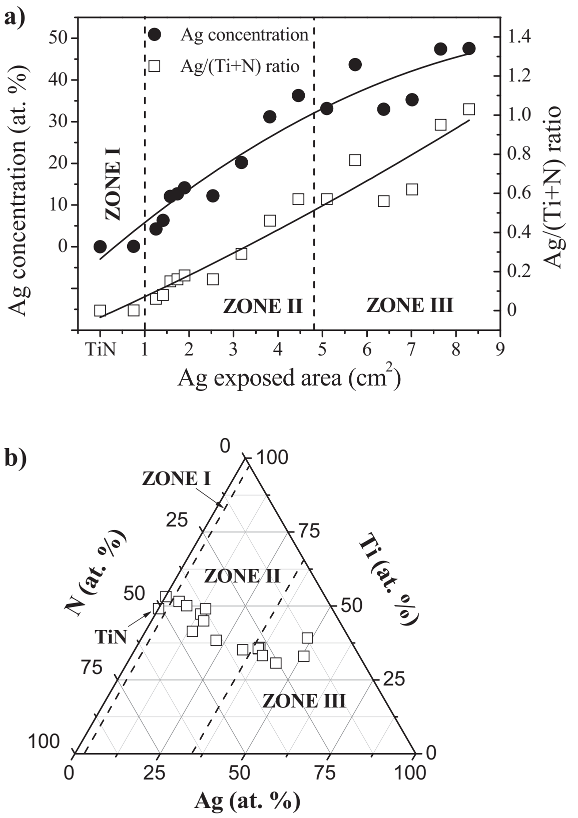

**Fig. 2.** Evolution of the coatings' Ag content and Ag/(Ti + N) ratio as a function of the Ag exposed area in the target (a) and Ti–N–Ag composition ternary phase diagram (b).

are quite low in this zone (which can also explain the low incorporation of Ag), but also in zone II. However, in this zone, one can observe an almost linear increase of Ag incorporation in the coatings with the increase of Ag exposed area. This could mean that the much higher Ag sputtering yield is taking control over the composition evolution process, as the Ag content in this area increases steadily from ~4 at.% to ~35 at.% with the increasing area of Ag (number of Ag pellets) available for sputtering in the target. As for zone III films, the increase of Ag content is smoother than in zone II, with Ag concentrations ranging from ~35 at.% to ~45 at.%, indicating that probably some kind of Ag saturation is being attained. Despite that no films with further Ag concentration were produced, taking into account the results exhibited by the last two samples, one can say that the Ag concentration is practically constant (~45 at.%). Regarding the Ag/(Ti + N) ratio, it directly correlates with the Ag content evolution, exhibiting an almost identical linear increase vs. Ag fraction in the target. It is worth noting that the last two samples from zone III, despite having similar Ag contents, do not present the same Ag/(Ti + N) ratio, indicating that the N/Ti ratio (initially ~1) is not constant. As the Ag fraction in the Ti/Ag target increases and the Ti fraction decreases as the Ag pellets are being placed on the Ti erosion track, this result is somewhat expected. In fact, by taking a closer look at Fig. 2(b), it is possible to see that N/Ti stoichiometry gradually changes to close-stoichiometry almost throughout all coatings, with ratios very close to 0.8–1. For the highest Ag concentrations, however, a steep decrease of the N/Ti ratio is observable, with values close to 0.3–0.5. In fact, Ti contents decrease steadily from 50 at.% to ~30 at.%, while N concentrations initially also decrease steadily from ~50 at.% to ~25 at.%, but then an abrupt decrease is observable, with values close to 11–15 at.%. This abrupt fall of N concentration causes the deposited films to change from stoichiometric to N-deficient Ag:TiN. Due to Ag low ISEE and high sputtering yield, as the Ag fraction in the target is continuously increased, the amount of species (mainly Ag) present in the reactor also increases, leading to a strong decrease of its mean free path. As no substrate bias voltage was used during the sputtering process, the available amount of nitrogen cannot easily react with the growing films due to mobility constraints [14].

### 3.3. Electrical and thermal properties: analysis and discussion

As stated before, one of the main requirements to develop a coating system that may be suitable for biopotential electrode applications is its good conductivity. Fig. 3 shows the resistivity variation as a function of the Ag/(Ti + N) ratio. Once again, the three-zone behaviour is patent in the resistivity evolution. The samples prepared within zone I exhibit relatively high resistivity values (between ~$2.25 \times 10^{-5}$ and $3.25 \times 10^{-5}$ Ω . m), which may, at first glance, seem not very typical for stoichiometric TiN films [46]. Anyway, what it is important to focus is that the preparation conditions used were quite specific due to the targeted application – a thin film system to be used in bio-electrodes, namely those for electroencephalography, EEG, and electrocardiography, ECG. In fact, the base substrates for the bio-electrodes are being built from relatively simple and well-known polymers: polyurethane, polycarbonate and polyethylene. A major concern in these substrates is that the thin films deposition conditions must not be too severe in order to avoid their melting or some kind of consistency problems such as deformation, structural and/or morphological changes in the polymers. For this, the deposition temperature of the films was fixed at a rather low value (not exceeding 100 °C), and the films were grown in grounded condition (no bias). Using these conditions, the adatom mobility was significantly reduced, which resulted in structural and morphological arrangements in the films that are certainly far from being optimised, as it will be shown later in the text. With this, one should expect relatively high values of resistivity, mainly in the almost pure TiN films (zone I films), when compared to other TiN films prepared with high adatom mobility, such as in the films that were prepared in the group at higher temperatures (250 °C) and using ion bombardment of several dozens of negative voltages [46].

Moreover, one can also consider that low Ag contents can also promote some increase of resistivity, which would be an indication that it could be acting as an impurity. For intermediate Ag concentrations in the coatings, resistivity decreases abruptly from ~$2.25 \times 10^{-5}$ to $5.2 \times 10^{-7}$ Ω . m, denoting that Ag, acting as a high

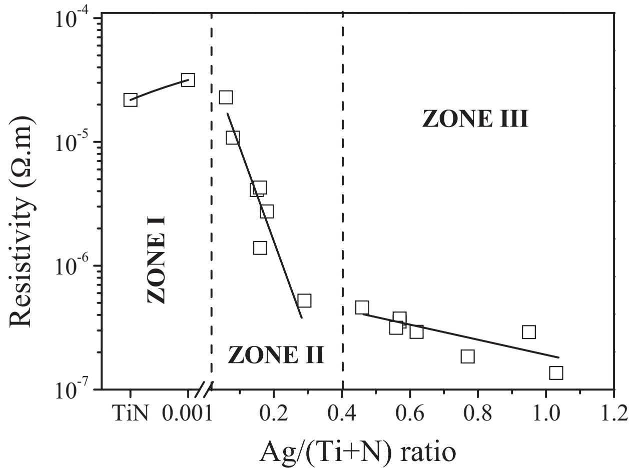

**Fig. 3.** Coatings' resistivity evolution with increasing Ag content and Ag/(Ti + N) ratio.

conductivity dopant [23], promotes the desired effect for the envisaged application. Moreover, zone III resistivity values are actually below that of the bulk Ti ($\sim 4.5 \times 10^{-7}\,\Omega\,.\,\mathrm{m}$ [47]). For the highest Ag content ($\mathrm{Ag/(Ti+N)} > 0.4$), a resistivity of $\sim 1.4 \times 10^{-7}\,\Omega\,.\,\mathrm{m}$ is attained.

To further investigate the electrical response of the films, the morphology of the deposited samples was studied by SEM. Fig. 4($a_{1-3}$) depicts the cross-section images, while Fig. 4($b_{1-3}$) shows the top view and Fig. 4($c_{1-3}$) the backscattered micrographs of the Ag:TiN films, corresponding to zone I, II and III, respectively.

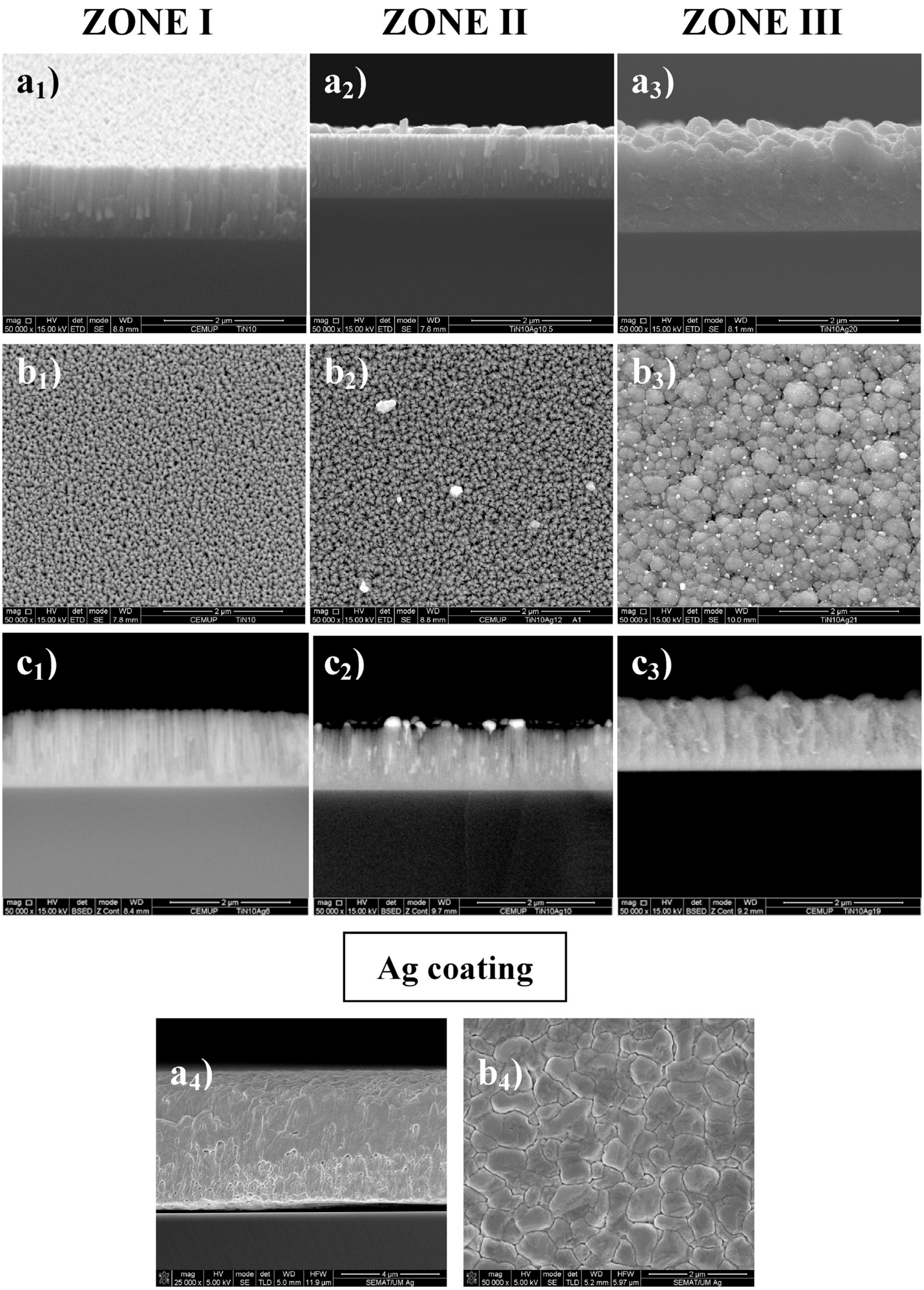

**Fig. 4.** SEM cross-section ($a_{1-4}$), top ($b_{1-4}$) and backscattered ($c_{1-3}$) micrographs of the Ag:TiN (zones I, II and III) and pure Ag coatings.

Fig. 4($a_4$ and $b_4$) displays cross-section and top view images for the pure Ag film. The zone I films' high resistivity can be ascribed not only to the non-metallic characteristic of the low Ag content TiN-like coatings, but also to the well-known pyramid top columns [5] which, in turn, exhibit some degree of porosity and roughness. Non-uniform, rough and porous surfaces are known to hinder charge carrier mobility, thus reducing the films' conductivity. The low deposition rate in these zone I films (Fig. 1) correlates with a low film thickness [48], a fact that can also explain the high resistivity values. Chan et al. [48], after studying the thickness dependence on the electrical properties of Cu thin films, stated that thicker coatings promote an enhanced microstructure (less defects) and crystalline quality which, in turn, lead to surface energy minimisation and to a reduction in grain boundary scattering due to charge carriers. Once all films are grown for 1 h, thickness values can be directly extracted from the deposition rate: zone I and zone II films can be considered low thickness coatings (from ~1.0 to ~1.3 μm), while zone III can be indexed to high thickness films (from ~1.3 to ~1.8 μm). As for zone II coatings (Fig. 4($a_2$ and $c_2$)) it is possible to see that the TiN matrix columns appear to become more disaggregated than in zone I coatings, although a strong decrease in resistivity was noticed. Moreover, a steep incorporation of high conductivity Ag occurs within this zone II, leading to the formation of Ag clusters/aggregates that extensively and uniformly cover the coating's surface. This result is consistent with the work of de los Arcos et al. [49] where the authors reported the formation of spherical Ag clusters embedded in the TiN matrix and also partially sitting on the surface. In fact, deep embedded clusters were also found in this work (Fig. 4($c_2$)). So, as the Ag incorporation increases within zone II, two phenomena occur: (i) the surface becomes more and more uniformly covered with the reported Ag clusters whereas (ii) the TiN matrix becomes increasingly embedded with smaller aggregates between its columns, that will eventually reach the percolation threshold, thus strongly changing the samples resistivity behaviour from non-metallic to metallic. The strong Ag incorporation and segregation that occur within zone II samples, in fact, seem to overcome the low-thickness regime that theoretically imposes higher resistivity values. When the highest Ag concentration and film thickness is reached – zone III coatings, Fig. 4($a_3$–$c_3$) – the morphology of the films changes dramatically. The columnar features are lost and the coatings develop a more granular, compact and rough morphology, similar to pure Ag thin films [50] (Fig. 4($a_4$ and $b_4$)). This morphological evolution can be related to the fact already mentioned that the TiN matrix is gradually changing from stoichiometric to N-deficient as Ag concentration increases, which in turn also exhibits a granular-like compact structure [5]. The low resistivity of the samples from this zone can be in partly ascribed to the combination of these morphological changes, as the content of high conductivity Ag is quite substantial and the sputtered films are very compact, dense and thick, which are prerequisites to low resistivity values. It is interesting to note that Ag clusters are still present in the coating's surface (Fig. 4($b_3$)), although smaller in size when compared to zone II ones, but no embedded aggregates are visible (Fig. 4($c_3$)). This could mean that some fraction of Ag may be dissolved in the N-deficient TiN matrix, opening the door to a possible formation of a TiAg intermetallic.

In order to further understand the growth mechanisms and the influence of the observed features patent in SEM observations on the resistivity evolution, a comprehensive structural characterisation of the Ag:TiN samples was performed. Fig. 5 shows the XRD diffractograms of the sputtered samples, taking into account their increasing Ag content. Once more, the three-zone behaviour is clearly visible, which is in great accordance with all previous analyses. A very close correlation between SEM observations and XRD data can be claimed, with the Ag distribution in the TiN matrix playing a pivotal role in the overall behaviour. Taking a closer look at Fig. 5(a), where the full range diffractograms are shown, zone I comprises, once more, only the stoichiometric TiN reference sample and the low Ag content one (0.1 at.%). Both coatings are highly textured, exhibiting a preferential fcc-TiN (1 1 1) growth (ICDD card no. 00-038-1420), typical for stoichiometric TiN films [5,14,46]. No Ag peaks were detected in the 0.1 at.% Ag sample due to the fact that the amount of incorporated Ag (as well as its grain size) may be too low to be detected [51]. The indistinguishable structural differences between these TiN-like coatings that comprise zone I may justify the rather similar high resistivity values, which remain close to that of TiN. As for zone II coatings, the preferential growth remains the same as the one for zone I films (fcc-TiN (1 1 1)), although some changes are clearly visible. A new peak at ~42.5° corresponding to the fcc-TiN (2 0 0) phase becomes perceivable from 20.2 at.% Ag contents onwards, while the fcc-TiN (2 2 2) peak shifts to lower diffraction angles for Ag contents ranging from 6.3 to 14.2 at.% and disappears almost completely from 20.2 at.% onwards. In fact, the main fcc-TiN (1 1 1) peak also shifts to lower $2\theta$ angles and its intensity strongly decreases as well (Fig. 5(b)). It indicates that the fcc-TiN structure is progressively destroyed by the formation of a new fcc-Ag (1 1 1) phase (ICDD card no. 00-004-0783), as a new peak rises at ~38°. The authors ascribe this peak to fcc-Ag (1 1 1), as several pure Ag aggregates are visible sitting on the surface and embedded in the TiN matrix of zone II

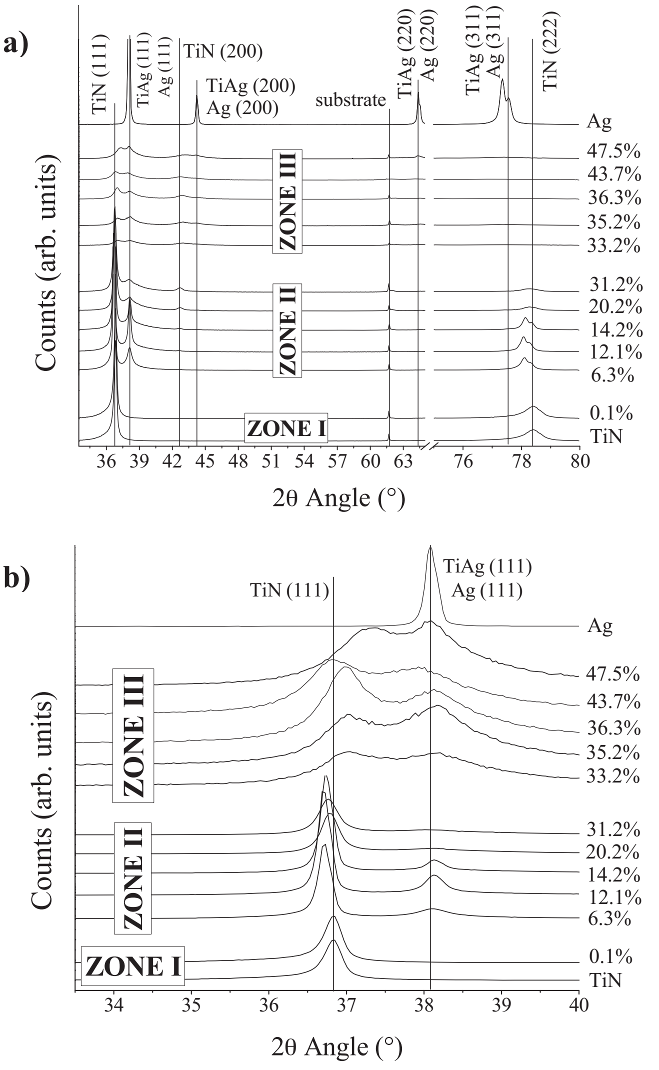

**Fig. 5.** XRD diffractograms as a function of Ag incorporation in the coatings; (a) full scale diffractograms and (b) 34–40° magnification.

coatings (Fig. 4). However, due to the fact that the tetragonal TiAg (1 1 1) peak (ICDD card no. 00-006-0560) occurs at approximately the same diffraction angle, the formation of a TiAg intermetallic may not be excluded, although unlikely, once zone II TiN matrix is stoichiometric or close-stoichiometric, with almost all interstitial sites occupied by N atoms). In addition, the slight shift towards lower $2\theta$ angles referred above, suggests the presence of small Ag inclusions in the fcc-TiN structure. Zone II is, in fact, a transition zone strongly defined by a steep decrease of the resistivity values (Fig. 3). It is now clear that a new highly conductive fcc-Ag phase, in the form of clusters, is produced sitting on the surface and embedded in an increasingly less crystalline TiN matrix. Gulbiński and Suszko [52] claimed that for high Ag contents, grain boundary segregation occurs, hindering the growth of the metallic nitride matrix and decreasing its crystallinity. Zone II and especially zone III data are in agreement with this claim, as for higher Ag concentrations the sputtered films exhibit a very low degree of crystallinity, with very broad peaks and baseline noise clearly patent, as it is possible to see from Fig. 5(b)). To note that the fcc-TiN (1 1 1) peak of the highest Ag concentration sample (47.5 at.%) exhibits a strong shift towards high diffraction angles, corroborating the assumption that the TiN matrix formed may be N-deficient, offering the possibility of some Ag atoms occupying interstitial sites (potential formation of TiAg intermetallics), thus exhibiting lower lattice parameters. These results are, as stated before, in great consistence with SEM observations (Fig. 4), where it is possible to see a gradual increase of the compactness of the films, with the organised columnar growth being progressively lost as the Ag content increases and also with composition analysis (Fig. 2), confirming the formation of a N-deficient TiN matrix for high Ag contents. To summarise, the growth behaviour of the Ag:TiN films provides a coherent justification to the resistivity evolution. As Ag content increases, the fcc-TiN structure is continuously hindered while the formation of a new highly conductive fcc-Ag phase takes place (in fact, fcc-Ag (1 1 1) phase becomes the preferential one for the highest Ag contents). This means that, as stated above, the sputtered films are evolving from a compound/nitride-based to a metallic-like character, thus exhibiting an overall decrease of the resistivity values.

In analytical terms, the resistivity of thin films can be expressed by the well-known Matthiessen's rule [48]:

$$\rho = \rho_p + \rho_m + \rho_f + \rho_i + \rho_s \tag{2}$$

where $\rho_p$, $\rho_m$, $\rho_f$, $\rho_i$ and $\rho_s$ represent the resistivity caused by scattering from phonons, impurities, defects, grain boundaries and the surface scattering, respectively. The scattering effect from impurities must not be considered, once no major impurities are detected in the composition analysis such as oxygen or argon inclusions. If present, their content should be within the standard error of the RBS technique, which is 3–4 at.%. Also, no important defects are perceivable in the coatings. Taking into account the Fuchs–Sondheimer (F–S) model [53,54], the resistivity contribution due to the scattering effect of conduction electrons at the film's surface should also be disregarded, as the surface scattering effect becomes relevant only when the film's thickness is below the mean free path of the conduction electrons. All sputtered Ag:TiN coatings exhibit thicknesses > 1 μm, thus being well above the electron mean free path of Ti and Ag, both in the range of tens of nanometres. Consequently, only the scattering from phonons and grain boundaries contributions should be taken into account, once the chemical composition of the samples is an important variable (already analysed) and the role of grain size evolution should also be fundamental.

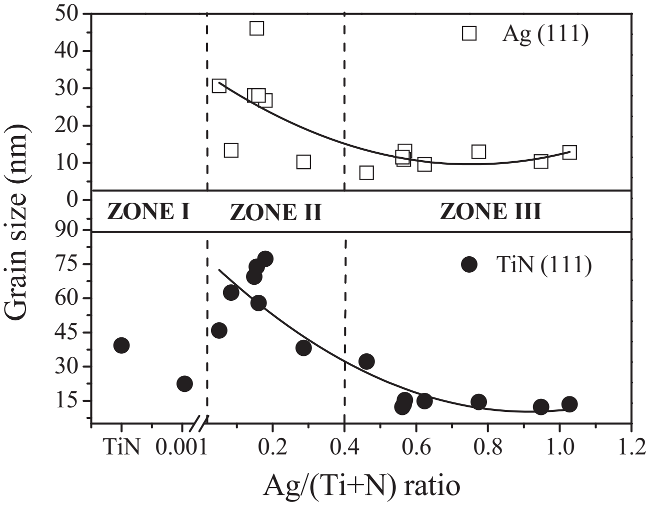

**Fig. 6.** Grain size evolution with increasing Ag/(Ti + N) ratio.

Consequently, the grain size evolution was investigated as function of the Ag/(Ti + N) ratio, taking into account the predominant fcc-TiN (1 1 1) and Ag (1 1 1) phases, as shown in Fig. 6. It is possible to see that the presence of small Ag incorporations – within zone I films – translates into a decrease of the grain size when comparing with the stoichiometric TiN reference coating. It must be remembered that no Ag (1 1 1) phase was detected in the 0.1 at.% Ag sample. Although no differences were detected in the XRD diffractograms, small additions of Ag have a profound effect on the grain size of the growing zone I films, decreasing from ∼37 nm to ∼22 nm. Once more, the rather high TiN-like resistivity values that are exhibited by low-Ag concentration samples are in great accordance with grain size data. It is known that grain size evolution is inversely connected to the resistivity [47], meaning that a decrease of the grain size is expected to give rise to an increase of the resistivity. As for zone II films, the previous relation is also valid, once a substantial increase of grain size values (until ∼75 nm and ∼30 nm for TiN (1 1 1) and Ag (1 1 1) phases, respectively) for the first samples within zone–6.3–14.2 at.% Ag–leads to a strong decrease of resistivity. This is also consistent with XRD data, since it is possible to see (Fig. 5(b)) a slight increase of both fcc-TiN (1 1 1) and Ag (1 1 1) peaks' intensity and definition, indicating an improvement of the crystallinity of the films, thus leading to low resistivity values. However, above 20.2 at.% Ag, a progressive decrease of the crystalline size values of the coatings takes place (as explained before), and although polycrystalline, the films seem to become less crystalline – zone III – a fact that is proven by the accentuated decrease of grain size from ∼75 nm to ∼15 nm for fcc-TiN (1 1 1) phase and from ∼30 nm to ∼10 nm for fcc-Ag (1 1 1). Therefore, with such strong decrease of crystallinity, an increase of the resistivity values was expected. In fact, the opposite is observed since the resistivity values further decrease in zone III. This could mean that the main contribution to resistivity is not related to grain boundary scattering, but scattering from phonons instead (due to the strong composition changes evidenced throughout the range of sputtered Ag:TiN films), confirming the paramount importance of Ag incorporation as the main controlling mechanism of the exhibited behaviour throughout all characterisation performed.

In fact, Ag may also be significantly increasing the charge carrier density, thus probably depleting the grain boundary scattering effect. Furthermore, Kitawaki et al. [55] suggested that Ag solidifies in the faces of the fcc-TiN cube, fact that may promote the formation of some kind of electronic path between the TiN grains, thus strongly decreasing the samples' resistivity. It is important to note that zone II and zone III samples exhibit strong Ag segregation (see Fig. 4) at the surface and in between the TiN columns, corroborating this assumption. Kitawaki et al.'s mechanism of Ag:TiN formation [55] is, indeed, in complete accordance with what is observed in the current study, considering a perfect TiN nanocrystalline structure (no N vacancies), which is true for zone I and zone II coatings (see Fig. 5). As for zone III, the high amounts of Ag may in some way encapsulate the fcc-TiN cubes (and even form Ti–Ag metal–metal bonding, once TiN is N-deficient), hindering their growth into columnar features (as suggested above), therefore leading to a more compact metallic-like structure.

As claimed before, all evidences show that the coatings are steadily changing from a nitride/compound-like (zone I) to a metallic-like (zone III) behaviour with a transition zone (zone II) in between. The resistivity evolution follows coherently this change, decreasing roughly two orders of magnitude from the lowest to the highest silver additions. Moreover, a recent study of the group showed that not only the resistivity is showing promising behaviour taking into account the targeted application, but also the Young's modulus is showing an important variation regarding common TiN known values. In fact, not only the values of the Young's modulus seem to decrease in about 10% as the silver amounts increase (from ~200 GPa to ~180 GPa, by varying Ag from ~20 to ~36 at.%), but they also reduce significantly with the annealing temperature, corresponding to structural and morphological changes that are induced [56]. This change can also be claimed from the observation of the thermal characteristics. The results presented are interpreted assuming a two-layer system, the first layer being the Ag:TiN film and the second layer the substrate. No interfacial thermal resistance was considered. In order to ensure that all the information related to the electronic path of the signal is suppressed, the modulated IR radiometry signals were normalised, using a semi-infinite opaque body of smooth surface. The resulting normalised amplitude and phase lag signals can directly be compared with the theoretical solutions for a two-layer system [57]. According to the two-layer method [57], the modulation frequency and the respective phase lag are measured at the relative extrema of the inverse calibrated frequency-dependent phase lag signals, in the range of the intermediate modulation frequencies. The obtained measurements contain direct information on the sample's thermal diffusion time and about the ratio of the thermal effusivities of the two layers ($e_c/e_b$). The subscript $c$ refers to coating and $b$ to the substrate. The determination of the thermal effusivity of the sample (once $e_b$ is usually know from literature) allows one to get the thermal conductivity ($k$), according to the following simple relations, where $\rho$ represents the density and $c$ the specific heat:

$$e = \sqrt{(k\rho c)} = k/\sqrt{\alpha} \rightarrow k = e\sqrt{\alpha} \qquad (3)$$

Fig. 7 shows the evolution of the ratio of the thermal effusivities of the two layers, as a function of the Ag/(Ti + N) ratio, for a set of Ag:TiN samples. Following a quite similar change tendency, the results obtained indicate that there are clearly two major zones of samples, with very similar limits as those reported before for the electrical characterisation as well as for the morphological and structural evolutions. The first major zone (corresponding to the previously identified zone I) reveals relatively high values of the effusivity ratio, while the second (previously identified zone III) has the lowest set of values for this same ratio. Zone II acts, again, as a transition zone. Furthermore, and in spite of the well-known different mechanisms that rule electrical and thermal conduction behaviours, it is also worth noticing that the type of values obtained in these two zones (almost constant and relatively high in the first and relatively low in the second) have a noticeable similarity to what was observed for the electrical variation, Fig. 3. In this way, it seems reasonable to claim that, again, the changes in the film's composition and the subsequent changes in both morphological and structural features are the most probable parameters that may explain such thermal behaviour. The changes in the crystalline growth that are clear within the films from both zones I and III, associated with the clear decrease of the crystalline sizes of the films from zone III (Figs. 3 and 5 results) are probably inducing a decrease of phonon transport through the thin film, thus reducing the film effusivity. Nevertheless, it is important to discuss two possible mechanisms that may act in opposite ways. First of all, there is the grain size reduction and the tendency for a decrease in the thermal transport properties, but one must also bring up the fact that silver phases are being formed in zone II and III films, as previously discussed. If a pure Ag phase were being grown in these zones (as it seems to be probable), one would expect that an increase of the film effusivity should occur, given the well-known good thermal conduction properties of this element. The fact that the opposite was in fact observed (a decrease of film's effusivity), the conclusion is that the very weak crystalline phases that are formed are actually the most important factors for the effusivity evolution. Anyway, it should also be noted that a possible weak thermal behaviour of a Ti–Ag phase that may be formed could account also for a decrease of the effusivity as it was observed.

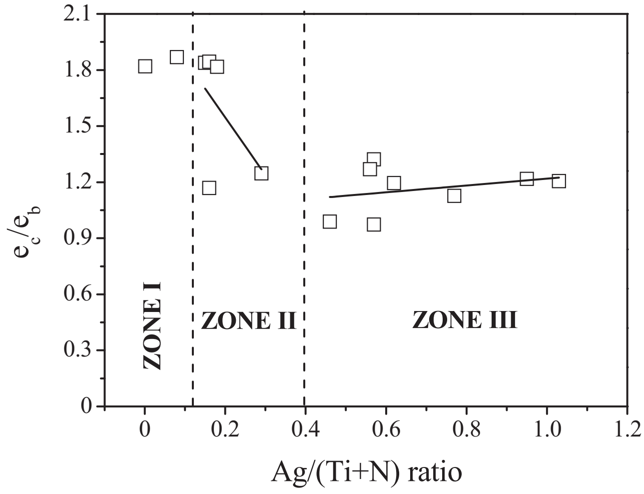

**Fig. 7.** Two-layer thermal effusivity evolution as a function of the Ag/(Ti + N) ratio.

## 4. Conclusions

In this work, nanocomposite Ag:TiN coatings were successfully sputtered in a wide range of compositions, ranging from 0 to ~50 at.% Ag and characterised, aiming at selecting the best compositional region for the use as biopotential electrodes. Throughout all characterisation performed, the behaviour of the whole set of produced coatings can consistently be ascribed to three major zones. It was found that the main governing mechanism affecting the behavioural indexing of the films into the three zones was Ag incorporation in the TiN matrix. Consequently, the coatings in zone I ($0 \leq$ Ag at.% $< 4.3$), despite their high degree of crystallinity (only fcc-TiN phases were detected), exhibit rather high TiN-like resistivity values due to its porous/disaggregated pyramid-like columnar structure, that also lead to high effusivity ratios. This zone I comprehends the samples whose behaviour can be considered as nitride/compound-like. As for zone II ($4.3 \leq$ Ag at.% $< 33.2$) coatings, the resistivity values suffer a strong decrease due to the formation of highly conductive Ag phases (aggregates) sitting on top and also embedded in the TiN matrix (hindering its growth), reaching the percolation threshold. The effusivity ratios also suffer a steep decrease due the strong reduction of the coatings' crystallinity, thus reducing the phonon transport phenomenon. Zone II can hence be considered as a transition zone, as it leads to a completely metallic-like behavioural zone – zone III ($33.2 \leq$ Ag at.% $\leq 47.5$). The polycrystalline and compact Ag:TiN thin films ascribed to zone III exhibit the lowest resistivity (even below bulk Ti) – although not very different from the samples with the most Ag content within zone II – and effusivity ratios, due to large incorporation/formation of highly conductive Ag phases. It is also important to refer that for the highest Ag contents the TiN matrix becomes N-deficient, opening the possibility for the formation of a Ti–Ag intermetallic.

Taking into account the envisaged application, and bearing in mind that low resistivity materials are preferable to be used as biopotential electrodes, the coatings from the top-end of zone II and the films from zone III (with Ag contents ranging from ~20 to ~50 at.%) seem to be, a priori, the most suitable ones.

## Acknowledgements

This research is partially sponsored by FEDER funds through the programme COMPETE–Programa Operacional Factores de Competitividade and by national funds through FCT–Fundação para a Ciência e a Tecnologia, under the projects PEst-C/EME/UI0285/2011, PTDC/SAU-ENB/116850/2010, PTDC/CTM-NAN/112574/2009 and Programa Pessoa 2012/2013 Cooperação Portugal/França, Project no. 27306UA Porous architectures in GRAded CERamic thin films for biosensors - GRACER. The authors would also like to acknowledge CEMUP for SEM analysis. P. Pedrosa acknowledges FCT for the Ph.D. grant SFRH/BD/70035/2010.

## References

[1] M. Teplan, Meas. Sci. Rev. 2 (2) (2002) 1–11.
[2] E. McAdams, Bioelectrodes, in: J.G. Webster (Ed.), Encyclopaedia of Medical Devices and Instrumentation, Wiley, New York, 1988, pp. 120–166.
[3] A. Searle, L. Kirkup, Physiol. Meas. 22 (2000) 271–283.
[4] W.K. Ko, J. Hynecek, Dry electrodes and electrode amplifiers, in: H.A. Miller, D.C. Harrison (Eds.), Biomedical Electrode Technology, Academic Press, New York, 1974.
[5] L.T. Cunha, P. Pedrosa, C.J. Tavares, E. Alves, F. Vaz, C. Fonseca, Electrochim. Acta 55 (1) (2009) 59–67.
[6] G. Gargiulo, R.A. Calvo, P. Bifulco, M. Cesarelli, C. Jin, A. Mohamed, A. van Schaik, Clin. Neurophysiol. 121 (5) (2010) 686–693.
[7] C. Fonseca, J.P. Silva Cunha, R.E. Martins, V. Ferreira, J.P. Marques de Sá, M.A. Barbosa, A. Martins Silva, IEEE Trans. Biomed. Eng. 54 (1) (2007) 162–165.
[8] K.-P. Hoffmann, R. Ruff, Proceedings of the 29th Annual International Conference of the IEEE EMBS, Lyon, France, August, 2007, pp. 23–26.
[9] J. Baek, J. An, J. Choi, K. Park, S. Lee, Sens. Actuat. A 143 (2008) 423–429.
[10] A. Gruetzmann, S. Hansen, J. Muller, Physiol. Meas. 28 (2007) 1375–1390.
[11] V. Marozas, A. Petrenas, S. Daukantas, A. Lukosevicius, J. Electrocardiol. 44 (2011) 189–194.
[12] S. Piscanec, L. Ciacchi, E. Vesselli, G. Comelli, O. Sbaizero, S. Meriani, A. De Vita, Acta Mater. 52 (2004) 1237.
[13] P. Pedrosa, E. Alves, N.P. Barradas, P. Fiedler, J. Haueisen, F. Vaz, C. Fonseca, Corros. Sci. 56 (2012) 49–57.
[14] S.L. Chui, J. Leu, P.S. Ho, J. Appl. Phys. 76 (1994) 5136.
[15] O. Kraft, M. Hommel, E. Arzt, Mater. Sci. Eng., A 288 (2000) 209.
[16] M. Hommel, O. Kraft, Acta Mater 49 (2001) 3935.
[17] B.E. Alaca, M.T.A. Saif, H. Sehitoglu, Acta Mater. 50 (2002) 1197.
[18] D.Y.W. Yu, F. Spaepen, J. Appl. Phys. 95 (2003) 2991.
[19] S.P. Lacour, S. Wagner, Z. Huang, Z. Suo, Appl. Phys. Lett. 82 (2003) 2404.
[20] Y. Xiang, T. Li, Z. Suo, J. Vlassak, Appl. Phys. Lett. 87 (2005) 161910.
[21] R.M. Niu, G. Liu, C. Wang, G. Zhang, X.D. Ding, J. Sun, Appl. Phys. Lett. 90 (2007) 161907.
[22] R.X. Wang, X.M. Tao, Y. Wang, G.F. Wang, S.M. Shang, Surf. Coat. Technol. 204 (2010) 1206–1210.
[23] R.C. Adochite, D. Munteanu, M. Torrell, L. Cunha, E. Alves, N.P. Barradas, A. Cavaleiro, J.P. Riviere, E. Le Bourhis, D. Eyidi, F. Vaz, Appl. Surf. Sci. 258 (2012) 4028–4034.
[24] H. Chiriac, M. Urse, F. Rusu, C. Hison, M. Neagu, Sens. Actuat. A 76 (1999) 376–380.
[25] K.-H. Liao, K.-L. Ou, H.-C. Cheng, C.-T. Lin, P.-W. Peng, Appl. Surf. Sci. 256 (2010) 3642–3646.
[26] M. Fiori, M. Paula, A. Bernardin, H. Riella, E. Angioletto, Mater. Sci. Eng. C 29 (2009) 1569–1573.
[27] M. Santos, C. Oliveira, C. Tachinski, M. Fernandes, C. Pich, E. Angioletto, H.G. Riella, M. Fiori, Int. J. Miner. Process. 100 (2011) 51–53.
[28] P.J. Kelly, H. Li, K.A. Whitehead, J. Verran, R.D. Arnell, I. Iordanova, Surf. Coat. Technol. 204 (2009) 1137–1140.
[29] P.J. Kelly, H. Li, P.S. Benson, K.A. Whitehead, J. Verran, R.D. Arnell, I. Iordanova, Surf. Coat. Technol. 205 (2010) 1606–1610.
[30] L.A. Geddes, L.E. Baker, A.G. Moore, Med. Biol. Eng. 7 (1969) 49–56.
[31] N.P. Barradas, C. Jeynes, R.P. Webb, Appl. Phys. Lett. 71 (1997) 291.
[32] A.F. Gurbich, Nucl. Instrum. Methods 268 (2010) 1703.
[33] L.J. van der Pauw, Philips Res. Rep. 13 (1958) 1–9.
[34] F. Macedo, F. Vaz, M. Torrell, R.T. Faria Jr., A. Cavaleiro, N.P. Barradas, E. Alves, K.H. Junge, B.K. Bein, J. Phys. D: Appl. Phys. 45 (2012) 105301.
[35] D. Depla, S. Heirwegh, S. Mahieu, J. Haemers, R. De Gryse, J. Appl. Phys. 101 (2007) 013301.
[36] D. Depla, G. Buyle, J. Haemers, R. De Gryse, Surf. Coat. Technol. 200 (2006) 4329–4338.
[37] D. Depla, S. Mahieu, R. De Gryse, Thin Solid Films 517 (2009) 2825–2839.
[38] J.A. Thornton, J. Vac. Sci. Technol. 15 (1978) 171.
[39] J.M. Chappé, F. Vaz, L. Cunha, C. Moura, M.C. Marco de Lucas, L. Imhoff, S. Bourgeois, J.F. Pierson, Surf. Coat. Technol. 203 (2008) 804–807.
[40] J. Borges, F. Vaz, L. Marques, Appl. Surf. Sci. 257 (2010) 1478–1483.
[41] J. Borges, N. Martin, N.P. Barradas, E. Alves, D. Eyidi, M.F. Beaufort, J.P. Riviere, F. Vaz, L. Marques, Thin Solid Films 520 (2012) 6709–6717.
[42] R. Arvinte, J. Borges, R.E. Sousa, D. Munteanu, N.P. Barradas, E. Alves, F. Vaz, L. Marques, Appl. Surf. Sci. 257 (2011) 9120–9124.
[43] J.F. Pierson, D. Wiederkehr, A. Billard, Thin Solid Films 478 (2005) 196–205.
[44] V.S. Smentkowski, Prog. Surf. Sci. 64 (2000) 1–58.
[45] C.D. Wanger, W.M. Riggs, L.E. Davis, J.F. Moulder, G.E. Muilenberg, Handbook of X-ray Photoelectron Spectroscopy, Perkin-Elmer Corp., Physical Electronics Division, Eden Prairie, Minnesota, USA, 1979.
[46] F. Vaz, J. Ferreira, E. Ribeiro, L. Rebouta, S. Lanceros-Méndez, J.A. Mendes, E. Alves, Ph Goudeau, J.P. Rivière, F. Ribeiro, I. Moutinho, K. Pischow, J. de Rijk, Surf. Coat. Technol. 191 (2005) 317–323.
[47] M.E. Day, M. Delfino, J.A. Fair, W. Tsai, Thin Solid Films 254 (1995) 285–290.
[48] K.-Y. Chan, T.-Y. Tou, B.-S. Teo, Microelectron. J. 37 (2006) 608–612.
[49] T. de los Arcos, P. Oelhafen, U. Aebi, A. Hefti, M. Düggelin, D. Mathys, R. Guggenheim, Vacuum 67 (2002) 463–470.
[50] Y. Xiong, H. Wu, Y. Guo, Y. Sun, D. Yang, D. Da, Thin Solid Films 375 (2000) 300–303.
[51] J.G. Han, H.S. Myung, H.M. Lee, L.R. Shaginyan, Surf. Coat. Technol. 163-164 (2003) 591–596.
[52] W. Gulbiński, T. Suszko, Surf. Coat. Technol. 201 (2006) 1469–1476.
[53] K. Fuchs, Proc. Camb. Philos. Soc. 34 (1938) 100.
[54] E.H. Sondheimer, Phys. Rev. 80 (1950) 401.
[55] K. Kitawaki, K. Kaneko, K. Inoke, J.C. Hernandez-Garrido, P.A. Midgley, H. Okuyama, M. Uda, Y. Sakka, Micron. 40 (2009) 308–312.
[56] P. Pedrosa, D. Machado, M. Evaristo, A. Cavaleiro, C. Fonseca, F. Vaz, Vacuum (2013), Submitted for publication.
[57] J.L. Nzodoum Fotsing, J. Gibkes, J. Pelzl, B.K. Bein, J. Appl. Phys. 98 (2005) 063522.

# Ag:TiN nanocomposite thin films for bioelectrodes: The effect of annealing treatments on the electrical and mechanical behavior

Paulo Pedrosa
*SEG-CEMUC—Department of Mechanical Engineering, University of Coimbra, 3030-788 Coimbra, Portugal; Universidade do Porto, Faculdade de Engenharia, Departamento de Engenharia Metalúrgica e de Materiais, Rua Dr. Roberto Frias, s/n, 4200-465 Porto, Portugal; and Centro de Física, Universidade do Minho, 4710-057 Braga, Portugal*

Diogo Machado
*Centro de Física, Universidade do Minho, 4710-057 Braga, Portugal*

Manuel Evaristo and Albano Cavaleiro
*SEG-CEMUC—Department of Mechanical Engineering, University of Coimbra, 3030-788 Coimbra, Portugal*

Carlos Fonseca
*SEG-CEMUC—Department of Mechanical Engineering, University of Coimbra, 3030-788 Coimbra, Portugal and Universidade do Porto, Faculdade de Engenharia, Departamento de Engenharia Metalúrgica e de Materiais, Rua Dr. Roberto Frias, s/n, 4200-465 Porto, Portugal*

Filipe Vaz[a)]
*Centro de Física, Universidade do Minho, 4710-057 Braga, Portugal*

(Received 11 February 2014; accepted 16 April 2014; published 1 May 2014)

Magnetron sputtered Ag:TiN thin films, with Ag contents ranging from 0 to ~50 at. %, were subjected to a set of annealing treatments at four different temperatures (from 200 to 500 °C), aiming at studying the effect of Ag addition on their morphological and structural features, as well as on their electrical and mechanical properties. The increase of the annealing temperature revealed that significant morphological modifications were induced, mainly in the samples with higher Ag contents (represented by the sample with an Ag content of 36.3 at. %), which revealed extensive Ag segregation to the surface. The increase of the annealing temperature up to 500 °C, besides confirming the presence of metallic Ag in the coatings, also resulted in some major structural changes, promoting an increase in the coating's crystallinity and an extensive Ag grain growth phenomenon. Nevertheless, the resistivity values of all annealed samples were found to be only slightly higher when comparing to the as-deposited ones, which indicated that beyond the significant changes in the samples morphology (e.g., Ag segregation), there seemed to be some important coating resistance in terms of the electrical response. Furthermore, the annealed samples also exhibited lower reduced modulus up to 400 °C when compared with the unannealed ones, consistent with some increase of the samples' elasticity. © *2014 American Vacuum Society.* [http://dx.doi.org/10.1116/1.4873555]

## I. INTRODUCTION

Titanium nitride thin films are characterized by a large number of properties such as good electrical conductivity, corrosion/oxidation resistance, heat resistance, high chemical stability, wear resistance, high hardness (~20 GPa), and scratch resistance, allowing its use in several applications, ranging from electrical and tribological ones[1,2] to those of biomedical nature such as electroencephalography (EEG) and electrocardiogram (ECG) electrodes.[3,4] Another important characteristic of TiN is that it reveals a notorious biocompatibility, which enabled its use in several important applications such as those of food processing.[5] Thin TiN films were reported to possess antibacterial characteristics when sputtered under light.[6] However, in order to enhance this important feature and to allow an even wider range of application areas, other elements are being incorporated in the TiN matrix, where silver is one of the most recent ones due to its well-known antibacterial characteristics and biomedical ability.[7] Another important effect that can be obtained when Ag is added to TiN coatings is the so-called "self-lubricating" effect. This is a very important characteristic for several types of applications, namely, the tribological-based ones.[8]

However, one of the problems that may arise within the Ag:TiN system consists of its relative structural and morphological stability.[9] Moreover, there are well-known problems related to mechanical and electrical properties failure in the coatings,[10] particularly due to the changing of the service temperature which, in turn, significantly aggravate the efficiency of the thin films during their in-service performance.[11–14] These problems reveal a major importance in situations that involve high operating temperatures, making the study of the temperature stability of the electrical and mechanical properties a rather important issue.[15–17]

According to Pestana and Filho,[18] annealing is a process that involves the coalescence of metal particles resulting from a gradient of concentration caused by increasing temperature

---

[a)] Electronic mail: fvaz@fisica.uminho.pt (driving force). In the case of thin films, this phenomenon occurs at lower temperatures than in bulk materials, as less driving force is necessary to promote the diffusion of solute atoms into the available grain boundaries.[19] In previous works, the thermal process has been studied serving as a model for an effective combination of hard nitride/soft metal phases, as noted by Köstenbauer *et al*.[20] in their TiN/Ag multilayer samples. Kawamura *et al*.[21] also found that with increasing annealing temperature, Ag has a tendency to diffuse and agglomerate due to its poor substrate adhesion and ease of migration,[22] concluding that Ag performs better when alloyed with metals like Ti and Al. Diffusion is one of the mechanisms of mass transport,[23] which influences the agglomeration of particles in thin films. This phenomenon may occur in thin films, not only at the grain boundaries but also along the thickness of the film. Initially, the diffusion of particles occurs at the grain boundaries, and after this region reaches a percolation threshold, it begins to spread to the neighboring crystals, toward the surface. Although both diffusion mechanisms occur in crystalline thin films, they happen at different rates (diffusion at the grain boundaries is faster than diffusion along the film crystal), thus necessitating different annealing temperatures (driving force) to occur. In this particular case, the annealing can also prove the presence of this Ag segregation phenomenon in the studied Ag:TiN samples.[24,25]

In this work, the authors discuss the influence of different annealing temperatures in the electrical and mechanical properties of Ag:TiN nanocomposite thin films, taking into account the morphological and structural changes that occurred in the samples. It was found that extensive Ag segregation and coalescence occurs for temperatures above 200 °C, significantly affecting the crystallinity of the samples,[9] which are expected to give rise to some changes in the electrical and mechanical properties of the annealed samples, when comparing with the as-deposited ones.

## II. EXPERIMENT

Nanocomposite Ag:TiN thin films were deposited on glass (microscope slides from NORMAX, ISO 8037-1) and (100) silicon substrates by reactive dc magnetron sputtering, in a laboratory-sized custom-made deposition system. All substrates were sonicated and cleaned with ethanol 96% (vol.) just before each deposition. The films were prepared with the substrate holder positioned at 70 mm from the Ti/Ag target. A dc density of 100 A $m^{-2}$ was applied to the target, composed of titanium (99.96 at. % purity, with a dimension of $200 \times 100 \times 6$ mm) and Ag pellets ($8 \times 8 \times 1$ mm pellets, glued on the surface of the target), distributed symmetrically along the erosion area. The total surface area of the Ag pellets varied between 75 and 830 $mm^2$. A gas atmosphere composed of argon + nitrogen was used. The argon flow was kept constant at 60 sccm for all depositions (corresponding to a pressure of $3 \times 10^{-1}$ Pa), and the nitrogen flow rate was set at 5 sccm (partial pressure of $3.4 \times 10^{-2}$ Pa). The working pressure was approximately constant during the depositions, varying only slightly between 0.35 and 0.38 Pa. No bias voltage was used and the deposition temperature was maintained approximately constant at 100 °C during the film growth. A thermocouple was placed close to the surface of the "substrate holder" on the plasma side (not in direct contact, since depositions were done in rotation mode, using a speed of 7 rpm), and the temperature was monitored during the entire film deposition time, which was 3600 s. A delay time of 5 min was used before positioning the surface of the samples in front of the Ti/Ag target in order to avoid film contamination resulting from previous depositions (which may have resulted in some target poisoning) and also to assure a practically constant deposition temperature during the film growth. No metallic interlayer was used for the Ag:TiN films' deposition.

The as-deposited samples were subjected to several annealing treatments in a vacuum furnace at a pressure of $\sim 10^{-6}$ millibars. The selected annealing temperature range varied from 200 to 500 °C (a 5 °C/min heating stage until the desired temperature, followed by a 60 min stabilization step). The maximum of 500 °C is commonly known as an upper limit temperature at which TiN coatings may be used.[26,27] Before removing the samples, they were cooled down freely to room temperature in vacuum conditions. The atomic composition of the as-deposited samples was measured by Rutherford backscattering spectroscopy (RBS) using (1.4, 2.3) MeV and (1.4, 2) MeV for the proton and $^4$He beams, respectively. Three detectors were used; one located at a scattering angle of 140° and two pin-diode detectors located symmetrical to each other, both at 165°. Measurements were made for two sample tilt angles, 0° and 30°. Composition profiles for the as-deposited samples were determined using the software NDF.[28] The area analyzed was about $0.5 \times 0.5$ $mm^2$. The uncertainty in the N concentrations is around 5 at. %. The structure and phase distribution of the coatings were assessed by x-ray diffraction (XRD), using a Bruker AXS Discover D8 diffractometer, operating with Cu $K_\alpha$ radiation and in a Bragg–Brentano configuration. The XRD patterns were deconvoluted and fitted with a pseudo-Voigt function to determine the structural characteristics of the films, such as the peak position ($2\theta$), the full width at half maximum (FWHM), and the crystallite size. The film strain was included as a parameter for the grain size evaluation, which was carried out with the help of a free software (WINFIT). Morphological features of the samples were probed by scanning electron microscopy (SEM), carried out in a FEI Nova 200 (field emission gun/SEM) microscope operating at 15 keV. The electrical resistivity measurements were done on glass substrates using the four-probe van der Pauw method.[29] Single-cycle loading nanoindentation tests were carried out with a Micro Materials NanoTest with a 3 mN load (indentation depths were always below 10% of the film's thickness) using a Berkovich diamond indenter. A matrix of 5×5 indentations was used. The reduced modulus was calculated using the Oliver–Pharr method.

## III. RESULTS AND DISCUSSION

### A. Selected group of samples

In a previous study, the authors codeposited nanocomposite Ag-alloyed TiN (from 0 to ~50 at. % Ag) and correlated the thin films' properties and behavior evolution with the deposition conditions used.[9] Three distinct zones were defined throughout all characterization (composition, resistivity, morphology, and structural features), directly related to their different Ag contents.[9] Taking this into account, five representative samples of the three zones were then selected, according to their different Ag incorporations. The sample with 0.1 at. % Ag represents the behavior of the low-Ag content coatings, which were indexed to a TiN-like zone, zone I, while the samples with 6.3 and 20.2 at. % Ag represent the coatings that were indexed to a transition zone, zone II. The samples with 36.3 and 47.5 at. % Ag represent the group of coatings that were indexed to a high-Ag content zone, zone III, where Ag was found to have a significant role in the coating's behavior.[9]

Regarding the samples from zone I (very low Ag incorporation), the overall characterization experiments revealed a TiN-like character, where the low values of the deposition rate (around 1.3 $\mu$m/h) are in good agreement with the available values for pure stoichiometric TiN (1.2 $\mu$m/h) deposition conditions.[9] Due to some poisoning of the Ti fraction of the Ti/Ag target, a thin nitride layer is formed, thus lowering its sputtering yield (and ion induced secondary electron emission coefficient). Moreover, the resistivity values of this 0.1 at. % Ag sample are, due to the low Ag incorporation (see Table I), very similar to those of the pure TiN sample—$3.2 \times 10^{-5}$ and $2.2 \times 10^{-5}\,\Omega$ m, respectively.[9] Regarding its morphology, this zone I film exhibits the same porous pyramid-like columnar growth as the reference TiN sample. Once again, this behavior is expected due to negligible compositional changes. No Ag phases were detected in the XRD analysis. Hence, due to the very low Ag content exhibited by the selected 0.1 at. % Ag sample, no significant morphological, structural, and electrical differences were detected when compared to the pure TiN sample. Due to this, zone I samples were ascribed as being part of a nitride-like zone.

A change of the deposition rate evolution was evident in the films indexed to zone II (6.3 and 20.2 at. % Ag), whose values seemed to stabilize around ~1.1 $\mu$m/h. However, the exhibited values are slightly lower than those of the films from zone I. This may be due to the fact that the increase of the Ag fraction in the Ti/Ag target (from 140 to 450 mm$^2$, see Table I) was not yet enough to deplete the above referred poisoning effect. This behavior can also be ascribed to a gradual redeposition of the Ti poisoned fraction with Ag, due to strong differences between their sputtering yield values, hence altering the discharge characteristics.[9] Initially, within this zone II, low levels of Ag composition are perceivable (0.1–6.3 at. %), followed by a steep linear increase (from 6.3 to 36.3 at. %). This abrupt Ag incorporation translated into a steep drop of the resistivity values from $4.1 \times 10^{-6}$ to $5.2 \times 10^{-7}\,\Omega$ m, since Ag is a highly conductive alloying element (Ag phases were detected in both zone II selected samples).[9] Both TiN and Ag grain sizes suffered a steep decrease from 70 to 38 nm and from 28 to 10 nm for the fcc-TiN (111) and fcc-Ag (111) phases, respectively. This fact may indicate that the Ag concentration and distribution in the TiN matrix is controlling the resistivity evolution, instead of the grain size, since smaller grains are expected to promote higher resistivity values (the contrary of what was observed).[9] Note that zone II samples exhibited a strong Ag segregation phenomenon, with Ag uniformly dispersed among the TiN columns, leading to a resistivity drop due to a probable creation of intercolumnar electronic paths. Moreover, a strong densification of the samples was observed, with the typical nitride-like columnar features being progressively lost. Hence, this zone II was classified as a transition zone, since a steep change from a nitride-like to a metallic-like behavior was observed.

Finally, the samples from zone III, 36.3 and 47.5 at. % Ag, displayed higher deposition rate values (maximum of 1.8 $\mu$m/h), due to a strong increase of the Ag exposed area ($\geq$500 mm$^2$) in the Ti/Ag target.[9] This deposition rate increase may indicate that the high Ag fraction content (note that Ag presents higher sputtering yield) was sufficient to deplete the Ti poisoning effect. The less accentuated Ag content increase for concentrations ranging from 36.3 to 47.5 at. % was probably due to Ag saturation in the TiN matrix. The resistivity values continue to decrease, although not as abruptly, until values lower that those of the pure Ti are attained ($1.4 \times 10^{-7}$ $\Omega$ m), which could be ascribed to an almost complete densification (the morphology becomes similar to the pure Ag coating[9]) that was observed in this zone. Moreover, the Ag segregation phenomena is not so clear, with the Ag aggregates suffering a moderate decrease both in number and in size. In terms of structure, the Ag grain size roughly maintains its low values, while the TiN matrix grain size continues to decrease, from 38 to 14 nm. Hence, zone III samples can be considered polycrystalline. Consequently, zone III was considered a metallic-like zone. Further details on the composition and sputtering rate analysis can be found elsewhere.[9]

TABLE I. Discharge characteristics and Ag composition variation with increasing Ag exposed area in the target.

| Ag exposed area in the target (cm$^2$) | Ag composition (at. %)[a] | Deposition rate ($\mu$m/h) | Zone |
|---|---|---|---|
| 0.8 | 0.1 | 1.29 ± 0.03 | Zone I |
| 1.4 | 6.3 | 1.12 ± 0.03 | Zone II |
| 3.2 | 20.2 | 1.07 ± 0.03 | |
| 4.5 | 36.3 | 1.11 ± 0.07 | Zone III |
| 8.3 | 47.5 | 1.81 ± 0.03 | |

[a] The error in the Ag concentration is around 0.02 at. % for the low concentrations.

## B. Morphological and structural characterization

Starting with the five representative samples—0.1 at.% Ag from zone I, 6.3 and 20.2 at. % Ag from zone II, and 36.3 and 47.5 at. % Ag from zone III—and in order to check the coatings' structural and morphological stability, a set of in-vacuum annealing experiments were carried out. The morphological evolution of the coatings as a function of the annealing temperature, carried out by SEM investigation, showed two major morphological modifications within the annealing temperature range (from 200 to 500 °C). The first one is related with the coating growth-type (comprising aspects as densification and porosity), while the second one can be associated to a systematic Ag grain growth and formation of extensive Ag aggregates. It is important to notice that it was possible to identify very similar changes in all five representative samples, although with much clearer evidence in the samples with the highest Ag amount (films from zone III). Taking this into account, Fig. 1 shows SEM backscattered cross-section micrographs ($a_1$–$a_4$) and backscattered top view ($b_1$–$b_4$) micrographs of the Ag:TiN sample with an Ag content of 36.3 at. %, uncovering the most important changes that occurred in the film's morphology. At 200 °C [Figs. 1($a_1$)–1($b_1$)], the sample revealed the same columnar growth as the non-annealed sample (as-deposited), with some disaggregation areas [see Fig. 1($b_1$)] and the presence of some nanosized Ag particles throughout the film thickness [see Fig. 1($a_1$)], in an apparent homogeneous distribution. This could mean that the 200 °C temperature does not promote enough driving force to induce Ag segregation to the surface, and thus the Ag nanoparticles still remain trapped among the TiN columns as in the non-annealed sample. Note that the only visible change promoted by the 200 °C annealed sample is a somewhat rougher surface than the as-deposited one. At 300 °C [Fig. 1($a_2$)], there are now major changes in morphological terms, namely, the formation of Ag diffusion lines [small Ag particles forming a kind of diffusion path—Fig. 1(c)] along the columnar boundaries, as if illustrating the way that these same particles traveled while diffusing to the surface. It is also possible to observe the formation of some rather large Ag clusters on the surface. At 400 °C [Figs. 1($a_3$) and 1($b_3$)], there is a slight decrease in the number of Ag aggregates, associated with an increase of the spherical definition of the Ag particles' shape (becoming nearly spherical), together with a slight increase in the aggregate's dimension on the surface-coalescence.[22,30]

In a previous study, Adochite *et al.*[31] proved that with increasing annealing temperatures, an amorphous structure of a dielectric TiO$_2$ matrix (containing dispersed Ag clusters) became more and more crystalline, which prevents the diffusion of the Ag grains, thus facilitating the dispersion of the Ag nanoparticles throughout the entire thin film thickness. Using TEM image analysis, Adochite *et al.* confirmed that at 500 °C, the Ag nanoparticles diffused preferentially to both the substrate/film interface, as well as to the coating's surface.[31] It was also found that the shape of the Ag nanoparticles became more irregular due to Ag aggregation, promoted by the thermally induced Ag diffusion process that results from the annealing experiments.

In the present study, a first general observation is that an extensive diffusion and agglomeration of the Ag nanoparticles is perceivable with increasing annealing temperatures, which will have a major influence in the films' overall behavior. Confirming this fact, a radical dimensional increase (coalescence) of the Ag clusters sitting in the sample's surface (similar to the coating thickness: $>1\,\mu$m) is visible at 500 °C [Figs. 1($a_4$) and 1($b_4$)], thus losing their

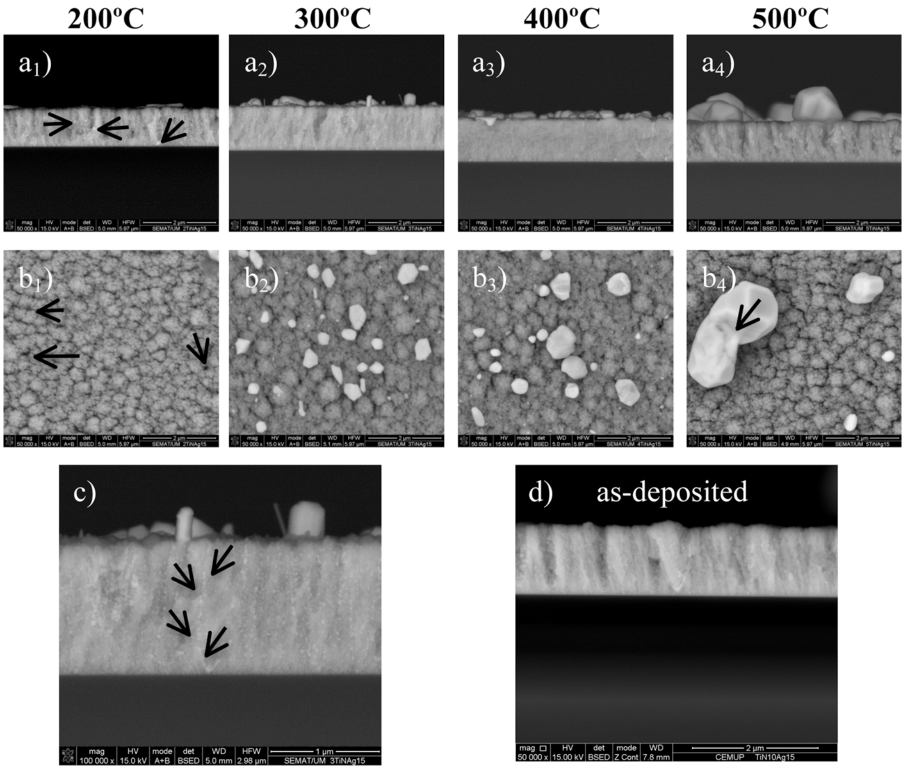

Fig. 1. SEM cross-section backscattered ($a_1$–$a_4$) and top backscattered micrographs ($b_1$–$b_4$) of the sample with an Ag content of 36.3 at. % with increasing annealing temperature. Bottom figures show the observed Ag diffusion lines of the 300 °C annealed sample (c), and the unannealed (as-deposited) sample is provided for comparison purposes (d).

spherical shape, resulting from the segregation of the small nanoparticles embedded along the column boundaries to the surface, as seen in Fig. 1(a$_4$). This Ag segregation phenomenon was also observed in other works.[32–35] RBS depth profiling of the samples, especially from the one with the highest Ag incorporation—47.5 at. % Ag, indicates that with increasing annealing temperature, Ag is gradually moving toward the coating's surface, resulting in a nonhomogeneous in-depth concentration. Consequently, it is possible to speculate that with longer annealing times, this diffusion of Ag nanoparticles toward the surface should be more pronounced. Note that even at 400 °C, Ag appears to be the dominant element at the coating's surface, as shown in Fig. 1(a$_3$). Combined SEM/energy-dispersive x-ray spectroscopy analysis confirmed that Ag is the only element present in these large clusters at the coating's surface. According to the work of Nilekar *et al.*,[36] the segregation energy of Ag solute atoms in transition metal matrixes is always inferior to −0.7 eV (except in a Au matrix), originating a "very strong segregation" phenomenon, so a complete segregation (which was not attained in this study) should be expectable using higher annealing times and/or temperatures. Furthermore, Zhang *et al.*[37] sputter deposited Ti–Ag–N films, claiming that Ag is immiscible with TiN, and thus a nanocomposite structure composed of Ag nanoparticles embedded in the TiN matrix is to be expected. This is also the case observed in the present study, reinforcing the fact that the Ag nanoparticles should gradually segregate to the surface, due to the temperature-promoted mobility increase.

Aiming at better understanding how the morphological changes that result from the application of annealing treatments are affecting the films' structural arrangements and their overall behavior, a detailed structural characterization was carried out, both in the as-deposited and annealed samples. Similarly to what was observed for the morphological evolution, the samples with the highest Ag contents (as it will be shown in detail for the sample with an atomic content of 36.3 at. %) revealed the most prominent changes. Figure 2 shows the XRD diffractograms of the Ag:TiN nanocomposites with an Ag content of 36.3 at. %, for both as-deposited and annealed samples. Accordingly, for the as-deposited sample, the development of a highly orientated coating is evident, showing two main crystalline phases: a fcc TiN-type structure—(111) peak located at an angular position of $2\theta \sim 36°$ (ICDD card 00-038-1420), typical for stoichiometric TiN thin films, and a fcc Ag-type structure—(111) peak located at an angular position of $2\theta$ at ∼38° (ICDD card 00-004-0783), typical for Ag thin films.[20,34,35] However, other secondary peaks can also be identified at diffraction angles of $2\theta \sim 42.5°$ [corresponding to a fcc-TiN type structure (200) diffraction pattern]; at $2\theta \sim 62°$ and $2\theta \sim 78°$, both indexed to the same fcc-TiN phase [(220) and (222) diffraction patterns, respectively].[38] Regarding the diffractograms corresponding to the annealing at 200 and 300 °C, it seems that an increasing definition/intensity of all diffraction peaks is present [Fig. 2(a)], which can be associated to a better definition of the crystalline phases that are present, namely, in what concerns the Ag-based ones with increasing temperature. It is noteworthy the diffraction peak at $2\theta \sim 44°$ [(200) of an Ag fcc-type structure], whose definition increased significantly, possibly indicating the beginning of the Ag nanoparticle segregation and their clustering, as well as the appearance of a new peak at a diffraction angle of $2\theta \sim 64°$, corresponding also to the Ag fcc-type structure [(220) diffraction planes]. From 400 up to 500 °C, there is clearly an approximation in terms of definition and intensity among Ag and TiN diffraction peaks, consistent with the formation of large Ag clusters, as first observed in the SEM micrographs (Fig. 1). It is also worth to highlight the formation of a new peak in the vicinity of $2\theta \sim 78°$, which can be indexed either to the diffraction of the fcc-Ag crystal structure [(311) planes] or to fcc-TiN (222). Also at 400 and 500 °C, the significant increase of definition (crystallinity) of the fcc-TiN (111) peak is noteworthy. A small shift of the peaks related to the fcc-TiN crystalline structure towards higher diffraction angles is evident, as seen in Fig. 2(b). In

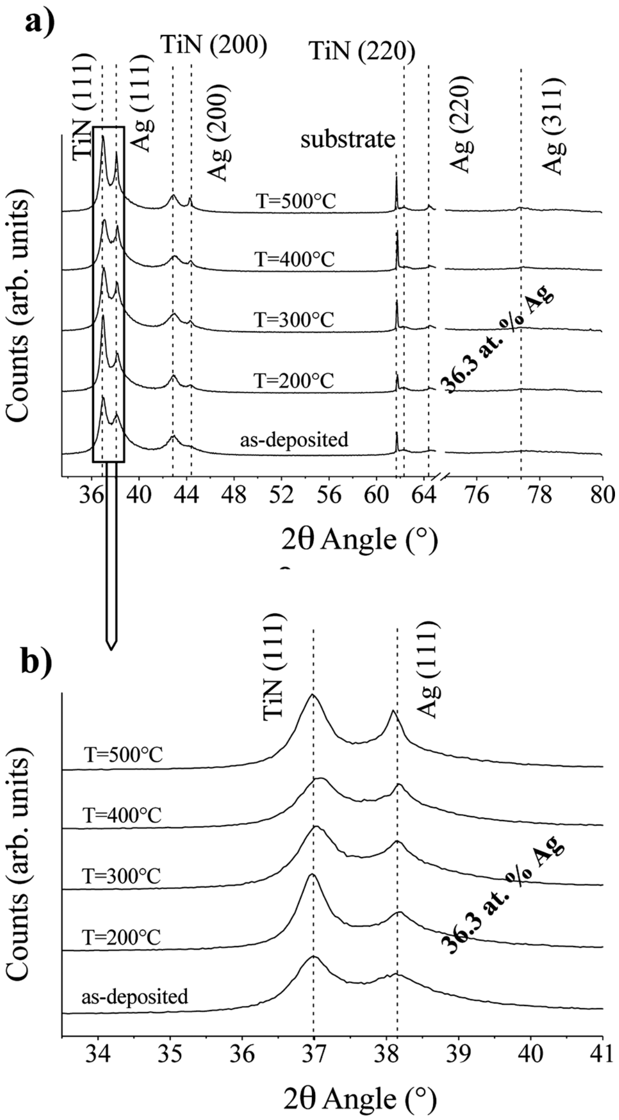

FIG. 2. XRD diffractograms of the sample with an Ag content of 36.3 at. % with increasing annealing temperature (a), and magnification of the 34°–41° region (b).

fact, this implies a decrease of the lattice parameter, which can be possibly explained by the contraction of the TiN structure, resulting from the migration of Ag atoms (that precipitated in the grain boundaries[2]) which segregated to the thin film surface, as found previously in SEM analysis.

In order to confirm all the structural modifications discussed, the influence of the annealing temperature in the evolution of the grain size of both main crystalline phases was also investigated [fcc-TiN (111) and fcc-Ag (111) peaks were used for the grain size determination by XRD peak fitting[39]] as shown in Figs. 3(a) and 3(b), respectively. From Fig. 3(a), it is possible to see that Ag additions promotes significant changes to the TiN matrix grain size. For the lowest Ag content, there are almost no perceivable changes for all temperatures, except for the 400 °C annealing, where a small increase of the crystalline size is evident. Increasing the Ag concentration up to 6.3 and 20.2 at. %, major changes are now patent, with the samples suffering an overall decrease of the grain size with increasing temperatures, when comparing to the unannealed samples (TiN grain size decreases from ∼65 nm and ∼40 nm to ∼20 nm for the 6.3 and 20.2 at. % Ag samples, respectively). Liu and Shen[40] proposed a phenomenological model for the solute-drag effect, concluding that in the case of Al additions to TiN, the segregation of Al solute atoms to the TiN grain boundaries result in an exponential drop of the average grain size values with increasing solute concentration. This solute-drag effect may, in fact, be responsible for the hindered growth of the TiN matrix grains. For the 36.3 at. % Ag, again, no substantial differences are found with increasing temperature. A maximum grain size of ∼23 nm is attained at 200 °C, decreasing sharply to a minimum of ∼7 nm at 300 °C. Subsequently, at 500 °C, the TiN crystalline size recovers to the as-deposited values (∼15 nm). This observation is consistent with SEM imaging [Fig. 1(a$_2$)], where it was possible to see that Ag was partly segregated. This means that, until this point, Ag is still acting as a pinning center for the TiN grain boundaries, inhibiting its growth. From this point onward, since the large Ag clusters (resulting from Ag nanoparticle aggregation) are now more extensively present at the surface [as confirmed in Fig. 1(b$_4$)], one can suppose that they are no longer acting as strongly as a barrier to the TiN grain growth. For the highest Ag content, a continuous decrease of the crystalline size is observed. At 500 °C, the grain size should be below 5 nm, thus not being able to be simulated. Note that this 47.5 at. % Ag sample is very dense, hence being possible to speculate that the Ag segregation to the surface should be more difficult due to the depletion of the intercolumnar spacing. This could mean that they should continuously act as pinning centers that inhibit TiN grain growth throughout all temperature range, since Ag should not be completely segregated to the surface.

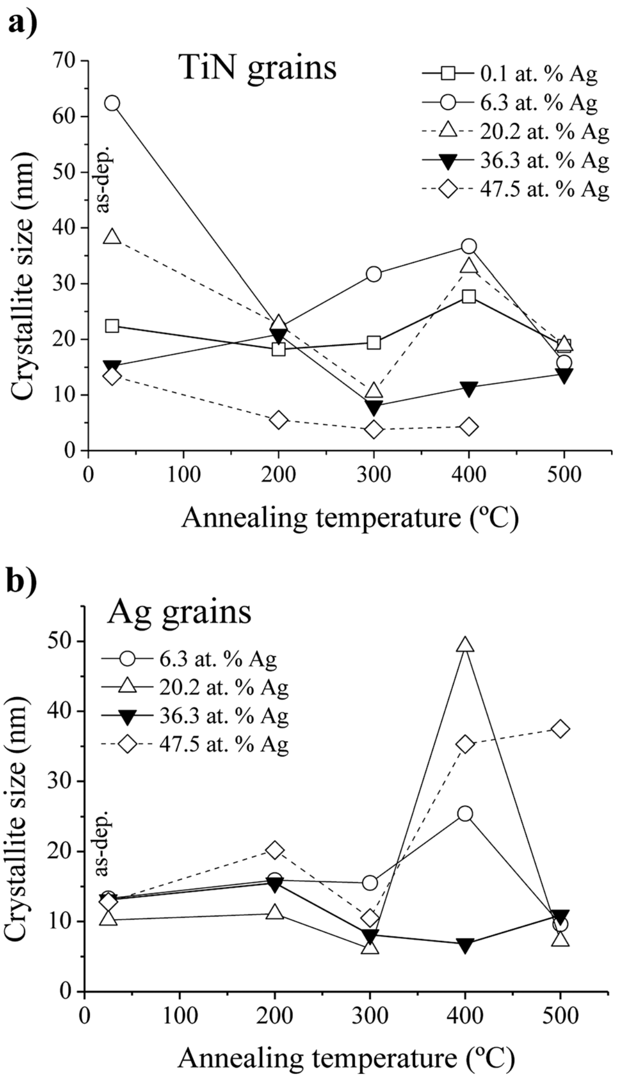

FIG. 3. Influence of the annealing temperature on the grain size evolution with increasing annealing temperature—(a) TiN (111) peak and (b) Ag (111) peak. The 500 °C TiN grain size of the 47.5 at. % Ag sample was not possible to simulate; at this temperature, the TiN matrix appears to suffer a strong decrease of its crystalline character (strong grain size reduction). The maximum variation of the grain size values throughout all simulations was always below 10%.

As for the Ag grain size evolution, Fig. 3(b), significant changes are only perceivable from 300 °C onward. At 400 °C, the samples with the lowest Ag contents exhibit maximum grain size values of ∼35 and ∼50 nm for the 6.3 and 20.2 at. % samples, respectively (no Ag peaks were detected in the 0.1 at. % sample). As for the sample with the highest amount of Ag, this maximum is achieved at 500 °C (∼47 nm). This could mean that for the two lowest Ag concentration samples, the fully coalesced Ag grains occur at 400 °C, while for the highest Ag composition, they continue to coalesce up to 500 °C. Taking into account the sample with 36.3 at.% Ag, the performed annealing treatments do not promote significant changes of crystalline size, with values varying slightly between ∼15 nm at 200 °C and ∼6 nm at 400 °C. In fact, most samples exhibit an abrupt change in the Ag crystalline size at 400 °C. This may be due to a temperature-promoted enhanced mobility of the Ag nanoparticles, since the appearing of large Ag clusters is initially seen at this temperature.

Based on Hentzell's model,[41] the authors propose a general model explaining the effect of solute additions on the grain structure and morphology evolution with increasing annealing temperatures: (i) for the lowest annealing temperature (200 °C), one can witness the enhancement of the Ag nanograin nucleation throughout the TiN matrix grain boundaries [as seen in Fig. 1($a_1$)]; in the as-deposited sample, there are already small evidences of nucleation [Fig. 1(d)]. No surface segregation is yet visible since there is not enough temperature-promoted driving force. However, some disaggregation areas are perceivable [Fig. 1($b_1$)], being possible to speculate that the paths through which Ag may be able to diffuse are in fact being formed. (ii) Increasing the annealing temperature up to 300 °C, the Ag atoms now possess enough mobility to move toward the top-end of the TiN matrix (with some of them able to reach the surface), using the disaggregation zones formed at 200 °C, leaving behind some kind of "diffusion paths" [Fig. 1(c)]. (iii) For the highest temperatures used (400 and 500 °C), a new process takes place. Once more and more Ag atoms are now present at the top-end of the coating and segregated to the surface in the form of nanograins [see Figs. 1($a_3$) and 1($a_4$)], they start to coalesce, gaining more definition in a first phase (400 °C). At 500 °C, the Ag clusters' size increases significantly, probably due to potential junctions (aggregation) of adjacent Ag nanograins, as it is possible to see from Fig. 1($b_4$). No significant grain growth is attained for most of the samples from 400 to 500 °C, Fig. 3, meaning that the observed dimensional increase of the Ag clusters must be due to agglomeration of smaller adjacent Ag clusters.

### C. Influence of the annealing temperature on the electrical and mechanical properties

As already mentioned, the main focus of the present thin film system is to be used in bioelectrodes, namely, those for EEG signal acquisition. For that purpose, two main properties are analyzed in this section: resistivity and the elastic modulus. The electrical resistivity of the five representative samples as function of the annealing temperature is shown in Fig. 4. As expected from XRD observations (Fig. 3), the increase of the annealing temperature promoted progressive disaggregation of the TiN columnar features and the decrease of the grain size gives rise to slightly higher resistivity values for almost all annealed samples, when compared to the as-deposited ones. The 6.3 and 47.5 at. % Ag samples seem to exhibit a rather constant behavior. However, one could expect that the higher grain size values exhibited by the Ag phase (enhanced crystallinity) with increasing annealing temperature should, on the contrary, promote a decrease of resistivity. Anyway, the obtained results do not seem to follow this tendency, indicating that it is probably not the Ag structural features that are playing the major role in the resistivity evolution but its morphology and distribution throughout the film thickness, as already observed in a previous work.[9] As mentioned before in this text, all annealed samples exhibited rougher features than the as-deposited ones, even at 200 °C, due to TiN column disaggregation. This roughness increase becomes clear when Ag starts to segregate to the surface (at 300 °C) and then coalesce (at 400 °C) and aggregate (at 500 °C)—see Fig. 1. Taking a closer look at the well-known Matthiessen's rule[42]

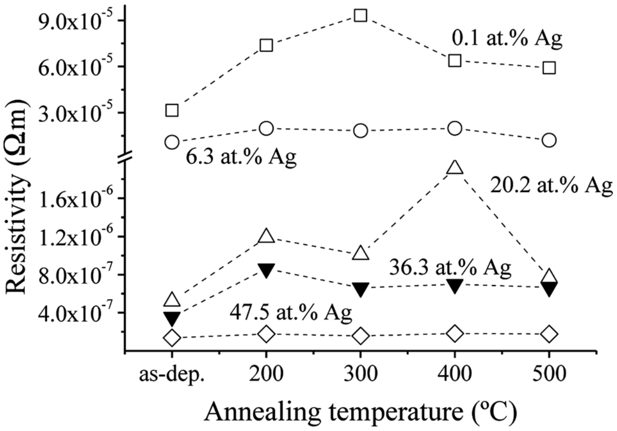

FIG. 4. Influence of the annealing temperature on the electrical resistivity evolution with increasing Ag content. The error associated to all measurements was always below 1% and the attachment of the contacts was checked prior to every measurement (the I/V correlation was always very close to 1).

$$\rho = \rho_p + \rho_m + \rho_f + \rho_i + \rho_s, \quad (1)$$

where $\rho_p$, $\rho_m$, $\rho_f$, $\rho_i$, and $\rho_s$ represent the resistivity caused by scattering from phonons, impurities, defects, grain boundaries, and the surface scattering, respectively, and also in the Fuchs–Sondheimer (F–S)[43,44] and Mayadas–Shatzkes (M–S) models,[45,46] one can claim that the surface-dependent mechanisms can influence significantly the resistivity evolution, as no significant impurities or defects were detected by RBS, and the thickness of the coatings is well above the mean free path of the conduction electrons. Consequently, besides the already referred influence of the grain size evolution[47] (which influences the grain boundary scattering—larger grains minimizes this effect), scattering from phonons, as well as surface (roughness) scattering, is probably playing a pivotal role in the resistivity increase.

Moreover, with the increase of the annealing temperature (up to 500 °C), the Ag nanoparticles consistently segregate toward the top-end of the TiN matrix, with many of them being able to segregate and coalesce on the surface. Therefore, a rise of the resistivity values can, *a priori*, be once again expected, as the Ag nanoparticles ought no longer be promoting enough conduction paths in-between the TiN column boundaries, since they are now extensively concentrated on the top-end of the coating. To summarize, the resistivity evolution is consistent with both the values of the grain sizes obtained by XRD (peak fitting) and SEM imaging. The observed increase of the resistivity values should be due to a combined effect of (i) the progressive grain size reduction of the TiN matrix, (ii) the roughness increase promoted by the gradual Ag segregation to the surface, and (iii) the reduction of the conduction paths in-between the TiN matrix that is once again promoted by the Ag segregation phenomenon.

Figure 5 depicts the reduced modulus ($E_r$) evolution with increasing annealing temperature, for one representative sample from each of the Ag composition zones. It becomes clear

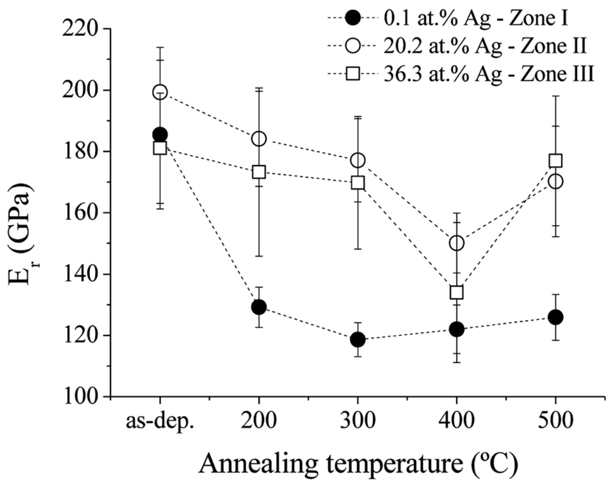

FIG. 5. Influence of the annealing temperature on the reduced Young's modulus evolution with increasing Ag content.

that the annealed samples from each zone reveal lower reduced modulus values, when compared with the as-deposited ones. In fact, the intermediate and high Ag content samples (20.2 and 36.3 at. % from zone II and zone III, respectively) exhibit a constant decrease of the $E_r$ values up to 400 °C. At this point, the absolute minimum of the reduced modulus values is attained. Looking back at Fig. 3(b), it is possible to confirm that the 400 °C annealing gives rise to higher Ag crystalline sizes, when comparing to the other annealing temperatures. This means that the Ag softer phases coalesced until their maximum size (at 500 °C, the large adjacent Ag clusters simply start to aggregate), being well distributed and occupying most of the TiN matrix top-end and surface, thus giving rise to a considerable drop of the $E_r$ values. At 500 °C, the large adjacent Ag clusters agglomerate, becoming more spaced throughout the TiN matrix surface. These highly localized Ag clusters, despite their bigger size, lead to a considerable increase of the $E_r$ values, as more TiN hard phases are "available."

As for the sample with the lowest Ag content (0.1 at. % from zone I), the mechanical behavior is somewhat different, with the minimum value of $E_r$ being reached at an earlier temperature (200–300 °C) interval. As shown in a previous work by the authors,[9] zone I as-deposited coatings exhibited a relatively porous structure that possibly facilitate the diffusion of the Ag nanoparticles to the TiN matrix surface, hence making the whole segregation and coalescence processes to occur in a lower temperature range. Therefore, the Ag atoms should require much less driving force (and mobility) to diffuse throughout a porous TiN matrix than through a compact one (late-zone II and zone III films exhibit a more compact morphology than zone I ones[9]). The effect of the highly porous coatings may perhaps shift the whole segregation process to lower temperatures due to an increased easiness of segregation (in the case of zone I sample). Consequently, the porous TiN matrix of the referred 0.1 at. % Ag sample should become uniformly covered with fully coalesced Ag particles in the 200–300 °C interval (instead of the 400 °C in the dense medium/high-Ag content samples—20.2 and 36.3 at. %), giving rise to lower $E_r$ values.

## IV. SUMMARY AND CONCLUSIONS

Regarding the morphological evolution with increasing annealing temperatures, it was possible to identify the existence of a significant Ag segregation phenomenon. The Ag nanoparticles embedded in the TiN matrix later spread to the top-end of the coating, with many of them being able to reach the surface where they agglutinate to form agglomerates with dimensions similar to those of the coating thickness by action of increasing annealing temperatures. The applied thermal treatments, beyond confirming the presence of free metallic Ag, also resulted in several structural changes on the studied samples, providing increasing Ag crystallinity within the coatings. The electrical resistivity values revealed small changes with increasing annealing temperature. The observed slightly higher values may be due to (i) a progressive disaggregation of the TiN columns; (ii) a substantial roughness increase that leads to a rise of the scattering from phonons and surface scattering and; (iii) Ag nanoparticle segregation to the surface that leads to a reduction of the conduction paths in-between the TiN features. Regarding the reduced modulus, a minimum value is attained at 400 °C for the samples with 20.2 at. % (zone II) and 36.3 at. % Ag (zone III). As for the low-Ag content sample (0.1 at. %—zone I), the lowest $E_r$ values are attained at a lower temperature interval (200 and 300 °C) due to increased porosity that may facilitate the diffusion of the Ag nanoparticles to the TiN matrix surface.

In conclusion, regarding the envisaged application as bioelectrodes, the occurrence of extensive Ag segregation only promotes beneficial changes concerning the elasticity improvement of the coatings. Moreover, Ag segregation gives rise to an unstable bioelectrode surface/interface. Consequently, in order to avoid (or, at least reduce) this unwanted phenomenon, the sputtering of dense/nonporous Ag:$TiN_x$ coatings (which may be attained by reducing the N/Ti ratio of the TiN matrix) is currently underway in the group, since it was found in the present study that denser films revealed lower levels of Ag segregation due to the absence of intercolumnar segregation pathways.

## ACKNOWLEDGMENTS

This research was partially sponsored by FEDER funds through the program COMPETE—Programa Operacional Factores de Competitividade and by national funds through FCT—Fundação para a Ciência e a Tecnologia, under the projects PEst-C/EME/UI0285/2011, PTDC/SAU-ENB/116850/2010, PTDC/CTM-NAN/112574/2009, and Programa Pessoa 2012/2013 Cooperação Portugal/França, Project No. 27306UA, Porous architectures in GRAded CERamic thin films for biosensors—GRACER. The authors would also like to acknowledge SEMAT-UM for SEM analysis. P. Pedrosa acknowledges FCT for the Ph.D. Grant SFRH/BD/70035/2010.

[1] T. de los Arcos, P. Oelhafen, U. Aebi, A. Hefti, M. Düggelin, D. Mathys, and R. Guggenheim, Vacuum **67**, 463 (2002).
[2] K. Kitawaki, K. Kaneko, K. Inoke, J. C. Hernandez-Garrido, P. Midgley, H. Okuyama, M. Uda, and Y. Sakka, Micron **40**, 308 (2009).

[3] L. T. Cunha, P. Pedrosa, C. J. Tavares, E. Alves, F. Vaz, and C. Fonseca, Electrochim. Acta **55**, 59 (2009).
[4] P. Pedrosa, E. Alves, N. P. Barradas, P. Fiedler, J. Haueisen, F. Vaz, and C. Fonseca, Corros. Sci. **56**, 49 (2012).
[5] G. Abadias, J. Appl. Phys. **95**, 2414 (2004).
[6] S. Rtimi, O. Baghriche, R. Sanjines, C. Pulgarin, M. Ben-Simon, J.-C. Lavanchy, A. Houas, and J. Kiwi, Appl. Catal., B **123–124**, 306 (2012).
[7] J. Zhao, H. J. Feng, H. Q. Tang, and J. H. Zheng, Surf. Coat. Technol. **201**, 5676 (2007).
[8] P. J. Kelly, H. Li, K. Whitehead, J. Verran, R. D. Arnell, and I. Iordanova, Surf. Coat. Technol. **204**, 1137 (2009).
[9] P. Pedrosa, D. Machado, C. Lopes, E. Alves, N. P. Barradas, N. Martin, F. Macedo, C. Fonseca, and F. Vaz, Appl. Surf. Sci. **285**, 40 (2013).
[10] K. Sivaramakrishnan, A. T. Ngo, S. Iyer, and T. L. Alford, J. Appl. Phys. **105**, 063525 (2009).
[11] O. Akhavan, J. Phys. D: Appl. Phys. **42**, 105305 (2009).
[12] A. W. Groenland, I. Brunets, A. Boogaard, A. A. I. Aarnink, A. Y. Kovalgin, and J. Schmitz, Proc. SAFE, 468 (2008).
[13] L. Vj, A. Katzenmeyer, M. S. Islam, N. P. Kobayashi, W. Wu, P. Chaturvedi, N. X. Fang, S. Y. Wang, and R. S. Williams, IEEE NANO, 92 (2008).
[14] N. J. Simrick, J. A. Kilner, and A. Atkinson, Thin Solid Films **520**, 2855 (2012).
[15] S. D. Kim, Curr. Appl. Phys. **7**, 124 (2007).
[16] T. Kushi, K. Sato, A. Unemoto, S. Hashimoto, K. Amezawa, and T. Kawada, J. Power Sources **196**, 7989 (2011).
[17] R. Ponnappan and T. S. Ravigururajan, J. Power Sources **129**, 7 (2004).
[18] R. Pestana and S. G. S. Filho, Rev. Bras. Apl. Vacuo **24**, 117 (2005).
[19] E. Rabkin, Scr. Mater. **42**, 1199 (2000).
[20] H. Köstenbauer, G. A. Fontalvo, J. Keckes, and C. Mitterer, Thin Solid Films **516**, 1920 (2008).
[21] M. Kawamura, Z. Zhang, R. Kiyono, and Y. Abe, Vacuum **87**, 222 (2013).
[22] O. Akhavan and A. Z. Moshfegh, Appl. Surf. Sci. **254**, 548 (2007).
[23] T. L. Alford, L. Chen, and K. S. Gadre, Thin Solid Films **429**, 248 (2003).
[24] T. Kaltenbach, W. Graf, and M. Ko, Sol. Energy Mater. Sol. Cells **54**, 363 (1998).
[25] H. Gao, L. Zhang, W. D. Nix, C. V. Thompson, and E. Arzt, Acta Mater. **47**, 2865 (1999).
[26] M. Wittmer, J. Noser, and H. Melchior, J. Appl. Phys. **52**, 6659 (1981).
[27] F. Suni, D. Sigurd, K. T. Ho, and M. A. Nicolet, J. Electrochem. Soc. **130**, 1210 (1983).
[28] N. P. Barradas, C. Jeynes, and R. P. Webb, Appl. Phys. Lett. **71**, 291(1997).
[29] L. J. Van der Pauw, Philips Res. Rep. **13**, 1 (1958).
[30] M. M. Viana, N. D. S. Mohallem, D. R. Miquita, K. Balzuweit, and E. Silva-Pinto, Appl. Surf. Sci. **265**, 130 (2013).
[31] R. C. Adochite *et al.*, Appl. Surf. Sci. **258**, 4028 (2012).
[32] P. J. Kelly, H. Li, P. S. Benson, K. A. Whitehead, J. Verran, R. D. Arnell, and I. Iordanova, Surf. Coat. Technol. **205**, 1606 (2010).
[33] V. Moreno, J. Creuze, F. Berthier, C. Mottet, G. Tréglia, and B. Legrand, Surf. Sci. **600**, 5011 (2006).
[34] W. Gulbiński and T. Suszko, Surf. Coat. Technol. **201**, 1469 (2006).
[35] D. Resnik, J. Kovač, D. Vrtačnik, and S. Amon, Thin Solid Films **516**, 7497 (2008).
[36] A. U. Nilekar, A. V. Ruban, and M. Mavrikakis, Surf. Sci. **603**, 91 (2009).
[37] M. Zhang, L. Hu, G. Lin, and Z. Shao, J. Power Sources **198**, 196 (2012).
[38] J. C. Sánchez-López, M. D. Abad, I. Carvalho, R. Escobar Galindo, N. Benito, S. Ribeiro, M. Henriques, A. Cavaleiro, and S. Carvalho, Surf. Coat. Technol. **206**, 2192 (2012).
[39] P. Thompson, D. E. Cox, and J. B. Hastings, J. Appl. Cryst. **20**, 79 (1987).
[40] Z.-J. Liu and Y. G. Shen, J. Vac. Sci. Technol. A **24**, 174 (2006).
[41] H. T. G. Hentzell, C. R. M. Grovenor, and D. A. Smith, J. Vac. Sci. Technol. A **2**, 218 (1984).
[42] K.-Y. Chan, T.-Y. Tou, and B.-S. Teo, Microelectron. J. **37**, 608 (2006).
[43] K. Fuchs, Proc. Cambridge Philos. Soc. **34**, 100 (1938).
[44] E. H. Sondheimer, Phys. Rev. **80**, 401 (1950).
[45] A. F. Mayadas, M. Shatzkes, and J. F. Janak, Appl. Phys. Lett. **14**, 345 (1969).
[46] A. F. Mayadas and M. Shatzkes, Phys. Rev. B **1**, 1382 (1970).
[47] M. E. Day, M. Delfino, J. A. Fair, and W. Tsai, Thin Solid Films **254**, 285 (1995).

Electrochimica Acta 125 (2014) 48–57

Contents lists available at ScienceDirect

Electrochimica Acta

journal homepage: www.elsevier.com/locate/electacta

# Electrochemical behaviour of nanocomposite $Ag_x$:TiN thin films for dry biopotential electrodes

P. Pedrosa [a,b,c], E. Alves [d], N.P. Barradas [e], N. Martin [f], P. Fiedler [g], J. Haueisen [g], F. Vaz [c], C. Fonseca [a,b,*]

[a] SEG-CEMUC–Department of Mechanical Engineering, University of Coimbra, Portugal
[b] Universidade do Porto, Faculdade de Engenharia, Departamento de Engenharia Metalúrgica e de Materiais, Rua Dr. Roberto Frias, s/n, 4200-465 Porto, Portugal
[c] Centro de Física, Universidade do Minho, 4710-057 Braga, Portugal
[d] Associação Euratom/IST, Instituto de Plasmas e Fusão Nuclear, Instituto Superior Técnico, Universidade Técnica de Lisboa, Av. Rovisco Pais, 1049-001, Lisboa, Portugal
[e] Campus Tecnológico Nuclear, Instituto Superior Técnico, Universidade Técnica de Lisboa, E.N. 10, 2686-953 Sacavém, Portugal
[f] Institut FEMTO-ST, UMR 6174, Université de Franche-Comté, CNRS, ENSMM, UTBM, 32, Avenue de l'observatoire, 25044 BESANÇON Cedex, France
[g] Institute of Biomedical Engineering and Informatics, Technische Universität Ilmenau, Ilmenau, Germany

## ARTICLE INFO

*Article history:*
Received 21 November 2013
Received in revised form 4 January 2014
Accepted 14 January 2014
Available online 27 January 2014

*Keywords:*
TiN
Ag-doping
Biopotential electrodes
Dry electrodes, EIS

## ABSTRACT

$Ag_x$:TiN nanocomposite thin films with Ag contents ranging from ~0.1 up to ~47.5 at% obtained by DC reactive sputtering on glass substrates were characterized regarding their electrochemical performance in a synthetic sweat solution, aiming at studying their potential application as bioelectrodes. Correlations between the electrochemical behaviour and their exhibited morphology (porosity) and structure (grain size) were established and discussed in detail. The coatings' open circuit potential (OCP) is ruled by the Ag/TiN galvanic coupling and it decreased with the increase of the Ag content. For Ag contents up to 12.1 at% the OCP was found to be close to that of bulk Ag, but for higher Ag contents the OCP of the $Ag_x$:TiN samples displayed a steep drop, which was ascribed to the effect of Ag grain size reduction (from ~28 to ~10 nm). Both SEM and voltammetric experiments confirmed a gradual porosity decrease (densification) of the coatings with increasing Ag content, leading to a reduction of the electroactive area. All samples, besides displaying good chemical stability in chloride media, exhibited low impedance moduli and electrochemical noise similar to that of commercial Ag/AgCl electrodes, thus making them suitable to be used as bioelectrodes, from the electrochemical point of view.

## 1. Introduction

High resolution monitoring of biopotentials produced by the human body, such as electroencephalographic (brain activity), electrocardiographic (heart activity) and electromyographic (muscular activity) potentials, are being actively used for the past decades in order to accurately assess several pathologies and physiological conditions of human patients. The conventional biopotential acquisition setup relies on the use of silver/silver chloride (Ag/AgCl) wet electrodes, which are widely considered as the "gold standard" [1–3]. These are non-polarizable and reveal excellent reliability, displaying low and almost frequency independent skin-contact impedance values, in the order of a few tens of k$\Omega$.cm$^2$ [2,3]. However, in order to achieve such low impedance values, a preliminary skin preparation and conductive gel paste application are of paramount importance. It follows that the use of such electrodes implies time-consuming preparation procedures that require trained staff. Moreover, allergic reactions to the conductive gel have been reported [3] and the risk of short-circuiting adjacent electrodes due to gel running has been pointed out as a common problem. Some other major drawbacks have also been reported, such as susceptibility to motion artifacts and inability to record biopotentials in long-term clinical monitoring (ambulatory) [2,3].

Eliminating the need to use the conductive gel paste would, in fact, reduce most of the above-referred disadvantages of the standard Ag/AgCl electrode system. Consequently, a new class of biopotential electrodes is being widely investigated, which are commonly called "dry" electrodes. These electrodes do not require any previous skin preparation or gel application and are commonly based on inert-like materials, either metallic-like or insulator-coated metals [3,4]. In a previous work [5], the authors investigated the possibility to use the TiN thin film system

---

* Corresponding author.
*E-mail address:* cfonseca@fe.up.pt (C. Fonseca).

http://dx.doi.org/10.1016/j.electacta.2014.01.082
0013-4686/© 2014 Elsevier Ltd. All rights reserved.

(deposited on titanium substrates) for dry electrode sensors, which exhibited very promising results such as low electrical noise levels and excellent chemical resistance to sweat. However, these electrodes still maintain some important drawbacks that have also been reported in other similar "dry" systems [6,7], such as incorrect and/or uncomfortable skin contact due to its intrinsic stiffness nature that do not allow them to conform to the human body. Moreover, focusing on the typical electroencephalography (EEG) acquisition setup, the use of lighter, cheaper and more comfortable electrodes would translate in numerous advantages to the patients in comparison with the standard Ag/AgCl ones, once the use of 128 or even 256 electrodes in a single exam is becoming an increasingly common practice.

Recently, several authors have focused on the development of polymer-based flexible dry electrodes [8–11], since they are able to promote a more reliable and comfortable skin contact, thus reducing some of the stated drawbacks. However, higher impedances at low frequencies and higher susceptibility to movement artefacts when comparing to the conventional Ag/AgCl electrodes [1,3,7] are still an issue. This is particularly important in ambulatory applications, where the patient must be able to move without constraints. As a result, and in opposition to most common approaches (where authors rely on composite materials, foams, conductive polymers, among others), the authors explored the sputtering viability of $Ag_x$:TiN coatings by optimizing the thin film's morphological, structural and electrical properties [12], envisaging the development of flexible dry biopotential electrodes.

TiN is a biocompatible and electrically conductive ceramic, with an excellent chemical stability in most media and outstanding mechanical properties, thus giving rise to a wide range of applications, with some of them in the biomedical area [13,14]. Silver is commonly known as a bactericide agent [15–17], particularly in its nanocrystalline form [18,19] and offers the possibility to tailor the mechanical properties of the TiN system, regarding the sputtering on flexible substrates, since Ag increases the plasticity of TiN (a brittle material); besides, it promotes excellent tribological properties to the composite [20]. Finally, silver is also an excellent biosensor material [21] for electrophysiological signal monitoring. Hence, in a more application-oriented study, a comprehensive electrochemical characterization of the sputtered $Ag_x$:TiN coatings is of paramount importance. The available literature is not very prolific about the electrochemical characterization of the Ti-N-Ag system, with very few works dedicated [22–24] to it. Adams et al. work [22] has the objective to form TiN encapsulation and passivation layers against Ag corrosion in integrated circuits (Adams started with a Ti-Ag film, nitriding it afterwards), while Zhao et al. [23] tried to implement some bactericide character to TiN films by Ag ion implantation to be used as biomedical implants, thus also studying its corrosion resistance in simulated body fluid. Zhang et al. [24], on the other hand, studied the potential application of Ti-Ag-N coatings as bipolar plates in fuel cells, by co-depositing Ti and Ag in a $N_2$ atmosphere using pure Ti and Ag targets. Hence, none of these references is related to the envisaged application, a fact that supports the scientific novelty of the present work.

The main objective of the present work is then to undertake a comprehensive electrochemical characterization of a selected group of $Ag_x$:TiN coatings, covering a wide range of Ag contents, and assess their viability to be used as biopotential electrodes, from the electrochemical point of view.

## 2. Experimental

### 2.1. Thin film production

The $Ag_x$:TiN films were deposited on glass and (100) silicon substrates by reactive DC magnetron sputtering, in a laboratory-sized deposition system. All substrates were sonicated and cleaned with ethanol 96% (vol.) just before each deposition. The films were prepared with the substrate holder positioned at 70 mm from the Ti/Ag composite target. A DC current density of 100 $A.m^{-2}$ was applied to the composite target, composed of titanium (99.96 at. % purity/$200 \times 100 \times 6$ $mm^3$) and silver pellets ($80 \times 80$ $mm^2$/1 mm thick pellets glued on the surface of the target) distributed symmetrically along the Ti target erosion area. The total surface area of the silver pallets varied between 75 to 830 $mm^2$. A gas atmosphere composed of argon + nitrogen was used. The argon flow was kept constant at 60 sccm for all depositions, as well as the nitrogen flow rate, which was set at 5 sccm (corresponding to a partial pressure of $3.4 \times 10^{-2}$ Pa). The working pressure was approximately constant during the depositions, varying only slightly between 0.35 and 0.38 Pa. No bias voltage was used, and the deposition temperature was maintained approximately constant at 100 °C during the films' growth. A thermocouple was placed close to the surface of the "substrate holder" on the plasma side (not in direct contact, since all depositions were done in rotation mode), and the temperature was monitored during the entire films' deposition time. A delay time of five minutes was used before positioning the surface of the samples in front of the Ti/Ag target in order to avoid films' contamination resulting from previous depositions (which may have resulted in some target poisoning), and also to assure a practically constant deposition temperature during the films' growth.

### 2.2. Structural and morphological characterization

The atomic composition of the as-deposited samples was measured by Rutherford Backscattering Spectroscopy (RBS) using (1.4, 2.3) MeV and (1.4, 2) MeV for the proton and $^4He$ beams, respectively. Three detectors were used. One located at a scattering angle of 140° and two pin-diode detectors located symmetrical to each other, both at 165°. Measurements were made for two sample tilt angles, 0° and 30°. Composition profiles for the as-deposited samples were determined using the software NDF [25]. For the $^{14}N$, $^{16}O$ and $^{28}Si$ data, the cross-sections given by Gurbich were used [26]. The area analysed was about $0.5 \times 0.5$ $mm^2$. The uncertainty in the N concentrations is around 5 at%. The structure and phase distribution of the coatings were assessed by X-ray diffraction (XRD), using a Bruker AXS Discover D8 diffractometer, operating with Cu $K_\alpha$ radiation and in a Bragg-Brentano configuration. The XRD patterns were deconvoluted and fitted with a Voigt function to determine the structural characteristics of the films, such as the peak position ($2\theta$), the full width at half maximum (FWHM) and the crystallite size. Morphological features of the samples were probed by scanning electron microscopy (SEM), carried out in a FEI Quanta 400FEG ESEM microscope operating at 15 keV. The resistivity measurements were done using the four-probe van der Pauw method [27].

### 2.3. Electrochemical characterization

The polished glass substrates, coated with $Ag_x$:TiN films were rinsed in isopropanol (10 minutes) and water (10 minutes) and dried with a hair drier, prior to the electrochemical experiments. A synthetic sweat solution with a pH of 4.7 and containing ammonium chloride, sodium chloride, urea, lactic acid and acetic acid was used in all electrochemical studies, in order to simulate the behaviour of the sensor in contact with the body sweat [28]. Cyclic voltammetry (CV) curves were performed at sweep rates varying from 1 mV/s to 5 V/s, by using the Gamry G300 equipment (Gamry Instruments, USA) driven by the Gamry PHE200 software. Electrochemical impedance spectroscopy (EIS) was performed at the open circuit potential (OCP), for frequencies ranging from 10 kHz

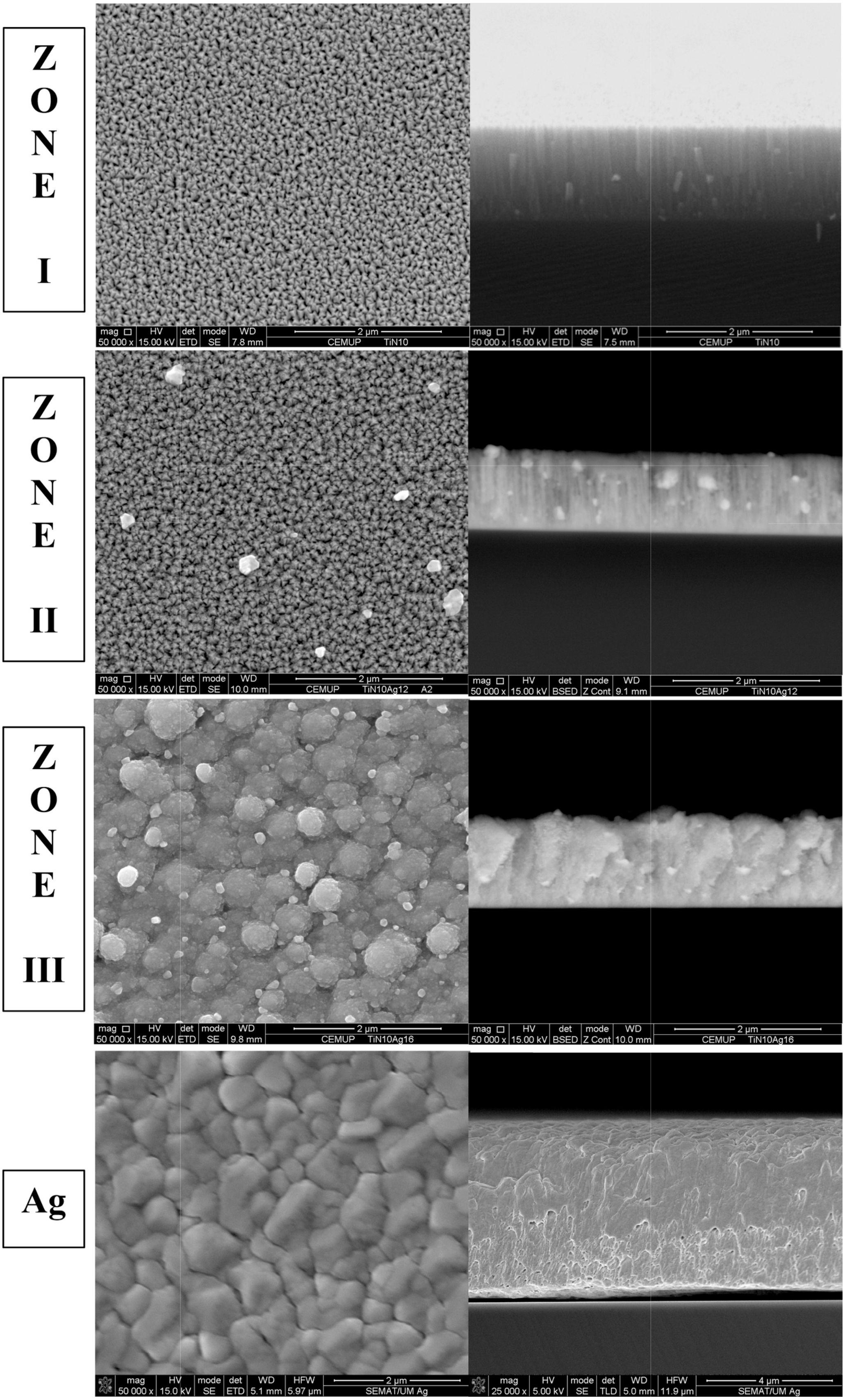

**Fig. 1.** Morphological features and classification of the as-deposited $Ag_x$:TiN coatings. The Ag coating is shown for comparison purposes.

to 2 mHz, with a 7 mV (rms) AC probe signal, using the EIS300 software from Gamry. Preliminary galvanic coupling experiments were performed by immersing both TiN and Ag control samples in the synthetic sweat solution, and connecting the samples to a zero resistance ammeter (Gamry ZRA mode). The current and potential acquisitions were performed with the ESA410 software from Gamry. All potentials were measured against the saturated calomel electrode (SCE). A platinum wire was used as counter electrode in the voltammetric and impedance measurements. Simulation of the experimental data was also performed with Gamry software. The electrochemical noise data was acquired using the ESA410 software from Gamry, by immersing two identical samples from each Ag composition batch in the synthetic sweat solution. Two Ag/AgCl commercial electrodes (B10, EASYCAP GmbH, Germany) were used as comparison reference. A stabilization time of 3 minutes was used in all runs. The results were then analysed using a custom MatLab (The Mathworks Inc., USA) algorithm. This analysis included application of a 20th order Butterworth bandpass filter with cut-off frequencies at 0.5 and 100 Hz before the Welch estimation of the power spectral density (PSD).

## 3. Results and discussion

### 3.1. Morphological and structural evaluation of $Ag_x$:TiN films

In a previous work by the authors, a set of Ag-alloyed TiN samples with compositions ranging from ~0.1 to ~47.5 at% Ag were sputtered using a compound Ti/Ag target (with an increasing number of Ag pellets) in a $N_2$ atmosphere [12]. The thin films' characteristics were then extensively studied regarding their composition, morphology, structural features and resistivity evolution with increasing Ag additions. Several correlations were also drawn with the discharge characteristics and the deposition conditions used. As a result of this study, the obtained samples were grouped in three composition zones, according with their electrical behaviour. Taking this into account, five representative samples of the three zones were then selected to conduct the present study, according to their different Ag content. The sample with 0.1 at% Ag represents the behaviour of the coatings from Zone I, the samples with 12.1 and 20.2 at% Ag represent the coatings from Zone II, while the samples with 36.3 and 47.5 at% Ag represent the coatings from Zone III, as described in Table I. Pure stoichiometric TiN and Ag sputtered samples, prepared in similar conditions, were also selected as control samples for comparison purposes.

Due to the very low Ag incorporation, Zone I sample (0.1 at% Ag) exhibits a typical TiN-like character, with low sputtering rates (~1.3 μm/h), rather close to the pure TiN control sample value (~1.2 μm/h). This is due to some poisoning of the Ti fraction of the target, which becomes covered by a very thin nitride layer, thus giving rise to low and TiN-like sputtering rates. The resistivity values of this Zone I sample are again very similar to the TiN control sample ($3.2 \times 10^{-5}$ and $2.2 \times 10^{-5}$ Ω.m, respectively), which is expected once the compositional differences are not significant. Although these values may seem rather high, one must bear in mind that all coatings were obtained at low temperatures and with no bias voltage, which translates into low adatom mobility. Note that the authors aim at coating polymer samples, hence aggressive deposition conditions were ruled out. In terms of morphology, Zone I coating presents well-defined columnar growth, with pyramid-like features at the surface, see Fig. 1, although with some disaggregation areas and inter-columnar porosity, thus being very similar to the pure TiN control sample [12]. Furthermore, no Ag phases were detected in this sample by XRD, Fig. 2, which is in line with the SEM observations that found no Ag clusters in any of the analysed samples within this zone. Due to its relatively low content, the presence of Ag in zone I didn't induce any significant structural, morphological or electric differences, when compared to TiN control sample.

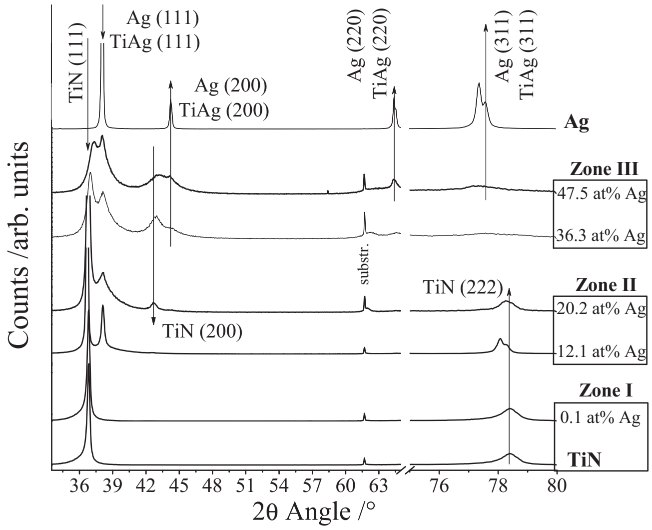

**Fig. 2.** XRD diffractograms of the as-deposited $Ag_x$:TiN coatings. The diffractograms are shown using different yy axis scales for a clearer observation of the diffraction patterns.

Zone II samples, 12.1 and 20.2 at% Ag, also exhibited low sputtering rates, since the Ag fraction of the Ti/Ag compound target is not yet enough to reduce the poisoning effect referred above. Moreover, it was found that gluing Ag pellets on the erosion track might change the target impedance, hence altering the discharge characteristics [12]. Nevertheless, a strong Ag incorporation was attained in this zone, resulting in a steep drop of the resistivity values (from $4.1 \times 10^{-6}$ to $5.2 \times 10^{-7}$ Ω.m), since highly conductive Ag phases are now present, Fig. 2. Note that both TiN and Ag grain sizes suffer a strong decrease within Zone II samples, varying from ~70 to ~38 nm for the fcc-TiN (111) phase and from ~28 to ~10 nm for the fcc-Ag (111) phase, which means that it is not the grain size that dictates the resistivity drop (in fact, grain size decrease is known to promote an increase of resistivity), but the Ag content and its distribution in the TiN matrix. In fact, from Fig. 1 it is possible to see that for Zone II samples, a strong Ag segregation phenomenon occurs, with Ag being well dispersed among the TiN columns, possibly creating electronic paths in-between them, that will contribute to a conductivity improvement [12]. On the other hand, the well-dispersed Ag throughout the TiN matrix, allied to the strong resistivity drop followed by a smooth variation, may indicate that the percolation threshold may have been reached, Table I. Hence, Zone II will be noted henceforth as a transition zone, following the observations for the next group of samples (with the highest Ag contents), where extensive morphological changes have occurred.

In fact, within Zone III, represented by the samples with 36.3 and 47.5 at% Ag, one can see a steep increase of the sputtering rate from ~1.1 to ~1.8 μm/h due to the depletion of the Ti fraction poisoning effect and the Ag superior sputtering yield [12]. As for the grain size evolution, it is possible to see that, when comparing to Zone II values, Ag grains roughly maintain their dimensions, while TiN grains decrease their crystalline size until ~14 nm, Table I. Zone III samples can thus be considered polycrystalline. Resistivity continues to decrease, although more smoothly, until values below pure Ti itself [12]. A complete densification, similar to the pure Ag control sample, of the $Ag_x$:TiN samples is also attained within Zone III and the Ag segregation phenomenon is not so clearly present (the number and dimension of the aggregates suffer a moderate decrease),

**Table I**
Growth rate, Ag composition, resistivity and grain size variation with increasing Ag exposed area in the target.

| Ag exposed area in the target/mm$^2$ | Ag composition/at%[a] | Deposition rate/μm/h | Grain size/nm[b] | | Resistivity/Ω m[c] | Zone |
|---|---|---|---|---|---|---|
| | | | TiN | Ag | | |
| TiN | 0 | 1.21 ± 0.07 | 39 | - | $2.2 \times 10^{-5}$ | Control sample |
| 75 | 0.1 | 1.29 ± 0.03 | 23 | - | $3.2 \times 10^{-5}$ | Zone I |
| 160 | 12.1 | 1.06 ± 0.03 | 70 | 28 | $4.1 \times 10^{-6}$ | Zone II |
| 320 | 20.2 | 1.07 ± 0.03 | 38 | 10 | $5.2 \times 10^{-7}$ | |
| 450 | 36.3 | 1.11 ± 0.07 | 15 | 13 | $3.5 \times 10^{-7}$ | Zone III |
| 830 | 47.5 | 1.81 ± 0.03 | 14 | 13 | $1.4 \times 10^{-7}$ | |
| Ag | 100 | 4.72 ± 0.03 | - | 78 | $1.6 \times 10^{-8}$ | Control sample |

[a] The error in the Ag concentration is around 0.02 at% for contents below 0.1 at%.
[b] The maximum variation of the grain size values throughout all simulations was always below 10%.
[c] The error associated to all measurements was always below 1% and the attachment of the contacts was checked prior to every measurement.

see Fig. 1. Furthermore, a N-deficient (under-stoichiometric) TiN matrix is attained in the 47.5 at% Ag sample, thus the formation of a TiAg intermetallic may be also taking place (see Fig. 2). The samples from this third zone can thus be considered as within a metallic-like zone. Further morphological, structural and electrical details can be found elsewhere [12].

### 3.2. Electrochemical characterization is synthetic sweat

#### 3.2.1. Open Circuit Potential (OCP)

When two dissimilar metals are immersed in an electrolyte and these metals are electrically connected externally, there will be an electronic flow (current) between them, driven by the different electron affinity of the metals [29]. As a result, the corrosion of the less noble metal (anode) is enhanced, while the corrosion of the nobler one (cathode) is decreased. Similarly, if a material is composed of two conductive phases in contact with an electrolyte, the mixed potential theory [29] suggests that the nobler phase will behave as the cathode, the other will be the anode and resulting potential will lie between the potentials of the phases. Therefore, according with our previous studies, it is expected that the mixed potential theory also applies for the $Ag_x$:TiN nanocomposites.

In order to check the electrochemical behaviour of the Ag and TiN phases in the $Ag_x$:TiN nanocomposites, a galvanic coupling experiment was first performed using TiN and Ag control coatings. As seen on Fig. 3, TiN displays the highest potential and, upon electrical connection of the samples, the mixed potential shifted closer to Ag, what may be ascribed to the stronger polarizability of TiN. Only ~20 s after the coupling of the dissimilar elements, the potential stabilizes at approximately the value of pure Ag, while the current reduced to a few μA. According with the initial OCP's of TiN and Ag and the direction of the observed current, TiN behaved as the cathode and Ag as the anode. The observed current should have two components, namely (i) a fast, initial current decrease, related with the double layer charging at the material/electrolyte interfaces and (ii) a slower faradic current, including the residual stationary current, related with silver oxidation at the silver anode and, possibly, silver reduction at the TiN cathode.

The OCP values of the $Ag_x$:TiN samples were monitored for a period of 2 h in a synthetic sweat solution in order to simulate the contact between the biopotential electrode and the sweat-hydrated skin during *in-vivo* applications, Fig. 4. The stoichiometric TiN control sample exhibited the expected noble value (~140 mV), reflecting its good chemical stability [5]. However, a significant variability among samples was observed. As for the pure Ag sample, the obtained OCP values, which were similar using either Ag wire or the Ag coating, are in-line with the value found in the bibliography, ~40 mV, indicating that the potential is ruled by the formation of a thin Ag/AgCl film through $Cl^-$ adsorption (Ag/AgCl exhibits OCP values of ~ 40 mV vs. SCE) [30,31].

As for the $Ag_x$:TiN samples, a clear difference in the overall behaviour is perceivable between the low- and medium-low Ag content samples (0.1 at% - Zone I and 12.1 at% - Zone II) and the medium-high and high-Ag content ones (20.2 at% - Zone II; 36.3 and 47.5 at% - Zone III). The 0.1 and 12.1 at% Ag samples, despite being mainly composed by stoichiometric TiN, exhibit OCP values rather similar to the Ag control sample, in line with the behaviour observed in the galvanic coupling experiment, Fig. 3. As the Ag content increases beyond 12 at%, the OCP values suffer a steep decrease towards less noble values (-160 mV < OCP < -100 mV). Thereafter, Ag additions in the 20.2-47.5 at% interval appear to lead to a gradual increase of the OCP. Such departure from the previsions of the

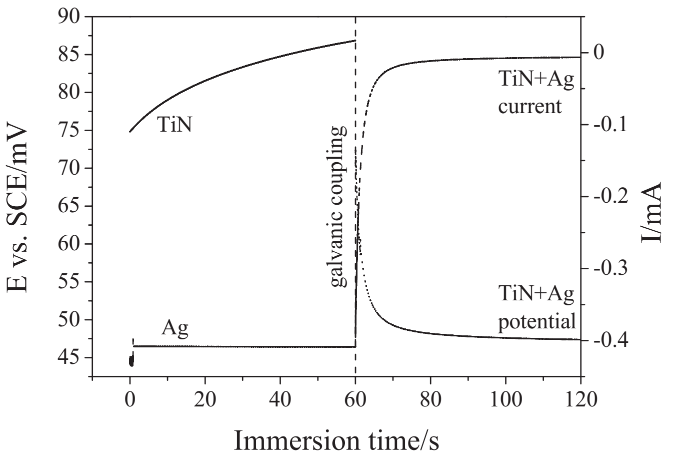

**Fig. 3.** TiN/Ag galvanic coupling experiment. The galvanic potential and current were initially monitored for each control sample individually. After ~60 s, the samples were electrically coupled.

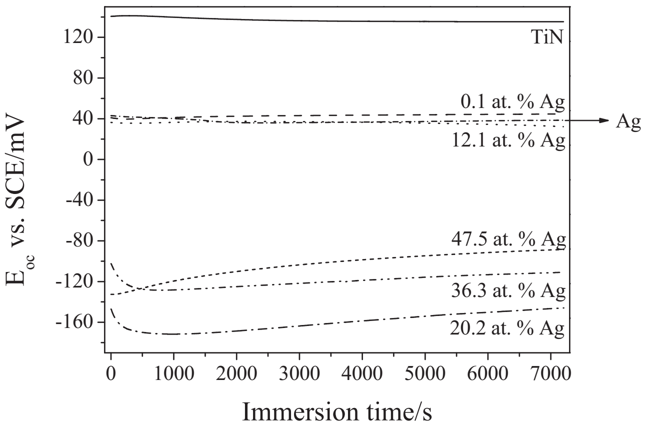

**Fig. 4.** OCP evolution of the as-deposited $Ag_x$:TiN samples as a function of immersion time. TiN and Ag control films are plotted for comparison.

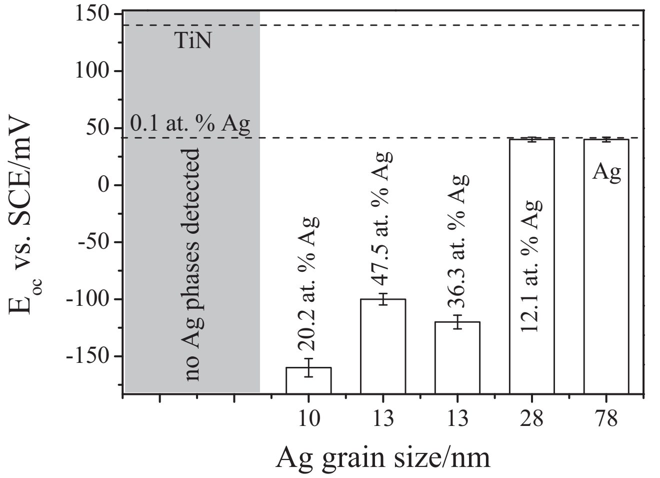

**Fig. 5.** OCP dependence on the Ag grain size. 0.1 at% Ag (~40 mV) and TiN control (~140 mV) OCP values are provided for comparison purposes.

simple TiN/Ag galvanic coupling experiment may be related with chemical changes underwent by the phases, more specifically by the Ag phase as Ag seems to control the electrochemical potential of the $Ag_x$:TiN system, Fig. 3. A plot of the OCP as a function of the Ag grain size (related with the Ag content) is reported in Fig. 5. It seems clear that a correlation can be established between the Ag grain size and OCP drops. While the 12.1 at% sample revealed rather large, crystalline Ag grains (~28 nm), the 20.2 at% one exhibited polycrystalline [12] Ag phases (~10 nm). As for the Zone III samples, 36.3 and 47.5 at% Ag, the same behaviour was observed, although they also possess a polycrystalline TiN matrix (~14 and ~15 nm, respectively) due to the hindered growth promoted by the Ag solute-drag effect [32].

Thus, it may be hypothesized that the galvanic coupling process is also taking place for these high-Ag content samples. However, since Ag is now polycrystalline, hence more reactive [33], its potential may, in fact, be less noble when compared to that obtained for the crystalline Ag control sample, shifting the Ag:TiN mixed potential in the anodic direction. The same OCP/grain size dependence was observed by Cao et al. [34], who studied two Cu-Ni-Cr alloys with the same composition but different grain sizes (in the micron and nanometre regions) in chloride solutions and El-Moneim et al. [35], who studied the corrosion behaviour of NdFeB nanomagnets. On the other hand, nanocrystallinity has also been associated with an increase of corrosion resistance in other cases, when the larger number of grain boundaries serve as short-circuit channels for element diffusion, hence facilitating passivation [36], or because it generates a more homogeneous elements distribution [37]. In both cases the corrosion potential was shown to shift to more noble potentials.

To summarize, the large Ag contents present at the 20.2, 36.3 and 47.5 at% Ag samples, associated with the small Ag grain sizes evidenced (below the ~20 nm threshold) ultimately lead to more reactive silver, thus less noble OCP values, while for lower Ag contents (0.1 and 12.1 at%), the higher Ag grain size present in the composites leads to an electrochemical behaviour similar to that of the well crystallized Ag-control sample.

### *3.2.2. Potentiodynamic analysis*

In order to further investigate the electrochemical behaviour of the $Ag_x$:TiN nanocomposites, a set of voltammetric experiments was performed at a constant sweep rate of 25 mV/s, Fig. 6. The stoichiometric TiN reference sample exhibits the voltammogram already observed in other works [38], with a stable micrometric current and no evidence of anodic or cathodic peaks in the scanned potential range, confirming its passive state. The low-Ag content samples, namely the 0.1 and 12.1 at% Ag, reveal, sharp and small anodic current peaks (Fig. 5 (a) inset on the bottom right corner, $a_1$ peak) that can be attributed to the formation of a thin tri-dimensional AgCl layer [39–42]. No cathodic peaks are perceivable, but a broad "bump" in the cathodic region can be noticed (Fig. 6 (a) inset on the upper left corner). As the Ag content is increased from 12.1 to 20.2 at% Ag, the anodic $a_1$ peak steeply increases and the standard potential of the correspondent reaction approaches that of the control Ag, Fig. 6 b). Two cathodic peaks ($c_1$ and $c_2$) are then observed, which might be related with the reduction of two types of AgCl nuclei: those formed instantaneously and those formed by progressive nucleation [39]. Although clearly identified in the cathodic sweep, these two stages of AgCl film growth cannot be distinguished in the anodic sweep. With further Ag content increase, the observed anodic current peak smoothly decreases. The anodic shift of the $a_1$ peak potential is related with the Ohmic drop that takes place through the AgCl film, which increases with the magnitude of the anodic current (the higher the anodic current the higher the peak shift). The same trend was reported by Hassan et al. [42], and it is also observed in the cathodic region, leading to a larger anodic-cathodic peak separation for higher currents.

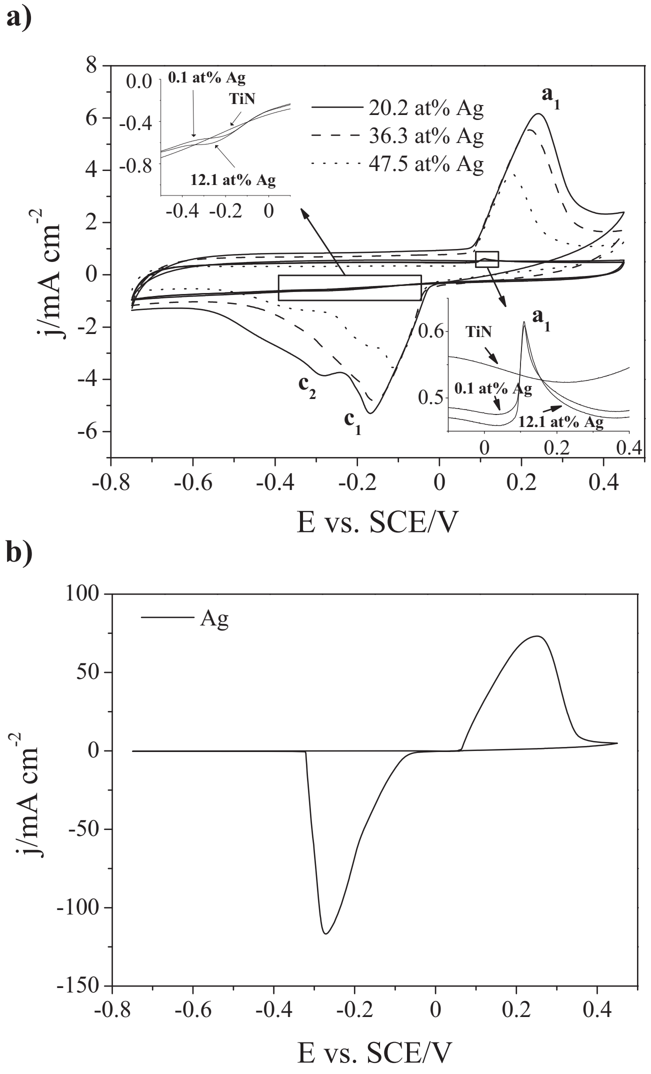

**Fig. 6.** Cyclic voltammograms of the (a) $Ag_x$:TiN samples (two insets are included to evidence the anodic and cathodic peaks of the low-Ag content and TiN control samples) and (b) Ag control sample voltammogram. The used sweep rate was 25 mV/s.

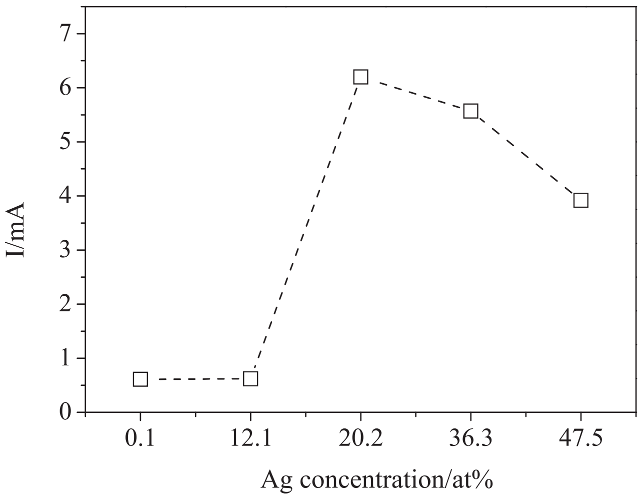

**Fig. 7.** Anodic peak current as a function of the Ag content.

To better illustrate the effect of silver, the $a_1$ current peak was plotted as a function of the Ag content, Fig. 7. The Ag-related current displays a residual value up to 12.1 at% Ag and then an abrupt increase occurs, from ~0.6 to ~6 mA, when the Ag content increases from 12.1 to 20.2 at%. Thereafter, a slight decrease of the current occurs, ~6 to ~4 mA, upon further increase of the Ag content. In order to explain the low oxidation currents displayed by the 12.1 at% Ag, in spite of the presence of large Ag aggregates that populate the TiN surface and inner structure, Fig. 1, it must be taken into account that the surface particles were easily removed by lightly wiping with a cloth, meaning that they had a poor mechanical contact with the underlying TiN matrix. Such lack of adhesion (not noticed in the silver richer samples) is probably related with the Ag segregation from the TiN matrix, as already reported by the authors [12,32]. It is therefore possible that the insulating oxynitride layer that forms on TiN in contact with water or oxygen [5] prevents an efficient Ag-TiN electric contact, so that most Ag becomes unavailable to contribute to the voltammetric processes. The same oxidation phenomenon was observed during the electrodeposition of Ag on titanium, where a poor adhesion of silver to titanium was obtained if a deep cathodic potential was not applied in order to avoid titanium oxidation [43].

When passing from 12.1-20.1 at% Ag a strong current increase is observed that may be ascribed to two factors: (i) the aggregates in the 20.2 at% Ag sample are now well embedded within the TiN intercolumnar pores and they should now be better bonded to the TiN matrix, given their higher reactivity. To note that no Ag came off as these samples were swept with a soft tissue; (ii) the Ag content increase is accompanied by a substantial decrease of the Ag grain size (Fig. 5), thus the Ag electroactive area increased. As for the highest Ag content samples (36.3 and 47.5 at% Ag), a decrease of the current values is perceivable, due to a reduction of the electroactive Ag area related to the densification already empirically observed by SEM, Fig. 1.

With the purpose of further clarifying the densification/porosity evolution of the $Ag_x$:TiN samples with increasing Ag contents, a set of new voltammetric experiments was conducted with increasing sweep rates (from 25 mV/s to 5 V/s) in a restricted potential range, in order to avoid the main Ag oxidation peak, Fig. 8. The stoichiometric TiN control sample exhibits a capacitive double layer-charging region [5,14] for low sweep rates (until 0.1 V/s), characterized by a *quasi*-independence of the current on the potential. However, for higher sweep rates (0.1-5 V/s), a strong resistive component is incorporated, which is a characteristic feature of porous films (the current vs. potential dependence is related to the ohmic drop within the pores [44,45]), a fact that was confirmed by SEM observation, Fig. 1. The opposite behaviour is observed for the coating with the highest Ag content, 47.5 at%, where the current is independent of the potential for all sweep rates, exhibiting a purely capacitive behaviour. This behaviour is characteristic of dense/non-porous materials, once again, in agreement with SEM observations.

When intermediate quantities of Ag are added (up to 12.1 at%), the mixed capacitive-resistive TiN-like behaviour does not suffer any perceivable changes, meaning that these coatings are also rather porous. When passing from 12.1 to 20.2 at% Ag, the typical resistive component of porous materials is reduced (when comparing to the low-Ag samples), although it is still present for the highest sweep rate, what may be ascribed to some residual porosity. Consequently, it can be confirmed that a progressive densification (or porosity reduction) is effectively taking place with increasing Ag content. Hence, the behaviour of the $Ag_x$:TiN nanocomposites can be divided according to their porosity: 0.1 and 12.1 at% Ag ones seem to be as porous as the control TiN sample; low porosity composites for higher Ag contents (20.2 and 36.3 at% Ag) and compact composites for 47.5 at% Ag. These observations are consistent with SEM imaging and the charge evolution for the 20.2 to 36.3 at% Ag films. On the other hand, the porosity-based classification fits the zone classification (considering 12.1 to 20.1 at% Ag increase as a transition zone–Zone II) defined in a previous work [12], according with the electrical and structural properties of the Ag:TiN nanocomposites.

Taking into account the structural and morphological analysis and the electrochemistry results, the authors propose the model depicted in Fig. 9 to explain the evolution of the electrochemical behaviour of the $Ag_x$:TiN samples, as function of the Ag content. The TiN control sample and the 0.1 at% Ag display a crystalline TiN columnar-like structure, with a strong porosity due to TiN columnar disaggregation. For slightly higher Ag contents (12.1 at%) large Ag aggregates can be identified sitting on the TiN surface, as a result of Ag segregation [12,32]. Such segregation and the formation of a superficial titanium oxynitride insulating layer will lead to a poor TiN-Ag adhesion. The increase of the Ag content to 20.2 at% is accompanied by a substantial decrease of the Ag grain size, which appears now well embedded in the TiN matrix, particularly among the TiN columns. There is a conductivity and a densification increase and the inter-columnar space is filled with Ag aggregates. The formation of electric conduction percolation paths cannot be discarded. For higher Ag contents (20.2-36.1 at%) the Ag grain size remains low, the TiN structure becomes amorphous, (Fig. 2), and the TiN:$Ag_x$ composite displays now a compact structure.

### 3.2.3. *Electrochemical Impedance Spectroscopy (EIS) studies*

The Bode diagrams for representative $Ag_x$:TiN, as well as for Ag and TiN control films are reported in Fig. 10. The simple circuit depicted in Fig. 11 proved to accurately simulate the $Ag_x$:TiN/synthetic sweat interface. Norlin [45] used a similar circuit to simulate the impedance behaviour of porous TiN films. A constant phase element (CPE) was used instead of a capacitor in order to account for roughness and/or other surface inhomogeneities and relaxation processes [5,14,46]. The impedance of a CPE was defined according with Eq. (1):

$$Z_{CPE} = 1/[T(j\omega)^p] \tag{1}$$

where "T" and "p" are the CPE parameters, while ω stands for the angular frequency [4,14,46]. In the parallel electric circuit the upper and lower branches stand for the non-Faradic and Faradic processes, respectively, and $R_e$ stands for the electrolyte resistance. In the non-Faradic branch, CPE aims at simulating the series combination of the double-layer and film capacitive behaviour at the film/electrolyte interface. The resistance to electronic charge

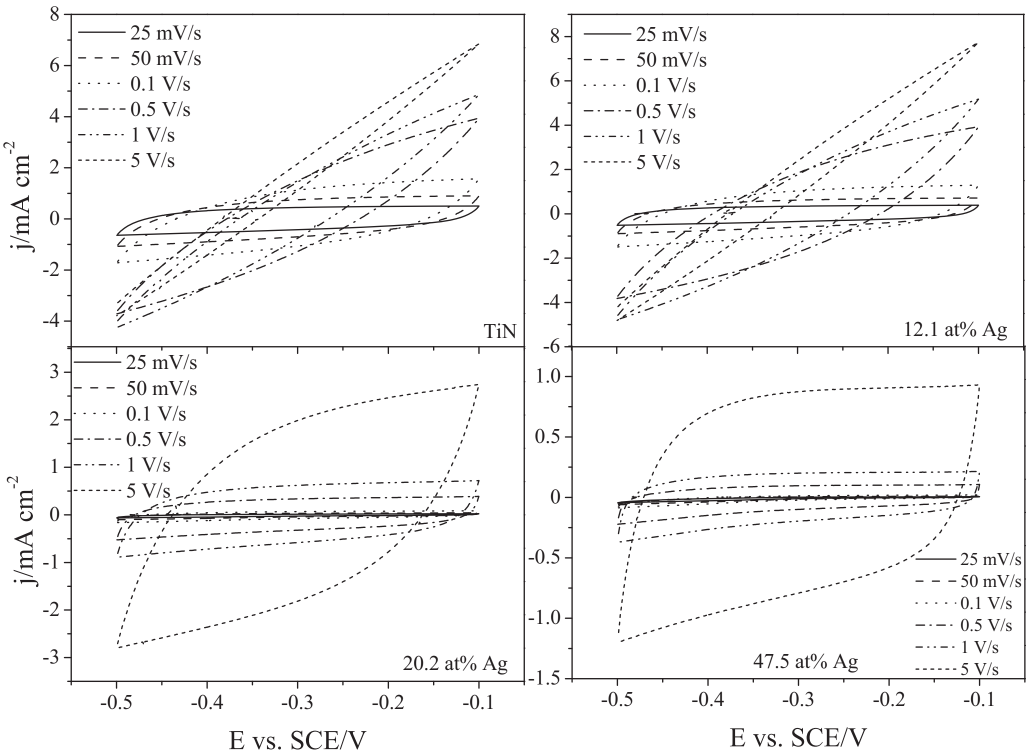

**Fig. 8.** Cyclic voltammograms of the low-Ag (12.1 at%) and high-Ag (20.2 and 47.5 at%) samples with increasing sweep rates. The current dependence on the sweep rate illustrates the porosity/densification changes with increasing Ag contents. Stoichiometric TiN control sample voltammogram is provided for comparison.

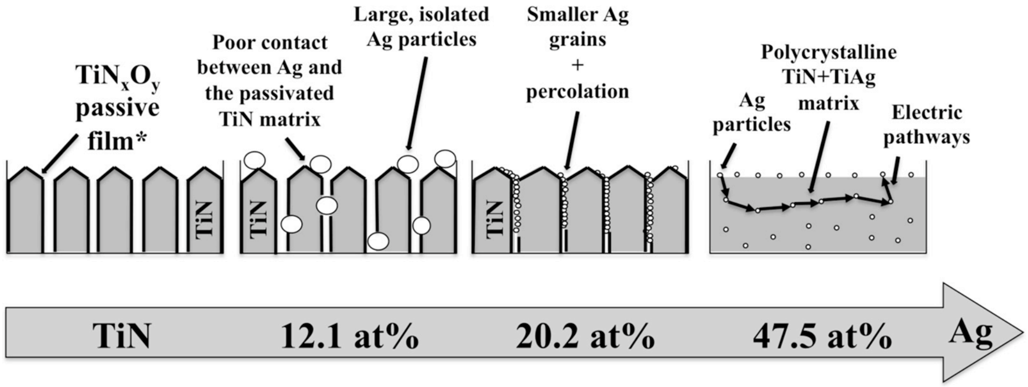

**Fig. 9.** Proposed model for the corrosion behaviour of the Ag$_x$:TiN samples. The oxynitride passive layer is present for all Ag compositions and was not depicted for the 47.5 at% Ag sample for clarity purposes.

transfer was not considered, as the OCP of the films lie in the water stability region. In the lower Faradic branch, $R_p$ was used to take account of the polarization resistance.

For the TiN control and 0.1 at% Ag samples the $R_p$ values were obtained with large errors (but not the other parameters), see Table II. More accurate values could eventually be obtained by extending the measurement range to even lower frequencies. In order to have approximate $R_p$ values for these samples, the CPE and $R_e$ parameters were first calculated by using the fitting tool. Then, the calculated parameters and increasing $R_p$ values were manually inserted in the model, starting at ~$5 \times 10^4$ Ω.cm$^2$, until the calculated curve fitted the experimental values and no further

**Table II**
Ag$_x$:TiN thin films' EIS fitting parameters.

| [Ag]/at% | $R_p$/Ω.cm$^2$ | $R_e$/Ω.cm$^2$ | CPE el. (T)/Ω$^{-1}$.cm$^{-2}$.s$^n$ | CPE el. (P) | $\chi^2$ |
|---|---|---|---|---|---|
| TiN | $\geq 3 \times 10^6$ | 41.9 | $7.9 \times 10^{-3}$ | 0.87 | $2 \times 10^{-4}$ |
| 0.1 | $\geq 6 \times 10^5$ | 33.3 | $8.1 \times 10^{-3}$ | 0.88 | $4 \times 10^{-4}$ |
| 12.1 | $6 \times 10^4$ | 31.5 | $8.2 \times 10^{-3}$ | 0.87 | $3 \times 10^{-4}$ |
| 20.2 | $6.2 \times 10^4$ | 25.2 | $1.3 \times 10^{-3}$ | 0.81 | $3 \times 10^{-4}$ |
| 36.3 | $7.2 \times 10^4$ | 24.6 | $9.9 \times 10^{-4}$ | 0.87 | $6 \times 10^{-4}$ |
| 47.5 | $5.4 \times 10^4$ | 25.9 | $5.8 \times 10^{-4}$ | 0.93 | $1 \times 10^{-3}$ |
| Ag | $5.2 \times 10^4$ | 24.5 | $6.5 \times 10^{-4}$ | 0.93 | $2 \times 10^{-3}$ |

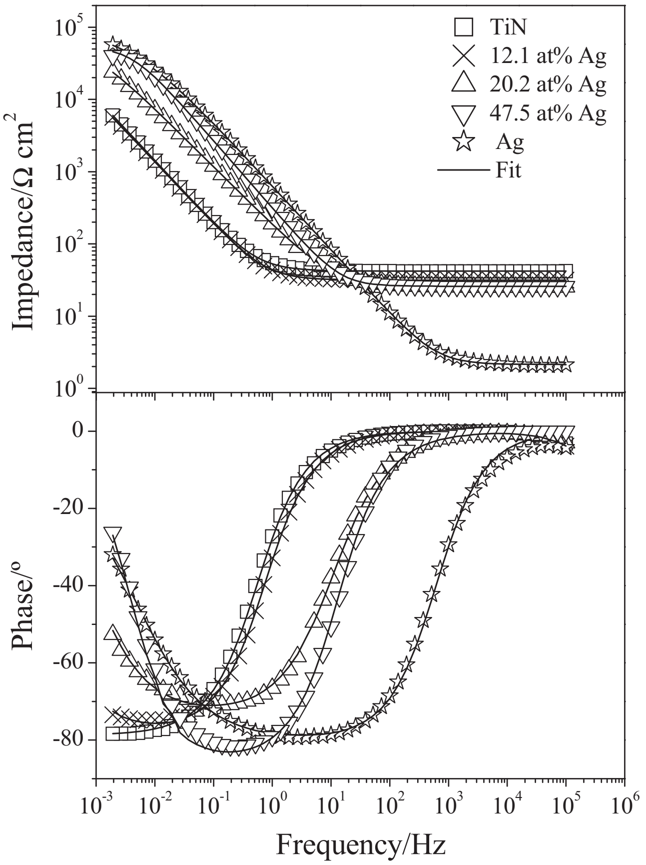

**Fig. 10.** Bode diagrams of the TiN and Ag control samples and representative $Ag_x$:TiN samples from the low- and high-Ag contents.

phase shift/impedance variation was perceived upon $R_p$ increase. Then, $R_p$ was assumed to be equal or higher than the calculated value.

The TiN and Ag control samples display the highest and lowest $R_p$ values respectively, in line with the reactivity of both materials in chloride solutions. The 0.1 at% Ag sample displays a $R_p$ value that seems close to that of the TiN control sample, but for the 12.1 at% Ag sample $R_p$ steeply decreases, adopting a value rather close to that of silver; for higher silver contents $R_p$ seems to suffer little changes. This $R_p$ drop is related to the silver oxidation reaction and formation of an AgCl layer that starts at about -0.2 V (SCE) [39]. As for the "T" values of the CPE, they should reflect essentially the capacitive behaviour of the interface, as p values are close to 0.9. It is possible to see a gradual decrease of "T" from $\sim 8 \times 10^{-3}$ to $\sim 6 \times 10^{-4}$ $\Omega^{-1}.cm^{-2}.s^n$, in line with the observed composite densification with increasing Ag content and the consequent reduction of the samples area. To note that Norlin et al. [45] and the authors [5,14] reported pseudo-capacitance values in the same range for TiN columnar porous films.

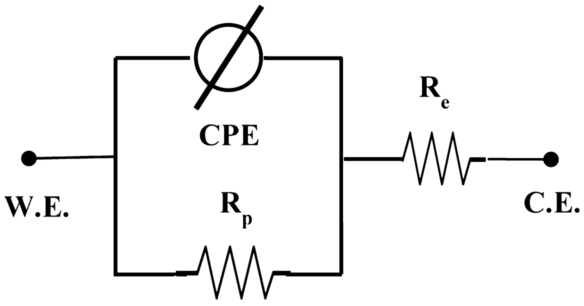

**Fig. 11.** Equivalent electric circuit proposed for the simulation of the $Ag_x$:TiN/synthetic sweat interface.

### 3.2.4. *Electrical noise measurements*

Since the present work aims at studying the suitability of the sputtered $Ag_x$:TiN thin films for bioelectric signal monitoring purposes, investigating their interfacial noise characteristics is of crucial importance in order to avoid signal distortion and extensive noise addition to the biopotential [47–50]. One of the sources of noise when a dry electrode is in contact with the skin comes from the electrochemical processes involving the electrode/sweat contact [47,49]. Hence, the monitoring of the electric noise generated at the thin film's/electrolyte interface in the frequency region of interest for the envisaged application (ECG, EEG, etc.) is of paramount importance. Supposing that a layer of sweat is formed between the electrode and the skin, the electric noise generated at the referred interface must be significantly lower than the ECG (~1 mV) or EEG (~50 μV) signal being recorded, in order not to mask the monitored biopotential. The power spectral density (PSD) of TiN, 12.1, 20.2 and 36.3 at% Ag couples in synthetic sweat is depicted in Fig. 12. The noise values for all representative samples are quite similar, increasing, as expected, for low frequencies (down to 0.5 Hz–lower limit for most exams). It is known that the noise increases as the frequency decreases, according to the 1/(freq.) law below 20-30 Hz [48]. Above this frequency range, the noise is supposedly introduced by the amplifier. The 1/(freq.) law is commonly associated to slow corroding systems [51] and related to adsorption/desorption or surface coverage processes that take place at the electrode/electrolyte interface.

However, some small differences can be perceived with increasing Ag contents, especially in the low frequency region (below about 5 Hz). The low-Ag content sample (~12.1 at%) reveals a noise curve similar to that of the pure TiN control sample. Then, as the Ag content increases, the noise slightly decreases. To sum up, the noise components of both low- and high-Ag content samples are

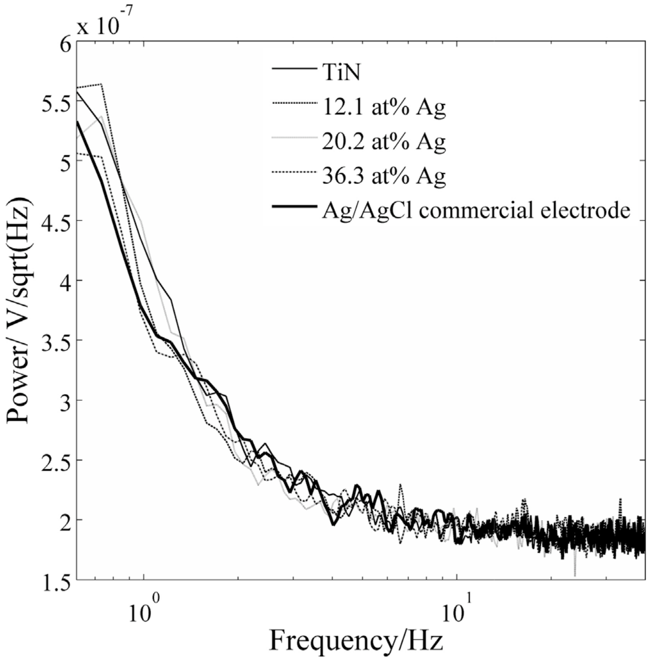

**Fig. 12.** Noise power spectral density spectra for TiN control and representative $Ag_x$:TiN samples. Ag/AgCl commercial electrode data is presented for comparison purposes.

very similar to those of the commercial Ag/AgCl electrodes, making them suitable to be used as biopotential electrodes.

## 4. Conclusions

In the present work, a set of $Ag_x$:TiN coatings with Ag contents ranging from ~0.1 to ~47.5 at% were investigated in order to assess their suitability to be used as bioelectrodes. For that purpose, a comprehensive electrochemical characterization was performed in a synthetic sweat solution to better simulate the electrode/skin interface for the envisaged application. Grain size reduction occurs with increasing Ag concentration up to 20.2 at% (a decrease from ~28 to ~10 nm is attained). This Ag grain size variation has a marked effect on the samples' OCP evolution. For higher grain sizes (TiN control, 0.1 and 12.1 at% Ag samples), the OCP values are very close to that of the pure Ag (~40 mV), while for the lower ones (20.2, 36.3 and 47.5 at% Ag samples) a steep reduction of the OCP is attained (until ~ -160 mV), which was ascribed to the increased reactivity of the nanosized Ag phases.

The potentiodynamic experiments revealed the presence of the typical Ag anodic and cathodic peaks resulting from the reaction with chloride, as well as a continuous densification/porosity decrease of the samples with increasing Ag concentrations. A steep current increase (10 fold) occurs when passing from 12.1 to 20.2 at% Ag, which was attributed to an increase of the electroactive Ag area (Ag area ratio achieves a maximum of 10) due to Ag grain refinement and an improved Ag-TiN electric contact. The $R_p$ values are significantly influenced by the Ag content, since they suffer a steep decrease (up to two orders of magnitude) when the Ag concentration is equal or higher than 12.1 at%, becoming very similar to that exhibited by the Ag control sample. For lower Ag contents, the samples exhibit TiN-like $R_p$ values. The electrochemical noise of $Ag_x$:TiN composites is similar to that of the commercial Ag/AgCl electrodes.

Finally, to summarize, it is possible to say that the obtained $Ag_x$:TiN samples exhibit good chemical stability and low interfacial noise when immersed in the synthetic sweat solution, thus making them potential candidates to be used as bioelectrodes. However, silver concentration should be above about 20% at.%, in order to avoid the segregation of silver, with the formation of loosely attached silver.

## Acknowledgements

This research is partially sponsored by FEDER funds through the program COMPETE–Programa Operacional Factores de Competitividade and by national funds through FCT–Fundação para a Ciência e a Tecnologia, under the projects PEst-C/EME/UI0285/2011, PTDC/SAU-ENB/116850/2010, PTDC/CTM-NAN/112574/2009 and Programa Pessoa 2012/2013 Cooperação Portugal/França, Project n° 27306UA Porous architectures in GRAded CERamic thin films for biosensors - GRACER. The authors would like to acknowledge CEMUP and SEMAT-UM for SEM analysis. P. Pedrosa acknowledges FCT for the Ph.D. grant SFRH/BD/70035/2010.

## References

[1] M. Teplan, Meas. Sci. Rev. 2 (2) (2002) 1–11.
[2] E. McAdams, Bioelectrodes, in: J.G. Webster (Ed.), Encyclopaedia of Medical Devices and Instrumentation, Wiley, New York, 1988, pp. 120–166.
[3] A. Searle, L. Kirkup, Physiolog. Meas. 22 (2000) 271–283.
[4] W.K. Ko, J. Hynecek, Dry electrodes and electrode amplifiers, in: H.A. Miller, D.C. Harrison (Eds.), Biomedical Electrode Technology, Academic Press, New York, 1974.
[5] L.T. Cunha, P. Pedrosa, C.J. Tavares, E. Alves, F. Vaz, C. Fonseca, Electrochim. Acta 55 (1) (2009) 59–67.
[6] G. Gargiulo, R.A. Calvo, P. Bifulco, M. Cesarelli, C. Jin, A. Mohamed, A. van Schaik, Clin. Neurophysiol. 121 (5) (2010) 686–693.
[7] C. Fonseca, J.P. Silva Cunha, R.E. Martins, V. Ferreira, J.P. Marques de Sá, M.A. Barbosa, A. Martins Silva, IEEE Trans. Biomed. Eng. 54 (1) (2007) 162–165.
[8] K.-P. Hoffmann, R. Ruff, Proceedings of the 29th Annual International Conference of the IEEE EMBS, Lyon, France, August, 2007, pp. 23–26.
[9] J. Baek, J. An, J. Choi, K. Park, S. Lee, Sens. Actuators A 143 (2008) 423–429.
[10] A. Gruetzmann, S. Hansen, J. Muller, Physiol. Meas. 28 (2007) 1375–1390.
[11] V. Marozas, A. Petrenas, S. Daukantas, A. Lukosevicius, J. Electrocardiology 44 (2011) 189–194.
[12] P. Pedrosa, D. Machado, C. Lopes, E. Alves, N.P. Barradas, N. Martin, F. Macedo, C. Fonseca, F. Vaz, Appl. Surf. Sci. 285P (2013) 40–48.
[13] S. Piscanec, L. Ciacchi, E. Vesselli, G. Comelli, O. Sbaizero, S. Meriani, A. De Vita, Acta Mater. 52 (2004) 1237.
[14] P. Pedrosa, E. Alves, N.P. Barradas, P. Fiedler, J. Haueisen, F. Vaz, C. Fonseca, Corros. Sci. 56 (2012) 49–57.
[15] K.-H. Liao, K.-L. Ou, H.-C. Cheng, C.-T. Lin, P.-W. Peng, Appl. Surf. Sci. 256 (2010) 3642–3646.
[16] M. Fiori, M. Paula, A. Bernardin, H. Riella, E. Angioletto, Mater. Sci. Eng., C 29 (2009) 1569–1573.
[17] M. Santos, C. Oliveira, C. Tachinski, M. Fernandes, C. Pich, E. Angioletto, H.G. Riella, M. Fiori, Int. J. Miner. Process. 100 (2011) 51–53.
[18] P.J. Kelly, H. Li, K.A. Whitehead, J. Verran, R.D. Arnell, I. Iordanova, Surf. Coat. Technol. 204 (2009) 1137–1140.
[19] P.J. Kelly, H. Li, P.S. Benson, K.A. Whitehead, J. Verran, R.D. Arnell, I. Iordanova, Surf. Coat. Technol. 205 (2010) 1606–1610.
[20] H. Köstenbauer, G.A. Fontalvo, J. Keckes, C. Mitterer, Thin Solid Films 516 (2008) 1920–1924.
[21] L.A. Geddes, L.E. Baker, A.G. Moore, Med. Biol. Eng. 7 (1969) 49–56.
[22] D. Adams, B.A. Julies, J.W. Mayer, T.L. Alford, Thin Solid Films 332 (1998) 235–239.
[23] J. Zhao, H.J. Feng, H.Q. Tang, J.H. Zheng, Surf. & Coat. Technol. 201 (2007) 5676–5679.
[24] M. Zhang, L. Hu, G. Lin, Z. Shao, J. Power Sources 198 (2012) 196–202.
[25] N.P. Barradas, C. Jeynes, R.P. Webb, Appl. Phys. Lett. 71 (1997) 291.
[26] A.F. Gurbich, Nucl. Instr. and Meth. B 268 (2010) 1703.
[27] L.J. van der Pauw, Philips Res. Repts. 13 (1958) 1–9.
[28] J.-O. Randin, J. Biomed. Mat. Res. 22 (1988) 649.
[29] M.G. Fontana, N.D. Greene, Corrosion Engineering, 3rd ed., McGraw-Hill Book Company, 1987.
[30] C.-C. Shih, C.-M. Shih, K.-Y. Chou, S.-J. Lin, Y.-Y. Su, R.A. Gerhardt, J. Biomed. Mater. Res. 82A (2007) 872–883.
[31] B.J. Polk, A. Stelzenmuller, G. Mijares, W. MacCrehan, M. Gaitan, Sens. Actuators B 114 (2006) 239–247.
[32] P. Pedrosa, D., Machado, M., Evaristo, A., Cavaleiro, C., Fonseca, F. Vaz, Ag:TiN nanocomposite thin films for biolectrodes: the effect of annealing treatments on the electrical and mechanical behaviour. Unpublished results, submitted to Journal of Nanomaterials.
[33] Y. Liu, Z. Zheng, J.N. Zara, C. Hsu, D.E. Soofer, K.S. Lee, R.K. Siu, L.S. Miller, X. Zhang, D. Carpenter, C. Wang, K. Ting, C. Soo, Biomaterials 33 (2012) 8745–8756.
[34] Z.-Q. Cao, J. Bian, R. Xue, W.-H. Liu, Trans. Nonferrous Met. Soc. China 17 (2007) 1236–1241.
[35] A.A. El-Moneim, A. Gebert, F. Schneider, O. Gutfleisch, L. Schultz, Corros. Sci. 44 (2002) 1097–1112.
[36] H.-B. Lu, Y. Li, F.-H. Wang, Surf. & Coat. Technol. 201 (2006) 3393–3398.
[37] W. Zeiger, M. Schneider, D. Schamwber, H. Worch, Nanostruct. Mat. 6 (1995) 1013–1016.
[38] Y. Massiani, A. Medjahed, P. Gravier, L. Argeme, L. Fedrizzi, Thin Solid Films 191 (1990) 305.
[39] V.I. Birss, C.K. Smith, Electrochim. Acta 32 (2) (1987) 259–268.
[40] B.M. Jović, V.D. Jović, D.M. Dražić, J. Electroanal. Chem 399 (1995) 197–206.
[41] J. Peng, Y. Deng, D. Wang, X. Jin, G.Z. Chen, J. Electroanal. Chem. 627 (2009) 28–40.
[42] H.H. Hassan, M.A.M. Ibrahim, S.S. Abd El Rehim, M.A. Amin, Int. J. Electrochem. Sci. 5 (2010) 278–294.
[43] I. Boskovic, S.V. Mentus, M. Pjescic, Electrochim. Acta 51 (2006) 2793–2799.
[44] J. Borges, C. Fonseca, N.P. Barradas, E. Alves, T. Girardeau, F. Paumier, F. Vaz, L. Marques, Electrochim. Acta 106 (2013) 23–34.
[45] A. Norlin, J. Pan, C. Leygraf, J. Electrochem. Soc. 152 (2005) J7–J15.
[46] M. Orazem, B. Tribollet, Electrochemical Impedance Spectroscopy, John Wiley & Sons, 2008, pp. 233.
[47] E. Huigen, A. Peper, C. Grimbergen, Med. Biol. Eng. Comput. 40 (2002) 332.
[48] M.M. Puurtinen, S.M. Komulainen, P.K. Kauppinen, J.A.V. Malmivuo, J.A.K. Hyttinen, Proceedings of the 28th IEEE EMBS Annual International Conference, New York City, USA, Aug. 30-Sept. 3, 2006, pp. 6012–6015.
[49] D.T. Godin, P.A. Parker, R.N. Scott, Med. & Biol. Eng. & Comput. 29 (1991) 585–590.
[50] H.J. Scheer, T. Sander, L. Trahms, Physiol. Meas. 27 (2006) 109–117.
[51] K. Hladky, J. Dawson, Corrosion Sci. 22 (1982) 231.

# CHAPTER 4

## THE UNDER-STOICHIOMETRIC $Ag_Y$:$TiN_X$ SYSTEM[*]

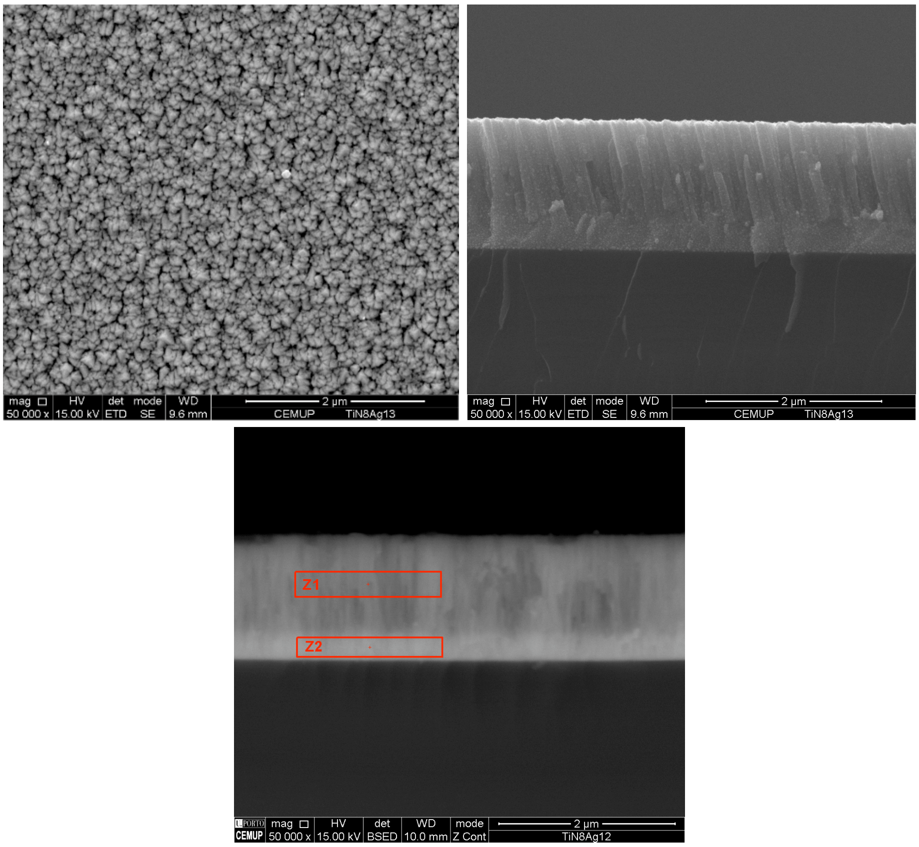

*"…the reduction of the [N]/[Ti] atomic ratio effectively acts as a segregation inhibitor."*

---

[*] This chapter is based on the following publications:

P. Pedrosa, D. Machado, J. Borges, M.S. Rodrigues, E. Alves, N.P. Barradas, N. Martin, M. Evaristo, A. Cavaleiro, C. Fonseca, F. Vaz, "*$Ag_y$:$TiN_x$ thin films for dry biopotential electrodes: the effect of composition and structural changes on the electrical and mechanical behaviours*", Applied Physics A: Materials Science and Processing, in press, accepted manuscript, DOI: 10.1007/s00339-014-8943-9.

P. Pedrosa, D. Machado, E. Alves, N.P. Barradas, F. Vaz, C. Fonseca, "*Electrochemical and structural characterization of nanocomposite $Ag_y$:$TiN_x$ thin films for dry biopotential electrodes: the effect of the N/Ti ratio and Ag content*", Electrochimica Acta 153 (2015) 602–611.

From the previous chapter, Chapter 3, it was possible to conclude about the effectiveness of Ag to tailor most of the properties of the $Ag_x$:TiN system. The sputtered coatings could be consistently divided into three composition zones, according to the exhibited sets of characteristics, ranging from nitride-like to metallic-like behaviour. With increasing Ag contents, increased densification and conductivity, as well as increasingly polycrystalline films were attained.

Therefore, as expected, the electrochemical behaviour of the $Ag_x$:TiN coatings was also effectively tailored, due to the morphological and structural changes promoted by increasing Ag additions. The films with higher Ag contents displayed higher Ag electroactive areas, but also much less noble OCP values. It was concluded that the electrochemical properties of the $Ag_x$:TiN coatings were strongly dependent on the Ag segregation phenomenon extensively patent in the samples sputtered with Ag contents lower than 20 at.%. The as-deposited films with Ag contents above 20 at.% did not show significant signs of Ag segregation, but only two months after the depositions took place, the surface of the referred samples was covered with nanosized Ag particles.

Consequently, due to the exhibited poor morphological, structural and electrochemical stability of the $Ag_x$:TiN system (which may translate into an unstable electrode/skin interface during the biosignal monitoring procedure), it was found necessary to investigate the effects of the $TiN_x$ matrix stoichiometry as a silver segregation inhibitor. Hence, a new set of $Ag_y$:$TiN_x$ coatings was sputtered with decreasing N/Ti atomic ratios (towards under-stoichiometric $TiN_x$ conditions), opening the possibility for the Ag atoms to form $Ti_xAg$ intermetallics, thus inhibiting its segregation. The following chapter reports on the properties and electrochemical behaviour of the $Ag_y$:$TiN_x$ thin film system.

The main conclusion from this chapter regards the apparent depletion of the extensive Ag segregation phenomenon (see cover figure) observed in the previous chapter, through the possible formation of $Ti_xAg$ intermetallics, since the $Ti_2Ag$, TiAg and Ag planes could not be clearly differentiated, Fig. 4.1.

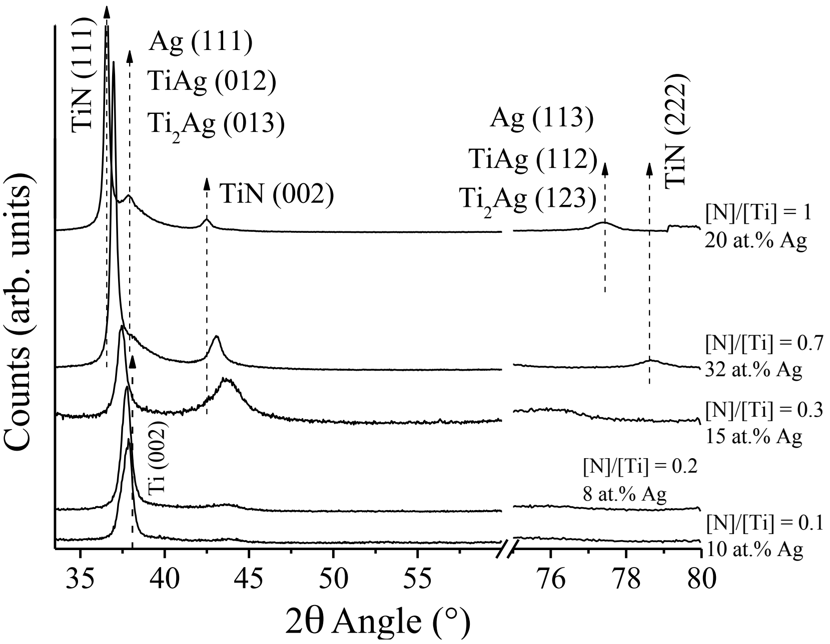

**Figure 4.1.** XRD diffractograms of representative samples of the $Ag_y$:$TiN_x$ system.

The under-stoichiometric $Ag_y$:$TiN_x$ thin films with N/Ti atomic ratios of 0.3 (15 at.% Ag) and 0.7 (32 at.% Ag) were found the most appropriate for bioelectrode application, since lower impedance, noise and potential drift rate values (similar to the wet Ag/AgCl electrodes) were attained.

Appl. Phys. A
DOI 10.1007/s00339-014-8943-9

**Applied Physics A**
**Materials Science & Processing**

# $Ag_y$:$TiN_x$ thin films for dry biopotential electrodes: the effect of composition and structural changes on the electrical and mechanical behaviours

**P. Pedrosa · D. Machado · J. Borges · M. S. Rodrigues · E. Alves · N. P. Barradas · N. Martin · M. Evaristo · A. Cavaleiro · C. Fonseca · F. Vaz**

Received: 24 September 2014 / Accepted: 11 December 2014

**Abstract** In the present work, $Ag_y$:$TiN_x$ thin films, obtained by reactive DC magnetron sputtering, with decreasing [N]/[Ti] atomic ratios (from 1 to 0.1) and a fixed amount of Ag pellets placed in the erosion zone of a pure Ti target, were studied envisaging their application as biopotential electrodes. The strongly under-stoichiometric samples, [N]/[Ti] = 0.1 and 10 at.% Ag; [N]/[Ti] = 0.2 and 8 at.% Ag, were found to be composed of a N-doped hcp-Ti structure, with possible formation of TiAg or $Ti_2Ag$ intermetallics. These samples exhibit high electrical resistivity values and low hardness and reduced modulus. In the set of samples indexed to a transition zone, [N]/[Ti] = 0.3 and 15 at.% Ag; [N]/[Ti] = 0.7 and 32 at.% Ag, a hcp-Ti to fcc-TiN phase transformation took place, giving rise to a disaggregated N-deficient TiN matrix. It correlates with the high resistivity values as well as the higher hardness and reduced modulus values that were obtained. The last identified zone comprised the stoichiometric Ag:$TiN_x$ sample—[N]/[Ti] = 1 and 20 at.% Ag. Extensive metallic Ag segregation was detected, contributing to a significant decrease of the resistivity and hardness values.

## 1 Introduction

Silver/silver chloride (Ag/AgCl) wet electrodes are being used for the past decades for biosignal monitoring of the human body. Techniques such as electroencephalography (EEG), electrocardiography (ECG) and electromyography (EEG) rely heavily on the use of such biopotential electrodes. They are non-polarizable, reliable and display low and almost frequency-independent electrode/skin contact impedances (few tens of k$\Omega$ cm$^2$) [1, 2], thus being widely considered as the gold standard for conventional biopotential acquisition setups [1–3]. However, a new class of devices, the so-called dry electrodes, is being extensively

---

P. Pedrosa (✉) · M. Evaristo · A. Cavaleiro · C. Fonseca
SEG-CEMUC–Department of Mechanical Engineering,
University of Coimbra, Coimbra, Portugal
e-mail: deb10012@fe.up.pt

P. Pedrosa · C. Fonseca
Universidade do Porto, Faculdade de Engenharia, Departamento de Engenharia Metalúrgica e de Materiais, Rua Dr. Roberto Frias, s/n, 4200-465, Porto, Portugal

P. Pedrosa · D. Machado · M. S. Rodrigues · F. Vaz
Centro de Física, Universidade do Minho, 4710-057 Braga, Portugal
e-mail: fvaz@fisica.uminho.pt

J. Borges
Department of Control Engineering, Faculty of Electrical Engineering, Czech Technical University in Prague, Technická 2, Prague 6, Czech Republic

E. Alves
Instituto de Plasmas e Fusão Nuclear, Instituto Superior Técnico, Universidade de Lisboa, Av. Rovisco Pais, 1049-001 Lisbon, Portugal

N. P. Barradas
Centro de Ciências e Tecnologias Nucleares, Instituto Superior Técnico, Universidade de Lisboa, E.N. 10 (km 139,7), 2695-066 Bobadela LRS, Portugal

N. Martin
Institut FEMTO-ST, UMR 6174, CNRS, ENSMM, UTBM, Université de Franche-Comté, 15B, Avenue des Montboucons, 25030 Besançon Cedex, France

investigated. These electrodes do not require any previous skin preparation procedure or application of a conductive gel, thus reducing many of the Ag/AgCl electrodes associated drawbacks that are widely found in the literature such as time-consuming skin preparation and gel application in order to achieve low electrode/skin impedances that require trained staff. Other gel-related disadvantages such as allergic reactions to the gel paste [2] and the risk of short-circuiting adjacent electrodes due to gel running are of particular importance. Furthermore, the commercial Ag/AgCl electrodes also exhibit susceptibility to motion artefacts, as well as the inability to be used in long-term ambulatory biopotential monitoring [1, 2] due to gel drying. Consequently, eliminating the need for the application of the conductive gel through the use of dry electrodes, while still attaining a stable, comfortable and low impedance electrode/skin contact is of the utmost interest.

In previous works, the authors studied the viability of a dry electrode based on a titanium nitride-coated titanium [4] and polycarbonate [5] discs. Despite the exhibited low electrical noise levels and excellent chemical resistance to sweat, a correct and comfortable electrode/skin contact was not achieved, due to the intrinsic stiffness and planar shape of both the titanium and polycarbonate substrates. These drawbacks were also reported in other works [6, 7], where an increased difficulty for the dry electrode to conform to the human skin was found. Hence, the use of flexible polymer substrates would fill in this gap, since they should be able to surpass the problems stated above. Several authors have recently focused on the development of various designs and coatings for flexible dry biopotential electrodes [8–14]. The authors, in turn, studied the viability of stoichiometric titanium nitride thin films with different silver contents ($Ag_x$:TiN) to be used as bioelectrodes [15–18]. The Ag:TiN system was chosen since it should be able to combine the properties of both their constituents. TiN is biocompatible [19], electrically conductive [15], offers excellent corrosion/oxidation resistance [20] and chemical stability in most media, as well as outstanding mechanical and tribological properties [21, 22]. Silver is an excellent biosensor material [23] and should promote improved mechanical properties to the composite [24]. It is also a soft material, thus also offering the possibility to tailor the mechanical properties of the TiN system, since its brittle character should be a major drawback when sputtered onto flexible polymeric substrates.

However, the stoichiometric $Ag_x$:TiN system is not structurally and morphologically stable, since extensive Ag segregation was already reported by the authors [15, 16, 18], as well as others [21, 22, 25–28]. This occurrence may translate into an unstable electrode/skin interface during the biosignal monitoring procedure. Hence, in order to overcome the Ag segregation phenomenon, the purpose of the present work was to study the effect of the [N]/[Ti] atomic ratio decrease towards under-stoichiometric conditions of the Ag:$TiN_x$ system on the structural, morphological, electrical and mechanical properties of the films. When [N]/[Ti] < 1, the TiN matrix should become N-deficient, opening the possibility for the Ag atoms to form TiAg or $Ti_2Ag$ intermetallics [29], inhibiting its segregation.

## 2 Experimental details

### 2.1 Thin film production

Glass (ISO 8037) and (100) silicon substrates were used to deposit $Ag_y$:$TiN_x$ coatings by reactive DC magnetron sputtering, in a custom-made laboratory-sized deposition system. All substrates were sonicated and cleaned with ethanol (96 vol%) before each deposition and then subjected to an in situ etching process, using pure Ar with a partial pressure of 0.3 Pa and a pulsed current of 0.5 A ($T_{on}$ = 1,536 ns and $f$ = 200 kHz) for 1,200 s. The thin films were prepared with the grounded substrate holder positioned at 70 mm from the magnetron. A DC current density of 100 A $m^{-2}$ was applied to the titanium target (99.96 at.% purity/200 × 100 × 6 mm), containing silver pellets (80 × 80 and 1 mm thick) on its surface distributed symmetrically along the erosion area. The total surface area of the silver pellets (~320 $mm^2$) was preserved throughout all depositions. A mixed gas atmosphere composed of Ar + $N_2$ was used to generate the plasma. The argon flow was kept constant at 60 sccm for all depositions (partial pressure of $3.0 \times 10^{-1}$ Pa), while the flow rate of nitrogen varied between 5 and 1 sccm (corresponding to a variation of the nitrogen partial pressure between $3.4 \times 10^{-2}$ and $1.8 \times 10^{-2}$ Pa [5]. The working pressure was varied only slightly between $3.5 \times 10^{-1}$ and $3.8 \times 10^{-1}$ Pa. The deposition temperature was kept approximately constant at 100 °C during the growth of the films. A thermocouple was placed near the surface of the substrate holder on the plasma side (not in direct contact, since all depositions were done in rotation mode), and the temperature was monitored during the entire deposition time. A delay time of 5 min was used prior to positioning the sample surface in front of the Ti/Ag target. This procedure avoids contamination of the coating resulting from previous depositions, which may have resulted in some target poisoning, as well as to ensure an almost constant deposition temperature during the growth of the films. All depositions were performed for 3,600 s.

The present $Ag_y$:$TiN_x$ system was characterized and optimized on traditional substrates (glass and silicon) to facilitate their characterization. The coatings will also be later sputter deposited onto well-known flexible polymeric substrates (polyurethane). Hence, the deposition conditions were chosen in order to be minimally aggressive (no bias voltage and low deposition temperatures were used) in order to avoid future polymeric substrate degradation.

### 2.2 Thin film characterization

The atomic composition of the as-deposited samples was measured by Rutherford backscattering spectrometry (RBS) with beams $^1$H at 1.4 and 2.3 MeV and with $^4$He at 1.4 and 2 MeV. Three detectors were used: one located at a scattering angle of 140° and two pin diode detectors located symmetrically to each other, both at 165°. Two sample tilt angles, 0° and 30°, were used for the measurements. The composition profiles of the as-deposited samples were obtained using the NDF software [30]. For the $^{14}$N, $^{16}$O and $^{28}$Si data, the cross sections given by Gurbich were used [31]. The analysed area was $0.5 \times 0.5$ mm$^2$. The uncertainty of the N concentrations is around 5 at.%.

The structure and phase distributions of the coatings were assessed by X-ray diffraction (XRD), using a Bruker AXS Discover D8 diffractometer, operating with Cu $K_\alpha$ radiation and in a Bragg–Brentano configuration. The XRD patterns were deconvoluted and fitted with a Pearson VII function to determine the structural characteristics of the films, such as the peak position ($2\theta$), the full width at half maximum (FWHM) and the crystallite size. Morphological features of the samples were probed by scanning electron microscopy (SEM), carried out in a FEI Quanta 400FEG ESEM microscope operating at 15 keV.

The resistivity measurements were taken using the four-probe van der Pauw method [32]. Single-cycle loading nanoindentation tests were carried out with a Micro Materials NanoTest system with a 3-mN load (indentation depths were always below 10 % of the thickness of the films) using a Berkovich diamond indenter. A matrix of $5 \times 5$ indentations was used. The reduced modulus was calculated using the Oliver–Pharr method [33].

## 3 Results and discussion

### 3.1 Target potential, deposition rate and composition of the sputtered $Ag_y$:$TiN_x$ films

In order to better understand the characteristics of the $Ag_y$:$TiN_x$ thin films, the main deposition parameters (target potential evolution and deposition rate during the growth of the films) were firstly analysed. Figure 1 shows the evolution of these two parameters as a function of the $N_2$ flow rate. It is worth to note that the target potential and the deposition rate display inverse behaviours with increasing $N_2$ flow rates [4, 34, 35]. Regarding the target potential, it can be identified an almost constant increase with increasing $N_2$ flow rates, exhibiting a variation between 345 and 378 V. For the highest flow rates, 4 and 5 sccm, the target potential appears to stabilize. On the other hand, the deposition rate exhibits an almost linear decrease from 1.6 to 1.2 µm h$^{-1}$. These two types of behaviour can be possibly explained by the poisoning phenomenon of the Ti fraction of the Ti/Ag target, caused by the increase of the $N_2$ flow rate [15, 36, 37]. As claimed by Spencer et al. [38], for a particular metal, the deposition rate significantly decreases by increasing the reactive gas partial pressure due to the progressive metal target poisoning. As the amount of $N_2$ increases, the higher is the Ti/Ag target contamination, through the formation of a thin TiN film on the surface of the Ti fraction of the target. Note that the formation of AgN is highly unlikely, so the Ag fraction of the target should remain in its metallic mode [37].

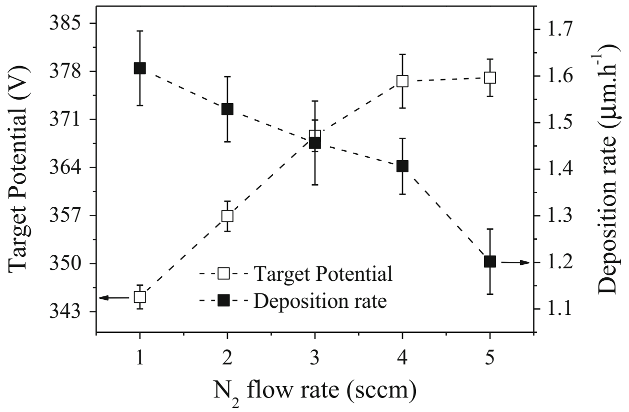

**Fig. 1** Target potential and deposition rate as a function of the $N_2$ flow rate used to sputter the $Ag_y$:$TiN_x$ samples

Depla et al. [39–41] studied the effect of several parameters on the ion-induced secondary electron emission (ISEE) coefficient, namely the target material dependency on the discharge voltage. It is well known, based on the Thornton relation, that the discharge voltage is inversely proportional to the ISEE coefficient of the target material [42]. Since the poisoning phenomenon of the Ti fraction of the target should increase with increasing $N_2$ flow rate, the target surface should shift from a metallic-like condition (mainly composed of Ti—ISEE of 0.114) towards a nitride-like one (TiN layer—ISEE of 0.049 [43–46]). As a result, the target potential exhibits the expected behaviour, since a strong decrease of the ISEE coefficient takes place with increasing $N_2$ flow rates, due to the poisoning of the Ti fraction of the target, thus increasing the discharge voltage values (from 345 to 378 V).

As a consequence of the poisoning phenomena, the deposition rate shows a steep decrease. For low $N_2$ flow rates (and $N_2$ partial pressures of $1.8 \times 10^{-2}$ Pa), the target surface is mostly metallic, meaning that the Ar-promoted sputtering rate should remain high. In addition, the ISEE coefficient of the target is also high (0.114), since it is still in its metallic condition. The low $N_2$ partial pressure inside the sputtering chamber should translate into a relatively high sputtering yield of the target [47], giving rise to high deposition rates (1.5–1.6 $\mu$m $h^{-1}$). Increasing the $N_2$ flow rate, the sputtering yield of the target [47] is significantly decreased due to increased nitrogen coverage of the target surface, a factor that contributes to the observed low deposition rates (1.2–1.4 $\mu$m $h^{-1}$).

Following the evolution of the deposition characteristics, which will have an effect on the subsequent properties of the films, the chemical composition of the sputtered $Ag_y$:$TiN_x$ coatings was studied. Figure 2 shows the results of the [N]/[Ti] atomic ratio and Ag incorporation as a function of the $N_2$ flow, obtained from the analysis of the RBS spectra of the produced films. By firstly analysing the evolution of the [N]/[Ti] atomic ratio as a function of the $N_2$ flow rate, it is important to note a gradual increase of the values from 0.1 to 1 (stoichiometric condition), due to increased nitrogen incorporation. Note that this increase is steeper for the higher $N_2$ flow rates, 4 and 5 sccm. In fact, this behaviour was expected and justifiable due to the higher amount of nitrogen molecules introduced into the reactor during the deposition process, as a result of the increase of the $N_2$ flow rate. Consequently, regarding the [N]/[Ti] atomic ratio values, the $Ag_y$:$TiN_x$ samples sputtered with 1–3 sccm (presenting ratios of 0.1, 0.2 and 0.3) can be considered as highly under-stoichiometric samples, while the films sputtered with 4 and 5 sccm ([N]/[Ti] atomic ratios of 0.7 and 1) can be classified as close-stoichiometric and stoichiometric samples, respectively.

Regarding the silver content, it is interesting to notice a large increase of the Ag concentration when the $N_2$ flow changes from 1 to 4 sccm, varying from 10 to 32 at.% of Ag. Then, a decrease until 20 at.% Ag is observed when the stoichiometric condition is achieved (5 sccm). Regarding the observed steep increase in the Ag incorporation when the $N_2$ flow rate is increased up to 4 sccm (from 8–10 to 32 at.% Ag), it should probably be due to the already referred increased number of nitrogen species in the reactor that contribute to the sputtering of the target, caused by the increase of the $N_2$ flow rate. Indeed, since the Ag sputtering yield is almost seven times higher than that of Ti (2.5 and 0.35, respectively [48]), the greater amount of species (argon and nitrogen) contributing to the sputtering of the target should, as observed, sputter more Ag atoms from the target that will be incorporated in the growing film, when compared to Ti. In addition, since the target should become gradually poisoned as the $N_2$ flow rate increases, the sputtering of the Ti fraction of the target should be even more hindered. When stoichiometry is attained at a flow of 5 sccm, the elevated number of species in the reactor should translate into a saturation of the system, meaning that the Ti fraction of the target should be completely covered by a compound layer (TiN), as discussed before. This saturation may lead to an increasing poisoning of the Ag pellets in the Ti/Ag target by extensive TiN coverage, thus reducing its sputtering yield, which would explain the decrease of the Ag concentration from 32 to 20 at.% when the nitrogen flow rate increases from 4 to 5 sccm.

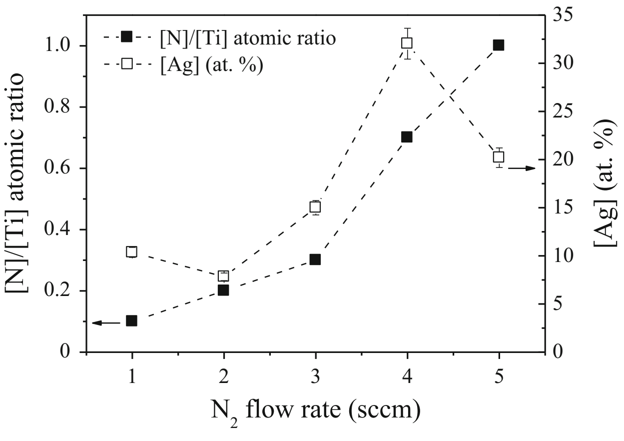

**Fig. 2** Evolution of the [N]/[Ti] atomic ratio and Ag concentration with increasing $N_2$ flow rates

## 3.2 Structural and morphological characterization

In order to better understand the influence of the deposition parameters and composition evolution, related to the $N_2$ flow rate increase, on the structure and morphology of the produced coatings, an extensive structural and morphological evaluation was performed.

From the XRD patterns, Fig. 3, it is possible to observe that the deposited samples reveal a consistent structural evolution, as the [N]/[Ti] atomic ratio increases. For the samples obtained with low [N]/[Ti] atomic ratios—0.1 and 0.2—the XRD patterns correspond to a N-doped Ti matrix [49]. Due to these low [N]/[Ti] atomic ratios and mobility constraints, an increased difficulty to form any type of nitride phase is expected. Consequently, the few available nitrogen atoms are most probably incorporated into the Ti structure, leading to an increase of the lattice parameter, as evidenced by the small shift of the hcp-Ti (002) peak towards lower diffraction angles. In addition, the SEM analysis (Fig. 4) seems to be consistent with this claim, since a rather dense and granular Ti-like morphology [29] is evident in these samples (Figs. 4a, b, respectively), mainly because of the relatively low grain sizes involved—11 to 12 nm. No metallic Ag phases or aggregates were detected by XRD and SEM analyses of these 0.1 and 0.2

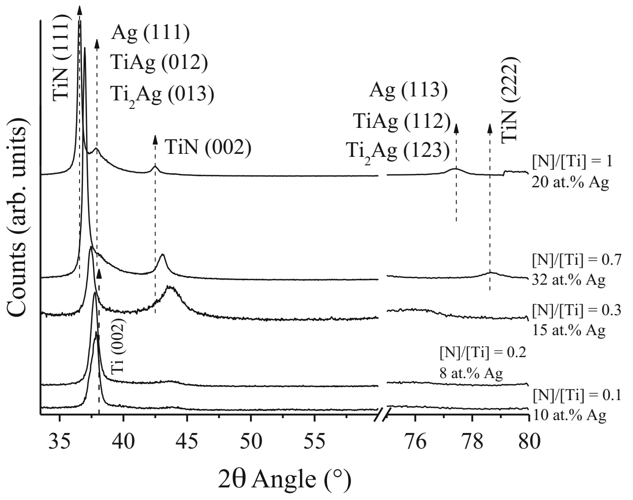

**Fig. 3** Structural evolution of the as-deposited Ag$_y$:TiN$_x$ samples. The XRD diffractograms are presented with different $y$-axis scales in order to allow a better understanding of the diffraction peaks

[N]/[Ti] atomic ratio samples. Thus, amorphous TiAg or Ti$_2$Ag intermetallics by Ag atomic dissolution may probably be produced, leading to a single-phase substitutional solid solution. For intermediate [N]/[Ti] atomic ratios—0.3 and 0.7—the XRD patterns seem to indicate some kind of transition zone, since small traces of N-deficient TiN appear in the [N]/[Ti] atomic ratio = 0.3 and 15 at.% Ag sample, as confirmed by the shifted fcc-TiN peaks (ICSD card #184916) at 37.5 and 43.5° (Fig. 3).

The higher nitrogen incorporation gave also rise to the formation of long cracks (observed throughout the surface of the sample), as evidenced by the SEM micrograph (Fig. 4c). This may be indicative of a strong increment of the internal stresses of the samples, due to the observed phase transformation of α-Ti into δ-TiN. No changes on the grain size were detected, with the values remaining around 11 nm for this sample. Once more, no Ag phases were detected according to the XRD analysis. When the [N]/[Ti] atomic ratio and Ag concentration increase from 0.3 to 0.7, and 15 to 32 at.%, respectively, the films become less N-deficient. Due to this steeply approach towards the stoichiometric condition of TiN, a fcc-TiN matrix grows, as demonstrated by the position and shape of the diffraction peak at ~37°. The later considerably changes in comparison with the diffraction patterns of the sample with [N]/[Ti] atomic ratio = 0.3. The fcc-TiN (111) peak is now shifted towards higher diffraction angles (indication of high tensile stresses, hence the observed cracks), meaning that there are still N vacancies in the cubic lattice, as in fact anticipated by its under-stoichiometric condition ([N]/[Ti] atomic ratio of 0.7). Nevertheless, and contrarily to what was observed in the previous samples, a single Ag phase is now noticeable, as it can be evidenced by the pronounced "tail" of the TiN (111) peak at about 38° and the higher Ag content exhibited by this sample (Fig. 3). However, the low-intensity signal of the diffraction pattern did not allow a reliable quantification of the Ag-related grain size. Furthermore, due to the relatively high amount of Ag in this sample, as well as the difficult indexation of the Ag-related peaks (Ag, TiAg and Ti$_2$Ag peaks occur at approximately the same diffraction angle—ICSD cards #181730, #605934 and #605935), one can never fully discard the possible formation of TiAg and Ti$_2$Ag intermetallics, or even a mixture of both. As it can be perceivable from the increased definition of the [N]/[Ti] atomic ratio = 0.7 (32 at.% Ag) sample fcc-TiN (111) peak when comparing with the [N]/[Ti] atomic ratio = 0.3 (15 at.% Ag) sample, the grain size suffered a twofold increase, from 11 to 21 nm.

Once more, the morphological characterization is consistent with these findings, since it is now evident the formation of the typical disaggregated pyramid-like TiN columns in the sample with [N]/[Ti] atomic ratio = 0.7 (32 at.% Ag), Fig. 4d$_1$). In addition, regarding this sample, the Ag nanograins are not uniformly distributed across the under-stoichiometric TiN matrix (Fig. 4d$_2$). Instead, Ag seems to be more concentrated near the substrate. Since in this under-stoichiometric [N]/[Ti] atomic ratio = 0.7 (32 at.% Ag) sample, the TiN matrix is somewhat denser than that of the stoichiometric one (which displays extensive column disaggregation and porosity), it may probably act as a silver diffusion barrier [27]. The denser under-stoichiometric matrix should prevent the Ag atoms to diffuse to the surface and aggregate, in opposition to what is visible in the stoichiometric (porous) one, where Ag may be using the intercolumnar spacing to diffuse towards the surface, forming large Ag clusters. This phenomenon was already observed by the authors in a previous work [18].

Finally, the film with [N]/[Ti] atomic ratio = 1 and 20 at.% Ag is formed by a stoichiometric matrix, with Ag now in its metallic form (Ag aggregates, Fig. 4e), instead of forming TiAg or Ti$_2$Ag intermetallics. This result is supported by the fact that the fcc-TiN (111) peak is no longer shifted towards higher diffraction angles. Moreover, two new Ag-related peaks (ICSD card #181730) around 38° (fcc-Ag (111)) and 78° (fcc-Ag (311)) are now clearly visible, thus supporting the occurrence of metallic Ag in this sample. Since coherent Ag diffracted peaks are now present, it was possible to calculate the Ag grain size, which was about 10 nm. A further definition increase of the fcc-TiN (111) peak is also observable; hence, the related grain size also exhibited a steep increase, from 21 to 38 nm, a value that is very close to that of pure stoichiometric TiN [16]. This is, again, consistent with SEM observations, where it is possible to see the typical TiN-like pyramidal columns with metallic Ag aggregates among and on the top of them (Fig. 4e$_{1-2}$).

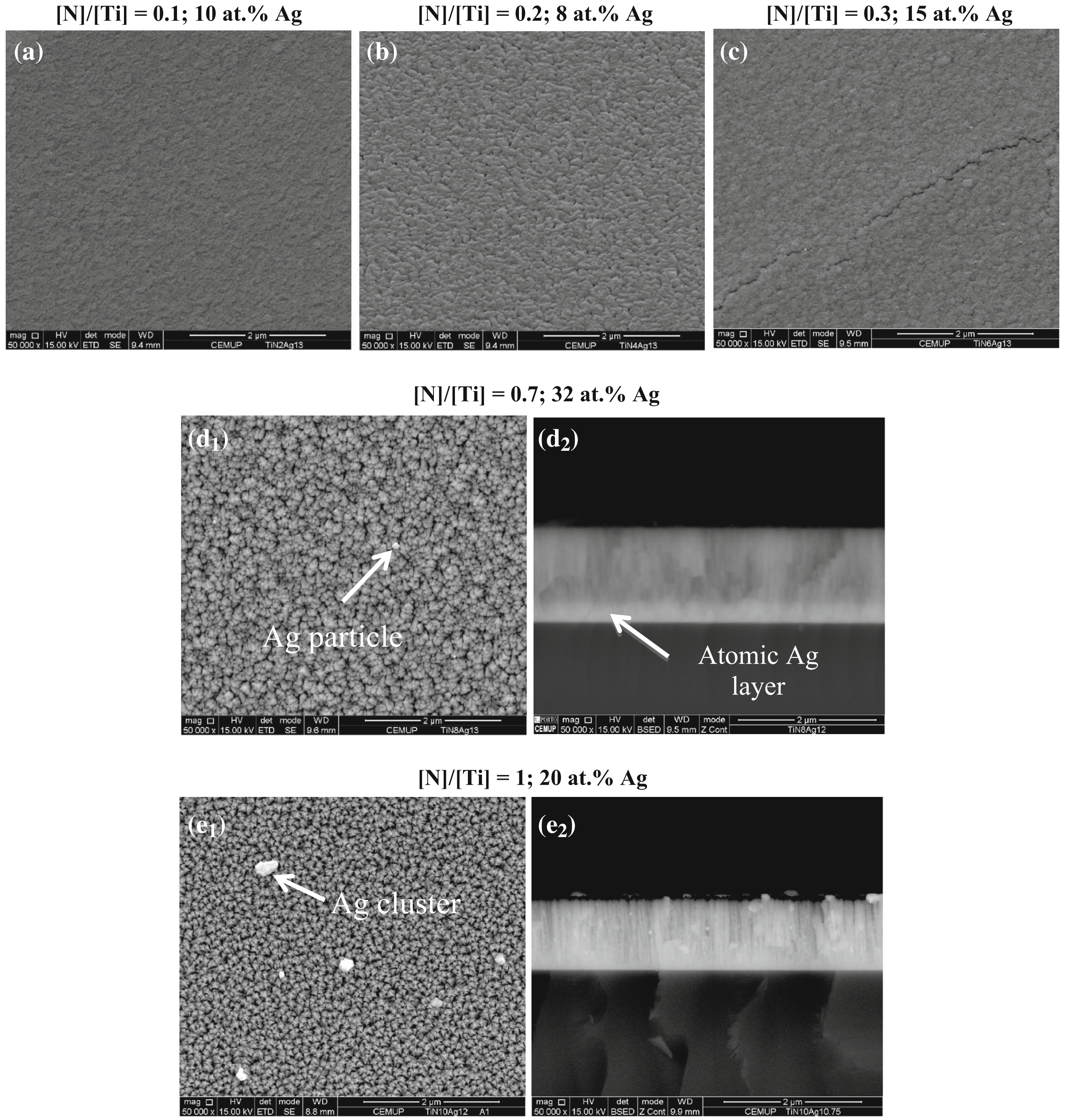
[N]/[Ti] = 0.1; 10 at.% Ag

[N]/[Ti] = 0.2; 8 at.% Ag

[N]/[Ti] = 0.3; 15 at.% Ag

[N]/[Ti] = 0.7; 32 at.% Ag

[N]/[Ti] = 1; 20 at.% Ag

**Fig. 4** Morphological features of the sputtered $Ag_y$:$TiN_x$ samples

To summarize, the samples obtained with low [N]/[Ti] atomic ratios (0.1, 0.2 and 0.3) exhibit a nitrogen-doped Ti matrix with small grain sizes (~11–12 nm), since the nitrogen contents seem to be too low to form a stable TiN matrix and no metallic Ag phases were found in XRD and SEM analyses (Figs. 3, 4). Since more nitrogen is inserted in the Ti interstitial spaces (with the consequent increase of the [N]/[Ti] atomic ratio), a N-deficient TiN matrix appears to be formed in the [N]/[Ti] atomic ratio = 0.7 and 32 at.% Ag sample, with some Ag phases that may start to develop. The sample obtained with the highest [N]/[Ti] atomic ratio, [N]/[Ti] = 1 and 20 at.% Ag, possesses a stoichiometric TiN matrix, with Ag in its metallic state forming rather large clusters on top and among the TiN columns.

### 3.3 Electrical and mechanical properties

The observed structural and morphological changes will have a major effect in the electrical and mechanical behaviour of the $Ag_y$:$TiN_x$ samples. As already referred, the sputtered coatings have been optimized and characterized, so that they can be later sputtered onto flexible polymeric substrates (polyurethane), which will be used for bioelectrode applications (EEG). Hence, low resistivity and high elasticity are desirable parameters, since the coatings should be able to deal with low-amplitude signals [16], as well as complying with the in-service substrate deformation when the bioelectrodes are placed in the human body.

The electrical resistivity of metallic systems strongly depends on their electronic structure, as well as on the mobility of the charge carriers [50]. Disorders in the crystalline structure of the metals such as impurities, grain boundaries and vacancies [51] work as scattering centres for charge carriers, thus increasing the resistivity of metals. The effect of these parameters on the resistivity of thin films can be expressed by Matthiessen's rule [52]:

$$\rho = \rho_p + \rho_m + \rho_f + \rho_i + \rho_s \qquad (1)$$

where $\rho_p$, $\rho_m$, $\rho_f$, $\rho_i$ and $\rho_s$ stand for the resistivity caused by scattering from phonons, impurities, defects, grain boundaries and the surface scattering, respectively. Figure 5 depicts the resistivity evolution of the coatings with increasing [N]/[Ti] atomic ratio. It is worth to note a significant effect of both parameters on the resistivity behaviour, since they lead to the structural and morphological changes as previously observed. The samples obtained with low [N]/[Ti] atomic ratios (up to 0.3) consist mainly of a nitrogen-doped hcp-Ti structure, as already observed in Sect. 3.2. Thus, the exhibited electrical resistivity values (in the range of 2.2–2.5 × $10^{-6}$ Ω m) indicate that nitrogen may act as impurities and charge carrier scattering centres. Moreover, besides the impurities effect, grain boundary scattering should also play a major role in the observed resistivity values, since the simulated grain size is very low (not exceeding 12 nm). Hence, more grain boundaries are available in these strongly under-stoichiometric samples, which also contribute to the observed higher values [53]. It is important to note that the typical resistivity value of a pure hcp-Ti structure is approximately 4 × $10^{-7}$ Ω m [29], thus illustrating the significant effect of small impurity incorporation in the present system. The small resistivity increase observed for the [N]/[Ti] atomic ratio = 0.3 and 15 at.% Ag sample can be justified by the formation of long intergranular cracks (Fig. 4c), which may act as a barrier for electronic transfer, thus decreasing the charge carrier mobility.

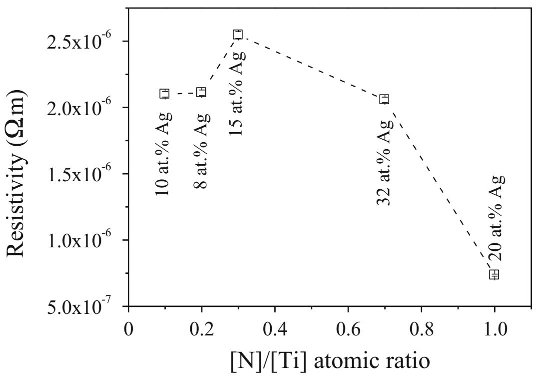

**Fig. 5** Resistivity behaviour of the sputtered $Ag_y$:$TiN_x$ samples. The error associated with all measurements was always below 1 %, and the attachment of the contacts was checked prior to every measurement (the I/V correlation was always very close to 1)

As for the close-stoichiometric $Ag_y$:$TiN_x$ sample, [N]/[Ti] atomic ratio = 0.7 and 32 at.% Ag, a N-deficient TiN phase is perceivable (Fig. 3), due to the hcp-Ti to fcc-TiN phase transformation undergone by this sample with increasing nitrogen incorporation. This may indicate that nitrogen should no longer be acting as an impurity and a steep drop of the resistivity values should, a priori, be expected. In addition, the Ag concentration also suffers a strong increase and so does the grain size of the samples (increases from 11 to 21 nm). However, the resistivity drop is not as sharp as expected (decreases until approximately 2 × $10^{-6}$ Ω m), since the hcp-Ti to fcc-TiN phase transformation gives rise to a somewhat disaggregated and porous pyramid-like morphology (see Fig. 4$d_1$), typical for slightly under-stoichiometric TiN coatings.

When stoichiometric TiN is attained, [N]/[Ti] atomic ratio = 1 and 20 at.% Ag sample, major structural and morphological changes were detected, giving rise to a decrease of the resistivity values until 7 × $10^{-7}$ Ω m. Firstly, a coherent metallic Ag phase is now present as evidenced by the fcc-Ag (111) peak, Fig. 3. This fact, associated with the high porosity and columnar disaggregation present in these samples, gives rise to a strong Ag segregation phenomenon, with Ag particles extensively present at the surface of the coatings and also among the TiN columns (Fig. 4$e_{1-2}$). In fact, as already observed by the authors, these Ag particles should form highly conductive electronic paths between the TiN columns [15, 16], since it is known that Ag predominantly precipitates in the faces of the fcc-TiN cubic lattice [22]. Furthermore, the TiN matrix crystallinity is significantly enhanced (grain size increases from 21 to 38 nm).

The hardness and reduced modulus ($E_r$) versus [N]/[Ti] atomic ratio of the sputtered $Ag_y$:$TiN_x$ samples are shown in Fig. 6. They exhibit an almost linear increase (from 6 to 12 GPa and 156 to 200 GPa, respectively) until the close-stoichiometry is reached, [N]/[Ti] atomic ratio = 0.7 and 32 at.% Ag sample. Then, for the stoichiometric coating,

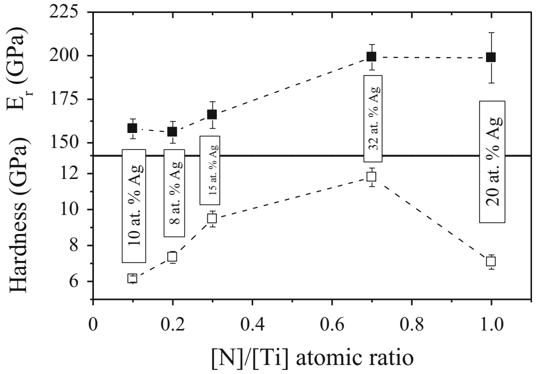

**Fig. 6** Evolution of the hardness and Young's modulus versus [N]/[Ti] atomic ratio of the as-deposited $Ag_y$:$TiN_x$ samples

[N]/[Ti] atomic ratio = 1 and 20 at.% Ag, the hardness value steeply decreases (from 12 to 7 GPa), while the reduced modulus remains approximately constant at about 200 GPa. Note that these values are somewhat lower than those exhibited by pure TiN [21, 34], since the coatings were prepared at low temperatures (100 °C) and without substrate bias. In addition, it may be an indication that Ag is promoting the desired lower hardness/modulus values. For the highly under-stoichiometric samples, [N]/[Ti] atomic ratio = 0.1, 0.2 and 0.3, the increase of both hardness and reduced modulus values can be attributed to the progressive hcp-Ti to fcc-TiN phase transformation that occurs due to the continuous insertion of nitrogen in the Ti lattice interstices. This continuous nitrogen enrichment should give rise to strong internal stresses [34, 50], since higher Ti lattice parameters are expected, as it can be confirmed by the hcp-Ti (002) peak shift towards lower diffraction angles (Fig. 3).

For the close-stoichiometric $Ag_y$:$TiN_x$ sample, [N]/[Ti] atomic ratio = 0.7 and 32 at.% Ag, the maximum hardness and reduced modulus are attained. As it was referred in the XRD analysis, the hcp-Ti to fcc-TiN phase transformation appears to be completed, since a stable yet slightly N-deficient TiN phase is formed (Fig. 3). Furthermore, some porosity and column disaggregation are evident (Fig. 4$d_1$), meaning that an internal stress relaxation process took place, which, in turn, should translate into a hardness and modulus decrease. However, as already referred, this sample possesses a defective TiN matrix (nitrogen vacancies), which may contribute to the increase of the hardness and reduced modulus values.

Finally, the stoichiometric $Ag_y$:$TiN_x$ sample—[N]/[Ti] atomic ratio = 1 and 20 at.% Ag—exhibits a rather inconsistent behaviour regarding the hardness and reduced modulus evolution. Comparing with the [N]/[Ti] atomic ratio = 0.7 and 32 at.% Ag sample, the reduced modulus value remains constant at 200 GPa, while the hardness value suffers a decrease from 12 to 7 GPa. This variation can be due to the Ag segregation phenomenon that extensively occurs in this sample (Fig. 4$e_{1–2}$), with metallic Ag particles and clusters among and on the top of the TiN columns. Hence, the formation of Ag particles promotes the decrease of the hardness values.

## 4 Conclusions

The present study addresses the deposition and characterization of a series of $Ag_y$:$TiN_x$ thin films produced with nitrogen flow rates varying between 1 and 5 sccm, in order to optimize the sputtering conditions and consequent properties so that they can be successfully sputtered onto flexible polymeric substrates. The main objective is to avoid the Ag segregation phenomenon that occurs for stoichiometric $Ag_y$:$TiN_x$ conditions, thus ensuring the stability of the coatings during in-service applications.

A first zone of samples with [N]/[Ti] atomic ratios of 0.1 and 0.2 (and correspondent Ag contents of 10 and 8 at.%, respectively), was characterized by low target potentials and high deposition rates, giving rise to a dense and granular hcp-Ti structure with N atoms incorporated in the interstices of the structure, acting as impurities. In this zone, the samples exhibit higher resistivity values ($2.2 \times 10^{-6}$ Ω m), while both hardness and reduced modulus remain low (6–7 and 158–156 GPa, respectively). Regarding the second (transition) zone, which comprises the samples with [N]/[Ti] atomic ratios of 0.3 (15 at.% Ag) and 0.7 (32 at.% Ag), a decrease of the deposition rate and an increase of the target potential occur. An increased porosity is also noticed for these samples. At this stage, the higher hardness (12 GPa) and reduced modulus (200 GPa) values are attained. In addition, a general decrease of the electrical resistivity is observed. The last zone refers to the stoichiometric $Ag_y$:$TiN_x$ sample—[N]/[Ti] atomic ratio = 1 and 20 at.% Ag—characterized by high target potential and the lowest deposition rate. A complete disaggregation of the TiN typical columnar structures and the formation of large Ag clusters are observed. Due to the exhibited changes, both the electrical resistivity ($7 \times 10^{-7}$ Ω m) and hardness (7 GPa) values suffer an abrupt decrease. It is important to note that extensive Ag segregation is only extensively present in the stoichiometric $Ag_y$:$TiN_x$ sample. Hence, the reduction of the [N]/[Ti] atomic ratio effectively acts as a segregation inhibitor. Thus, it is possible to state that the samples with [N]/[Ti] atomic ratios of 0.3 (15 at.% Ag) and 0.7 (32 at.% Ag) seem to be electrically and mechanically more suitable to be used for bioelectrode applications.

**Acknowledgments** This research is partially sponsored by FEDER funds through the program COMPETE—Programa Operacional Factores de Competitividade and by national funds through FCT—Fundação para a Ciência e a Tecnologia, under the projects PEst-C/EME/UI0285/2011, PTDC/SAU-ENB/116850/2010, PTDC/CTM-NAN/112574/2009 and Programa Pessoa 2012/2013 Cooperação Portugal/França, Project No. 27306 UA "Porous architectures in GRAded CERamic thin films for biosensors"—GRACER. The authors would also like to acknowledge CEMUP for SEM analysis. P. Pedrosa acknowledges FCT for the Ph.D. Grant SFRH/BD/70035/2010. J. Borges acknowledges the support by the European social fund within the framework of the project "Support of inter-sectoral mobility and quality enhancement of research teams at Czech Technical University in Prague", CZ.1.07/2.3.00/30.0034.

## References

1. E. McAdams, *Encyclopedia of Medical Devices and Instrumentation* (Wiley, New York, 1998)
2. A. Searle, L. Kirkup, A direct comparison of wet, dry and insulating bioelectric recording electrodes. Physiol. Meas. **21**, 271 (2000)
3. M. Teplan, Fundamentals of EEG measurement. Meas. Sci. Rev. **2**, 1–11 (2002)
4. L.T. Cunha, P. Pedrosa, C.J. Tavares, E. Alves, F. Vaz, C. Fonseca, The role of composition, morphology and crystalline structure in the electrochemical behaviour of $TiN_x$ thin films for dry electrode sensor materials. Electrochim. Acta **55**, 59–67 (2009)
5. P. Pedrosa, E. Alves, N.P. Barradas, P. Fiedler, J. Haueisen, F. Vaz, C. Fonseca, $TiN_x$ coated polycarbonate for bio-electrode applications. Corros. Sci. **56**, 49–57 (2012)
6. G. Gargiulo, R.A. Calvo, P. Bifulco, M. Cesarelli, C. Jin, A. Mohamed, A. van Schaik, A new EEG recording system for passive dry electrodes. Clin. Neurophysiol. Off. J. Int. Fed. Clin. Neurophysiol. **121**, 686–693 (2010)
7. C. Fonseca, J.P.S. Cunha, R.E. Martins, V.M. Ferreira, J.P.M. de Sá, M.A. Barbosa, A.M. da Silva, A novel dry active electrode for EEG recording. IEEE Trans. Biomed. Eng. **54**, 162–165 (2007)
8. K.P. Hoffmann, R. Ruff, Flexible dry surface-electrodes for ECG long-term monitoring, *2007 Annual International Conference of the IEEE Engineering in Medicine and Biology Society*, vol. 1–16 (IEEE, New York, 2007), pp. 5740–5743
9. J.-Y. Baek, J.-H. An, J.-M. Choi, K.-S. Park, S.-H. Lee, Flexible polymeric dry electrodes for the long-term monitoring of ECG. Sens. Actuators A **143**, 423–429 (2008)
10. A. Gruetzmann, S. Hansen, J. Muller, Novel dry electrodes for ECG monitoring. Physiol. Meas. **28**, 1375–1390 (2007)
11. V. Marozas, A. Petrenas, S. Daukantas, A. Lukosevicius, A comparison of conductive textile-based and silver/silver chloride gel electrodes in exercise electrocardiogram recordings. J. Electrocardiol. **44**, 189–194 (2011)
12. C.-Y. Chen, C.-L. Chang, T.-F. Chien, C.-H. Luo, Flexible PDMS electrode for one-point wearable wireless bio-potential acquisition. Sens. Actuators A **203**, 20–28 (2013)
13. P. Salvo, R. Raedt, E. Carrette, D. Schaubroeck, J. Vanfleteren, L. Cardon, A 3D printed dry electrode for ECG/EEG recording. Sens. Actuators A **174**, 96–102 (2012)
14. S. Kaitainen, A. Kutvonen, M. Suvanto, T.T. Pakkanen, R. Lappalainen, S. Myllymaa, Liquid silicone rubber (LSR)-based dry bioelectrodes: the effect of surface micropillar structuring and silver coating on contact impedance. Sens. Actuators A **206**, 22–29 (2014)
15. P. Pedrosa, D. Machado, C. Lopes, E. Alves, N.P. Barradas, N. Martin, F. Macedo, C. Fonseca, F. Vaz, Nanocomposite Ag:TiN thin films for dry biopotential electrodes. Appl. Surf. Sci. **285**(Part A), 40–48 (2013)
16. P. Pedrosa, E. Alves, N.P. Barradas, N. Martin, P. Fiedler, J. Haueisen, F. Vaz, C. Fonseca, Electrochemical behaviour of nanocomposite $Ag_x$:TiN thin films for dry biopotential electrodes. Electrochim. Acta **125**, 48–57 (2014)
17. P. Pedrosa, C. Lopes, N. Martin, C. Fonseca, F. Vaz, Electrical characterization of Ag:TiN thin films produced by glancing angle deposition. Mater. Lett. **115**, 136–139 (2014)
18. P. Pedrosa, D. Machado, M. Evaristo, A. Cavaleiro, C. Fonseca, F. Vaz, Ag:TiN nanocomposite thin films for bioelectrodes: the effect of annealing treatments on the electrical and mechanical behavior. J. Vac. Sci. Technol. A **32**, 031515 (2014)
19. S. Jin, Y. Zhang, Q. Wang, D. Zhang, S. Zhang, Influence of TiN coating on the biocompatibility of medical NiTi alloy. Colloids Surf. B **101**, 343–349 (2013)
20. R. Tian, J. Sun, Corrosion resistance and interfacial contact resistance of TiN coated 316L bipolar plates for proton exchange membrane fuel cell. Int. J. Hydrogen Energy **36**, 6788–6794 (2011)
21. F. Vaz, P. Machado, L. Rebouta, P. Cerqueira, Ph Goudeau, J.P. Rivière, E. Alves, K. Pischow, J. de Rijk, Mechanical characterization of reactively magnetron-sputtered TiN films. Surf. Coat. Technol. **174–175**, 375–382 (2003)
22. P.J. Kelly, T. vom Braucke, Z. Liu, R.D. Arnell, E.D. Doyle, Pulsed DC titanium nitride coatings for improved tribological performance and tool life. Surf. Coat. Technol. **202**, 774–780 (2007)
23. L.A. Geddes, L.E. Baker, A.G. Moore, Optimum electrolytic chloriding of silver electrodes. Med. Biol. Eng. **7**, 49–56 (1969)
24. H. Köstenbauer, G.A. Fontalvo, J. Keckes, C. Mitterer, Intrinsic stresses and stress relaxation in TiN/Ag multilayer coatings during thermal cycling. Thin Solid Films **516**, 1920–1924 (2008)
25. J. Zhao, H.J. Feng, H.Q. Tang, J.H. Zheng, Bactericidal and corrosive properties of silver implanted TiN thin films coated on AISI317 stainless steel. Surf. Coat. Technol. **201**, 5676–5679 (2007)
26. T.L. Alford, L. Chen, K.S. Gadre, Stability of silver thin films on various underlying layers at elevated temperatures. Thin Solid Films **429**, 248–254 (2003)
27. L. Gao, J. Gstöttner, R. Emling, M. Balden, C. Linsmeier, A. Wiltner, W. Hansch, D. Schmitt-Landsiedel, Thermal stability of titanium nitride diffusion barrier films for advanced silver interconnects. Microelectron. Eng. **76**, 76–81 (2004)
28. M. Zhang, L. Hu, G. Lin, Z. Shao, Honeycomb-like nanocomposite Ti–Ag–N films prepared by pulsed bias arc ion plating on titanium as bipolar plates for unitized regenerative fuel cells. J. Power Sources **198**, 196–202 (2012)
29. C. Lopes, C. Gonçalves, P. Pedrosa, F. Macedo, E. Alves, N.P. Barradas, N. Martin, C. Fonseca, F. Vaz, $TiAg_x$ thin films for lower limb prosthesis pressure sensors: effect of composition and structural changes on the electrical and thermal response of the films. Appl. Surf. Sci. **285**(Part A), 10–18 (2013)
30. N.P. Barradas, C. Jeynes, R.P. Webb, Simulated annealing analysis of Rutherford backscattering data. Appl. Phys. Lett. **71**, 291–293 (1997)
31. A.F. Gurbich, Evaluated differential cross-sections for IBA. Nucl. Instrum. Methods Phys. Res. Sect. B **268**, 1703–1710 (2010)
32. L.J. Van Der Pauw, A method of measuring specific resistivity and Hall effect of discs of arbitrary shape. Philips Res. Rep. **13**, 1–9 (1958)
33. Q. Kan, W. Yan, G. Kang, Q. Sun, Oliver–Pharr indentation method in determining elastic moduli of shape memory alloys—a

phase transformable material. J. Mech. Phys. Solids **61**, 2015–2033 (2013)

34. F. Vaz, P. Machado, L. Rebouta, J.A. Mendes, S. Lanceros-Méndez, L. Cunha, S.M.C. Nascimento, P. Goudeau, J.P. Rivière, E. Alves, A. Sidor, Physical and morphological characterization of reactively magnetron sputtered TiN films. Thin Solid Films **420–421**, 421–428 (2002)
35. F. Vaz, J. Ferreira, E. Ribeiro, L. Rebouta, S. Lanceros-Méndez, J.A. Mendes, E. Alves, P. Goudeau, J.P. Rivière, F. Ribeiro, I. Moutinho, K. Pischow, J. de Rijk, Influence of nitrogen content on the structural, mechanical and electrical properties of TiN thin films. Surf. Coat. Technol. **191**, 317–323 (2005)
36. C.-S. Shin, S. Rudenja, D. Gall, N. Hellgren, T.-Y. Lee, I. Petrov, J.E. Greene, Growth, surface morphology, and electrical resistivity of fully strained substoichiometric epitaxial $TiN_x(0.67 < x < 1.0)$ layers on MgO(001). J. Appl. Phys. **95**, 356–362 (2004)
37. J.F. Pierson, D. Wiederkehr, A. Billard, Reactive magnetron sputtering of copper, silver, and gold. Thin Solid Films **478**, 196–205 (2005)
38. A.G. Spencer, R.P. Howson, R.W. Lewin, Pressure stability in reactive magnetron sputtering. Thin Solid Films **158**, 141–149 (1988)
39. D. Depla, S. Heirwegh, S. Mahieu, J. Haemers, R. De Gryse, Understanding the discharge voltage behavior during reactive sputtering of oxides. J. Appl. Phys. **101**, 013301 (2007)
40. D. Depla, G. Buyle, J. Haemers, R. De Gryse, Discharge voltage measurements during magnetron sputtering. Surf. Coat. Technol. **200**, 4329–4338 (2006)
41. D. Depla, S. Mahieu, R. De Gryse, Magnetron sputter deposition: linking discharge voltage with target properties. Thin Solid Films **517**, 2825–2839 (2009)
42. J.A. Thornton, Magnetron sputtering: basic physics and application to cylindrical magnetrons. J. Vac. Sci. Technol. **15**, 171–177 (1978)
43. J.M. Chappé, F. Vaz, L. Cunha, C. Moura, M.C. Marco de Lucas, L. Imhoff, S. Bourgeois, J.F. Pierson, Development of dark Ti(C, O, N) coatings prepared by reactive sputtering. Surf. Coat. Technol. **203**, 804–807 (2008)
44. J. Borges, F. Vaz, L. Marques, $AlN_xO_y$ thin films deposited by DC reactive magnetron sputtering. Appl. Surf. Sci. **257**, 1478–1483 (2010)
45. J. Borges, N. Martin, N.P. Barradas, E. Alves, D. Eyidi, M.F. Beaufort, J.P. Riviere, F. Vaz, L. Marques, Electrical properties of $AlN_xO_y$ thin films prepared by reactive magnetron sputtering. Thin Solid Films **520**, 6709–6717 (2012)
46. R. Arvinte, J. Borges, R.E. Sousa, D. Munteanu, N.P. Barradas, E. Alves, F. Vaz, L. Marques, Preparation and characterization of $CrN_xO_y$ thin films: the effect of composition and structural features on the electrical behavior. Appl. Surf. Sci. **257**, 9120–9124 (2011)
47. S. Mahieu, D. Depla, Reactive sputter deposition of TiN layers: modelling the growth by characterization of particle fluxes towards the substrate. J. Phys. D Appl. Phys. **42**, 053002 (2009)
48. V.S. Smentkowski, Trends in sputtering. Prog. Surf. Sci. **64**, 1–58 (2000)
49. L.A. Rocha, E. Ariza, J. Ferreira, F. Vaz, E. Ribeiro, L. Rebouta, E. Alves, A.R. Ramos, P. Goudeau, J.P. Rivière, Structural and corrosion behaviour of stoichiometric and substoichiometric TiN thin films. Surf. Coat. Technol. **180–181**, 158–163 (2004)
50. B.-Y. Oh, M.-C. Jeong, D.-S. Kim, W. Lee, J.-M. Myoung, Post-annealing of Al-doped ZnO films in hydrogen atmosphere. J. Cryst. Growth **281**, 475–480 (2005)
51. S. Nagarjuna, K. Balasubramanian, D.S. Sarma, Effect of Ti additions on the electrical resistivity of copper. Mater. Sci. Eng. A **225**, 118–124 (1997)
52. K.-Y. Chan, T.-Y. Tou, B.-S. Teo, Thickness dependence of the structural and electrical properties of copper films deposited by dc magnetron sputtering technique. Microelectron. J. **37**, 608–612 (2006)
53. M.E. Day, M. Delfino, J.A. Fair, W. Tsai, Correlation of electrical resistivity and grain size in sputtered titanium films. Thin Solid Films **254**, 285–290 (1995)

Electrochimica Acta 153 (2015) 602–611

Contents lists available at ScienceDirect

Electrochimica Acta

journal homepage: www.elsevier.com/locate/electacta

# Electrochemical and structural characterization of nanocomposite $Ag_y$:$TiN_x$ thin films for dry bioelectrodes: the effect of the N/Ti ratio and Ag content

P. Pedrosa [a,b,c], D. Machado [c], P. Fiedler [d], E. Alves [e], N.P. Barradas [f], J. Haueisen [d,g], F. Vaz [c], C. Fonseca [a,b,*]

[a] SEG-CEMUC – Department of Mechanical Engineering, University of Coimbra, Portugal
[b] Universidade do Porto, Faculdade de Engenharia, Rua Dr. Roberto Frias, s/n, 4200-465 Porto, Portugal
[c] Centro de Física, Universidade do Minho, 4710-057 Braga, Portugal
[d] Institute of Biomedical Engineering and Informatics, Technische Universität Ilmenau, Ilmenau, Germany
[e] Instituto de Plasmas e Fusão Nuclear, Instituto Superior Técnico, Universidade de Lisboa, Av. Rovisco Pais, 1049-001, Lisboa, Portugal
[f] Centro de Ciências e Tecnologias Nucleares, Instituto Superior Técnico, Universidade de Lisboa, E.N. 10 (km 139,7), 2695-066 Bobadela LRS, Portugal
[g] Biomagnetic Center, Dept. of Neurology, University Hospital Jena, Friedrich Schiller University Jena, Jena, Germany

ARTICLE INFO

*Article history:*
Received 21 September 2014
Received in revised form 9 November 2014
Accepted 4 December 2014
Available online 5 December 2014

*Keywords:*
Biopotential
Dry electrodes
EIS
voltammetry
TiN
Ag-doping
Sputtering

ABSTRACT

$Ag_y$:$TiN_x$ nanocomposite thin films sputtered with different N/Ti atomic ratios and Ag atomic contents were characterized from the structural and morphological points of view. Their electrochemical behaviour was studied in a synthetic sweat solution, aiming at selecting a suitable material for biolectrode applications. An increase of the N/Ti atomic ratio, which is accompanied by an increase of the Ag atomic content, leads to a substantial increase of the roughness and porosity of the samples, especially for N/Ti ratios >0.2. For N/Ti atomic ratios up to 0.3 (15 at.% Ag) no metallic Ag segregation is visible in the $TiN_x$ matrix. Hence, the possible formation of TiAg and $Ti_2Ag$ intermetallics or even a Ag/TiAg/$Ti_2Ag$ phase mixture, although not demonstrated, should not be disregarded. As for the N/Ti atomic ratio = 0.7 (32 at.% Ag) sample, the Ag phases are predominantly concentrated near the interface with the substrate. The amount of Ag phases at the surface of the films remains somewhat low for all TiN under-stoichiometric films, even for Ag atomic contents up to 32 at.%. When the $TiN_x$ matrix reaches the stoichiometric condition (sample with N/Ti atomic ratio = 1 and 20 at.% Ag), Ag segregation occurs and metallic Ag aggregates are visible at the surface of the film, leading to a substantially different electrochemical behaviour. The impedance of the $Ag_y$:$TiN_x$ films in synthetic sweat solution is mainly ruled by the roughness/porosity variation, thus the higher the N/Ti atomic ratio, the lower the impedance. The interfacial film/sweat electrochemical noise and drift were similar for all films and comparable to the results obtained for commercial Ag/AgCl electrodes (except for the N/Ti atomic ratio = 1 and 20 at.% Ag film). In view of the results, it may be concluded that the samples with N/Ti atomic ratios = 0.3 (15 at.% Ag) and 0.7 (32 at.% Ag) are the most appropriate for further bioelectrode development.

## 1. INTRODUCTION

Biopotential monitoring of the brain activity (electroencephalography, EEG) is of paramount importance to modern medicine, in order to investigate a wide range of physiological and pathological brain functions or even for brain computer interfaces (BCI) research [1,2]. The Ag/AgCl electrodes [3–5] are considered the most appropriate for signal acquisition, exhibiting an essentially non-polarizable, resistive behaviour, also displaying an excellent reliability and low, almost frequency-independent skin-contact impedance values, in the order of few tens of k$\Omega$ cm$^2$ [4,5]. Unfortunately, these wet electrodes rely on a time-consuming preparation for an optimal electrical (low impedance) contact between the electrode and the skin, which involves the removal of interfering hair and the application of an electrically conductive paste or gel. This long and semi-invasive procedure may cause skin irritation, allergic reactions to the most commonly used gel or pastes, patient discomfort, dirty or damaged hair and limited mobility [4,5].

---

[*] Corresponding author at: Universidade do Porto, Faculdade de Engenharia, Rua Dr. Roberto Frias, s/n, 4200-465, Porto, Portugal. Tel.: +351 225081995.
*E-mail address:* cfonseca@fe.up.pt (C. Fonseca).

http://dx.doi.org/10.1016/j.electacta.2014.12.020
0013-4686/© 2014 Elsevier Ltd. All rights reserved.

In order to obtain an easier, faster and unobtrusive biopotential monitoring process, a new generation of electrodes is being investigated for several years now. The so-called dry electrodes are applied without preliminary skin preparation and gel application [5–7], although at the expense of a considerably higher electrode/skin contact impedance. The electrically conductive materials initially used in dry electrodes were metals such as stainless steel [8] and aluminium [5], but their low corrosion resistance when in contact with the human sweat made them inappropriate. Subsequently, gold [9], metal oxide and nitride coatings like $TiO_2$ or TiN, which are much more resistant to corrosion, have been proposed [6,10–14]. Materials such as graphite [15], conductive silicone or rubber [16] have also been suggested, but these materials also display too high electrical impedances (>500 k$\Omega$ cm$^2$).

In terms of design, the dry electrodes also exhibit concept-specific fundamental problems. Many dry electrode systems [13] display an incorrect and/or uncomfortable skin contact due to the intrinsic stiff nature of the base materials or even because of conceptual problems (rigid planar plates/disks unable to interfuse the hair layer [14,17]). Consequently, several authors have recently focused on the development of textile and polymer-based flexible dry electrodes [16,18–21], since they should be able to promote a more reliable and comfortable skin contact, thus reducing some of the stated drawbacks. Therefore, in opposition to the most common approaches (conductive polymers, composite materials, foams, etc.), the authors recently explored the sputtering viability of $Ag_x$:TiN coatings (with close-stoichiometric TiN) by optimizing their deposition parameters and properties [22,23], architecture [24] and electrochemical behaviour [25] on classic substrates (glass and silicon), so that they can be later sputtered onto flexible polymer-based substrates. Preliminary investigations by the authors demonstrated that the use of flexible polymer electrodes with nanocoatings of electrically conductive $TiN_x$ allowed for comfortable dry EEG recording, providing signal quality comparable to conventional Ag/AgCl wet electrodes [26], although the coatings displayed a low mechanical stability. Silver was then added to TiN in order to tailor several properties of the matrix (e.g. ductility) and the behaviour of the subsequent $Ag_x$:TiN system was investigated by the authors [22,25]. However, it was found that Ag segregates to the surface of the samples (similar phenomena can be found in other Ag-containing systems [27–30]), potentially leading to an unstable skin/electrode interface. The major conclusions of these previous works were focused on the fact that since the TiN matrix exhibited a N/Ti atomic ratio close to 1 (stoichiometric TiN, all Ti interstitial sites should be occupied by nitrogen atoms) [22–25], the un-bonded Ag species aggregate and segregate to the surface of the coating.

In the present work, and in order to try to overcome the upper mentioned Ag segregation, a systematic change of the TiN stoichiometry towards relatively low-N contents was performed by varying the nitrogen flow rate and using a fixed area of Ag exposed (fixed number of Ag pellets) in the Ti/Ag target during the sputtering process. With N/Ti atomic ratios <1, the TiN matrix should become N-deficient [31], thus the occurrence of free Ti is expected, opening the possibility for the formation of TiAg or $Ti_2Ag$ intermetallics, hence inhibiting the referred Ag segregation. This will allow, in a first approach, to take advantage of the interesting properties of both Ag (excellent bioelectrode material, bactericide and high plasticity) and TiN systems (biocompatible, electrically conductive, outstanding chemical stability and mechanical properties) to design a composite biosensing thin film material.

## 2. EXPERIMENTAL DETAILS

### 2.1. Thin film production

$Ag_y$:$TiN_x$ (8 at.% $\leq$ y $\leq$ 32 at.% and x $\leq$ 1) coatings were deposited by reactive DC magnetron sputtering on glass and (1 0 0) silicon substrates, in a custom-made laboratory-sized deposition system. All substrates were sonicated and cleaned with ethanol 96% (vol.) before each deposition. The films were prepared with the substrate holder positioned at 70 mm from the Ti/Ag target. A DC current density of 100 A m$^{-2}$ was applied to the target, composed of titanium (99.96 at.% purity; 200 × 100 × 6 mm) and silver pellets (80 × 80 mm; 1 mm thick pellets glued on the surface of the target) distributed symmetrically along the erosion area. The total surface area of the silver pellets, ~3.2 × 10$^2$ mm$^2$, was maintained throughout all depositions. A mixed gas atmosphere composed of argon + nitrogen was used. The argon flow was kept constant at 60 sccm in all runs, corresponding to a partial pressure of 0.3 Pa. The nitrogen flow rate, which was previously set at 5 sccm – stoichiometric TiN, was successively reduced to 4, 3, 2 and 1 sccm, corresponding to partial pressure values varying from $3.4 \times 10^{-2}$ Pa (5 sccm) to $1.8 \times 10^{-2}$ Pa (1 sccm) [17]. The working pressure was approximately constant during the depositions, varying only slightly between 0.35 and 0.38 Pa. No bias voltage was used, and the deposition temperature was maintained approximately constant at 100 °C during the growth of the films. A thermocouple was placed close to the surface of the substrate holder on the plasma side (not in direct contact, since all depositions were done in rotation mode), and the temperature was monitored during the entire deposition time. Before positioning the surface of the samples in front of the Ti/Ag target, a delay time of five minutes was used in order to avoid contamination resulting from previous depositions, which may have resulted in some target poisoning, and also to assure a practically constant deposition temperature during the growth of the films.

Note that the present $Ag_y$:$TiN_x$ system is being characterized and optimized in traditional substrates (glass and silicon) to facilitate their characterization, but the coatings will be later sputtered onto well-known flexible polymeric substrates (polyurethane, polycarbonate, polyethylene, etc.), so the deposition conditions were chosen in order to be minimally aggressive (no bias voltage and low deposition temperatures were used) in order to avoid future polymeric substrate degradation.

### 2.2. Composition, morphology and structure characterization

The atomic composition (bulk) of the as-deposited samples was measured by Rutherford Backscattering Spectrometry (RBS) with a 1.4 and 2.3 MeV $^{1}H^{+}$ beam and a 2.0 MeV $^{4}He^{+}$ beam. Three detectors were used: one located at a scattering angle of 140° and two pin-diode detectors located symmetrically to each other, both at 165°. Two sample tilt angles, 0° and 30°, were used for the measurements. The composition profiles of the as-deposited samples were obtained using the NDF software [32]. For the $^{14}N$, $^{16}O$ and $^{28}Si$ data, the cross-sections given by Gurbich were used [33]. The area analysed was about 0.5 × 0.5 mm$^2$. The uncertainty in the N concentrations is around 5 at.%. The structure and phase distribution of the coatings were assessed by X-ray diffraction (XRD), using a Bruker AXS Discover D8 diffractometer, operating with Cu K$\alpha$ radiation and in a Bragg–Brentano configuration. The XRD patterns were deconvoluted and fitted with a Pearson VII function to determine the structural characteristics of the films, such as the peak position (2$\theta$), the full width at half maximum (FWHM) and the crystallite size. The SEM/EDS analysis was carried out in a FEI Quanta 400FEG ESEM/EDAX Genesis microscope equipped with X-Ray Microanalysis operating at 15 keV.

**Table 1**
Composition and grain size data of the $Ag_y$:$TiN_x$ thin films.

| Sample name | $N_2$ flow/sccm | [N]/at.% | [Ti]/at.% | [Ag]/at.% | N/Ti ratio | Grain size/nm[a] |
|---|---|---|---|---|---|---|
| ref_TiN0.2 | 1 | 17 | 83 | – | 0.2 | 13 |
| ref_TiN0.85 | 4.5 | 46 | 54 | – | 0.85 | 26 |
| ref_TiN | 5 | 50 | 50 | – | 1 | 39 |
| TiN0.1Ag10 | 1 | 6 | 84 | 10 | 0.1 | 11 |
| TiN0.2Ag8 | 2 | 16 | 76 | 8 | 0.2 | 12 |
| TiN0.3Ag15 | 3 | 18 | 67 | 15 | 0.3 | 11 |
| TiN0.7Ag32 | 4 | 29 | 39 | 32 | 0.7 | 21 |
| TiNAg20 | 5 | 40 | 40 | 20 | 1 | TiN-38 + Ag-10 |
| ref_Ag | – | – | – | 100 | – | 78 |

[a] The maximum variation of the grain size values throughout all simulations was always below 10%.

### 2.3. Electrochemical characterization

The polished glass substrates, coated with the $Ag_y$:$TiN_x$ films were rinsed in isopropanol and water and dried with a hair drier, prior to all electrochemical experiments. In order to take account of the well-known irreproducibility of the thin film systems, a minimum of three measurements (in three different sputtered samples of the same batch) were performed in all electrochemical characterization. A synthetic sweat solution with a pH of 4.7 containing ammonium and sodium chloride, urea, lactic acid and acetic acid was used in all electrochemical studies, in order to simulate the behaviour of the electrode in contact with the body sweat [34]. Cyclic voltammetry (CV) curves were performed at a constant sweep rate of 25 mV/s, using the Gamry G300 equipment (Gamry Instruments, USA) driven by the Gamry PHE200 software. Electrochemical impedance spectroscopy (EIS) studies were performed using the EIS300 software from Gamry at the open circuit potential (OCP), in the potentiostatic mode (7 mV RMS AC signal), for frequencies ranging from 10 kHz to 2 mHz. All experiments were performed using a reference saturated calomel electrode (SCE) and a platinum wire as counter electrode. The simulation of the experimental data was also performed with the Gamry software. The electrochemical noise data was acquired using the ESA410 software from Gamry, by immersing two identical samples (same sputtering batch) in the synthetic sweat solution. Two sintered Ag/AgCl commercial electrodes (B10, EASYCAP GmbH, Germany) were used as comparison reference. A stabilization time of 3 minutes was used in all runs. The results were acquired using a 1000 Hz sampling rate for a period of 12 minutes and then analysed using a custom MatLab (The Mathworks Inc. USA) algorithm. The electrochemical noise analysis was performed by first applying a 20th order Butterworth bandpass filter with cut-off frequencies at 0.5 and 100 Hz. The first 10 s of each filtered data set were neglected to avoid including considerable filter artifact in subsequent evaluations. Then, successive segments of 30 s were considered for the calculation of the RMS values of noise and drift rate, over the total acquisition times. The power spectral density (Welch estimation) was calculated for 12 minutes segments, representative of all the Ag/AgCl commercial electrodes, pure TiN and $Ag_y$:$TiN_x$ sample pairs [17].

## 3. RESULTS AND DISCUSSION

### 3.1. Open Circuit Potential (OCP) and structural characterization

The mixed potential theory suggests that if a material is composed of two electrically connected conductive phases which, in turn, are in contact with an electrolyte, an electric current will flow between them (one phase is the cathode, while the other is the anode, according to the magnitude of their electrochemical potentials) and the resulting OCP (also called mixed potential) should lie between the OCP's of the phases [35].

The OCP evolution of representative sputtered $Ag_y$:$TiN_x$ samples (see Table 1 for the used nomenclature), shown in Fig. 1, was assessed during an immersion period of 2 h in a

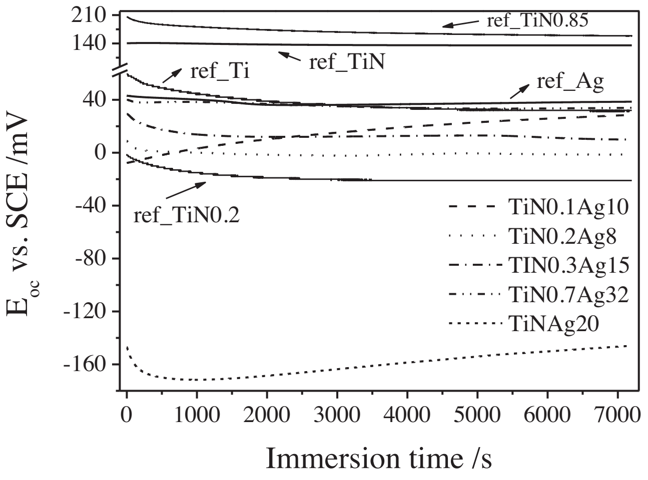

**Fig. 1.** OCP behaviour of the sputtered $Ag_y$:$TiN_x$ samples as function of the immersion time in synthetic sweat. The reference samples ref_Ag, ref_Ti, ref_TiN0.2, ref_TiN0.85 and ref_TiN are shown for comparison purposes. The data referring to the pure Ti and under-stoichiometric $TiN_x$ samples was adapted from ref. [17].

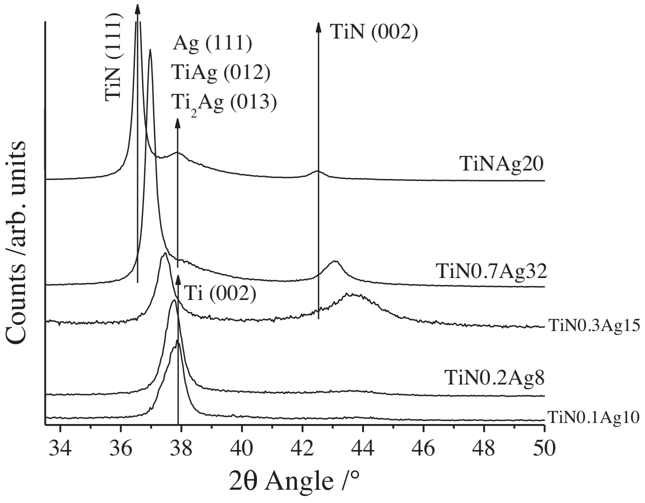

**Fig. 2.** XRD diffractograms of the sputtered $Ag_y$:$TiN_x$ samples. The patterns are presented with different yy axis scales for clarity purposes. The phases were indexed using the ICSD cards #181730 (Ag), #605934 (TiAg), #605935 ($Ti_2$Ag), #181718 (Ti) and #184916 (TiN).

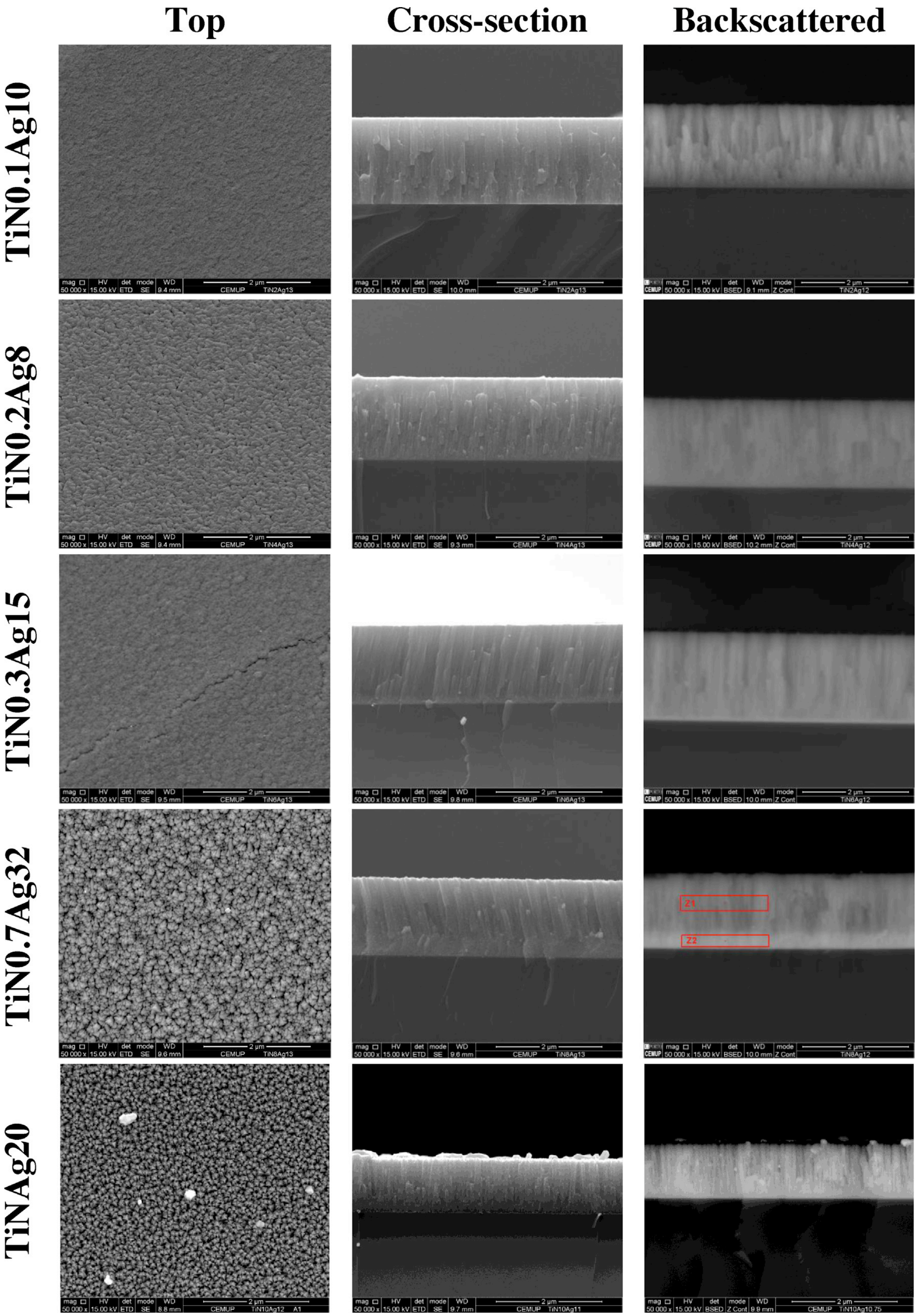

**Fig. 3.** SEM topographic, cross-section and backscattered micrographs of the Ag$_y$:TiN$_x$ samples with different N/Ti atomic ratios.

synthetic sweat solution. All reference samples – ref_Ti, ref_Ag, ref_TiN, ref_TiN0.2 and ref_TiN0.85 coatings – exhibited the expected OCP values: ~40 mV (vs. SCE) for pure Ti and Ag [25,36], while the TiN$_x$ samples displayed OCP values of ~ −20 mV, 160 mV [14] and 140 mV (vs. SCE) [25] for ref_TiN0.2, ref_TiN0.85 and ref_TiN respectively. The potential of Ag indicates the formation of a thin Ag/AgCl film [36] as it was expected from the contact with a chloride-containing medium (synthetic sweat).

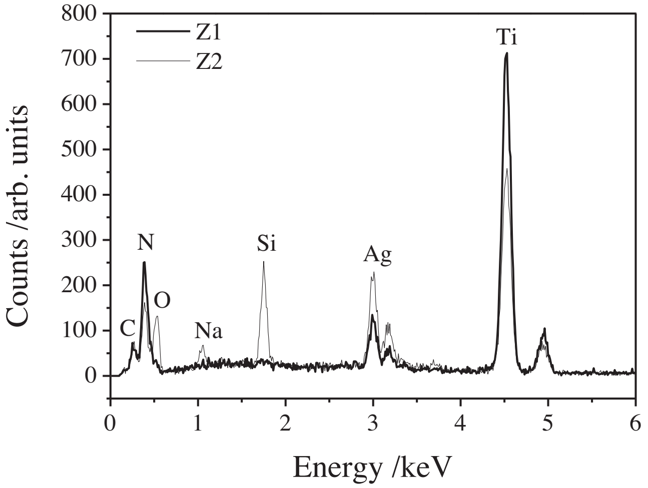

**Fig. 4.** EDS spectra of the TiN0.7Ag32 sample depicting a preferential concentration of Ag phases near the substrate.

The strongly under-stoichiometric ref_TiN0.2 sample displays the least noble OCP value of the $TiN_x$ group, due to the existence of a substantial amount of non-oxidised Ti [17], in opposition to the slightly under-stoichiometric ref_TiN0.85 and stoichiometric ref_TiN reference samples that display the noblest OCP values.

As for the Ag-alloyed TiN samples, $Ag_y$:$TiN_x$, it is apparent that they all exhibit similar OCP values (within the experimental variation among similar samples), lying between −40 and 40 mV, except for the TiNAg20 sample, that shows an OCP value very distinct from the set of under-stoichiometric samples. In order to help explaining these results, the authors performed a Ti/Ag galvanic coupling experiment using reference Ti and Ag samples that were immersed in synthetic sweat, following a procedure similar to that used in reference [25] for the TiN/Ag couple (results not shown). Similarly to that experiment, a mixed potential value close to that of Ag was found, showing that the mixed potential is ruled by the OCP of Ag in both cases. However, for some of the compositions of the $Ag_x$:TiN system studied in reference [25] the OCP was shown to be far below that of Ag or TiN reference values. This was demonstrated to be due to the presence of nanograined, highly reactive Ag aggregates.

An additional insight to explain the behaviour of these samples comes from their structural evolution, Fig. 2. For the $Ag_yTiN_x$ samples with low N/Ti atomic ratios (0.1, 0.2 and 0.3), the XRD patterns are consistent with a N-doped Ti matrix [31], with some Ag atoms probably forming TiAg or $Ti_2Ag$ intermetallics [37]. The low nitrogen contents inhibit the formation of any type of nitride phase, meaning that the matrix of these low N/Ti atomic ratio samples should be mainly composed of pure Ti. The SEM analysis, shown in Fig. 3, seems to be consistent with this claim, since a rather dense and granular Ti-like morphology is evident in these samples. Furthermore, despite the exhibited Ag atomic contents of 8–15 at.%, no Ag phases or metallic aggregates were detected in the XRD and SEM analysis of these 0.1, 0.2 and 0.3 N/Ti atomic ratio samples (Figs. 2 and 3), which may also support the idea that the formation of amorphous (thus not detected in the XRD analysis) TiAg or $Ti_2Ag$ intermetallics (or phase mixture of both) should not be disregarded.

As for the TiN0.7Ag32 sample, the XRD patterns appear to indicate the existence of a transition zone, since a fully formed N-deficient TiN matrix is already evident. A single Ag phase might also be formed, as it can be evidenced by the pronounced tail of the TiN (111) peak at about 38° and by the higher Ag content exhibited by this sample, see Fig. 2 and Table 1. However, due to the fact that the Ag, TiAg and $Ti_2Ag$ phases all occur at approximately the same diffraction angle (38°), and no metallic Ag aggregates can be seen in SEM imaging, a clear differentiation between Ag and its titanium intermetallics is rather difficult. Once more, the morphological characterization is consistent with these findings, since the formation of the typical disaggregated pyramid-like TiN columns is now evident, as seen in Fig. 3. Similarly to the low N/Ti atomic ratio samples, no metallic Ag aggregates can be seen on the surface of the film or even among the intercolumnar spacing. This can be, once more, an indication of the probable formation of TiAg or $Ti_2Ag$ intermetallics. Moreover, the formed Ag phases are not evenly distributed across the TiN matrix (see Fig. 3 backscattered image). Instead, these Ag phases appear to be mainly concentrated in a small band near the substrate, as it was proved by the EDS analysis, shown in Fig. 4, performed near the surface (Z1) and the substrate (Z2). Since in this sample the TiN matrix is still quite dense, it is probably acting as an Ag diffusion barrier, preventing the Ag phases from diffusing to the surface, where they would have a lower energy, in opposition to what is visible in the stoichiometric (porous) one, see Fig. 3. In this case Ag may be using the intercolumnar spacing to diffuse towards the surface, a fact that was previously observed by the authors [23]. Therefore, as for the other under-stoichiometric samples (N/Ti atomic ratios $\leq$0.3), a low Ag concentration at the film/electrolyte interface is also expected in this case. Hence, the stoichiometric TiNAg20 sample is the only one where the presence of metallic Ag aggregates can be clearly identified at the surface of the film, thus possibly excluding the formation of TiAg or $Ti_2Ag$ intermetallics.

Finally, since a galvanic coupling between the phases present in the $Ag_yTiN_x$ composites should exist at the film/electrolyte interface, the Evans diagram must also be considered. As no Ag (or Ag phase) was detected at the films surfaces, it will be hypothesized that only a residual amount of Ag should exist and, owing to the broad XRD Ag-related peaks, such Ag (or $Ti_xAg$) will be in the form of nanograins, hence with a potential anodic to that of the $TiN_x$ matrix [25]. Thus, the relevant redox processes in the (simplified) Evans diagram will be Ag oxidation to AgCl, while the reduction process will take place on the $TiN_x$ surface, see Fig. 5. To note that the Ag/AgCl redox process displays a fast kinetics, with an exchange current ($i_0$) of about 0.13 mA/cm$^2$ [38], while the oxidation processes occurring on the $TiN_x$ surface (could even be $Ag^+$ reduction) should occur with a substantially slower kinetics and lower exchange current [14]. According with this figure, if the amount of surface Ag is low, the associated current will be small and the mixed potential (OCP of the composite) should be closer to the OCP of the $TiN_x$ phase, Fig. 5, line 1. This should be the case for all the N/Ti under-stoichiomeric samples (TiN0.1Ag10, TiN0.2Ag8, TiN0.3Ag15 and TiN0.7Ag32). On the other hand, as soon as the

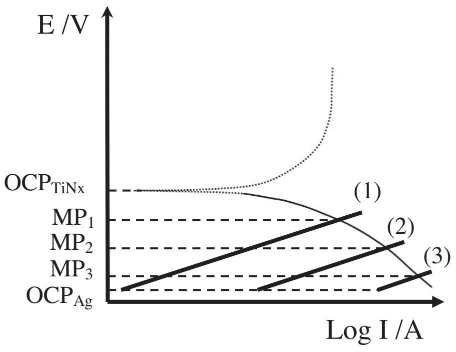

**Fig. 5.** Schematic Evans diagram depicting the effect of the Ag electroactive area (area increasing from 1 to 3) on the $TiN_x$/Ag galvanic coupling behaviour. Adapted from ref. [35].

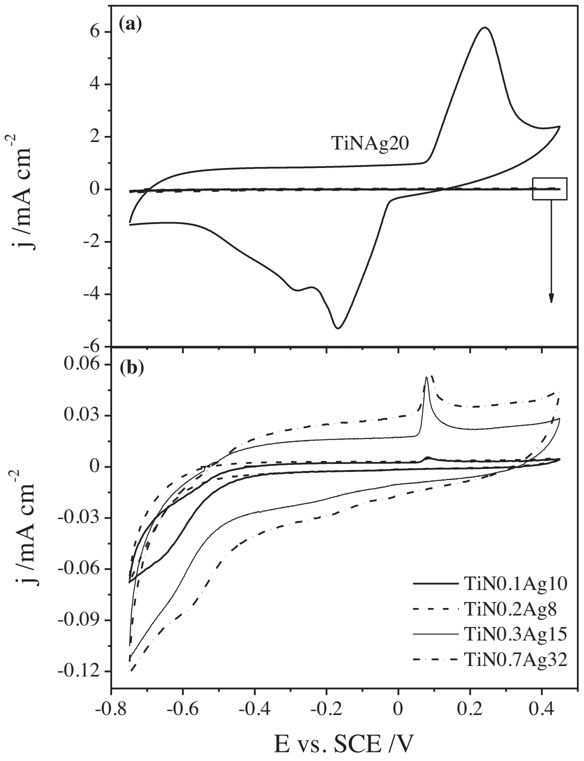

**Fig. 6.** Cyclic voltammograms of (a) the sputtered $Ag_y$:$TiN_x$ samples and (b) magnification showing the behaviour of the under-stoichiometric samples. The used sweep rate was 25 mV/s.

amount of surface Ag increases the Tafel line shifts to the right (higher currents, lines 2 and 3), originating a more anodic OCP value, closer to that of Ag (or Ag phases). This explains the strongly anodic OCP value (−150 mV) observed for the TiNAg20 sample, where the presence of high amounts of nanograined Ag at the film/electrolyte interface was clearly demonstrated (see Figs. 2 and 3).

To summarize, the samples obtained with low N/Ti atomic ratios (0.1, 0.2 and 0.3) exhibit a nitrogen-doped Ti matrix with the probable formation of TiAg or $Ti_2Ag$ intermetallics [37]. The small amount of Ag at the film/electrolyte interface explains the OCP behaviour, which is close to that of the under-stoichiometric $TiN_x$ matrix. When a N-deficient $TiN_x$ matrix appears to be formed, as in the TiN0.7Ag32 sample, the OCP behaviour is also dictated by the $TiN_x$ matrix, but with slightly nobler values than those of the former samples (less free titanium). Contrarily, the sample obtained with the highest N/Ti atomic ratio, TiNAg20, possesses a stoichiometric TiN matrix, with a considerable amount of metallic Ag aggregates in contact with the electrolyte. In this case, the highly reactive polycrystalline Ag [39] shifts the OCP to less noble potentials.

### *3.2. Potentiodynamic behaviour*

The electrochemical behaviour of the $Ag_y$:$TiN_x$ samples was further studied by performing a set of voltammetric experiments at a constant sweep rate of 25 mV/s, Fig. 6. Similarly to what was found in the OCP characterization, the stoichiometric sample (TiNAg20) exhibits a distinct behaviour (Fig. 6a) when compared to the under-stoichiometric ones (Fig. 6b), the first displaying considerably higher currents. Taking into account the anodic curve, all samples exhibit a sharp anodic peak, which depicts the formation of an AgCl layer [40–43]. However, the magnitude of the anodic peak current varies from 6–60 μA for the under-stoichiometric samples, until 6 mA for the stoichiometric one. This increase of the anodic current results in a shift of the anodic peak position, which is related with the Ohmic drop that occurs through the formed AgCl film (the higher the charge involved the thicker the film and the larger the potential shift) [43]. Note that the small current peaks observed for the under-stoichiometric samples indicate the presence of trace amounts of Ag at the surface of the film, in agreement with the analysis of the OCP results. Similar current variations are observed in the cathodic region.

The current changes in the voltammograms should be attributed to morphological and chemical alterations of the sputtered samples, namely to their roughness and porosity, that change the sample area in contact with the electrolyte (base current, capacitive), and to the surface Ag content, which is responsible for the magnitude of the peak current (Faradic current). As it is possible to see from Fig. 3, the $Ag_y$:$TiN_x$ samples with low N/Ti atomic ratios (TiN0.1Ag10 and TiN0.2Ag8) are quite compact, since their matrix is mainly composed of titanium, and show similar Ag contents. Hence, there are practically no major differences in terms of the exhibited voltammetric behaviour. Then, with further increase of the N/Ti atomic ratio from 0.3 to 0.7, major changes are noticeable. The intergranular porosity increases for the TiN0.3Ag15 sample, due to the formation of long and continuous intergranular cracks, besides the increase of the columnar definition, as it can be seen in the cross-section micrograph, Fig. 3. This and the increase of the Ag content from 10 to 15 at.% lead to an overall increase of the base current and the peak current, respectively. However, it is important to note that the increase of Ag incorporation from 15 to 32 at.% does not translate into a significant increase of the peak current (~52 μA in both samples), which confirms, as stated in section 3.1., that the Ag phases mainly concentrated near the substrate should be

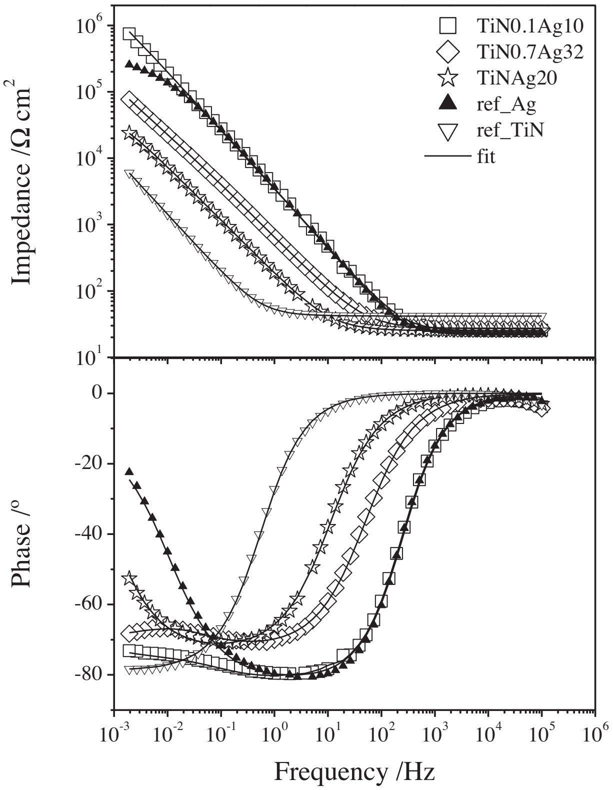

**Fig. 7.** Bode diagram of representative as-deposited $Ag_y$:$TiN_x$ samples. Pure stoichiometric TiN and Ag samples are plotted for comparison purposes. The impedance values are referred to the geometrical area, which is similar for all samples.

inaccessible to the electrolyte, thus not being able to participate in the redox process. On the other hand, the higher base current of the TiN0.7Ag32 sample (27.9 μA vs. 17.3 μA for the TiN0.3Ag15 sample) indicates a higher specific area, confirming the results patent in Fig. 3. From the integration of the anodic peaks of both samples, TiN0.3Ag15 and TiN0.7Ag32, negligible charge differences were found (55 μC vs. 48 μC), indicating that the amount of Ag species in contact with the electrolyte should be roughly the same in both samples.

When the N/Ti atomic ratio stoichiometry is achieved, as in the TiNAg20 sample, a fully pyramid-like columnar morphology is attained. The intercolumnar disaggregation/spacing is also steeply increased, thus facilitating the segregation of the metallic Ag grains visible at the surface of this sample (see Fig. 3) and allowing their effective contact with the electrolyte. The combined effects of a highly porous and disaggregated TiN matrix and the low grain size of the metallic Ag aggregates now available at the interface with the electrolyte, significantly increase the electroactive area. Hence, an almost 100 fold increase of the anodic peak current (from 0.06 to 6 mA) occurs when the N/Ti atomic ratio increases from 0.7 to 1, despite the total Ag concentration being slightly lower (20 at.% vs. 32 at.%).

These results confirm the hypothesis developed to justify the OCP values of the composites that the amount of surface Ag is only expressive for the TiN stoichiometric sample, in spite of the amounts of Ag quantified for the $TiN_x$ under-stoichiometric composites (between 8% and 32%).

### 3.3. Electrochemical Impedance Spectroscopy (EIS) analysis

The Bode spectra of representative as-deposited $Ag_y$:$TiN_x$ samples, as well as the ref_Ag and ref_TiN reference coatings, are shown in Fig. 7. Note that the data that refers to the TiN0.2Ag8 and TiN0.3Ag15 samples is not plotted for clarity purposes, since their impedance spectra are partially overlaid with those of TiN0.1Ag10 and TiN0.7Ag32, respectively. As in the previous sections, two factors seem to be determining the observed impedance moduli, namely the real exposed area and the amount of available Ag at the film/electrolyte interface. Knowing that the geometrical area exposed to the solution is similar for all samples, the ones that exhibited the highest impedance moduli values ($\sim 10^6\,\Omega\,cm^2$ at 2 mHz) were those that displayed the smoother and more compact structures, as well as the lower amounts of Ag in contact with the electrolyte, namely the TiN0.1Ag10 and TiN0.2Ag8 samples. The TiN0.3Ag15 and TiN0.7Ag32 samples present lower impedance values $\sim 10^5\,\Omega\,cm^2$ at 2 mHz), in agreement with the observed higher specific area, Fig. 3. The Ag content seems not to be determinant for the impedance values.

The sample with the highest specific area and Ag availability to the electrolyte – TiNAg20 – exhibits the lowest impedance modulus value ($\sim 2 \times 10^4\,\Omega\,cm^2$ at 2 mHz) of all $Ag_y$:$TiN_x$ sputtered samples. Note that for frequencies between 1 and 50 Hz (EEG frequency range), all $Ag_y$:$TiN_x$ samples display impedance moduli values $< 10\,k\Omega\,cm^2$, below the typical impedance of the dry electrode/skin interface, attesting their suitability to be used as bioelectrodes from the impedance point of view [44–46].

A visual analysis of the phase vs frequency spectra allows to conclude that the equivalent circuit of ref_TiN, ref_Ag and TiNAg20 films seem to display a single time constant. However, more complex curves appear for decreasing N/Ti atomic ratios (TiN0.1Ag10 and TiN0.7Ag32). In order to simulate the electrical behaviour of the films in contact with sweat, the circuit depicted in Fig. 8 a) was used. Constant phase elements ($CPE_{i-k}$) were used to account for roughness and/or other surface/film inhomogeneities or relaxation processes [48,51]. The impedance of a CPE was defined by the following relationship:

$$Z_{CPE} = 1/[T(j\omega)^p] \tag{1}$$

with “T” and “p” as the CPE parameters, and ω as the angular frequency [44,47]. $R_e$ represents the electrolyte resistance and the upper and lower branches in the parallel circuit stand for the non-Faradic and Faradic processes. In the non-Faradic branch, the $CPE_i$ element was used in order to simulate the series combination of the double-layer and film capacitive behaviour at the film/electrolyte interface. The resistance to electronic charge transfer was not considered since the OCP of the sputtered samples are within the water stability region. In the lower Faradic branch, the ($CPE_k$, $R_p$) parallel combination was used to simulate the interfacial capacitance and polarization resistance of the samples and $CPE_j$ was used to take account of the ionic diffusion processes occurring within the film. In the first trials a Warburg element was used but it was concluded that the quality of the fits improved significantly if the “p” value was left unconstrained. The physical meaning of this variation will be later discussed. This circuit (Fig. 8a) was effective in simulating all parameters except for the $CPE_k$, whose values were in the nF range and were obtained with large errors. Consequently, this element was removed from the circuit without compromising the quality of the fits, giving rise

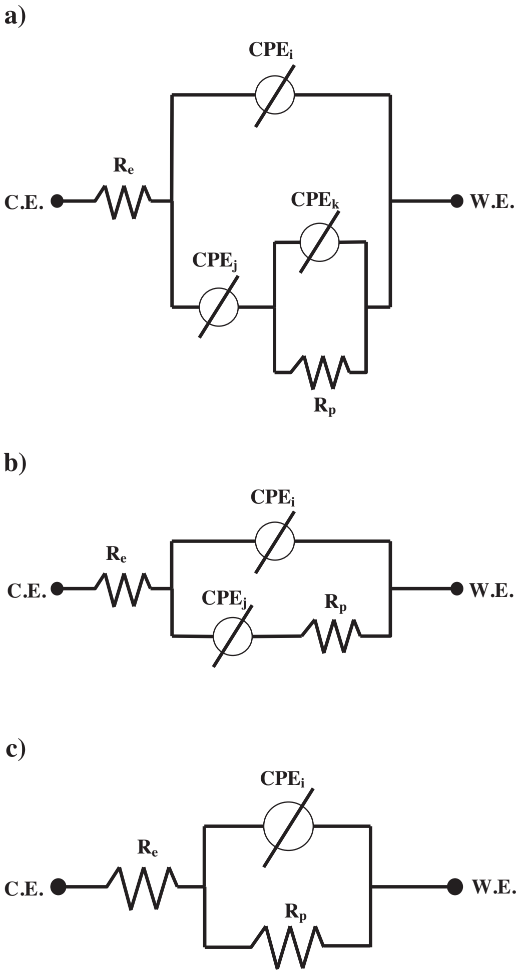

**Fig. 8.** Equivalent electric circuits proposed for the simulation of the $Ag_y$:$TiN_x$/synthetic sweat interface. (a) general model, (b) simplified model used for the simulation of the under-stoichiometric $Ag_y$:$TiN_x$/synthetic sweat interface and (c) simplified model used for the fitting of the ref_TiN, ref_Ag and stoichiometric $Ag_y$:$TiN_x$/synthetic sweat interface.

**Table 2**
ESI fit parameters.

| Sample name | $R_p/\Omega\,cm^2$ | $R_e/\Omega\,cm^2$ | $CPE_i$ (T)/$\Omega^{-1}\,cm^{-2}\,s^n$ | $CPE_i$ (P) | $CPE_j$ (T)/$\Omega^{-1}\,cm^{-2}\,s^n$ | $CPE_j$ (P) | $\chi^2$ |
|---|---|---|---|---|---|---|---|
| ref_TiN1 | $\geq 3 \times 10^6$ | 41.9 | $7.9 \times 10^{-3}$ | 0.87 | – | – | $2 \times 10^{-4}$ |
| TiN0.1Ag10 | $1.5 \times 10^5$ | 25.3 | $5.2 \times 10^{-5}$ | 0.91 | $7.9 \times 10^{-6}$ | 0.64 | $6 \times 10^{-4}$ |
| TiN0.2Ag8 | $2.6 \times 10^5$ | 24.9 | $6.9 \times 10^{-5}$ | 0.91 | $6.6 \times 10^{-6}$ | 0.46 | $2 \times 10^{-4}$ |
| TiN0.3Ag15 | $8.5 \times 10^4$ | 27.4 | $2.7 \times 10^{-4}$ | 0.84 | $2.2 \times 10^{-5}$ | 0.59 | $3 \times 10^{-4}$ |
| TiN0.7Ag32 | $6.8 \times 10^4$ | 27.0 | $3.5 \times 10^{-4}$ | 0.81 | $8.2 \times 10^{-5}$ | 0.72 | $3 \times 10^{-4}$ |
| TiN1Ag20 | $6.2 \times 10^4$ | 25.2 | $1.3 \times 10^{-3}$ | 0.81 | – | – | $6 \times 10^{-4}$ |
| ref_Ag | $2.5 \times 10^5$ | 23.2 | $5.7 \times 10^{-5}$ | 0.89 | – | – | $3 \times 10^{-3}$ |

to the modified Randles circuit depicted in Fig. 8b). This simplified circuit was used to simulate the behaviour of all under-stoichiometric $Ag_y$:$TiN_x$ coatings (N/Ti atomic ratios from 0.1 to 0.7). For the ref_TiN and ref_Ag samples, as well as for TiNAg20, the diffusion impedance proved not to be necessary, thus the simplified circuit patent in Fig. 8c) was successfully used, as predicted above. The disappearance of the ionic diffusion impedance component is not surprising owing to the strong columnar disaggregation underwent by these films.

The EIS fit parameters are presented in Table 2 and the simulated curves can be seen in Fig. 7. The $R_p$ value for the ref_TiN sample was adapted from a previous work by the authors [25]. The $R_p$ evolution with the N/Ti atomic ratio increase for the $Ag_y$:$TiN_x$ samples should be ascribed, as explained, to the combined effects of the increase of surface area and Ag content in contact with the electrolyte. The area increase is also reflected in the evolution of $T_i$. The $T_j$ parameter takes account of the ionic diffusion within the film. In fact, pure TiN is well known for its ionic diffusion blocking characteristics [14,17]. The increase of the $T_j$ with the increase of the N/Ti atomic ratio (and Ag content) may be connected either to an increase of the sample area or to a decrease of the diffusion impedance, due to intergranular cracking and column disaggregation, Fig. 3.

Finally, it was noticed that the quality of the fits significantly improved if the "$p_j$" parameter was left unconstrained. This case is taken into account in the generalized diffusion model proposed by McDonald [48]. In this model, McDonald attributes the shifts from the $p = 0.5$ value to non-uniform diffusion. Non-uniform diffusion arises, for example, when the diffusion coefficient is a function of distance and may take place in materials with some degree of inhomogeneity. Since the studied films are columnar-like and it was demonstrated that the Ag phases are not evenly distributed inside the films, it can be hypothesised that there should be a direction-dependent ionic diffusion coefficient that is responsible for the observed non-uniform diffusion.

In conclusion, from the impedance point of view (and excluding the TiNAg20 sample, which was considered unsuitable to be used as biopotential electrodes due to its poor structural stability), the TiN0.3Ag15 and TiN0.7Ag32 samples display the lowest impedance values of all sputtered $Ag_y$:$TiN_x$ films. On the other hand, the possible formation of TiAg or $Ti_2Ag$ intermetallics may ensure that these composites will remain stable (no Ag segregation was noticeable after 2 months). Therefore, these would probably be the most appropriate compositions to develop the novel bioelectrodes.

### 3.4. Electrical noise and drift rate measurements

The study of the electrical noise in the frequency region of interest for the envisaged application in EEG is of paramount importance in order to assess the suitability of the developed $Ag_y$:$TiN_x$ systems to be used as bioelectrodes. Signal distortion caused by electrical noise addition to the monitored biopotential [49–52], coming from the contact of the electrode with a sweat layer and related with eventual corrosion processes, should be avoided. With that purpose, the power spectral density (PSD) of representative $Ag_y$:$TiN_x$ couples of identical samples in synthetic sweat is patent in Fig. 9. As expected [49], the noise values follow the 1/(freq.) law, commonly associated to slow corroding systems [53], increasing as the frequency decreases. In the lower frequency range for most EEG exams–approximately 1 Hz – the sputtered samples exhibit similar noise values, always between ~0.48 and ~0.55 $\mu V/\sqrt{Hz}$, despite the significant morphological and structural differences

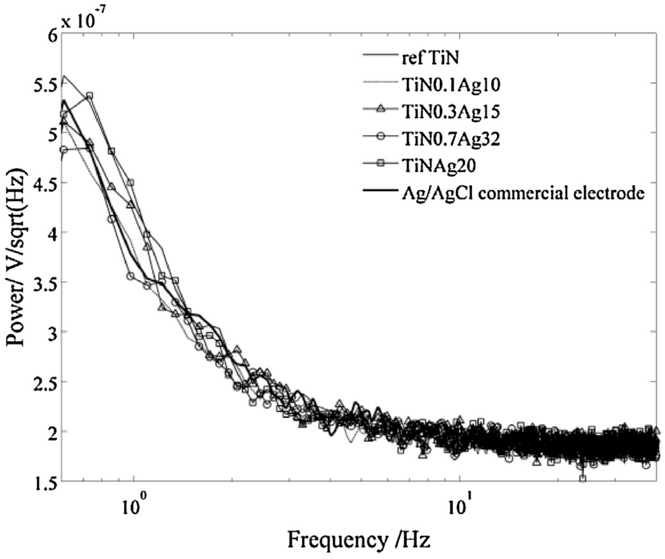

**Fig. 9.** Noise spectra for stoichiometric TiN reference and $Ag_y$:$TiN_x$ samples. Ag/AgCl commercial electrode data is presented for comparison purposes.

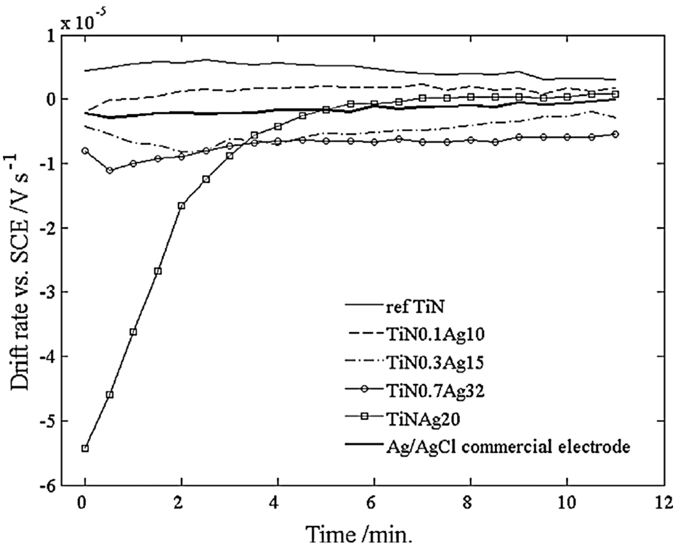

**Fig. 10.** Electrochemical potential drift rate of the stoichiometric TiN reference and $Ag_y$:$TiN_x$ samples. Ag/AgCl commercial electrode data is plotted as comparison.

(Fig. 3). When comparing with the reference Ag/AgCl commercial electrodes, it is possible to see that the noise values are similar to those of the sputtered $Ag_y$:$TiN_x$ samples.

Furthermore, fast stabilization times and reduced drift rates are essential in order to avoid unwanted masking of the low frequency and/or small amplitude biosignals [17]. Fig. 10 depicts the drift rate evolution of the $Ag_y$:$TiN_x$ samples during the 12 minutes immersion time used for the noise characterization. Most samples exhibit low drift rates and fast stabilization times, close to the ones observed for the commercial Ag/AgCl electrode, except for the TiNAg20 sample, what may be related with the presence of reactive nanograined Ag aggregates. The unstable nature of the TiNAg20 sample drift rate makes it unsuitable to be used in bioelectrode applications.

To sum up, the noise added by the $Ag_y$:$TiN_x$/sweat interfaces, as well as the drift rate behaviour do not limit their use as bioelectrodes, namely for the TiN0.3Ag15 and TiN0.7Ag32 samples which seem to be the best candidates for the development of the new bioelectrodes from the electrochemical point of view.

## 4. CONCLUSIONS

In the present study, a set of $Ag_y$:$TiN_x$ coatings were sputtered with increasing N/Ti atomic ratios, ranging from 0.1–0.7 (under-stoichiometric) to 1 (stoichiometric) and Ag contents (8–32%), with the ultimate objective of reducing the Ag segregation and film instability phenomenon observed in previous works by the authors. The obtained thin films were studied regarding the influence of the TiN matrix stoichiometry and Ag content changes on their electrochemical behaviour, aiming their use as bioelectrodes.

The mixed potential behaviour of the TiN0.1Ag10 and TiN0.2Ag8 samples seems to be dictated by the OCP of the $TiN_x$ matrix, due to the residual amounts of interfacial Ag. The TiN0.7Ag32 sample, in turn, exhibits coherent Ag phases, but those phases are mainly confined to the interface with the substrate and, again, the mixed potential is ruled by the OCP of the $TiN_x$ matrix. When a fully formed stoichiometric TiN matrix is attained (TiNAg20 sample), the OCP values suffer a steep drop from $\sim$40 to $\sim -160$ mV, far from the ref_Ag and ref_TiN own OCP. It was concluded that the $TiN_x$/Ag mixed potential is now controlled by the highly reactive metallic Ag nanograins extensively present at the film/electrolyte interface.

The porosity of the samples (thus also their electroactive area) and Ag availability to be in contact with the electrolyte increases with increasing N/Ti atomic ratios, leading firstly to a 10-fold increase of the exhibited anodic/cathodic currents (from 6 to 60 $\mu$A) for the TiN0.7Ag32 sample voltammograms. Then, for the stoichiometric TiNAg20 sample, a steep (100-fold) increase from 60 $\mu$A to 6 mA is noticeable. The EIS data is consistent with the observed structural morphological and chemical changes, with the samples exhibiting lower impedances and $R_p$ values with increasing N/Ti atomic ratios and Ag contents, due to the observed enhanced porosity/electroactive area.

The most promising $Ag_y$:$TiN_x$ films for bioelectrode fabrication should be the TiN0.3Ag15 and TiN0.7Ag32 ones, due to their structural stability, low impedance values (of the order of those of pure Ag) and low noise and drift rate values (of the order of what was observed for commercial Ag/AgCl electrodes).

## ACKNOWLEDGEMENTS

This research is partially sponsored by FEDER funds through the program COMPETE - Programa Operacional Factores de Competitividade and by national funds through FCT - Fundação para a Ciência e a Tecnologia, under the projects PEst-C/EME/UI0285/2011, PTDC/SAU-ENB/116850/2010, PTDC/CTM-NAN/112574/2009 and Programa Pessoa 2012/2013 Cooperação Portugal/França, Project no. 27306UA Porous architectures in GRAded CERamic thin films for biosensors – GRACER. The authors would also like to acknowledge CEMUP for SEM analysis. P. Pedrosa acknowledges FCT for the Ph.D. grant SFRH/BD/70035/2010.

## References

[1] Z. Iscan, Z. Dokur, “A novel steady-state visually evoked potential-based brain–computer interface design: Character Plotter”, Biomed. Signal Proces. 10 (2014) 145–152, doi:http://dx.doi.org/10.1016/j.bspc.2013.11.009.

[2] F. Akram, H.-S. Han, T.-S. Kim, “A P300-based brain computer interface system for words typing”, Comput. Biol. Med. 45 (2014) 118–125, doi:http://dx.doi.org/10.1016/j.compbiomed.2013.12.001.

[3] M. Teplan, “Fundamentals of EEG measurement”, Meas. Sci. Rev. 2 (2) (2002) 1–11.

[4] E. McAdams, “Bioelectrodes”, in Encyclopaedia of Medical Devices and Instrumentation, in: J.G. Webster (Ed.), New York, Wiley, 1988, pp. 120–166, doi:http://dx.doi.org/10.1002/0471732877.

[5] A. Searle, L. Kirkup, “A direct comparison of wet, dry and insulating bioelectric recording electrodes”, Physiol. Meas. 22 (2000) 271–283, doi:http://dx.doi.org/10.1088/0967-3334/21/2/307.

[6] B.A. -Taheri, R.T. Knight, R.L. Smith, “A dry electrode for EEG recording”, Electroen. Clin. Neuro 90 (1994) 376–383, doi:http://dx.doi.org/10.1016/0013-4694(94)90053-1.

[7] P. Brunner, L. Bianchi, C. Guger, F. Cincotti, G. Schalk, “Current trends in hardware and software for brain–computer interfaces (BCIs)”, J. Neural Eng. 8 (2011) 025001, doi:http://dx.doi.org/10.1088/1741-2560/8/2/025001.

[8] E.S. Valchinov, N.E. Pallikarakis, “An active electrode for biopotential recording from small localized bio-sources”, Biomed. Eng. OnLine 3 (2004) 25–39, doi: http://dx.doi.org/10.1186/1475-925X-3-25.

[9] A.C. Metting Van Rijn, A.P. Kuiper, T.E. Dankers, C.A. Grimbergen, “Low-cost active electrode improves the resolution in biopotential recordings”, Proc. IEEE EMBC 18 (1996) 101–102.

[10] R.T. B.A.-Taheri, Knight, R.L. Smith, “An active, microfabricated, scalp electrode array for EEG recording”, Sens Actuat. A 54 (1996) 606–611, doi:http://dx.doi.org/10.1016/S0924-4247(97)80023-4.

[11] N.S. Dias, J.P. Carmo, A.F. da Silva, P.M. Mendes, J.H. Correia, “New dry electrodes based on iridium oxide (IrO) for non-invasive biopotential recordings and stimulation”, Sens. Actuat. A 164 (2010) 28–34, doi:http://dx.doi.org/10.1016/j.sna.2010.09.016.

[12] P. Fiedler, L.T. Cunha, P. Pedrosa, S. Brodkorb, C. Fonseca, F. Vaz, J. Haueisen, “Novel $TiN_x$-based biosignal electrodes for electroencephalography”, Meas. Sci. Technol. 22 (2011) 124007, doi:http://dx.doi.org/10.1088/0957-0233/22/12/124007.

[13] C. Fonseca, J.P. Silva Cunha, R.E. Martins, V. Ferreira, J.P. Marques de Sá, M.A. Barbosa, A. Martins Silva, “A novel dry active electrode for EEG recording”, IEEE Trans. Biomed. Eng. 54 (1) (2007) 162–165, doi:http://dx.doi.org/10.1109/TBME.2006.884649.

[14] L.T. Cunha, P. Pedrosa, C.J. Tavares, E. Alves, F. Vaz, C. Fonseca, “The role of composition, morphology and crystalline structure in the electrochemical behaviour of $TiN_x$ thin films for dry electrode sensor materials”, Electrochim. Acta 55 (1) (2009) 59–67, doi:http://dx.doi.org/10.1016/j.electacta.2009.08.004.

[15] M. Negishi, M. Abildgaard, I. Laufer, T. Nixon, R.T. Constable, “An EEG (electroencephalogram) recording system with carbon wire electrodes for simultaneous EEG-fMRI (functional magnetic resonance imaging) recording”, J. Neurosci. Meth. 173 (2008) 99–107, doi:http://dx.doi.org/10.1016/j.jneumeth.2008.05.024.

[16] G. Gargiulo, R.A. Calvo, P. Bifulco, M. Cesarelli, C. Jin, A. Mohamed, A. van Schaik, “A new EEG recording system for passive dry electrodes”, Clin. Neurophysiol. 121 (5) (2010) 686–693, doi:http://dx.doi.org/10.1016/j.clinph.2009.12.025.

[17] P. Pedrosa, E. Alves, N.P. Barradas, P. Fiedler, J. Haueisen, F. Vaz, C. Fonseca, “$TiN_x$ coated polycarbonate for bio-electrode applications”, Corros. Sci. 56 (2012) 49–57, doi:http://dx.doi.org/10.1016/j.corsci.2011.11.008.

[18] R. Hoffmann, K.-P. Ruff, “Flexible Dry Surface-electrodes for ECG Long-term Monitoring”, Proceedings of the 29th Annual International Conference of the IEEE EMBS, Lyon, France, August, 2007, pp. 23–26.

[19] J. Baek, J. An, J. Choi, K. Park, S. Lee, “Flexible polymeric dry electrodes for the long-term monitoring of ECG”, Sens. Actuators A. 143 (2008) 423–429, doi: http://dx.doi.org/10.1016/j.sna.2007.11.019.

[20] A. Gruetzmann, S. Hansen, J. Muller, “Novel dry electrodes for ECG monitoring”, Physiol. Meas. 28 (2007) 1375–1390, doi:http://dx.doi.org/10.1088/0967-3334/28/11/005.

[21] V. Marozas, A. Petrenas, S. Daukantas, A. Lukosevicius, “A comparison of conductive textile-based and silver/silver chloride gel electrodes in exercise electrocardiogram recordings”, J. Electrocardiology 44 (2011) 189–194, doi: http://dx.doi.org/10.1016/j.jelectrocard.2010.12.004.

[22] P. Pedrosa, D. Machado, C. Lopes, E. Alves, N.P. Barradas, N. Martin, F. Macedo, C. Fonseca, F. Vaz, “Nanocomposite Ag:TiN thin films for dry biopotential

electrodes", Appl. Surf. Sci. 285P (2013) 40–48, doi:http://dx.doi.org/10.1016/j.apsusc.2013.07.154.
[23] P. Pedrosa, D. Machado, M. Evaristo, A. Cavaleiro, C. Fonseca, F. Vaz, "Ag:TiN nanocomposite thin films for bioelectrodes: The effect of annealing treatments on the electrical and mechanical behavior", J. Vac. Sci. Technol. A 32 (2014) 031515, doi:http://dx.doi.org/10.1116/1.4873555.
[24] P. Pedrosa, C. Lopes, N. Martin, C. Fonseca, F. Vaz, "Electrical characterization of Ag:TiN thin films produced by glancing angle deposition", Materials Letters 115 (2014) 136–139, doi:http://dx.doi.org/10.1016/j.matlet.2013.10.044.
[25] P. Pedrosa, E. Alves, N.P. Barradas, N. Martin, P. Fiedler, J. Haueisen, F. Vaz, C. Fonseca, "Electrochemical behaviour of nanocomposite Agx:TiN thin filmsfor dry biopotential electrodes", Electrochim. Acta. 125 (2014) 48–57, doi:http://dx.doi.org/10.1016/j.electacta.2014.01.082.
[26] P. Fiedler, P. Pedrosa, S. Griebel, C. Fonseca, F. Vaz, F. Zanow, J. Haueisen, "Novel flexible dry PU/TiN-Multipin electrodes: First application in EEG measurements", Proc. IEEE EMBS 33 (2011) 55–58, doi:http://dx.doi.org/10.1109/IEMBS.2011.6089895.
[27] J.H. Hsieh, C.H. Chiu, C. Li, W. Wu, S.Y. Chang, "Development of anti-wear and anti-bacteria TaN-(Ag,Cu) thin films – a review", Surf. & Coat. Technol. 233 (2013) 159–168, doi:http://dx.doi.org/10.1016/j.surfcoat.2013.05.013.
[28] H.K. Lee, R.W. Hyland Jr., H.I. Aaronson, P.P. Wynblatt, "Surface segregation in an Al–4.2 at% Ag alloy", Surf. Sci. 408 (1998) 288–299, doi:http://dx.doi.org/10.1016/S0039-6028(98)00254-4.
[29] R.A. Manzhos, A.G. Krivenko, S.V. Doronin, M.A. Choba, V.A. Safonov, "Surface segregation of silver atoms on Au–Ag alloys according to data of laser-heating induced temperature potential shifts, XPS and conventional electrochemical methods", J. Electroanal. Chem. 704 (2013) 175–182, doi:http://dx.doi.org/10.1016/j.jelechem.2013.07.010.
[30] V. Moreno, J. Creuze, F. Berthier, C. Mottet, G. Tréglia, B. Legrand, "Site segregation in size-mismatched nanoalloys: Application to Cu–Ag", Surf. Sci. 600 (2006) 5011–5020, doi:http://dx.doi.org/10.1016/j.susc.2006.08.030.
[31] L.A. Rocha, E. Ariza, J. Ferreira, F. Vaz, E. Ribeiro, L. Rebouta, E. Alves, A.R. Ramos, Ph. Goudeau, J.P. Rivière, "Structural and corrosion behaviour of stoichiometric and substoichiometric TiN thin films", Surf. & Coat. Technol. 180–181 (2004) 158–163, doi:http://dx.doi.org/10.1016/j.surfcoat.2003.10.059.
[32] N.P. Barradas, C. Jeynes, R.P. Webb, "Simulated annealing analysis of Rutherford backscattering data", Appl. Phys. Lett. 71 (1997) 291, doi:http://dx.doi.org/10.1063/1.119524.
[33] A.F. Gurbich, "Evaluated differential cross-sections for IBA", Nucl. Instr. and Meth. B 268 (2010) 1703, doi:http://dx.doi.org/10.1016/j.nimb.2010.02.011.
[34] J.-P. Randin, "Corrosion behavior of nickel-containing alloys in artificial sweat", J. Biomed. Mat. Res. 22 (1988) 649, doi:http://dx.doi.org/10.1002/jbm.820220706.
[35] M.G. Fontana, N.D. Greene, "Corrosion Engineering", 3rd ed., McGraw-Hill Book Company, 1986 ISBN-13:1986 978-0070214637.
[36] C.-C. Shih, C.-M. Shih, K.-Y. Chou, S.-J. Lin, Y.-Y. Su, R.A. Gerhardt, "Mechanism of degradation of AgCl coating on biopotential sensors", J. Biomed. Mater. Res. 82A (2007) 872–883, doi:http://dx.doi.org/10.1002/jbm.a.31140.
[37] C. Lopes, C. Gonçalves, P. Pedrosa, F. Macedo, E. Alves, N.P. Barradas, N. Martin, C. Fonseca, F. Vaz, "TiAg$_x$ thin films for lower limb prosthesis pressure sensors: Effect of composition and structural changes on the electrical and thermal response of the films", Appl. Surf. Sci. 285P (2013) 10–18, doi:http://dx.doi.org/10.1016/j.apsusc.2013.07.021.
[38] H. Ha, J. Payer, "The effect of silver chloride formation on the kinetics of silver dissolution in chloride solution", Electrochim. Acta. 56 (2011) 2781–2791, doi:http://dx.doi.org/10.1016/j.electacta.2010.12.050.
[39] Y. Liu, Z. Zheng, J.N. Zara, C. Hsu, D.E. Soofer, K.S. Lee, R.K. Siu, L.S. Miller, X. Zhang, D. Carpenter, C. Wang, K. Ting, C. Soo, "The antimicrobial and osteoinductive properties of silver nanoparticle/poly (dl-lactic-co-glycolic acid)-coated stainless steel", Biomaterials 33 (2012) 8745–8756, doi:http://dx.doi.org/10.1016/j.biomaterials.2012.08.010.
[40] V.I. Birss, C.K. Smith, "The anodic behavior of silver in chloride solutions – I. The formation and reduction of thin silver chloride films", Electrochim. Acta 32 (1987) 259–268, doi:http://dx.doi.org/10.1016/0013-4686(87)85033-8.
[41] B.M. Jović, V.D. Jović, D.M. Dražić, "Kinetics of chloride ion adsorption and the mechanism of AgCl layer formation on the (111), (100) and (110) faces of silver", J. Electro. Analytical Chemistry 399 (1995) 197–206, doi:http://dx.doi.org/10.1016/0022-0728(95)04291-1.
[42] J. Peng, Y. Deng, D. Wang, X. Jin, G.Z. Chen, "Cyclic voltammetry of electroactive and insulative compounds in solid state: A revisit of AgCl in aqueous solutions assisted by metallic cavity electrode and chemically modified electrode", J. Electroanal. Chem. 627 (2009) 28–40, doi:http://dx.doi.org/10.1016/j.jelechem.2008.12.016.
[43] H.H. Hassan, M.A.M. Ibrahim, S.S. Abd El Rehim, M.A. Amin, "Comparative Studies of the Electrochemical Behavior of Silver Electrode in Chloride, Bromide and Iodide Aqueous Solutions", Int. J. Electrochem. Sci. 5 (2010) 278–294.
[44] A. Norlin, J. Pan, C. Leygraf, "Investigation of Electrochemical Behavior of Stimulation/Sensing Materials for Pacemaker Electrode Applications I. Pt, Ti, and TiN Coated Electrodes", J. Electrochem. Soc. 152 (2005) J7–J15, doi:http://dx.doi.org/10.1149/1.1842092.
[45] S. Grimmes, "Impedance measurement of individual skin surface electrodes", Med. & Biol. Eng. And Comput. 21 (1983) 750–755.
[46] J. Rosell, J. Colominas, P. Riu, R. Pallas-Areny, J.G. Webster, "Skin Impedance From 1 Hz to 1 MHz", IEEE Trans. Biomed. Eng. 35 (1988) 649–651.
[47] M. Orazem, B. Tribollet, "Electrochemical Impedance Spectroscopy", John Wiley & Sons, 2008 ISBN 978-0-470-04140-6.
[48] J.R. Macdonald, "Impedance Spectroscopy Emphasizing Solid Materials and Systems", Wiley, New York, 1987, doi:http://dx.doi.org/10.1016/0584-8539(88)80155-7.
[49] E. Huigen, A. Peper, C. Grimbergen, "Investigation into the origin of the noise of surface electrodes", Med. Biol. Eng. Comput. 40 (2002) 332.
[50] M.M. Puurtinen, S.M. Komulainen, P.K. Kauppinen, J.A.V. Malmivuo, J.A.K. Hyttinen, "Measurement of noise and impedance of dry and wet textile electrodes, and textile electrodes with hydrogel", Proceedings of the 28th IEEE EMBS Annual International Conference, New York City, USA, Aug. 30-Sept., 32006, pp. 6012–6015.
[51] D.T. Godin, P.A. Parker, R.N. Scott, "Noise characteristics of stainless-steel surface electrodes", Med. & Biol. Eng. & Comput. 29 (1991) 585–590.
[52] H.J. Scheer, T. Sander, L. Trahms, "The influence of amplifier, interface and biological noise on signal quality in high-resolution EEG recordings", Physiol. Meas. 27 (2006) 109–117, doi:http://dx.doi.org/10.1088/0967-3334/27/2/002.
[53] K. Hladky, J. Dawson, "The measurement of corrosion using electrochemical 1/f noise", Corrosion Sci. 22 (1982) 231, doi:http://dx.doi.org/10.1016/0010-938X(82)90107-X.

# CHAPTER 5

## Ag:TiN FILM ARCHITECTURE VARIATION[*]

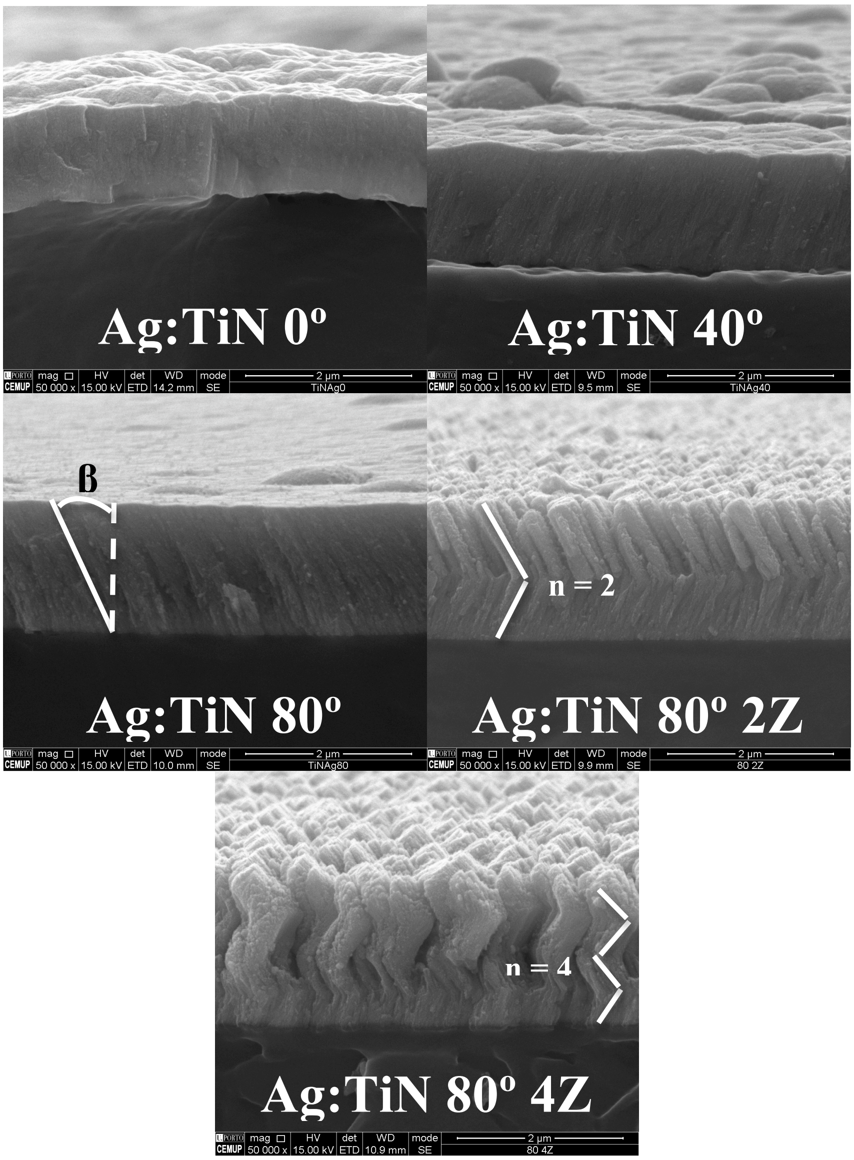

*"…the porous samples appear to exhibit the most promising set of properties to be used as biopotential electrodes."*

---

[*] This chapter is based on the following publications:

P. Pedrosa, C. Lopes, N. Martin, C. Fonseca, F. Vaz, "*Electrical characterization of Ag:TiN thin films produced by glancing angle deposition*", Materials Letters 115 (2014) 136-139.

P. Pedrosa, D. Machado, E. Alves, N.P. Barradas, N. Martin, F. Vaz, C. Fonseca, "*Ag:TiN-coated polyurethane for dry biopotential electrodes produced by glancing angle deposition*", submitted to Journal of the Electrochemical Society, under review.

In the previous chapter, the authors explored the possibility of reducing the Ag segregation phenomenon observed in the stoichiometric $Ag_x$:TiN system (chapter 3) by decreasing the N/Ti atomic ratio of the TiN matrix towards under-stoichiometric conditions – $Ag_y$:$TiN_x$ system, in order to ensure the stability of the coatings during in-service EEG applications. From the previous morphological, structural, mechanical and electrochemical study, it was found that the reduction of the TiN matrix stoichiometry effectively acts as a silver segregation inhibitor, due to the probable formation of TiAg intermetallics. In combination with the electrochemical characterization, it could be concluded that the TiN0.3Ag15 and TiN0.7Ag32 coatings exhibit the best set of properties (no evidences of Ag segregation, thus good structural stability, low impedance, low electrochemical noise and drift rate values) to be used as bioelectrodes.

After the composition optimization of the Ag:TiN thin film system in terms of Ag content (chapter 3) and $TiN_x$ matrix stoichiometry (chapter 4), the next step of the present thesis is shown on the following chapter and consisted on the tailoring of the architecture of the coatings using the GLancing Angle Deposition (GLAD) technique. The nanoscale tailoring of the Ag:TiN thin film system was performed in order to obtain more compliant films that should be able to withstand the large deformations inherent to the adaptation to the human body, without significantly compromising its conductivity, electrochemical response and structural stability, so that they could be effectively used as flexible dry bio-potential electrodes. This technique can be used to tailor the plasticity of thin films, since inclined and zigzag microstructures often behave as micro-springs.

The GLAD technique employs oblique angle deposition and substrate motion to engineer thin film microstructures on a nanometre scale in three dimensions[1,2]. It relies on a non-stationary substrate holder that allows two types of movements, α (which refers to the particle

---

[1] K. Robbie, M.J. Brett, A. Lakhtakia, "*Chiral sculptured thin films*", Nature 384 (1996) 616-616.

[2] M.J. Brett, J. Hawkeye, M. Matthew, "*New Materials at a Glance*", Science 319 (2008) 1192-1193.

incidence angle) and φ rotation (360º concentric rotation of the substrate holder), in order to obtain three main film architectures: (i) inclined columns with α ranging from 0º (standard columnar coatings) to 80º, (ii) zigzag columns (φ rotation = 180º for each zigzag period, after fixing the desired α angle) and (iii) spiral columns (continuous 360º φ rotation, after fixing the desired α angle).

The GLAD sputtered Ag:TiN film system was then morphologically, structurally, electrically and electrochemically investigated on the following chapter, in order to assess its suitability to be used as EEG bioelectrodes. It was found that the architecture of the coatings could be effectively tailored (see cover figure) without compromising the aforementioned properties. Also, strong porosity changes occurred when the incidence angle α increased from 40 to 80º, thus making the porous Ag:TiN 80º, Ag:TiN 80º 2Z (two zigzag periods) and Ag:TiN 80º 4Z (four zigzag periods) GLAD coatings the most promising for the envisaged application as dry biopotential electrodes, since they displayed lower impedance (Fig. 5.1.) and electrochemical noise values, as well as more stable potentials (low drift rates), comparable to those of the wet Ag/AgCl commercial electrodes. In addition, no Ag segregation was detected on this thin film system.

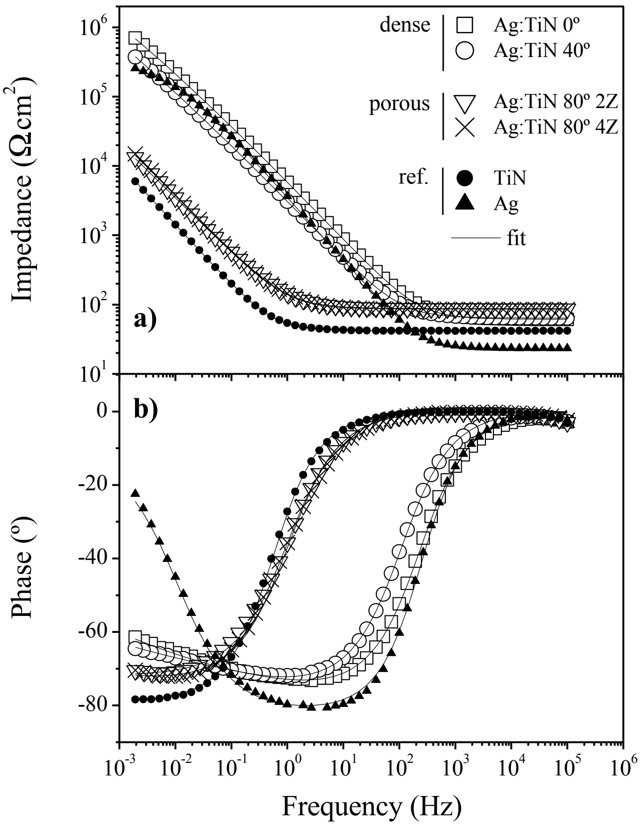

**Figure 5.1.** Bode diagram exhibiting the (a) impedance and (b) phase behaviour of representative samples of the GLAD sputtered Ag:TiN films.

Materials Letters 115 (2014) 136–139

Contents lists available at ScienceDirect

Materials Letters

journal homepage: www.elsevier.com/locate/matlet

# Electrical characterization of Ag:TiN thin films produced by glancing angle deposition

P. Pedrosa [a,b,c], C. Lopes [c], N. Martin [d], C. Fonseca [a,b], F. Vaz [c,*]

[a] SEG-CEMUC – Department of Mechanical Engineering, University of Coimbra, Portugal
[b] Universidade do Porto, Faculdade de Engenharia, Departamento de Engenharia Metalúrgica e de Materiais, Rua Roberto Frias, s/n, 4200-465 Porto, Portugal
[c] Centro de Física, Universidade do Minho, 4710-057 Braga, Portugal
[d] Institut FEMTO-ST, UMR CNRS 6174 – Université de Franche Comté – CNRS – ENSMM – UTBM, ENSMM 26 Chemin de l'Epitaphe,
F-25030 Besançon Cedex, France

## ARTICLE INFO

*Article history:*
Received 3 September 2013
Accepted 13 October 2013
Available online 19 October 2013

*Keywords:*
Glancing Angle Deposition
Titanium nitride
Silver-doping
Resistivity

## ABSTRACT

Columnar Ag:TiN thin films were prepared by d.c. magnetron sputtering with a Ag content of ~10 at.% on silicon and glass substrates. The Glancing Angle Deposition, GLAD, technique was implemented to transform the typical columnar microstructure into the desired inclined, zigzag and spiral profiles. A periodic variation of the angle of incidence '$\alpha$' (40°, 60° and 80°) was applied to deposit Ag:TiN thin films with inclined, zigzag and spiral microstructures. The film's electrical properties were studied. Higher $\alpha$ values lead to more porous microstructures with column angle $\beta$ varying from 13° ($\alpha=40°$) to 30° ($\alpha=80°$) for 8 zigzags. Resistivity, $\rho$, at 293 K or versus temperature was found to be connected to the porosity and $\beta$ angles. The more compact films exhibited lower and more stable resistivity values than the more porous ones. Ag segregation and TiN columnar oxidation are favored by temperature and were also found to depend on the produced architectures.

## 1. Introduction

Thin films grown by physical vapor deposition (PVD) techniques are conventionally produced with a normal incidence of the particle flux. From the first experimental investigations performed by Movchan and Demchishin [1] and later by Thornton [2], to the recent structural models developed by other researchers [3,4], most studies were mainly focused on the operating conditions affecting the morphology and microstructure of deposited films under normal incidence. Very few have been devoted to thin films prepared using an oblique incidence of the particle flux [5–7]. Young and Koval [8] showed that fluorite films with a helical structure exhibited an anisotropic optical activity. They also showed that the latter was linked to the angle of incidence of evaporated particles and periodicity of the film microstructure. Similarly, Smith [9] established that the orientation of Permalloy films chiefly influenced their magnetic properties. A few years later, Nieuwenhuizhen and Haanstra [10] observed that the orientation of the columnar structure of aluminum coatings could be related to the angle of incidence of evaporated particles by an empirical law known as "the tangent rules". Other authors took again and improved these geometrical rules to easily predict the influence of the direction of the vapor flux on the final arrangement of columnar grains [11–13]. It was not until the investigation carried out by Brett's team that the GLAD technique (Glancing Angle Deposition) has really evolved and finally emerged [14,15]. The preparation of thin films under oblique, fixed or mobile substrate was successfully applied to numerous materials including metals, alloys, oxides, fluorides and so on [16–19]. The originality of the properties generated in the field of photonics, mechanics, catalysis or biology, easily explain the growing interest of the GLAD approach. This interest is mostly noticeable for metal and oxide coatings sputter deposited at oblique incidence [20–22] but very few studies report on metallic nitrides [23,24], especially about the relation between the possible achieved structures by GLAD and the resulting electrical properties. This letter demonstrates that the electrical properties of Ag-doped TiN films exhibiting an inclined, zigzag or spiral microstructure can be tuned according to several orders of magnitude. It is shown that temperature also affects the electronic transport properties due to Ag segregation and a porous structure depending on the grown architecture. The present Ag:TiN system is being studied and optimized to be used as flexible polymer-based bioelectrodes, following previous studies by the authors [25–27], where the influence of increasing Ag additions on several properties of 0° Ag:TiN films was assessed. The paper aims at giving further insights on this particular system by studying the influence of the GLAD features on the resistivity evolution.

---

[*] Corresponding author. Tel.: +351 253 601530; fax: +351 253 604398.
*E-mail address:* fvaz@fisica.uminho.pt (F. Vaz).

0167-577X/$ - see front matter © 2013 Elsevier B.V. All rights reserved.
http://dx.doi.org/10.1016/j.matlet.2013.10.044

## 2. Experimental details

Ag:TiN thin films were deposited by d.c. reactive magnetron sputtering, inside a stainless-steel custom-made vacuum reactor, with a volume of 40 L. The reactor, equipped with a circular planar and water cooled magnetron sputtering source, was evacuated with a turbomolecular pump, backed by a mechanical pump, in order to obtain an ultimate pressure of $10^{-5}$ Pa. A titanium target (purity 99.6 at.%, 51 mm diameter) was used and 12 Ag inserts (purity 99.9 at.%, 2 mm diameter) were located equidistant from each other in the preferential erosion zone of the target. The pumping speed was set constant at $S = 10\ \mathrm{L\,s^{-1}}$. This mosaic target was d.c. sputtered in a reactive atmosphere composed of argon and nitrogen gases. Argon flow rate was kept at 2.4 sccm and nitrogen flow rate was maintained at 2 sccm, corresponding to argon and nitrogen partial pressures of $3 \times 10^{-1}$ and $3 \times 10^{-2}$ Pa, respectively. Substrates, introduced through a 1 L airlock, were glass microscope slides (ISO norm 8037-1, with roughness better than 0.5 nm) and (100) silicon wafers (p-type, $\rho = 1$–$30\ \Omega$.cm). Before each run, all substrates were cleaned with acetone and alcohol, and the target was pre-sputtered in a pure argon atmosphere for 5 min before introducing nitrogen, in order to remove the target surface contamination layer. The target to substrate distance was kept at 50 mm in all runs. Substrates were grounded and all depositions were carried out at room temperature. The deposition time was adjusted in order to obtain a thickness close to 1 μm. All sputtering parameters were optimized to allow a successful reproducibility of the features into polymer substrates [27]. Morphological features of the samples were probed by scanning electron microscopy (SEM) at 15 keV. Films produced on (100) Si were used to observe their architecture and morphology. Films deposited on glass microscope slides were used for resistivity measurements, using the four-probe van der Pauw method in the temperature range of 293–793 K (vs. $T$ measurements were done in a custom-made chamber, which is covered in order to have a dark environment; humidity and cleanness have been considered as constant). The error associated to all measurements was always below 1% and the attachment of the contacts was checked prior to every measurement (the $I/V$ correlation was always very close to 1) to ensure that an ohmic contact is attained (use of gold coated tips). Films deposited on glass microscope slides were used for resistivity measurements.

## 3. Results and discussion

Fig. 1 depicts the cross-section images of the sputtered GLAD samples. With increasing $\alpha$ angle, the $\beta$ angle rises from 13° ($\alpha = 40°$) to a maximum of 30° ($\alpha = 80°$) for 8 zigzags. Furthermore, the set of sputtered samples can be grouped according to their porosity. There is a clear morphological change when $\alpha$ increases from 60° to 80°. The TiN and Ag-doped films sputtered with $\alpha = 0°$ are compact and almost featureless. With $\alpha = 40°$ and 60° the TiN columnar features start to become more defined (the columnar definition being more pronounced in the latter sample). As already mentioned, when $\alpha = 80°$ the coating's columnar features are well

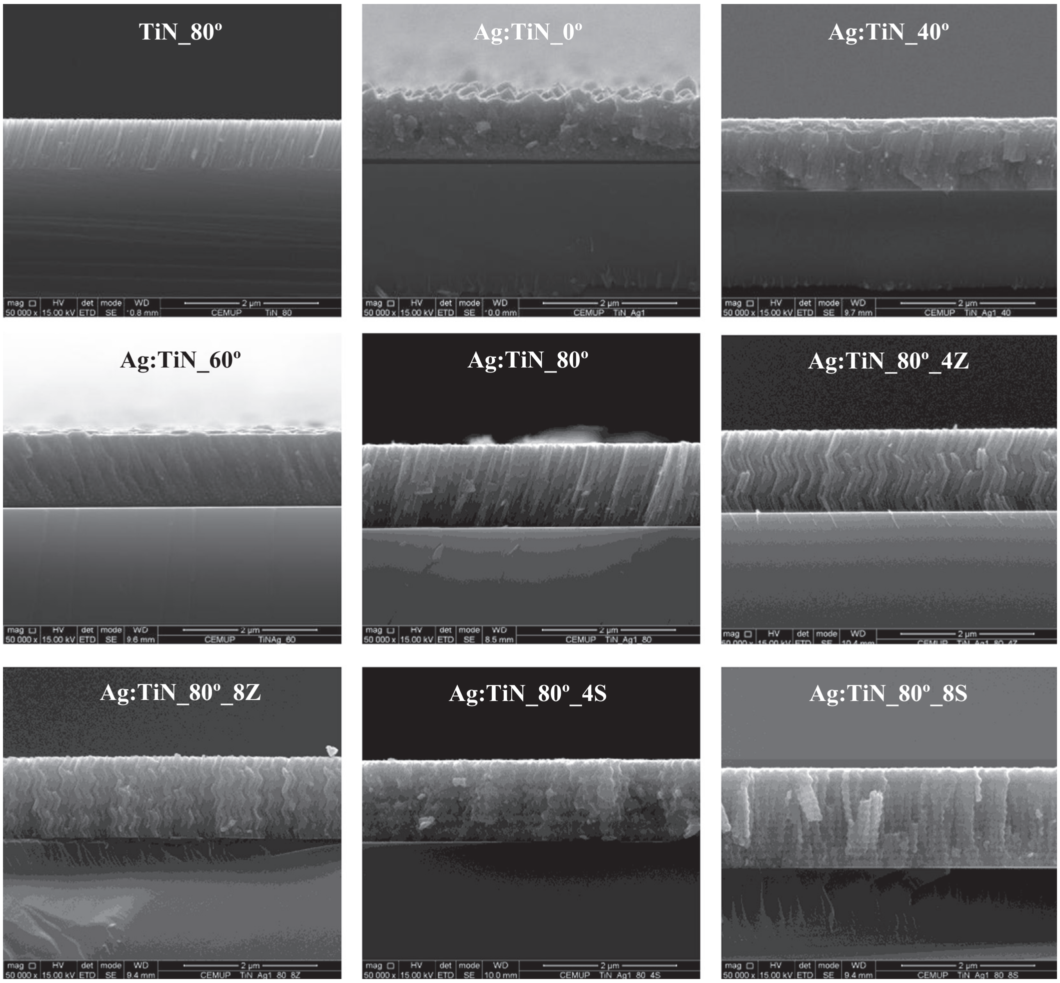

**Fig. 1.** SEM cross-section micrographs of the sputtered TiN and Ag:TiN samples.

defined and evidences of inter-columnar spacing are perceivable. Regarding the zigzag samples, no significant changes in porosity are apparent. This conclusion is supported by the little change observed in the column angle values ($\beta=27^\circ$ for 4 periods and $\beta=30^\circ$ for 8 periods). Consequently, no significant changes of the $\rho_{293\ \mathrm{K}}$ values, Fig. 2, are measured with increasing zigzag periods. For the spiral features, the coatings seem to be compact (the 8 spiral periods sample exhibits more defined features than the 4 spiral one). As a result of this compactness, the spiraled samples should exhibit lower $\rho_{293\ \mathrm{K}}$ values than the more porous zigzag ones.

The room temperature ($\rho_{293\ \mathrm{K}}$) resistivity evolution with increasing $\alpha$ is presented in Fig. 2. The results are in great accordance with SEM analysis. The TiN $\alpha=80^\circ$ sample result is provided (dashed line) to illustrate an almost one order of magnitude increase of conductivity attained with a 10 at.% Ag doping. In recent works by the authors [25,26], the effects of Ag additions to a stoichiometric TiN matrix were studied and it was found that for intermediate Ag contents (between ~6 and ~20 at.%), highly conductive Ag particles nucleate among the TiN columns, hence providing an increased number of conduction paths. Regarding all Ag-doped samples, there seems to be a relation between resistivity and morphology. The more conductive ones are those with denser structures. In the case of the inclined features, the increase of both $\alpha$ and $\beta$ values should give rise to increased porosity (Fig. 1). Thus, scattering at the column's interface is favored, which reduces the electronic transport properties of the coatings. A similar analysis can be applied to the zigzag and spiral samples. From SEM imaging, the increasing number of zigzag periods does not promote substantial changes in the resistivity behavior. The $\beta$ angle is not significantly affected by the period increase. The $\alpha=40^\circ$ zigzag sample exhibits similar $\rho_{293\ \mathrm{K}}$ value to the $\alpha=0^\circ$ one due to their poorly defined columnar structure (low porosity), hence being rather compact (SEM images not shown). The same trend is patent in the spiral coatings. As referred, the $\alpha=80^\circ$ with 4 and 8 spirals samples display lower $\rho_{293\ \mathrm{K}}$ values than the correspondent zigzag ones due to their reduced porosity. As suggested from SEM analysis, the sample with $\alpha=80^\circ$_8 spirals presents higher resistivity due to a better spiral feature definition, hence more porous.

The resistivity behavior with increasing temperature, $\rho_T$, was also studied (Fig. 3). The denser coatings exhibit lower and more stable $\rho_T$ up to higher temperatures than the porous ones. This is evidenced by the stronger shift exhibited by the porous samples (shift 2, Fig. 3) towards lower temperatures of the TiN ($\alpha=0^\circ$) critical oxidation temperature, $T_C$, defined by Wang et al. [28], due to an increased porosity, favoring the TiN columnar oxidation. It is worth noting that the $T_C$ at 773 K defined by Wang et al. for few nm thick films is strongly influenced by the film thickness. The real

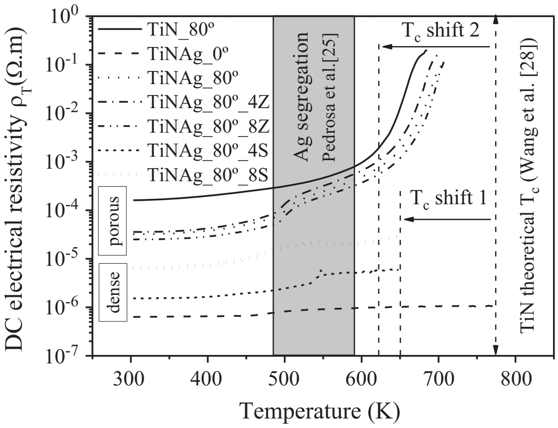

**Fig. 3.** Resistivity evolution vs. temperature for TiN and Ag:TiN films for $\alpha=0^\circ$ and 80° with inclined, zigzag and spiral architectures (4 and 8 periods).

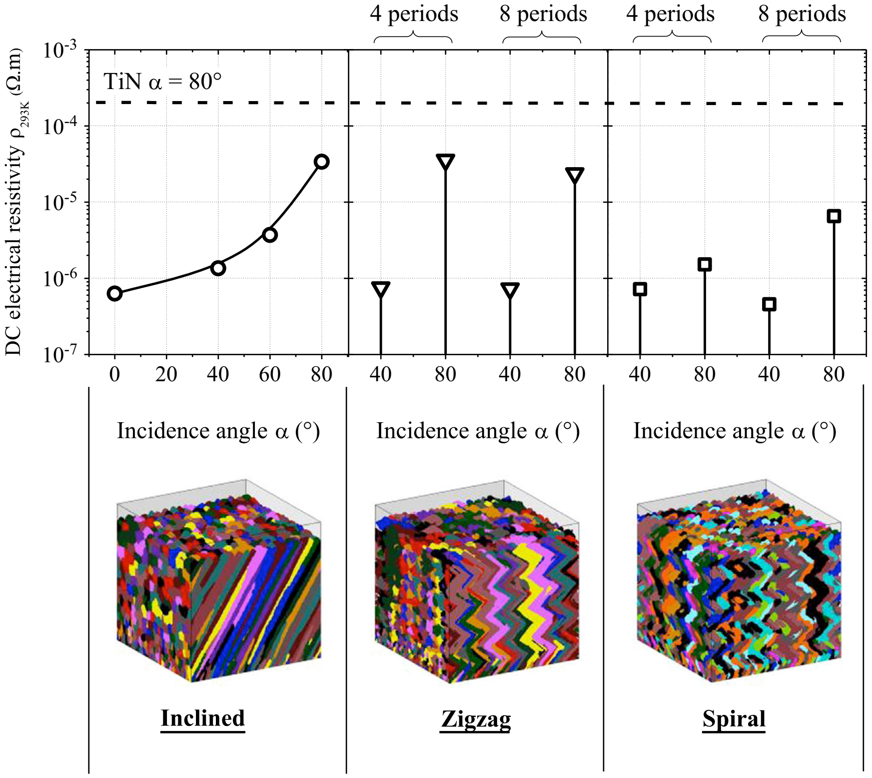

**Fig. 2.** Room temperature resistivity evolution according to the incidence angle and zigzag/spiral periods.

theoretical $T_C$ of the studied samples (800–1000 nm) should be much higher, making both $T_C$ shifts more pronounced. This probably explains why the TiNAg_0° sample does not exhibit the oxidation-promoted increase of $\rho_T$ until 773 K. Above $T_C$, both dense and porous coatings suffer a logarithmical increase of $\rho_T$ (both spiral coating's data are not plotted above this point due to inaccurate signals during resistivity measurements). This resistivity increase can be due to a strong reduction of the electron mean free path, as a result of the TiN columnar oxidation. Ag doping also plays an important role, which is evidenced by a small "bump" in the $\rho_T$ values in-between 473–573 K. This "bump" can be ascribed to the Ag segregation and coalescence phenomenon that was also studied by the authors [26], which is responsible for an overall grain size reduction (solute-drag effect) due to the pinning of TiN grain boundaries to the Ag solute atoms. For the densest sample, TiNAg_0°, this $\rho_T$ increase is smoothened by a greater difficulty of the Ag particles to diffuse to the surface, maintaining some intercolumnar Ag electrical pathways, which in the case of the more porous samples are continuously being depleted. To summarize, the un-doped TiN sample $\rho_T$ value is only significantly affected above $T_C$ due to column oxidation, while in the Ag-doped ones the $\rho_T$ value initially suffers a small "bump" between 500 and 600 K due to the reported Ag nucleation and segregation.

The GLAD Ag:TiN films are thus a good candidate to be used as bioelectrodes, since they exhibit low $\rho$ values and their elasticity may be further tailored, in order to be sputtered into polymer samples due to their increased porosity and architectures, when comparing to the normal incidence samples [25–27].

## 4. Conclusions

Correlations between morphology and electrical properties of GLAD sputtered Ag:TiN coatings were studied. It was found that $\beta$ angles vary from 13° for the $\alpha = 40°$ to 30° for the $\alpha = 80°$ with 8 zigzags. Resistivity results are connected to the morphological evolution. The porous samples consistently exhibit higher $\rho_{293\ \mathrm{K}}$ values than the denser ones. Regarding the $\rho_T$ behavior, a clear division between porous and dense coatings is observable, with the latter exhibiting lower and more stable values with increasing temperature. Porosity increase is also responsible for a steeper decrease of $T_C$, when comparing to the denser films. Ag doping also promotes lower $\rho_T$ values and its segregation is perceivable in the 473–573 K interval.

## Acknowledgments

This research is partially sponsored by FEDER Funds through the Program COMPETE—Programa Operacional Factores de Competitividade and by National Funds through FCT—Fundação para a Ciência e a Tecnologia, under the Projects PEst-C/EME/UI0285/2011, PTDC/SAU-ENB/116850/2010, PTDC/CTM-NAN/112574/2009 and Programa Pessoa 2012/2013 Cooperação Portugal/França, Project no. 27306UA. The authors would also like to acknowledge CEMUP for SEM analysis. P. Pedrosa acknowledges FCT for the Ph.D. Grant SFRH/BD/70035/2010.

## References

[1] Movchan BA, Demchishin AV. Fiz. Metal. Metalloyed. 1969;28(4):653–60.
[2] Thornton JA. J. Vac. Sci. Technol. 1974;11(4):666–70.
[3] Messier R, Giri AP, Roy RA. J. Vac. Sci. Technol. 1984;A2:500–3.
[4] Anders A. Thin Solid Films 2010;518:4087–90.
[5] Tait RN, Smy T, Brett JM. J. Vac. Sci. Technol. 1992;A10(4):1518–21.
[6] Mbise GW, Niklasson GA, Granqvist CG. J. Appl. Phys. 1995;77(6):2816–8.
[7] Hodgkinson I, Wu QH, McPhun A. J. Vac. Sci. Technol. 1998;B16(5):2811–6.
[8] Young NO, Kowal J. Nature 1959;183:104–5.
[9] Smith DO. J. Appl. Phys. 1959;30(4):264–5.
[10] Nieuwenhuizen JM, Haanstra HB. Philips Tech. Rev. 1966;27(3–4):87–91.
[11] Leamy HJ, Dirks AG. J. Appl. Phys. 1978;49(6):3430–8.
[12] Knorr TG. Phys. Rev. 1959;113(4):1039–46.
[13] Lintymer J, Martin N, Chappé JM, Takadoum J, Delobelle P. Thin Solid Films 2006;503:177–89.
[14] Robbie K, Brett MJ, Lakhtakia A. Nature 1996;384:616.
[15] Brett MJ, Hawkeye J, Matthew M. Science 2008;319:1192–3.
[16] Besnard A, Martin N, Carpentier L, Gallas B. J. Phys. D Appl. Phys. 2011;44:215301–8.
[17] Smith W, Zhang ZY, Zhao YP, Vac. J. Sci. Technol. 2007;B25:1875–81.
[18] Robbie K, Shafai C, Brett MJ. J. Mater. Res. 1999;14(7):3158–63.
[19] Taschuk MT, Hawkeye MM, Brett MJ. Glancing Angle Deposition. In: Martin PM, editor. Handbook of Deposition Technologies and for Films and Coatings. 3rd ed. Oxford: Elsevier; 2010.
[20] Gonzalez-Garcia L, Parra-Barranco J, Sanchez-Valencia JR, Barranco A, Borras A, Gonzalez-Elipe AR, et al. Nanotechnology 2012;23:205701–10.
[21] Karabacak T, Mallikarjunan A, Singh JP, Ye DX, Wang GC, Lu TM. Appl. Phys. Lett. 2003;83:3096–8.
[22] Besnard A, Martin N, Sthal F, Carptentier L, Rauch JY. Funct. Mater. Lett. 2013;6:1250051–5.
[23] Cheng LC, Tien CH, Liu XG, Xu BS. J. Nanomater. 2012;2012:409123–6.
[24] Frederick JR, D'Arcy-Gall J, Gall D. Thin Solid Films 2006;494(1–2):330–5.
[25] Pedrosa P, Machado D, Lopes C, Alves E, Barradas NP, Martin N, Macedo F, Fonseca C, Vaz F. Appl. Surf. Sci. 2013; 285P:40–8.
[26] Pedrosa P, Machado D, Evaristo M, Cavaleiro A, Fonseca C, Vaz F. Vacuum (2013), under review.
[27] Pedrosa P, Alves E, Barradas NP, Fiedler P, Haueisen J, Vaz F, et al. Corros. Sci. 2012;56:49–57.
[28] Wang JM, Liu WG, Mei T. Ceram. Int. 2004;30:1921–4.

# Optimization of nanostructured Ag:TiN thin films produced by plasma discharge glancing angle deposition on polyurethane substrates for biomedical electrodes

P. Pedrosa[a,b,c], D. Machado[c], P. Fiedler[d], E. Alves[e], N.P. Barradas[f], N. Martin[g], J. Haueisen[d], F. Vaz[c], C. Fonseca[a,b*]

[a]SEG-CEMUC – Department of Mechanical Engineering, University of Coimbra, Portugal

[b]Universidade do Porto, Faculdade de Engenharia, Rua Dr. Roberto Frias, s/n, 4200-465 Porto, Portugal

[c]Centro de Física, Universidade do Minho, 4710-057 Braga, Portugal

[d]Institute of Biomedical Engineering and Informatics, Technische Universität Ilmenau, Ilmenau, Germany

[e]Instituto de Plasmas e Fusão Nuclear, Instituto Superior Técnico, Universidade de Lisboa, Av. Rovisco Pais, 1049-001, Lisboa, Portugal

[f]Centro de Ciências e Tecnologias Nucleares, Instituto Superior Técnico, Universidade de Lisboa, E.N. 10 (km 139,7), 2695-066 Bobadela LRS, Portugal

[g]Institut FEMTO-ST, UMR 6174, Université de Franche-Comté, CNRS, ENSMM, UTBM, 32, Avenue de l'Observatoire, 25044 BESANÇON Cedex, France

## ABSTRACT

Flexible polyurethane substrates were coated with Ag:TiN thin films with different incidence angles and architectures, using the Glancing Angle Deposition (GLAD) plasma discharge technique. The coatings were characterized in order to assess the best thin film

---

[*] Corresponding author: C. Fonseca; email address: cfonseca@fe.up.pt; Universidade do Porto, Faculdade de Engenharia, Departamento de Engenharia Metalúrgica e de Materiais, Rua Dr. Roberto Frias, s/n, 4200-465, Porto, Portugal, Tel.: +351 225081995.

architecture to be used for biomedical electrode applications. The electrochemical behaviour of the samples is consistently linked to the porosity differences, which is accompanied by an increase of the surface Ag content. Furthermore, the porous samples exhibit lower impedances, as well as electrochemical noise and drift rate values similar to those of the commercial Ag/AgCl electrodes. Hence, the porous Ag:TiN GLAD coatings seem to be the most promising architectures for the envisaged biomedical electrode applications.

**Keywords:** dry electrodes; glancing angle deposition; polyurethane; silver-doping; titanium nitride

## 1. INTRODUCTION

The majority of thin films grown by physical vapour deposition (PVD) techniques are conventionally produced with a normal incidence of the particle flux. This well established method of in-vacuum plasma process, commonly used for the preparation of several types of coatings has led to extensive applications in areas as diverse as electronics, optics, mechanics, decoration and biomedical.

Nevertheless, one can claim that some technologies are now completely dependent on the whole properties of the deposited films, especially their micro- and nanostructure. Since the first studies performed by Movchan and Demchishin[1] and later by Thornton[2], to the recent structural models developed by other authors[3-7], most works were mainly focused on the operating conditions affecting the morphology and microstructure of deposited films under normal incidence. Only a few have been devoted to thin films prepared using special thin film architectures such as oblique incidence of the particle flux.[8-12] However, in 1959, Young and Kowal[13] showed that fluorite films with a helical structure presented an anisotropic optical activity and correlated these findings to the angle of incidence of the plasma sputtered particles and periodicity of the film microstructure. Smith[14] also established that the orientation of Permalloy films had a major influence in their magnetic properties. Nieuwenhuizhen and Haanstra[15] posteriorly demonstrated that the columnar orientation of aluminium thin films was related to the incidence angle of the plasma sputtered particles by an empirical law known as “the tangent rules”. Then, other authors studied and improved these geometrical rules in order to easily predict the influence of the direction of the plasma flux on the final arrangement of columnar grains.[9,16-18] All these works focused on coatings deposited by means of an oblique incidence of the particle flux converge to an identical conclusion: an extended range of physico-chemical properties of as-deposited materials, which concern their density, state of stress, optical, mechanical, electrical and magnetic behaviours, can be tailored using the plasma discharge GLAD technique for other relevant characteristics and properties of a given thin film system for a specific set of targeted applications.

However, the plasma discharge GLAD technique only became widely spread after the studies performed by Brett et al.[19,20] According to Brett’s team, GLAD can be defined as a technique that “employs oblique angle plasma deposition and substrate motion to engineer thin film microstructures on a nanometre scale in three dimensions”. Hence, oblique, fixed or mobile substrates were then successfully applied to the sputtering of numerous materials such as metals, alloys, oxides and fluorides, among others.[21-25] In recent years, the extensive dissemination of their works in leading scientific journals demonstrates the strong interest generated by nanostructured thin films prepared with this method. Moreover, the growing interest of the plasma discharge GLAD technique shown by many researchers coming from academia and industry[26-28] is due to the possibility to tailor even further the majority of the properties of most thin film systems, which can be of major interest in the fields of photonics, mechanics, catalysis or biology. Thus, GLAD thin films, prepared by either evaporation or magnetron sputtering are becoming an attractive strategy to obtain a wide variety of architectures and sculptured materials at the micro- and nanoscale. This involvement is mostly evident for metal and oxide coatings sputter deposited with inclined architectures[29-33] but very few studies are dedicated to metallic nitrides produced by the GLAD technique[34,35], especially regarding the relations between the possible achieved structures by GLAD (e.g. inclined columns, zigzags, spirals) and the resulting properties in terms of mechanical response, electrical conductivity or even electrochemical behaviour. Bearing these concerns in mind, the present paper will be focused on the optimization of sputtered thin film-based flexible (using polyurethane as substrate) biomedical electrodes, produced by GLAD.

Ag/AgCl electrodes are widely used in a wide range of biosignal monitoring techniques, such as electroencephalography (EEG), electrocardiography (ECG) and electromyography (EMG), among others.[36-38] However, these biomedical electrodes need to be applied in combination with electrolyte gels or pastes, involving uncomfortable and time-consuming procedures. In order to avoid these drawbacks, a new class of biomedical devices is being investigated, for which no previous skin preparation or gel paste application is needed, the so-called "dry" electrodes.[39-41] These electrodes are commonly quite rigid, which can give rise to a deficient and uncomfortable skin contact. Consequently, several authors have focused on the development of flexible dry electrodes.[42-48]. The possibility to tailor important electrode properties, e.g. flexibility, by exploring the architecture of the films offered by the plasma discharge GLAD technique, is a very challenging approach to solve some of the difficulties patent in the fabrication of skin conformable biomedical electrodes using flexible polymeric substrates.

Following a previous study by the authors[49], the main goal of this work is to optimize the deposition conditions and the architecture of the coatings, in order to obtain more compliant films that should be able to withstand the large deformations inherent to the adaptation to the human body, without significantly compromising its conductivity and electrochemical response, so that they could be used as flexible dry biomedical electrodes.

The plasma discharge GLAD technique can be used to tailor the plasticity of thin films, since inclined and zigzag microstructures often behave as micro-springs.[18]

The resulting properties of the GLAD sputtered Ag-doped under-stoichiometric TiN thin films (so as to avoid Ag segregation[50-52]), will be presented regarding the structural and morphological characteristics produced at the micro- and nanoscales. The electrical and electrochemical response of the sputtered coatings will be studied, in order to assess the viability of the flexible polymer/Ag:TiN system to be used as biomedical electrodes.

## 2. EXPERIMENTAL DETAILS

### *2.1. Thin film production*

The depositions of the plasma sputtered Ag:TiN thin films were performed with inclinations (α angles) of 0, 40 and 80º with columnar and zigzag architectures. After fixing a certain α angle (80º in the present study), the zigzag architecture is attained by periodically rotating the GLAD substrate holder (φ rotation = 180º for each period), see Figure 1 and 2. All films were obtained by d.c. reactive magnetron sputtering, using a stainless-steel home-made vacuum reactor with a volume of 40 L. The reactor, equipped with a circular planar and water-cooled magnetron sputtering source, was evacuated with a turbomolecular pump backed by a mechanical pump in order to obtain an ultimate pressure of $10^{-5}$ Pa (Figure 1).

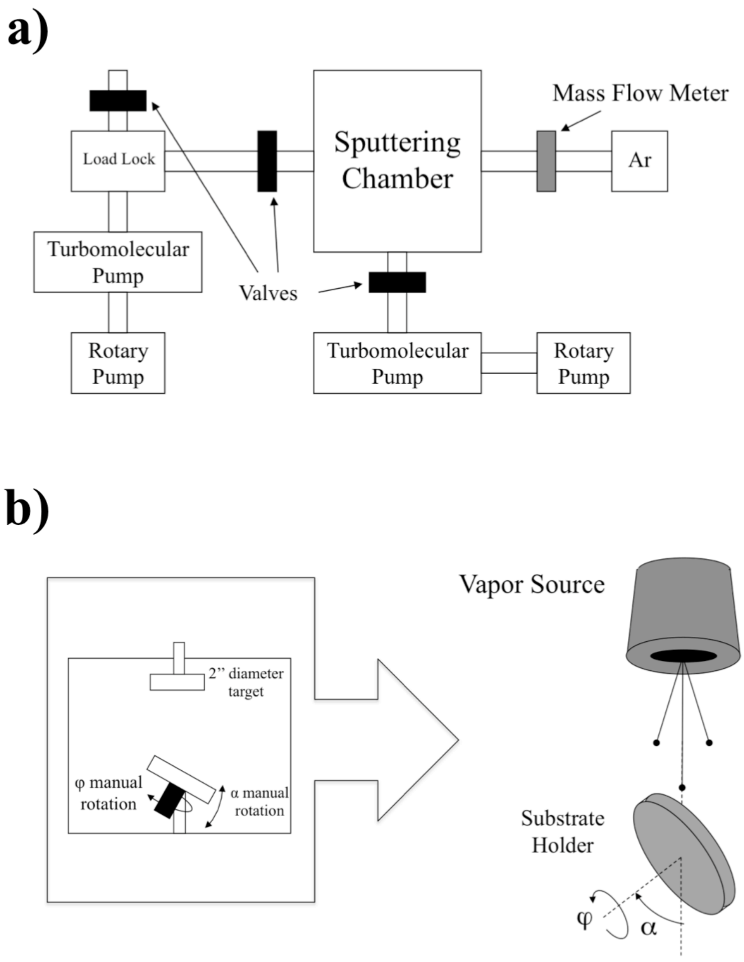

**Figure 1.** (a) Schematic view of the laboratory-sized deposition chamber and (b) illustration of the homemade GLAD substrate holder.

A titanium target (purity 99.6 at.%, 51 mm diameter) was used and 12 Ag inserts (purity 99.9 at.%, 2 mm diameter) were uniformly distributed in the erosion zone of the target. The pumping speed was set constant at S = 10 L $s^{-1}$. The Ti/Ag target was d.c. sputtered in a Ar+$N_2$ reactive plasma atmosphere. The argon flow rate was kept constant at 2.4 sccm, while nitrogen was introduced using 2 sccm pulses ($T_{on}$ = 4 s, Period = 16 s) corresponding to argon and nitrogen partial pressures of $3\times10^{-1}$ and $3\times10^{-2}$ Pa, respectively. Operating conditions are summarized in Table I. The polyester-based thermoplastic polyurethane (TPU) substrates, ref. WHT-1495EC, from Yantai Wanhua Polyurethanes Co., Ltd. were introduced through a 1 L airlock. Before each run they were cleaned with ethanol (96% vol.), and the target was pre-sputtered in a pure argon plasma atmosphere for five minutes before introducing nitrogen, in order to remove any remaining target surface contamination layer. The target-to-substrate distance was 50 mm. Substrates were grounded and room temperature condition was used for all depositions. The deposition time was adjusted in order to obtain a thickness close to 1 μm.

**Table I.** Experimental parameters used in all depositions.

| **Deposition parameters** | |
|---|---|
| **Ag exposed area ($mm^2$)** | 37.7 |
| **Ar (Pa)** | $3\times10^{-1}$ |
| **$N_2$ (Pa)** | $3\times10^{-2}$ |
| **$P_{work}$ (Pa)** | $3.3\times10^{-1}$ |
| **$P_{base}$ (Pa)** | $\sim10^{-5}$ |
| **t (h)** | Adjusted in order to obtain ~1 μm thickness (varied between 2 and 5h) |
| **I ($A.cm^{-2}$)** | $10^{-2}$ |
| **T (ºC)** | Room temperature |
| **Bias (V)** | Grounded |
| **α angles used (º)** | 0, 40 and 80º |
| **Architectures** | Columnar and zigzag (α = 80º, with 2 and 4 periods) |

### *2.2. Composition, structure, morphology and electrical resistivity*

The atomic composition of the as-deposited samples was measured by Rutherford Backscattering Spectrometry (RBS) using (1.4, 2.3) MeV and (1.4, 2) MeV for the proton and $^4$He beams, respectively. Three detectors were used: one located at a scattering angle of 140º, and two pin-diode detectors located symmetrically to each other, both at 165º. Measurements were made for two sample tilt angles, 0º and 30º. Composition profiles for the as-deposited samples were determined using the NDF software.[53] For the $^{14}$N, $^{16}$O and $^{28}$Si data, the cross-sections given by Gurbich were used.[54] The area analysed was about 0.5×0.5 $mm^2$. The uncertainty in the N concentrations is between 3 to 5 at. %. The structure and phase distribution of the coatings were assessed by X-ray diffraction (XRD), using a Bruker AXS Discover D8 diffractometer, operating with Cu $K_\alpha$ radiation and in a Bragg-Brentano configuration. The XRD patterns were deconvoluted and fitted with a Pearson VII function to determine the structural characteristics of the films, such as the peak position (2θ), the full width at half maximum (FWHM) and the crystallite size. Morphological features of the samples were probed by scanning electron microscopy (SEM), carried out in a FEI Quanta 400FEG ESEM microscope operating at 15 keV. The resistivity measurements were performed using the four-probe van der Pauw method[55] at room temperature.

### *2.3. Electrochemical behaviour*

The Ag:TiN-coated TPU substrates were rinsed in water and dried with a hair drier, prior to all electrochemical experiments. A synthetic sweat solution with a pH of 4.7 containing ammonium and sodium chloride, urea, lactic acid and acetic acid was used in all electrochemical studies, in order to simulate the behaviour of the electrode in contact with the body sweat.[56] The plasma discharge GLAD sputtered samples were immersed in the synthetic sweat solution for 2h before all experiments, in order to allow stabilization with the electrolyte. The geometrical area of the samples was kept constant in all runs. Cyclic voltammetry (CV) curves were performed at a constant sweep rate of 25 mV/s, using the Gamry G300 equipment (Gamry Instruments, USA) driven by the Gamry PHE200 software. The electrochemical impedance spectroscopy (EIS) studies were performed at the open circuit potential (OCP) for frequencies ranging from 10 kHz to 2 mHz, with a 7 mV (RMS) AC probe signal, using the EIS300 software from Gamry. All potentials were measured against a saturated calomel electrode (SCE) and a platinum wire was used as counter electrode. Simulation of the experimental data was also performed with Gamry software. The electrochemical noise data was acquired using the Gamry ESA410 software, by immersing two identical samples (same sputtering batch) in the synthetic sweat solution. Two sintered Ag/AgCl commercial electrodes (B10, EASYCAP GmbH, Germany) were used as comparison reference. The data was acquired using a 1000 Hz sampling rate for a period of 12 minutes and then analysed using a custom MatLab (The Mathworks Inc., USA) algorithm. The electrochemical noise analysis was performed by first applying a 20th order Butterworth bandpass filter with cut-off frequencies at 0.5 and 100 Hz. The first 10 seconds of each filtered data set were neglected to avoid including considerable filter artefact in subsequent evaluations. Then, successive segments of 30 seconds were considered for the calculation of the RMS values of noise and drift rate, over the total acquisition times. The power spectral density (Welch estimation) was calculated for 12 minutes segments, representative of all the Ag/AgCl commercial electrodes, pure TiN and Ag:TiN sample couples.

## 3. RESULTS AND DISCUSSION

### *3.1. Morphological, structural and electrical characterization*

RBS composition analysis showed that there was a roughly constant composition throughout all samples, with a N/Ti atomic concentration ratio of about 0.7 and a Ag atomic content of approximately 10 at.%. In spite of the different architectures and the correspondent changes in the deposition characteristics, the use of the same target and the constant deposition parameters may explain the almost constant composition profiles.

The morphological features of the GLAD sputtered Ag:TiN coatings are patent in Figure 2. The SEM images clearly show that the change in the incidence angle (α, from 0 to 40 and 80º) and zigzag periods (2 and 4, both at α = 80º) translates into significant morphological alterations regarding the correspondent column angle (ß) and related porosity. The films deposited with lower α angle are compact and almost featureless (with α = 40º, small traces of columnar definition are noticeable). In opposition, the coatings sputtered with α = 80º (especially the ones with 2 and 4 zigzag periods) are highly porous. Note that the film prepared with α = 80º exhibits enhanced column definition. This porosity increase is closely related with the increase of the number of zigzag periods [18,21,24,29,32,49].

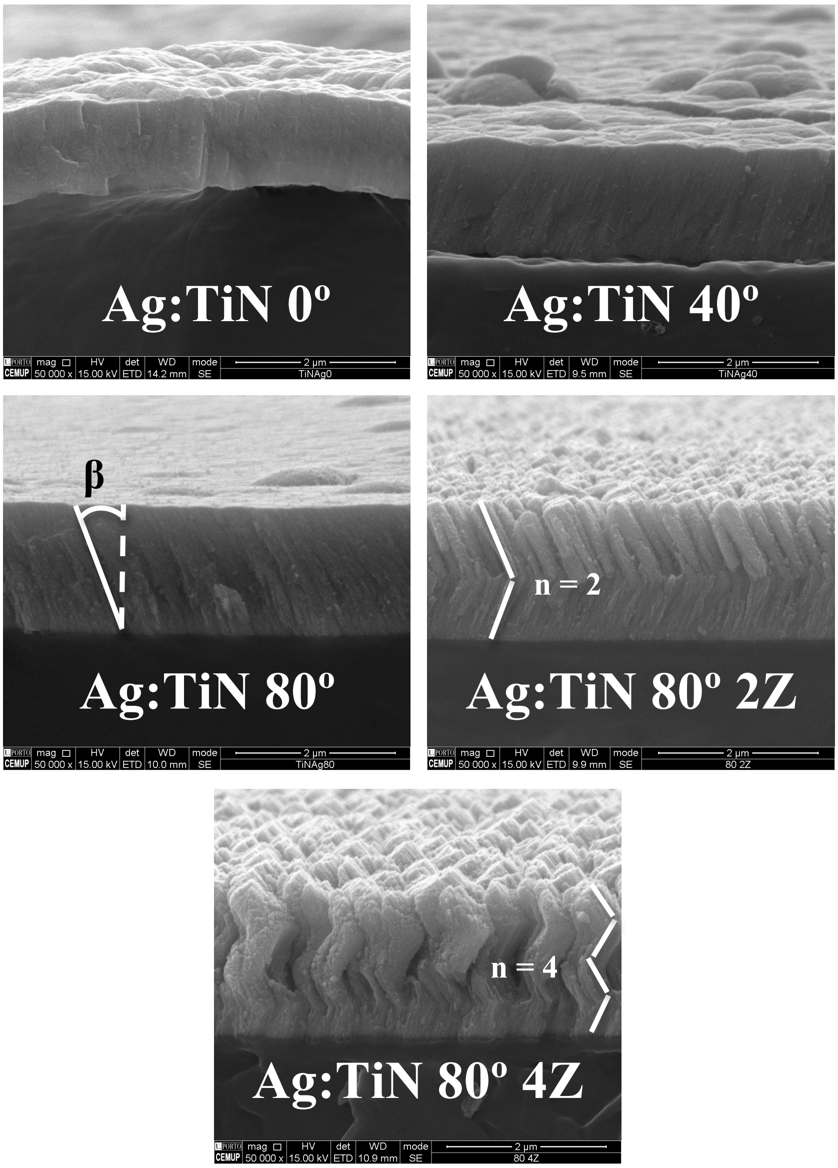

**Figure 2.** Morphological features of the GLAD sputtered Ag:TiN samples evidencing their distinct architectures and zigzag periods (n = 2 and 4).

The obtained ß angles corroborate the morphology and porosity changes, since they vary from a minimum of 23º (for the compact α = 40º sample) to an average of 29º for the porous films. Moreover, the results are in accordance with a previous study by the authors[49], where Ag-doped stoichiometric TiN films sputtered into glass and silicon substrates were analysed and the samples suffered similar changes (porosity increase and column disaggregation) with increasing α angles.

From the XRD patterns that are present in Figure 3, it is possible to see the structural evolution of the samples according to the α angle increase and their different architectures. Despite the baseline noise present in all diffractograms (consistent with low crystallinity, which can be attributed to the particularities of thin films deposition in polymeric-based substrates – low deposition temperatures, hence low mobility of the sputtered species[57]), the structural behaviour of the GLAD sputtered Ag:TiN samples seems to be, *a priori*, independent from their porosity and morphological features that were already analysed. Thus, both the dense and porous samples exhibit the main fcc TiN crystallographic phase planes (ICSD card no. 184916) – (111) at 36.7º, (002) at 42.6º and (022) at 61.8º. An important point is that no substantial shift of the more significant TiN phases is perceivable, meaning that a relatively stable TiN matrix was grown.

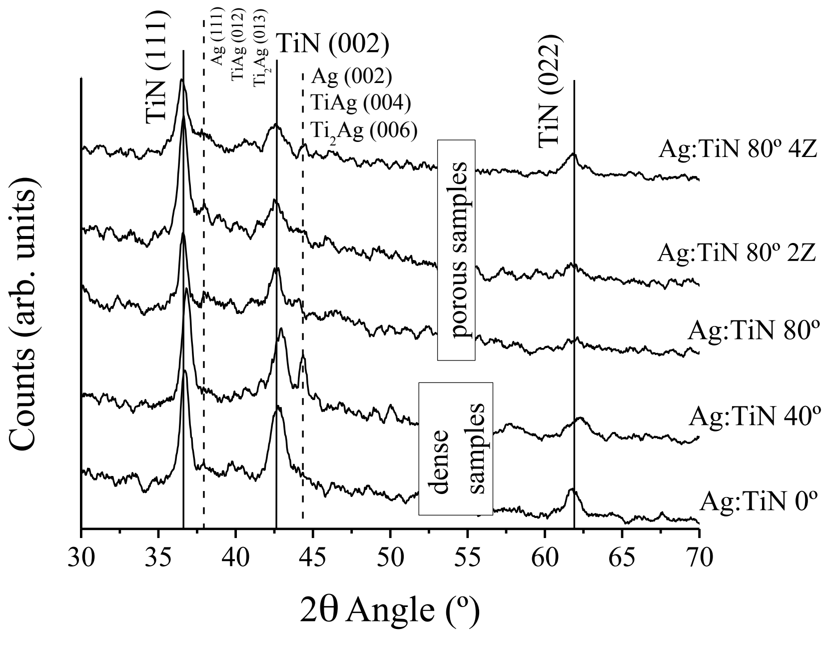

**Figure 3.** XRD diffractograms of the GLAD sputtered Ag:TiN coatings.

Regarding the peaks at 38.1º and 44.1º, they may be ascribed either to the tetragonal TiAg (012) and (004) planes (ICSD card no. 605934), $Ti_2Ag$ (013) and (006) planes (ICSD card no. 605935), or even the (111) and (002) planes of the fcc Ag phase (ICSD card no. 181730). Indeed, the absence of the Ti characteristic peaks in the diffractograms of Figure 3 and the fact that no evidence of Ag particles was found on SEM images (Figure 2) strongly suggest that $Ti_xAg$ intermetallic phases may exist in the Ag:TiN films.[58,59] Note that the used sputtering conditions – low temperature and no bias, hence low mobility of the sputtered species and low attained crystallinity – favours the growth of coatings far from the thermodynamic equilibrium. The occurrence of a Ag/TiAg/$Ti_2Ag$ phase mixture was already hypothesized in previous works by the authors.[50,58] Also, due the low amounts of Ag concentration and the low intensity of the Ag-related phase peaks (Ag/TiAg/$Ti_2Ag$), no reliable quantification of the Ag phase grain size was possible. This could mean that the poorly crystallized Ag-related phase may not be able to form a coherent diffraction pattern, which is evidenced by the broad peak that can be seen around 38.1º. As for the TiN-related grain size, taking into account the most intense phase – fcc TiN (111) – it was found to be 11±2 nm.

In opposition to the structural behaviour, the resistivity evolution of the GLAD sputtered Ag:TiN samples, Figure 4, is strongly influenced by the morphological features of the coatings.

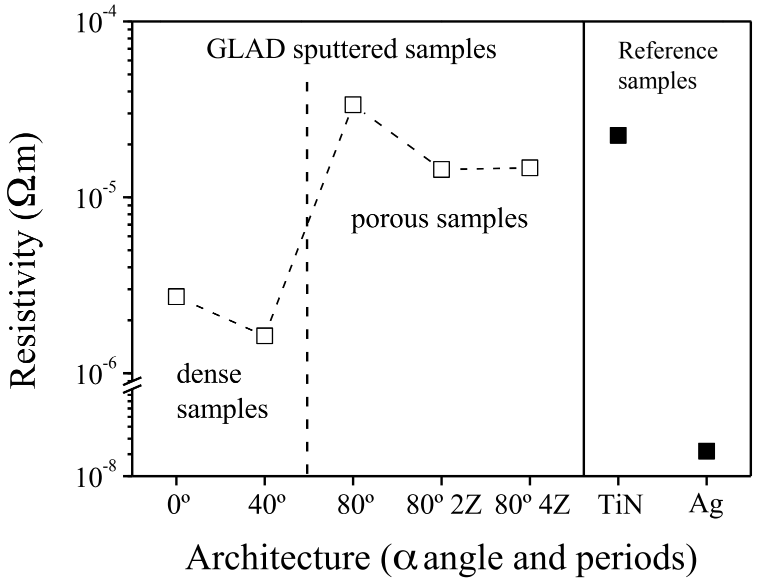

**Figure. 4.** Resistivity behaviour according to the different architectures and periods of the GLAD sputtered Ag:TiN thin films, as well as for the TiN (adapted from ref.[50]) and Ag reference samples. The error associated to all measurements was always below 1% and the attachment of the contacts was checked prior to every measurement (the I/V correlation was always very close to 1).

Taking a closer look at Figure 4, it is possible to see significant resistivity differences between the dense and porous samples, as already observed by the authors.[49] With increasing α angles, from 40 to 80º (and consequent increase of ß angles from 23 to 29º), the resistivity values suffer an almost one order of magnitude increase, varying from the $10^{-6}$ to the $10^{-5}$ Ω.m range. This increase derives from the observed porosity increase[29,49,60] (see Figure 2), which should lead to increased scattering at the interface of the columns, as predicted by the Matthiessen's rule.[61] The Matthiessen's rule takes into account several morphological and structural parameters that contribute to the resistivity evolution, such as scattering from phonons, impurities, defects, grain boundaries and surface scattering. Note that the reference stoichiometric TiN sample also shows high levels of porosity and extensive column disaggregation (see refs.[50,51]), presenting resistivity values that are also in the $10^{-5}$ Ω.m range. This translates the paramount influence of the porosity of the samples and also of the sputtering parameters, namely the used substrate temperature (no temperature was used in the present study for the coating of the polyurethane substrates). Hence, the charge carrier mobility should be significantly decreased, thus reducing the electronic transport properties of the GLAD sputtered films. Regarding the increase of the number of zigzag periods (from 2 to 4), a slight decrease of the resistivity values is attained (although remaining in the $10^{-5}$ Ω.m range), a fact that was also observed by the authors in a previous work.[49]

### *3.2. Electrochemical evaluation of the sputtered Ag:TiN films*

#### *3.2.1. Cyclic Voltammetry*

The cyclic voltammograms of the GLAD sputtered Ag:TiN samples, Figure 5, clearly illustrates the striking effects of the α angle variation on the electrochemical properties of the films.

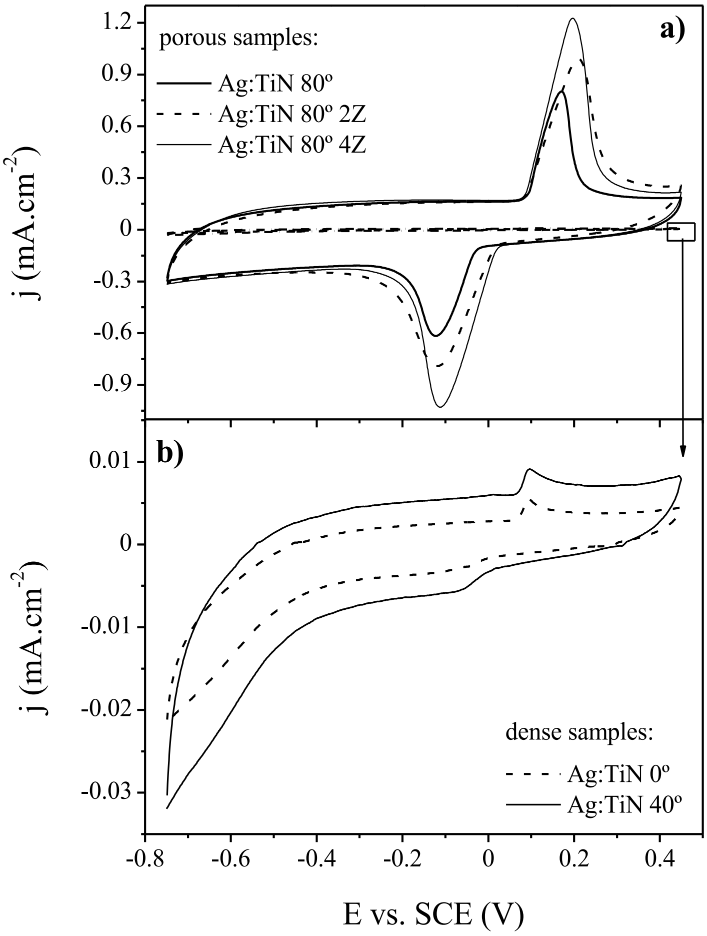

**Figure 5.** Cyclic voltammograms performed with a sweep rate of 25 mV/s of (a) the GLAD sputtered Ag:TiN samples and (b) magnification showing the behaviour of the more compact coatings, Ag:TiN 0º and Ag:TiN 40º.

Taking into account the anodic curve, the formation of an AgCl layer is identified by the occurrence of a peak around 0.1-0.2 V in all voltammograms.[62-65] Furthermore, due to the observed current increase when α increases from 40º to 80º, a shift of the anodic peak is noticeable in the porous samples, which can be attributed to the ohmic drop that occurs through the AgCl film.[65] Note that higher anodic currents indicate the formation of thicker AgCl films, thus a more pronounced potential shift is expected. The cathodic peaks around -0.1 V depict the reduction of the AgCl layer formed during the anodic sweep.

The current plateau extending from about -0.4 V to 0.0 V corresponds to a purely capacitive behaviour, therefore it will be proportional to the film/electrolyte exposed area.[51] On the other hand, the anodic peak current will reflect the amount of Ag available at the film/electrolyte interface. Thus, a plot of the normalized anodic peak current vs. normalized sample area (calculated from the capacitance) for all films reveals important information about the morphological and chemical evolution of the samples, Figure 6. First, the porosity increase identified in the SEM images when the α angle increased from 40º to 80º, Figure 2, corresponds to an eighty-fold increase of the real area. Second, the 80-times area increase corresponds to a 300-fold increase of the anodic peak current. Hence, the increase of surface Ag cannot be fully ascribed to the surface area increase and it should be concluded that the increase of the α angle leads both to film morphological changes (porosity increase) and chemical changes (higher surface Ag content).

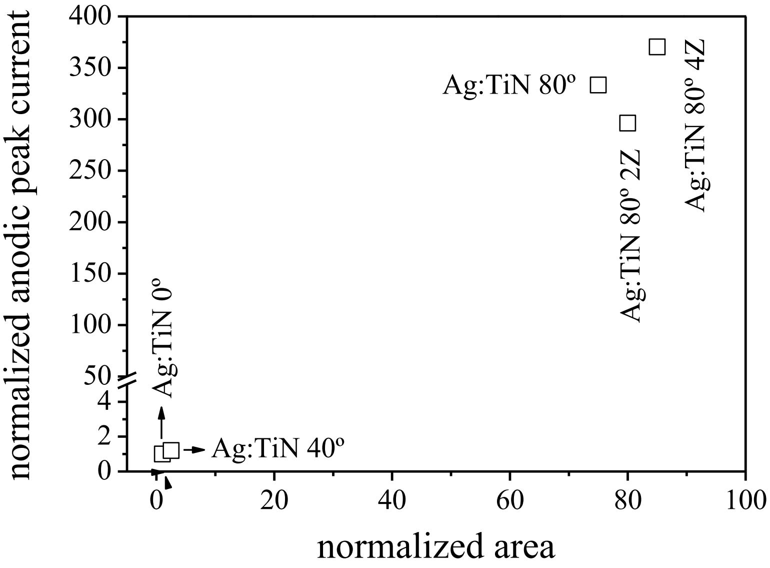

**Figure 6.** Plot of the normalized anodic peak current vs. normalized area of the GLAD sputtered Ag:TiN coatings.

To summarize, the voltammetric findings may attest the pivotal role of the α angle in the properties of the GLAD sputtered Ag:TiN films, namely regarding the increase of specific film area and Ag content in contact with the electrolyte.

### *3.2.2. Electrochemical Impedance Spectroscopy (EIS)*

Figure 7 depicts the Bode diagrams of representative Ag:TiN GLAD sputtered samples. Reference stoichiometric TiN and pure Ag samples spectra were added for comparison purposes. All impedance values refer to the geometrical area, which was kept constant for all samples.

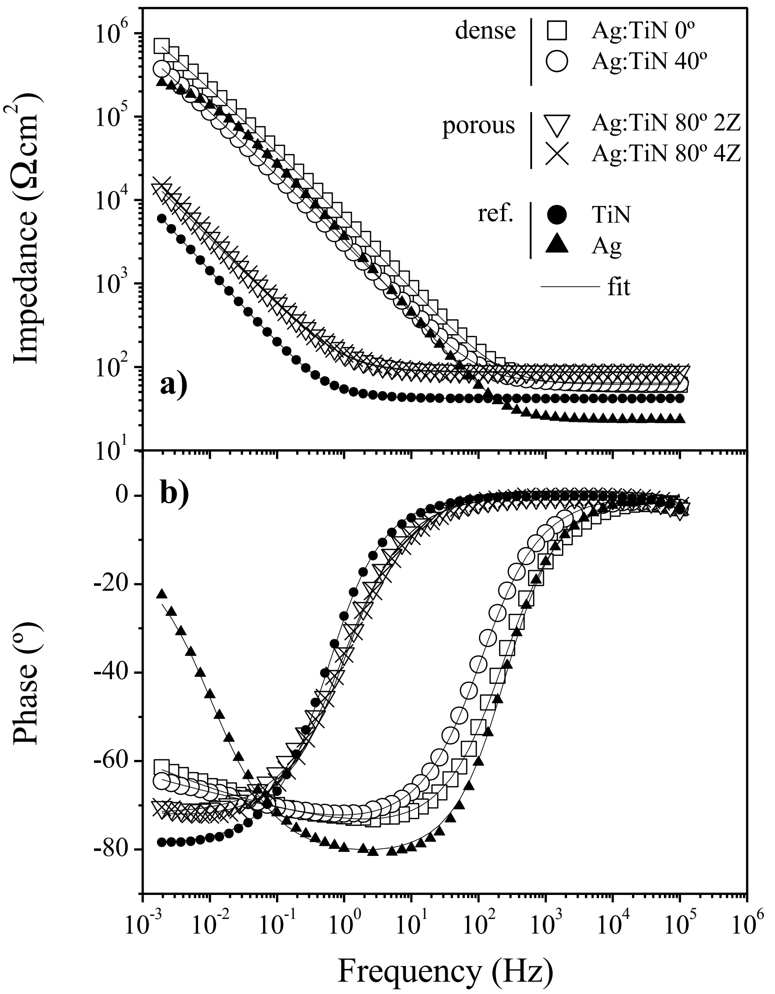

**Figure 7.** Bode diagram exhibiting the (a) impedance and (b) phase behaviour of the GLAD sputtered Ag:TiN films. Pure TiN and Ag samples are plotted for comparison purposes (adapted from ref.[51]).

It is apparent that the denser samples, Ag:TiN 0º and Ag:TiN 40º, exhibit higher impedance values ($7\times10^5$ Ω.cm$^2$ and $4\times10^5$ Ω.cm$^2$ at 2 mHz, respectively) than the porous ones, Figure 7 a). In fact, an important impedance decrease is perceivable with increasing α (and β) angles from 40º to 80º ($2\times10^4$ Ω.cm$^2$ at 2 mHz), which should be ascribed (at least in part) to the area increase verified when passing from the compact to the porous films. The data referring to the porous Ag:TiN 80º sample was not plotted since it was overlaid with the impedance spectra of the other porous samples, Ag:TiN 80º 2Z and Ag:TiN 80º 4Z. Note that the significant increase of the surface Ag content observed for the porous samples in the voltammetric curves cannot entirely justify the observed impedance drop, since the impedance curve for the reference Ag sample is of the same order of that observed for the compact Ag:TiN 0º and 40º films.

On the other hand, from the application side, it is important to keep the electrode/skin impedance as low as possible to facilitate signal transfer (< $10^4$ $\Omega.cm^2$ at 1 kHz, the typical impedance of the wet electrodes/skin interface).[66-68] With regard to this point the porous samples, namely the Ag:TiN 80º, Ag:TiN 80º 2Z and Ag:TiN 80º 4Z films, are the most appropriate ones.

Beyond the impedance differences observed for the compact and porous samples, also the phase curves display quite different structures, Figure 7 b). Indeed, the compact samples (Ag:TiN 0º and Ag:TiN 40º) display a capacitive behaviour that extends to significantly higher frequencies than the porous ones (Ag:TiN 80º 2Z and Ag:TiN 80º 4Z ), an indication of lower interfacial capacitances. Again, this may be ascribed to the specific area difference (higher area leads to lower capacitance values) between the two types of GLAD sputtered Ag:TiN samples. Furthermore, the porous samples seem to display a single time constant in the associated equivalent circuit, unlike the compact samples that display a more complex electrical behaviour, particularly in the low frequency region. The equivalent circuit used to simulate the electrical behaviour of the Ag:TiN/synthetic sweat interface is depicted in Figure 8 a). A constant phase element ($CPE_i$) was used to account for roughness and/or other surface/film inhomogeneities or relaxation processes.[69,70] The impedance of a CPE was defined according to Equation (1)

$$Z_{CPE} = 1/[T(j\omega)^p] \tag{1}$$

where $T$ and $p$ stand for the CPE parameters and $\omega$ is the angular frequency.[66,71] $R_e$ represents the electrolyte resistance and, in the parallel circuit, the upper and lower branches stand for the non-Faradic and Faradic processes, respectively. In the non-Faradic branch, the $CPE_i$ element simulates the series combination of the double-layer and film capacitive behaviour at the film/synthetic sweat interface. Since the OCP values of the GLAD sputtered

Ag:TiN and reference films lay in the water stability region and no redox couples are active in this potential region, the resistance to electronic charge transfer was not considered ($R_{el} = \infty$). In the Faradic branch, $R_p$ stands for the polarization resistance related with Faradic interfacial processes and $W_\sigma$ (semi-infinite Warburg diffusion element) was used to take account of the ionic diffusion processes occurring within the film. The Warburg diffusion coefficient ($\sigma$) was calculated from Equation (2):[57]

$$\sigma = 1/(\sqrt{2}T_W) \qquad (2)$$

This circuit was effective for simulating the electrical behaviour of the Ag:TiN 0º and Ag:TiN 40º dense samples. In the first trials, a CPE was inserted in parallel with $R_p$, in order to simulate the capacitance associated to the Faradic processes. However, *T* and *p* were dependent on the initial simulation parameters and were obtained with large associated errors (in excess of 100%).

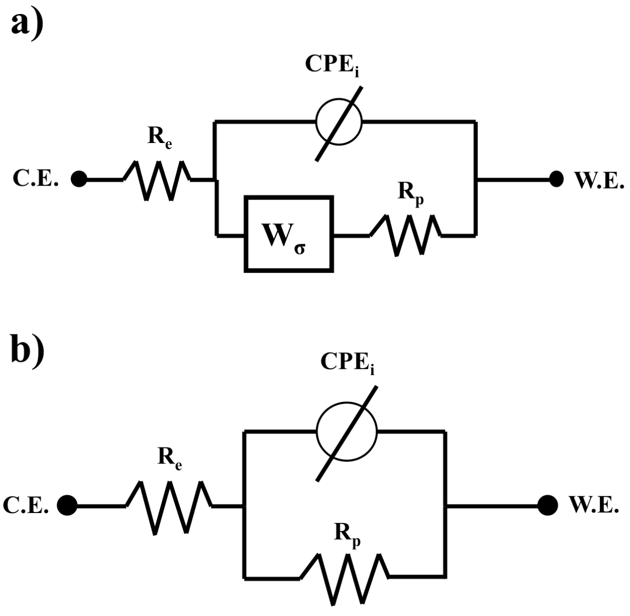

**Figure 8.** Proposed equivalent circuits for the simulation of the Ag:TiN/synthetic sweat interface.

On its turn, for the Ag:TiN 80º, Ag:TiN 80º 2Z and Ag:TiN 80º 4Z samples, as well as for the stoichiometric TiN and pure Ag reference ones, the $T_W$ Warburg parameter was rejected in the simulations (large errors and high $T_W$ values). Therefore, the circuit of Figure 8

b) was used instead, confirming the initial assumption of the existence of a single time constant for these cases.

The simulation of the impedance curves of Figure 7 led to the equivalent circuit parameters presented in Table II. The $R_p$ value for the TiN and Ag reference samples were adapted from a previous work by the authors [51].

**Table II.** EIS fitting parameters.

| Sample | $R_p$ /Ω.cm$^2$ | $R_e$ /Ω.cm$^2$ | $CPE_i$ ($T$) /Ω$^{-1}$.cm$^{-2}$.s$^n$ | $CPE_i$ ($p$) | $T_W$ /Ω$^{-1}$.cm$^{-2}$.s$^{-1/2}$ | $\chi^2$ |
|---|---|---|---|---|---|---|
| **TiN** | $\geq 3\times10^6$ | 41.9 | $7.9\times10^{-3}$ | 0.87 | - | $2\times10^{-4}$ |
| **Ag:TiN 0º** | * | 61.3 | $3.4\times10^{-5}$ | 0.85 | $6.5\times10^{-6}$ | $2\times10^{-4}$ |
| **Ag:TiN 40º** | * | 64.0 | $6.6\times10^{-5}$ | 0.84 | $1.0\times10^{-5}$ | $2\times10^{-4}$ |
| **Ag:TiN 80º** | $\geq 1\times10^7$ | 78.4 | $2.3\times10^{-3}$ | 0.79 | - | $4\times10^{-4}$ |
| **Ag:TiN 80º 2Z** | $\geq 1\times10^6$ | 87.5 | $2.6\times10^{-3}$ | 0.80 | - | $3\times10^{-4}$ |
| **Ag:TiN 80º 4Z** | $\geq 3\times10^5$ | 85.9 | $2.5\times10^{-3}$ | 0.81 | - | $6\times10^{-4}$ |
| **Ag** | $2.5\times10^5$ | 23.2 | $5.7\times10^{-5}$ | 0.89 | - | $3\times10^{-3}$ |

*$R_p$ values obtained with large errors.

Due to the predominantly capacitive behaviour in the low frequency range, Figure 7, the $R_p$ values for the TiN and porous GLAD sputtered Ag:TiN samples (Ag:TiN 80º, Ag:TiN 80º 2Z and Ag:TiN 80º 4Z) could not be calculated. The $R_p$ values could, however, be estimated by using the procedure detailed in reference.[51] The high $R_p$ values (> $10^5$ Ω.cm$^2$) point to the excellent chemical stability of the coatings in chloride medium (synthetic sweat, in the present case). Finally, the $R_p$ values for Ag:TiN 0º and 40º are not reported since they were obtained with large errors, most probably because of the predominant contribution of the Warburg impedance in these cases.

As already observed by Norlin for TiN porous films[66], the sample roughness/porosity influences the $CPE_i$ $T$ and $p$ parameters. $T$ increases almost two orders of magnitude (from

~$10^{-5}$ to ~$10^{-3}$ $\Omega.cm^{-2}.s^{n}$) when the α angle (thus also the porosity) increases from 40º to 80º. Yet, the increase of the number of zigzag periods from 2Z to 4Z does not translate into significant differences of the *T* parameter. It is interesting to note that the *T* increase is of the same order of magnitude of the voltammetric area increase measured for the same samples. As for the $CPE_i$ *p* parameter, its value decreases, as expected, for the porous films, but in general it is close enough to 1 for the $CPE_i$ to be considered an essentially capacitive element.

The porosity increase also affects the $R_e$ values, since the porous films exhibit higher values than the Ag:TiN 0º and Ag:TiN 40º dense samples, an effect that is apparent in the Bode curves at high frequencies, Figure 7 a). This effect should be related with the increased electrolyte resistance inside the pores (see Figure 2).

Finally, the high values obtained for the Warburg coefficient (σ), $1\times10^{5}$ and $7\times10^{4}$ $\Omega.cm^{-2}.s^{-1/2}$ for the Ag:TiN 0º and Ag:TiN 40º samples, respectively, are representative of the ionic blocking properties of the GLAD sputtered dense coatings. Such blocking properties are lost when the films are fractured, as observed with the porous films.

In conclusion, from the impedance behaviour point of view, the porous Ag:TiN 80º, Ag:TiN 80º 2Z and Ag:TiN 80º 4Z thin films seem to be the most appropriate to be used as biomedical electrodes, owing to their good chemical stability and low impedance values.

### *3.2.3. Electrochemical noise and drift analysis*

In order to avoid unwanted masking of the low frequency and/or small amplitude biosignals, reduced drift rates and fast stabilization times are of paramount importance.[57] Consequently, the drift rate of representative GLAD sputtered Ag:TiN samples immersed in the synthetic sweat electrolyte was evaluated and is presented in Figure 9.

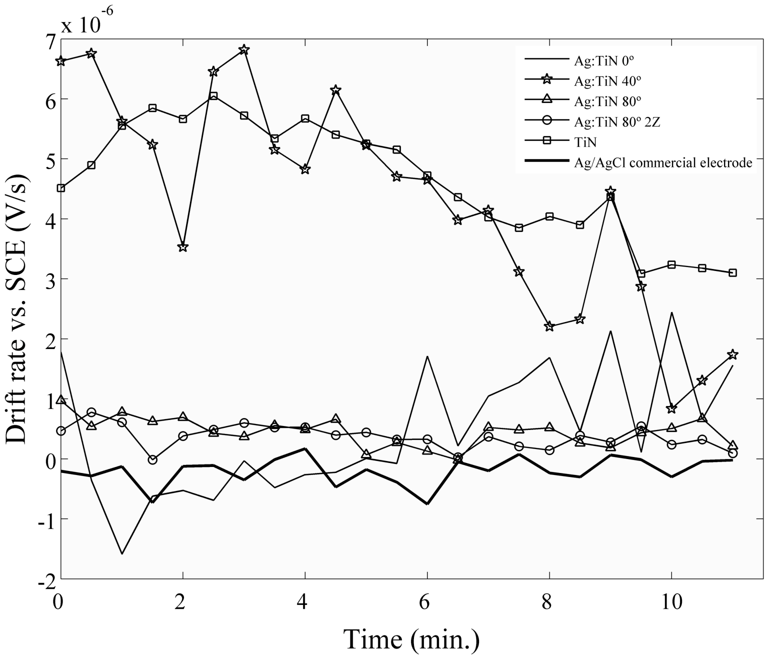

**Figure 9.** Electrochemical potential drift rate evolution of representative GLAD sputtered Ag:TiN films. Pure TiN and Ag/AgCl commercial electrode data was adapted from ref.[51].

Significant differences were found between the dense and the porous samples, which can be related to their different morphologies and architectures. Specifically, the porous Ag:TiN coatings, Ag:TiN 80º and Ag:TiN 80º 2Z, display small drift rates in the range of 1 μV/s and similar to those presented for the commercial Ag/AgCl electrodes, whereas the dense Ag:TiN 0º and Ag:TiN 40º films and the reference TiN sample, display higher or unstable drift rates. Such drift rates may be ascribed to the slow redox processes involving TiN, such as the oxidation of the TiN phase, with the formation of titanium oxynitrides and consequent thickening of the passive film.[72] In opposition, the porous samples display far more stable potential values, close to those of the reference wet Ag/AgCl electrodes. Since this behaviour is in line with the strong increase of Ag at the surface of the films, as confirmed by the voltammetric results of Figure 5, the potential stabilization is possibly related to the formation of an AgCl layer at the surface of the porous coatings.

Moreover, biomedical electrodes should also allow a clean signal transfer from the body to the recording apparatus, meaning that the threshold level of noise at the electrode/skin interface should be considerably lower than the signal amplitude.[70,73,74] Hence, the monitoring of the electrical noise of the films in contact with sweat in the frequency region of interest for the envisaged application (EEG) is of paramount importance, in order to assess the suitability of the developed GLAD sputtered Ag:TiN films to be used as flexible biomedical electrodes.

The power spectral density (PSD) of representative Ag:TiN couples, as well as of a commercial Ag/AgCl electrode, in synthetic sweat are shown in Figure 10.

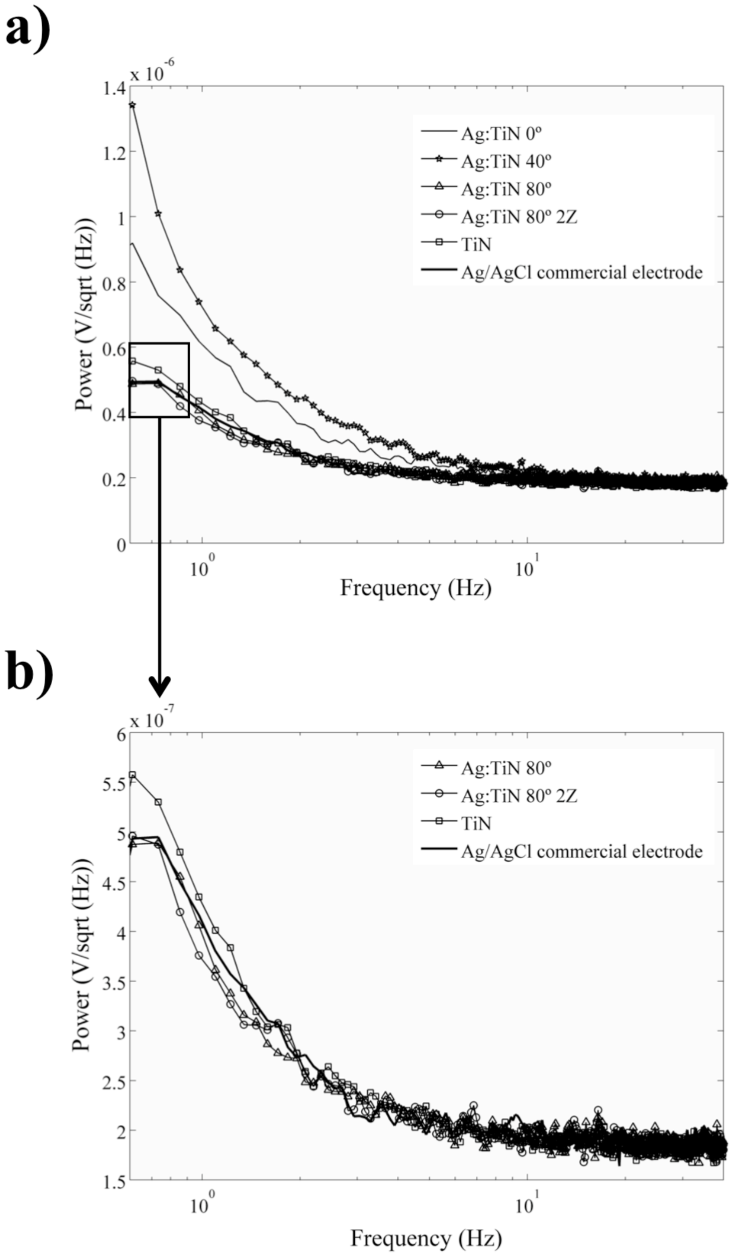

**Figure 10.** Noise power spectral density spectra of representative GLAD sputtered Ag:TiN coatings. Pure TiN and Ag/AgCl commercial electrode data (adapted from ref.[51]) is plotted for comparison purposes.

The noise values follow the 1/(freq.) law commonly associated to slow corroding systems[75], increasing as the frequency decreases. Although the noise level is acceptable for all films, even in the low frequency region, a clear behavioural difference in terms of noise addition can be seen with increasing porosity, Figure 10 a). The dense Ag:TiN 0º and Ag:TiN 40º samples exhibit noise values that are approximately double than those of the porous samples at the lower frequency range for EEG exams (0.5 Hz). Looking in detail at the noise data of the porous Ag:TiN 80º and Ag:TiN 80º 2Z samples, Figure 10 b), no significant differences can be found when comparing with the reference Ag/AgCl commercial electrode, with values ranging from 0.5 to 0.55 μV/√Hz.

To conclude, the noise and drift rate behaviours reinforce the idea that the GLAD sputtered Ag:TiN porous coatings (Ag:TiN 80º, Ag:TiN 80º 2Z and Ag:TiN 80º 4Z) are the most promising ones to be used for the envisaged flexible biomedical electrode application.

## 4. CONCLUSIONS

In the present work, a set of Ag:TiN thins films with 10 at.% Ag were GLAD sputtered onto flexible polyurethane substrates with different architectures, with the ultimate goal of selecting the most promising coating architectures to be used as biomedical electrodes. The plasma discharge GLAD technique was successfully used to tailor the porosity of the samples by continually increasing the plasma incidence angle from 0º to 40º and 80º, and also by changing the architecture of the columns from columnar to zigzag with 2 and 4 periods.

A substantial increase of the electroactive area and surface Ag content were observed when the α angle increased from 40º to 80º, leading to low impedance and low electrochemical noise values, as well as stable potentials (low drift rates), comparable to those of Ag/AgCl commercial electrodes, in the Ag:TiN 80º, Ag:TiN 80º 2Z and Ag:TiN 80º 4Z porous samples. In opposition, the Ag:TiN 0º and Ag:TiN 40º dense samples consistently presented more unstable potential values (higher drift rates), higher impedance values and electrical noise.

No Ag segregation was found in any deposited coating, what was ascribed to the formation of TiAg or $Ti_2Ag$ intermetallics. Hence, the obtained samples should be morphologically and structurally stable.

In conclusion, and regarding the electrochemical results, it is possible to say that the Ag:TiN 80º, Ag:TiN 80º 2Z and Ag:TiN 80º 4Z porous films exhibit the most promising properties for the fabrication of flexible dry biomedical electrodes. The next works by the authors will focus on the optimization of the Ag:TiN/polyurethane interfacial adhesion (through surface plasma activation of the polyurethane substrates), as well as the mechanical and electrical behaviours of the coatings under deformation.

## ACKNOWLEDGEMENTS

This research is partially sponsored by FEDER funds through the program COMPETE – Programa Operacional Factores de Competitividade and by national funds through FCT – Fundação para a Ciência e a Tecnologia, under the projects PEst-C/EME/UI0285/2011, PTDC/SAU-ENB/116850/2010, PTDC/CTM-NAN/112574/2009 and Programa Pessoa 2012/2013 Cooperação Portugal/França, Project no. 27306UA Porous architectures in GRAded CERamic thin films for biosensors - GRACER. The authors would also like to acknowledge CEMUP for SEM analysis and Yantai Wanhua Polyurethanes Co., Ltd for providing the thermoplastic polyurethane pellets. P. Pedrosa acknowledges FCT for the Ph.D. grant SFRH/BD/70035/2010.

## BIBLIOGRAPHY

[1] B.A. Movchan, A.V. Demchishin, "Study of the Structure and Properties of Thick Vacuum Condensates of Nickel. Titanium, Tungsten, Aluminum Oxide and Zirconium Dioxide", Fiz. Metal. Metalloved, 28 (4) (1969) 653-660.

[2] J.A. Thornton, "Influence of apparatus geometry and deposition conditions on the structure and topography of thick sputtered coatings", J. Vac. Sci. Technol., 11(4) (1974) 666-670. DOI: 10.1116/1.1312732.

[3] A. Malaurie, A. Bessaudou, "Numerical simulation of the characteristics of the different metallic species falling on the growing film in d.c. magnetron sputtering", Thin Solid Films, 286 (1996) 305-316. DOI: 10.1016/S0040-6090(95)08523-8.

[4] V.I. Trofimov, "Morphology evolution in a growing film", Thin Solid Films, 428 (2003) 56-65. DOI: 10.1016/S0040-6090(02)01270-1.

[5] H. Wei, Z. Liu, K. Yao, "The influence of the incidence energy of deposited particles on the growth morphology of thin films", Vacuum, 57 (2000) 87-97. DOI: 10.1016/S0042-207X(00)00112-3.

[6] R. Messier, A.P. Giri, R.A. Roy, "Revised structure zone model for thin film physical structure", J. Vac. Sci. Technol., A 2(2) (1984) 500-503. DOI: 10.1116/1.572604.

[7] A. Anders, "A structure zone diagram including plasma-based deposition and ion etching", Thin Solid Films, 518 (2010) 4087-4090. DOI: 10.1016/j.tsf.2009.10.145.

[8] L. Dong, R.W. Smith, D.J. Srolovitz, "A two-dimensional molecular dynamics simulation of thin film growth by oblique deposition", J. Appl. Phys., 80(10), (1996) 5682-5690. DOI: 10.1063/1.363621.

[9] R.N. Tait, T. Smy, J.M. Brett, "Structural anisotropy in oblique incidence thin metal films", J. Vac. Sci. Technol., A 10(4), (1992) 1518-1521. DOI: 10.1116/1.578037.

[10] G.W. Mbise, G.A. Niklasson, C.G. Granqvist, "Obliquely evaporated Cr films with large angular selectivity", J. Appl. Phys., 77(6), (1995) 2816-2818. DOI: 10.1063/1.358690.

[11] R.J. Ditchburn, G.B. Smith, "Useful angular selectivity in oblique columnar aluminum", J. Appl. Phys., 69(6) (1991) 3769-3771. DOI: 10.1063/1.348474.

[12] I. Hodgkinson Q.H. Wu, A. McPhun, "Incremental-growth model for the deposition of spatially modulated thin film nanostructures", J. Vac. Sci. Technol., B 16(5) (1998) 2811-2816. DOI: 10.1116/1.590276.

[13] N.O. Young, J. Kowal, "Optically Active Fluorite Films",Nature, 183 (1959) 104-105. DOI: 10.1038/183104a0.

[14] D.O. Smith, "Static and Dynamic Behavior of Thin Permalloy Films", J. Appl. Phys., 29

(1959) 264-265. DOI: 10.1063/1.1723097.

[15] J.M. Nieuwenhuizen, H.B. Haanstra, "Microfractography of thin films", Philips Techn. Rev., 27(3-4) (1966) 87-91.

[16] H.J. Leamy, A.G. Dirks, "Microstructure and magnetism in amorphous rare-earth-transition-metal thin films. I. Microstructure", J. Appl. Phys., 49(6) (1978) 3430-3438. DOI: 10.1063/1.325249.

[17] T.G. Knorr, R.W. Hoffman, "Dependence of Geometric Magnetic Anisotropy in Thin Iron Films", Phys. Rev., 116 (1959) 1620. DOI: 10.1103/PhysRev.116.1620.2.

[18] J. Lintymer, N. Martin, J.M. Chappé, J. Takadoum, P. Delobelle, "Modeling of Young's modulus, hardness and stiffness of chromium zigzag multilayers sputter deposited", Thin Solid Films, 503 (2006) 177-189. DOI: 10.1016/j.tsf.2005.12.157.

[19] K. Robbie, M.J. Brett, A. Lakhtakia, "Chiral sculptured thin films", Nature, 384 (1996) 616-616. DOI: 10.1038/384616a0.

[20] M.J. Brett, J. Hawkeye, M. Matthew, "New Materials at a Glance", Science, 319 (2008) 1192-1193. DOI: 10.1126/science.1153910.

[21] A. Besnard, N. Martin, L. Carpentier, B. Gallas, "A theoretical model for the electrical properties of chromium thin films sputter deposited at oblique incidence", J. Phys. D Appl. Phys., 44 (2011) 215301-8. DOI: 10.1088/0022-3727/44/21/215301.

[22] C.-C. Li, J.-L. Huang, R.-J. Lin, H.-P. Lin, D.-F. Lii, C.-P. Liu, "Microstructures, surface areas, and oxygen absorption of Ti and Ti–Zr–V films grown using glancing-angle sputtering", J. Mater. Res., 23 (2008) 579-587. DOI: 10.1557/JMR.2008.0076.

[23] W. Smith, Z.Y. Zhang, Y.P. Zhao, "Structural and optical characterization of $WO_3$ nanorods/films prepared by oblique angle deposition", J. Vac. Sci. Technol., B25 (2007) 1875-1881. DOI: 10.1116/1.2799968.

[24] C. Charles, N. Martin, M. Devel, " Optical properties of $WO_3$ thin films modelled by FDTD and fabricated by glancing angle deposition", J. Nanosci. Nanotech., 12 (2012) 9125-9130. DOI: 10.1166/jnn.2012.6761.

[25] K. Robbie, C. Shafai, M.J. Brett, "Thin films with nanometer-scale pillar microstructure", J. Mater. Res., 14(7) (1999) 3158-3163. DOI: 10.1557/JMR.1999.0423.

[26] M.T. Taschuk, M.M. Hawkeye, M.J. Brett, "Glancing Angle Deposition", in "Handbook of deposition technologies and for films and coatings", by P.M. Martin, Third Edition, Elsevier, Oxford, (2010). ISBN: 978-0-8155-2031-3.

[27] M.M. Hawkeye, M.J. Brett, "Glancing angle deposition: Fabrication, properties, and applications of micro- and nanostructured thin films", J. Vac. Sci. Technol., 25(5) (2007)

1317-1335. DOI: 10.1116/1.2764082.

[28] Y.P. Zhao, D.X. Ye, G.C. Wang, T.M. Lu, “Novel nano-column and nano-flower arrays by glancing angle deposition”, Nano Lett., 2 (2002) 351-354. DOI: 10.1021/nl0157041.

[29] J. Lintymer, J. Gavoille, N. Martin, J. Takadoum, “Glancing angle deposition to modify microstructure and properties of sputter deposited chromium thin films”, Surf. Coat. Technol., 174 (2003) 316-323. DOI: 10.1016/S0257-8972Ž03.00413-4.

[30] L. González-García, J. Parra-Barranco, J.R. Sanchéz-Valencia, A. Barranco, A. Borrás, A.R. Gonzaléz-Elipe, M.C. García-Gutiérrez, J.J. Hernandéz, D.R. Rueda, T.A. Ezquerra, “Correlation lengths, porosity and water adsorption in $TiO_2$ thin films prepared by glancing angle deposition”, Nanotechnology, 23 (2012) 205701-10. DOI: 10.1088/0957-4484/23/20/205701.

[31] T. Karabacak, A. Mallikarjunan, J.P. Singh, D.X. Ye, G.C. Wang, T.M. Lu, “β-phase tungsten nanorod formation by oblique-angle sputter deposition”, Appl. Phys. Lett., 83 (2003) 3096-3098. DOI: 10.1063/1.1618944.

[32] A. Besnard, N. Martin, F. Sthal, L. Carpentier, J.Y. Rauch, “Metal-to-dieletric transition induced by annealing of oriented titanium thin films”, Funct. Mater. Lett., 6 (2013) 1250051-5. DOI: 10.1142/S1793604712500518.

[33] M.T. Taschuk, K.M. Krause, J.J. Steele, M.A. Summers, M.J. Brett, “Growth scaling of metal oxide columnar thin films deposited by glancing angle depositions”, J. Vac. Sci. Technol., 27 (2009) 2106-2111. DOI: 10.1116/1.3196782.

[34] L.-C. Chen, C.-H. Tien, X. Liu, B. Xu, “Zigzag and Helical AlN Layer Prepared by Glancing Angle Deposition and Its Application as a Buffer Layer in a GaN-Based Light-Emitting Diode”, J. Nanomater., 2012 (2012) 409123-6. DOI: 10.1155/2012/409123.

[35] J.R. Frederick, J. D’Arcy-Gall, D. Gall, “Growth of epitaxial CrN on MgO (001): Role of deposition angle on surface morphological evolution”, Thin Solid Films, 494 (1-2) (2006) 330-335. DOI: 10.1016/j.tsf.2005.08.244.

[36] M. Teplan, “Fundamentals of EEG measurement”, Meas. Sci. Rev., 2 (2) (2002) 1-11.

[37] E. McAdams, “Bioelectrodes”, in Encyclopaedia of Medical Devices and Instrumentation, Webster J. G. Ed., New York, Wiley, (1988) 120-166. DOI: 10.1002/ 0471732877.

[38] A. Searle, L. Kirkup, “A direct comparison of wet, dry and insulating bioelectric recording electrodes”, Physiol. Meas. 22 (2000) 271-283. DOI: 10.1088/0967-3334/21/2/307.

[39] L.T. Cunha, P. Pedrosa, C.J. Tavares, E. Alves, F. Vaz, C. Fonseca, “The role of composition, morphology and crystalline structure in the electrochemical behaviour of $TiN_x$

thin films for dry electrode sensor materials", Electrochim. Acta 55 (1) (2009) 59–67. DOI: 10.1016/j.electacta.2009.08.004.

[40] G. Gargiulo, R.A. Calvo, P. Bifulco, M. Cesarelli, C. Jin, A. Mohamed, A. van Schaik, "A new EEG recording system for passive dry electrodes", Clin. Neurophysiol. 121 (5) (2010) 686–693. DOI: 10.1016/j.clinph.2009.12.025.

[41] C. Fonseca, J.P. Silva Cunha, R.E. Martins, V. Ferreira, J.P. Marques de Sá, M.A. Barbosa, A. Martins Silva, "A novel dry active electrode for EEG recording", IEEE Trans. Biomed. Eng. 54 (1) (2007) 162–165. DOI: 10.1109/TBME.2006.884649.

[42] K.-P. Hoffmann and R. Ruff, "Flexible Dry Surface-electrodes for ECG Long-term Monitoring", Proceedings of the 29th Annual International Conference of the IEEE EMBS, Lyon, France, August, (2007) 23-26.

[43] J. Baek, J. An, J. Choi, K. Park, S. Lee, "Flexible polymeric dry electrodes for the long-term monitoring of ECG", Sens. Actuators A 143 (2008) 423–429. DOI: 10.1016/j.sna.2007.11.019.

[44] A. Gruetzmann, S. Hansen, J. Muller, "Novel dry electrodes for ECG monitoring", Physiol. Meas. 28 (2007) 1375–1390. DOI: 10.1088/0967-3334/28/11/005.

[45] V. Marozas, A. Petrenas, S. Daukantas, A Lukosevicius, "A comparison of conductive textile-based and Silver/Silver chloride gel electrodes in exercise electrocardiogram recordings", J. Electrocardiology 44 (2011) 189–194. DOI: 10.1016/j.jelectrocard.2010.12.004.

[46] C.-Y. Chen, C.-L. Chang, T.-F. Chien, C.-H. Luo, "Flexible PDMS electrode for one-point wearable wireless bio-potential acquisition", Sens. Actuators A, 203 (2013) 20-28. DOI: 10.1016/j.sna.2013.08.010.

[47] P. Salvo, R. Raedt, E. Carrette, D. Schaubroeck, J. Vanfleteren, L. Cardon, "A 3D printed dry electrode for ECG/EEG recording", Sens. Actuators A, 174 (2012) 96-102. DOI: 10.1016/j.sna.2011.12.017.

[48] S. Kaitainen, A. Kutvonen, M. Suvanto, T.T Pakkanen, R. Lappalainen, S. Myllymaa, "Liquid silicone rubber (LSR)-based dry bioelectrodes: The effect of surface micropillar structuring and silver coating on contact impedance", Sens. Actuators A, 206 (2014) 22-29. DOI: 10.1016/j.sna.2013.11.020.

[49] P. Pedrosa, C. Lopes, N. Martin, C. Fonseca, F. Vaz, "Electrical characterization of Ag:TiN thin films produced by glancing angle deposition", Materials Letters 115 (2014) 136–139. DOI: 10.1016/j.matlet.2013.10.044.

[50] P. Pedrosa, D. Machado, C. Lopes, E. Alves, N.P. Barradas, N. Martin, F. Macedo, C.

Fonseca, F. Vaz, “Nanocomposite Ag:TiN thin films for dry biopotential electrodes”, Appl. Surf. Sci. 285P (2013) 40-48. DOI: 10.1016/j.apsusc.2013.07.154.

[51] P. Pedrosa, E. Alves, N.P. Barradas, N. Martin, P. Fiedler, J. Haueisen, F. Vaz, C. Fonseca, “Electrochemical behaviour of nanocomposite $Ag_x$:TiN thin filmsfor dry biopotential electrodes”, Electrochim. Acta 125 (2014) 48-57. DOI: 10.1016/j.electacta.2014.01.082.

[52] P. Pedrosa, D. Machado, M. Evaristo, A. Cavaleiro, C. Fonseca, F. Vaz, “Ag:TiN nanocomposite thin films for bioelectrodes: The effect of annealing treatments on the electrical and mechanical behavior”, J. Vac. Sci. Technol. A, 32 (2014), 031515. DOI: 10.1116/1.4873555.

[53] N.P. Barradas, C. Jeynes, R.P. Webb, “Simulated annealing analysis of Rutherford backscattering data”, Appl. Phys. Lett. 71 (1997) 291. DOI: 10.1063/1.119524.

[54] A.F. Gurbich, “Evaluated differential cross-sections for IBA”, Nucl. Instr. and Meth. B, 268 (2010) 1703. DOI: 10.1016/j.nimb.2010.02.011.

[55] L.J. van der Pauw, “A method of measuring specific resistivity and Hall effect of disks of arbitrary shape”, Philips Res. Repts., 13 (1958) 1-9.

[56] J.-P. Randin, “Corrosion behavior of nickel-containing alloys in artificial sweat”, J. Biomed. Mat. Res. 22 (1988) 649. DOI: 10.1002/jbm.820220706.

[57] P. Pedrosa, E. Alves, N.P. Barradas, P. Fiedler, J. Haueisen, F. Vaz, C. Fonseca, “$TiN_x$ coated polycarbonate for bio-electrode applications”, Corros. Sci. 56 (2012) 49–57. DOI: 10.1016/j.corsci.2011.11.008.

[58] C. Lopes, C. Gonçalves, P. Pedrosa, F. Macedo, E. Alves, N.P. Barradas, N. Martin, C. Fonseca, F. Vaz, “$TiAg_x$ thin films for lower limb prosthesis pressure sensors: Effect of composition and structural changes on the electrical and thermal response of the films”, Appl. Surf. Sci. 285P (2013) 10-18. DOI: 10.1016/j.apsusc.2013.07.021.

[59] M. Takahashi, M. Kikuchi Y. Takada, O. Okuno, “Corrosion Resistance of Dental Ti-Ag Alloys in NaCl Solution”, Mater. Trans., JIM 51 (2010) 762-766. DOI: 10.2320/matertrans.M2009355.

[60] J. Lintymer, N. Martin, J-.M. Chappé, P. Delobelle, J. Takadoum, “Influence of zigzag microstructure on mechanical and electrical properties of chromium multilayered thin films”, Surf. Coat. Technol., 180-181 (2004) 26-32. DOI:10.1016/j.surfcoat.2003.10.027.

[61] K.-Y. Chan, T.-Y. Tou, B.-S. Teo, “Thickness dependence of the structural and electrical properties of copper films deposited by dc magnetron sputtering technique”, Microelectron. J. 37 (2006) 608-612. DOI: 10.1016/j.mejo.2005.09.016.

[62] V. I. Birss, C.K. Smith, “The anodic behavior of silver in chloride solutions—I. The formation and reduction of thin Silver chloride films”, Electrochim. Acta, 32 (1987) 259-268. DOI: 10.1016/0013-4686(87)85033-8.

[63] B.M. Jović, V.D. Jović, D.M. Dražić, “Kinetics of chloride ion adsorption and the mechanism of AgCl layer formation on the (111), (100) and (110) faces of Ag”, J. Electroanal. Chem. 399 (1995) 197-206. DOI: 10.1016/0022-0728(95)04291-1.

[64] J. Peng, Y. Deng, D. Wang, X. Jin, G.Z. Chen, “Cyclic voltammetry of electroactive and insulative compounds in solid state: A revisit of AgCl in aqueous solutions assisted by metallic cavity electrode and chemically modified electrode”, J. Electroanal. Chem. 627 (2009) 28–40. DOI: 10.1016/j.jelechem.2008.12.016.

[65] H.H. Hassan, M.A.M. Ibrahim, S.S. Abd El Rehim, M.A. Amin, “Comparative Studies of the Electrochemical Behavior of Silver Electrode in Chloride, Bromide and Iodide Aqueous Solutions”, Int. J. Electrochem. Sci., 5 (2010) 278 – 294.

[66] A. Norlin, J. Pan, C. Leygraf, “Investigation of Electrochemical Behavior of Stimulation/Sensing Materials for Pacemaker Electrode Applications I. Pt, Ti, and TiN Coated Electrodes”, J. Electrochem. Soc., 152 (2005) J7–J15. DOI: 10.1149/1.1842092.

[67] S. Grimmes, “Impedance measurement of individual skin surface electrodes”, Med. & Biol. Eng. And Comput., 21 (1983) 750-755.

[68] J. Rosell, J. Colominas, P. Riu, R. Pallas-Areny, J.G. Webster, “Skin Impedance From 1 Hz to 1 MHz”, IEEE Trans. Biomed. Eng., 35 (1988) 649-651.

[69] J.R. Macdonald, “Impedance Spectroscopy Emphasizing Solid Materials and Systems”, Wiley, New York, 1987. DOI: 10.1016/0584-8539(88)80155-7.

[70] D.T. Godin, P.A. Parker, R.N. Scott, “Noise characteristics of stainless-steel surface electrodes”, Med. & Biol. Eng. & Comput., 29 (1991) 585-590.

[71] M. Orazem, B. Tribollet, “Electrochemical Impedance Spectroscopy”, John Wiley & Sons, 2008, 233. ISBN 978-0-470-04140-6.

[72] M.G. Fontana, N.D. Greene, “Corrosion Engineering”, McGraw-Hill Book Company, 3rd ed., 1986. ISBN-13: 978-0070214637.

[73] M.M. Puurtinen, S.M. Komulainen, P.K. Kauppinen, J.A.V. Malmivuo, J.A.K. Hyttinen, “Measurement of noise and impedance of dry and wet textile electrodes, and textile electrodes with hydrogel”, Proceedings of the 28th IEEE EMBS Annual International Conference, New York City, USA, Aug. 30-Sept. 3 (2006) 6012-6015.

[74] H.J. Scheer, T. Sander, L. Trahms, “The influence of amplifier, interface and biological noise on signal quality in high-resolution EEG recordings”, Physiol. Meas., 27 (2006) 109–

117. DOI: 10.1088/0967-3334/27/2/002.

[75] K. Hladky, J. Dawson, “The measurement of corrosion using electrochemical 1/f noise”, Corrosion Sci. 22 (1982) 231. DOI: 10.1016/0010-938X(82)90107-X.

# Table of Contents

**The plasma discharge glancing angle deposition technique was successfully used to tailor the architecture and nanostructure of Ag-doped TiN coatings sputtered on flexible polyurethane substrates.** The aim is to optimize the morphological, structural, electrical and electrochemical behaviour of the coatings so that they can be used as biomedical electrodes. The porous films are the most suitable for the envisaged application.

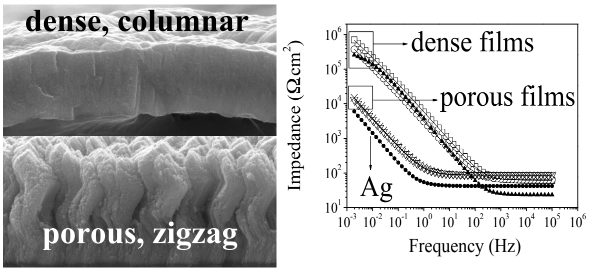

# CHAPTER 6

# Ag:TiN FILM ADHESION TO PU AND EEG MONITORING[*]

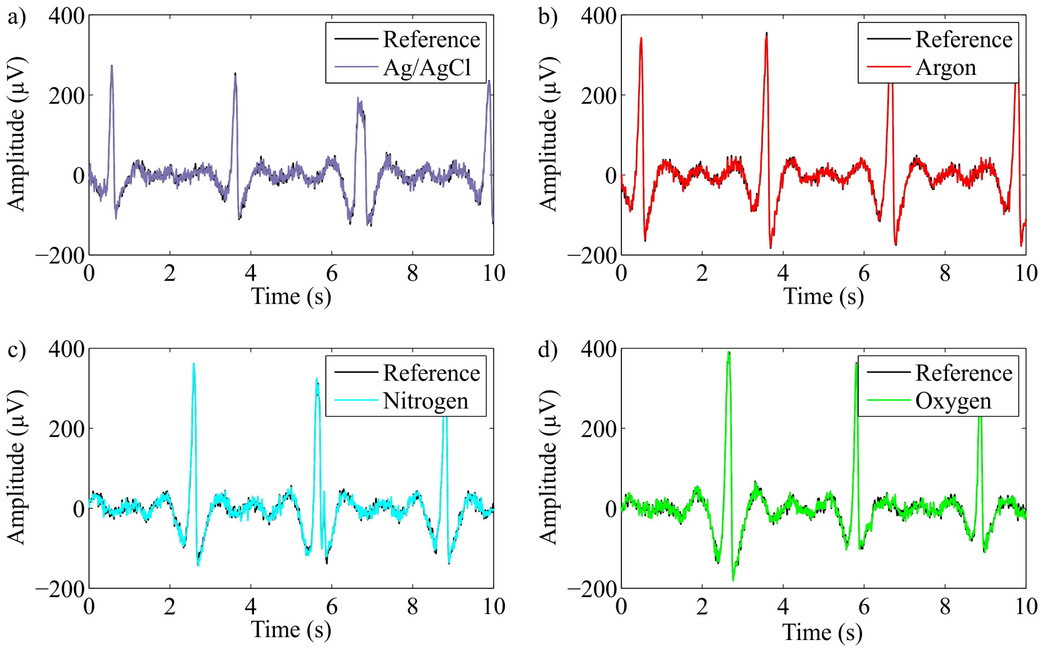

*"…no considerable differences were found in terms of shape, amplitude and spectral characteristics of the signals when comparing reference wet and dry electrodes."*

---

[*] This chapter is based on the following publication:

P. Pedrosa, C. Lopes, P. Fiedler, E. Alves, N.P. Barradas, J. Haueisen, A.V. Machado, C. Fonseca, F. Vaz, "*Ag:TiN-coated polyurethane for dry biopotential electrodes: from polymer plasma activation to the first EEG measurements*", submitted to Applied Materials and Interfaces, under review.

The architecture of the Ag:TiN thin film system was effectively tailored in the previous chapter, using the GLAD technique. Several thin film architectures were firstly optimized and then sputtered onto flexible polyurethane substrates, which were subsequently morphologically, structurally and electrochemically characterized. Since a previously optimized Ag contents (10 at.%) and $TiN_x$ matrix stoichiometry (N/Ti atomic ratio of 0.7) were used in the study performed in chapter 5, no silver segregation was found. Once more, the structural stability of the Ag:TiN films could be ascribed to the possible formation of $Ti_xAg$ intermetallics. Moreover, a steep porosity increase of the coatings occurred when the incidence angle increases from 40º to 80º (including the films with two and four zigzag periods), which gave rise to higher electroactive areas. Consequently, the Ag:TiN 80º, Ag:TiN 80º 2Z and Ag:TiN 80º 4Z porous coatings were considered the most suitable to be used as bioelectrodes, due to the displayed lower impedances, as well as noise and drift rates comparable to those of the wet Ag/AgCl commercial electrodes.

However, since the Ag:TiN GLAD films were sputtered into flexible polyurethane substrates, long-term adhesive failure of the coatings should not be disregarded, due to the well-known low surface energies displayed by most polymers. Adhesive failure often occurs during the manual placement of the dry electrodes, which may need slight adjustments in order to interfuse thick hair layers. Hence, the in-service validation of all previous investigations patent in chapters 2 to 5 through coating of the final polyurethane multipin electrodes is of paramount importance and must be complemented with a comprehensive thin film/polyurethane adhesion characterization. Therefore, the following chapter focuses not only on the selection of the best polyurethane plasma activation treatment conditions in order to enhance the thin film/polyurethane interfacial adhesion, but also on an extensive EEG signal quality comparison between the proposed Ag:TiN-coated dry multipin electrode and the wet commercial Ag/AgCl ones.

The selected plasma treatment conditions (100 W, 15 min., regardless of the used gas – argon, nitrogen or oxygen) were highly effective on the chemical activation (grafting of reactive oxygen-containing species) and roughness promotion, thus giving rise to lower water contact angle values, when comparing to the untreated sample. A decrease from 90º (untreated PU) to a minimum of 12º (argon treatment) was attained. Consequently, one of the main objectives of this chapter was attained, since the PU/Ag:TiN interfacial adhesion was steeply enhanced, as it can be seen on Figure 6.1.

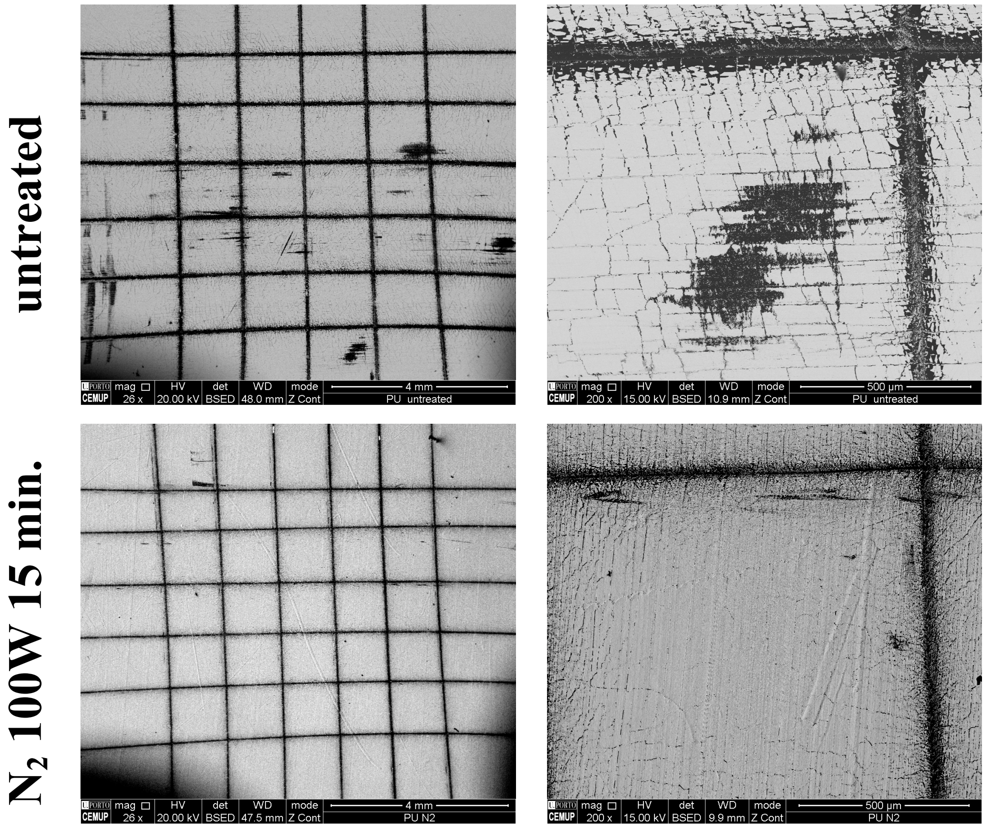

**Figure 6.1.** Cross-cut tape test results for the untreated and nitrogen activated Ag:TiN-coated PU samples. The adhesion level of the untreated sample was classified as 3B, while for the plasma treated samples the maximum classification was chosen (5B).

In addition, no considerable differences were found in terms of shape, amplitude and spectral characteristics of the signals when comparing reference wet and dry electrodes (see cover figure). Hence, the in-service validation indicates that the plasma activated and Ag:TiN-coated polyurethane dry MP electrode are, in fact, suitable candidates to replace the standard

Ag/AgCl ones in specific clinical and ambulatory applications where fast and easy montages may be needed.

# Ag:TiN-coated polyurethane for dry biopotential electrodes: from polymer plasma activation to the first EEG measurements

P. Pedrosa[a,b,c], C. Lopes[c], P. Fiedler[d], E. Alves[e], N.P. Barradas[f], J. Haueisen[d,g], A.V. Machado[h], C. Fonseca[a,b], F. Vaz[c†]

[a]SEG-CEMUC – Department of Mechanical Engineering, University of Coimbra, Portugal

[b]Universidade do Porto, Faculdade de Engenharia, Rua Dr. Roberto Frias, s/n, 4200-465 Porto, Portugal

[c]Centro de Física, Universidade do Minho, 4710-057 Braga, Portugal

[d]Institute of Biomedical Engineering and Informatics, Technische Universität Ilmenau, Ilmenau, Germany

[e]Instituto de Plasmas e Fusão Nuclear, Instituto Superior Técnico, Universidade de Lisboa, Av. Rovisco Pais, 1049-001, Lisboa, Portugal

[f]Centro de Ciências e Tecnologias Nucleares, Instituto Superior Técnico, Universidade de Lisboa, E.N. 10 (km 139,7), 2695-066 Bobadela LRS, Portugal

[g]Biomagnetic Center, Dept. of Neurology, University Hospital Jena, Friedrich Schiller University Jena, Jena, Germany

[h]IPC – Institute for Polymers and Composites, Universidade do Minho, Campus de Azurém, 4800-058 Guimarães, Portugal

**Keywords:** Dry electrodes, EEG, Plasma activation, interfacial adhesion, TiN, Ag-doping.

---

[†]Corresponding author: F. Vaz; email address: fvaz@fisica.uminho.pt; Universidade do Minho, Escola de Ciências, Centro de Física, Campus de Gualtar, 4170-057, Braga, Portugal, Tel.: +351 253510471.

## ABSTRACT

In the present work, several plasma treatments using argon, oxygen and nitrogen as working gases were optimized in order to increase the interfacial adhesion of the polyurethane/Ag:TiN system in order to be used as biopotential electrodes. The optimized plasma treatments conditions (100 W, 15 min., regardless of the gas) promoted a steep decrease of the water contact angle values from 90º (untreated) to 42º (oxygen), 25º (nitrogen) and 12º (argon). The observed chemical and topographic alterations translated into excellent polyurethane/Ag:TiN interfacial adhesion of the plasma treated samples, when comparing to the untreated ones. Moreover, the in-service validation of the proposed Ag:TiN-coated polyurethane multipin electrodes was performed by acquiring EEG signals in parallel with the standard wet Ag/AgCl electrodes. No considerable differences were found in terms of shape, amplitude and spectral characteristics of the signals when comparing reference wet and dry electrodes. Hence, the proposed dry biopotential electrodes seem to be promising candidates to replace the standard wet Ag/AgCl electrodes.

## 1. INTRODUCTION

The conventional wet silver/silver chloride (Ag/AgCl) electrodes are considered the most suitable for biosignal acquisition [1-3] and are widely used in routine clinical practices and medical research, such as multichannel electroencephalography (EEG) [4,5], or even brain-computer interfaces [6-8]. They exhibit an essentially non-polarizable, resistive behaviour, also displaying an excellent reliability and low, almost frequency-independent skin-contact impedance values, in the order of few tens of kΩ.cm$^2$ [2,3]. However, the wet Ag/AgCl electrodes suffer from intrinsic technological drawbacks, including difficult, time-consuming, and error-prone skin preparation [1], as well as limited long-term stability of the gel electrolytes and constant risk of hair damage and skin irritation [2,3,8].

For the past few years, a new class of dry biopotential electrodes have been studied as potential substitutes for the commercially used wet Ag/AgCl electrodes in applications where, for instance, fast and easy montages are required. This new generation of electrodes does not rely on the application of conductive gels and previous extensive skin preparation [3,9,10], which translates into higher interfacial impedances. Moreover, incorrect and/or uncomfortable skin contact may arise due to the stiff nature of some of the proposed base materials (aluminium [3], steel [11,12], silicon [13,14], titanium [15] and polycarbonate [16]), and design-specific conceptual problems (micro-needle electrodes [13,14] and rigid planar plates/disks unable to interfuse the hair layer [15,16]). Hence, in order to reduce some of the referred drawbacks, several authors focused not only on the development of new electrode designs, which allow an effective hair interfusion [17-20], but also on the use of more compliant base materials, such as textiles [21] and, above all, flexible polymers [22-25].

Thermoplastic polyurethanes (TPU) have been extensively applied in several fields that range from technical coatings to biomedical applications [26-28], due to their excellent balance between mechanical properties (high flexibility, dependent on the composition), chemical barrier behaviour, soft tact and biocompatibility [29,30], thus being appropriate to be used as biopotential electrode base material. Nonetheless, since the present study aims at coating TPU substrates with a previously optimized Ag:TiN thin film system [31-34], the TPU surface must be suitably activated/functionalized [35-37], in order to take account of the low surface energy and hydrophobicity (common to most polymers), which may result into poor TPU/Ag:TiN interfacial adhesion. To improve this drawback, a set of low-pressure plasma treatments will be studied, since they are able to tailor important surface characteristics, such as the wettability and topography [38-40], without compromising the bulk properties of the polymer. Moreover, the low environmental impact promoted by this technique, when compared to other surface activation methods (chemical, thermal and electrical), has also been reported [29,41]. Depending on the plasma gases and parameters (gas flows, power, pressure and treatment time), several individual physicochemical effects may be achieved [42-47], such as surface cleaning (removal of contaminants), etching (roughness promotion), crosslinking, formation of new functional groups and chain scission (formation of free radicals). The occurrence of these individual effects, or even combination of them (namely increased roughness and formation of new reactive groups), may promote beneficial effects on the adhesion, by acting as interlock points for active polar groups [47], thus an increase of the surface wettability is expected [44,47].

The present work, therefore, investigates, in a first stage, the effect of several argon [35], oxygen [30,35,39,48,49] and nitrogen [29,35] plasma activation treatments, performed with different times and powers on the surface characteristics of the TPU substrates, and subsequent adhesion of the sputtered Ag:TiN film. Then, the plasma activated (using the best treatment time and power for the different gases) novel dry Ag:TiN-coated polyurethane multipin electrodes, which intends to combine the use of a flexible base material (polyurethane, PU) with an optimized design (multipin, MP), were used in several EEG trials in comparison with the wet Ag/AgCl ones. Finally, the quality of the monitored EEG signals was compared in order to select the best plasma treatment/Ag:TiN coating combination to be used as biopotential electrodes.

## 2. EXPERIMENTAL DETAILS

### *2.1. Activation and characterization of the polyurethane substrates*

The polyester-based thermoplastic polyurethane (TPU) substrates, ref. WHT-1495EC, from Yantai Wanhua Polyurethanes Co., Ltd. were obtained by compression moulding in the sheet form. Before all plasma activation treatments, the polyurethane substrates were cleaned with ethanol (96% vol.). A Zepto laboratory-sized plasma system from Diener Electronics (ø = 105 mm, L = 300 mm, V = 2.6 L) was used for the plasma activation of the samples. Several plasma treatments were performed, taking into account the effect of three main parameters: (i) used gas, (ii) plasma treatment time and (iii) plasma treatment power. The plasma treatment experimental parameters are summarized in Table I.

**Table I.** Plasma treatment parameters.

| Parameter | Gas | Power (W) | Time (min.) | Pressure$_{base}$ (Pa) | Pressure$_{work}$ (Pa) |
|---|---|---|---|---|---|
| **ΔTime** | Ar | 100 | 2, 5, 10, 15 and 20 | $3\times10^{-3}$ | $8\times10^{-3}$ |
| | $O_2$ | 100 | 2, 5, 10, 15 and 20 | $3\times10^{-3}$ | $8\times10^{-3}$ |
| | $N_2$ | 100 | 2, 5, 10, 15 and 20 | $3\times10^{-3}$ | $8\times10^{-3}$ |
| **ΔPower** | Ar | 100, 75 and 50 | 15 | $3\times10^{-3}$ | $8\times10^{-3}$ |
| | $O_2$ | 100, 75 and 50 | 15 | $3\times10^{-3}$ | $8\times10^{-3}$ |
| | $N_2$ | 100, 75 and 50 | 15 | $3\times10^{-3}$ | $8\times10^{-3}$ |

Before and immediately after (maximum of 10 minutes) all activation experiments, the water contact angle (sessile drop method [50,51]) was measured at room temperature, using a OCA 20 unit from Dataphysics, in air-facing polyurethane surfaces. A minimum of six contact angle measurements were performed for each condition. An optimized plasma treatment time (15 minutes) and power (100 W) were selected from the water contact angle measurements. The chemical bonding characteristics were analysed by Fourier Transform Infrared Spectroscopy (FTIR) in Attenuated Total Reflectance (ATR) mode, using a Jasco FT/IR 4100 system, equipped with a Specac MkII Golden Gate single reflection ZnSe ATR crystal. All ATR-FTIR measurements (64 scans, 4 cm$^{-1}$ nominal resolution) were performed before and immediately after the activation of the samples. In addition, the surface chemistry of the untreated and activated polyurethane samples was also assessed by X-ray Photoelectron Spectroscopy (XPS), performed using a Kratos Axis Ultra spectrometer, equipped with the VISION software for data acquisition and CASAXPS for data analysis. The experiments were carried out with a monochromatic Al $K_\alpha$ x-ray source (1486.7 eV), operating at 15 kV (90W) in fixed analyser transmission (FAT) mode, with a pass energy of 40 eV for the regions of interest and 80 eV for the overall surveys. Data acquisition was performed with a pressure lower than $1\times10^{-6}$ Pa, and a charge neutralization system was used. The effect of the electric charge was corrected by the reference of the carbon peak (285 eV). The modelling of the spectra was performed with the CASAXPS program, in which an adjustment of the peaks was done using peak fitting with Gaussian-Lorentzian peak shape and Shirley-type background subtraction [52].

The surface topography and average roughness ($R_a$) of the polyurethane substrates was assessed before and after the plasma activation using a Multimode Atomic Force Microscope (AFM) from Digital Instruments using the tapping mode (scan size 3 µm and scan rate 1 Hz). A Nanoscope III controller and Tesp AFM tips from Bruker were also used.

### *2.2. Thin film production and adhesion characterization*

The plasma activated polyurethane substrates were used to deposit Ag:TiN coatings with a N/Ti atomic ratio of 0.7 and 6 at.% Ag by reactive DC magnetron sputtering, in a 60 L custom-made laboratory-sized deposition system. This specific Ag:TiN composition was optimized in previous works by the authors, in order to avoid Ag segregation through the potential formation of $Ti_xAg$ intermetallics [31-34]. The thin films were prepared with the grounded substrate holder positioned at 75 mm from the magnetron and with a 5 rpm rotational speed. A DC current density of 75 $A.m^{-2}$ was applied to the titanium target (99.96 at. % purity / 200×100×6 mm), containing silver pellets (80×80 mm and 1 mm thick) on its surface distributed symmetrically along the erosion area. The total surface area of the silver pellets (~192 $mm^2$) was preserved throughout all depositions. A mixed gas atmosphere composed of $Ar+N_2$ was used to generate the plasma. The argon flow was kept constant at 25 sccm in all depositions (partial pressure of $5.4\times10^{-1}$ Pa), while the flow rate of nitrogen fixed at 2 sccm (partial pressure of $4.6\times10^{-2}$ Pa). The working pressure was about $3.8\times10^{-1}$ Pa. A delay time of five minutes was used prior to positioning the sample surface in front of the Ti/Ag target, in order to avoid contamination of the coating resulting from previous depositions, which may have resulted in some target poisoning, as well as to ensure an almost constant deposition temperature during the growth of the films. All depositions were performed for 1800 s at room temperature to avoid polymer degradation (together with the grounded condition of substrate holder). Operating conditions are summarized in Table II.

**Table II.** Ag:TiN thin film deposition parameters.

| | |
|---|---|
| **Plasma treatments (performed before all depositions)** | Ar 100 W 15 min.<br>$O_2$ 100 W 15 min.<br>$N_2$ 100 W 15 min. |
| **Ar (Pa)** | $5.4\times10^{-1}$ |
| **$N_2$ (Pa)** | $4.6\times10^{-2}$ |
| **t (s)** | 1800 |
| **I ($A.cm^{-2}$)** | $7.5\times10^{-3}$ |
| **T (ºC)** | Room temperature |
| **Bias (V)** | GND |
| **$Pressure_{work}$ (Pa)** | $3.5\text{-}3.8\times10^{-1}$ |
| **$Pressure_{base}$ (Pa)** | $\sim10^{-4}$ |
| **Area of Ag exposed ($mm^2$)** | 192 |

The atomic composition of the as-deposited samples was measured by Rutherford Backscattering Spectrometry (RBS) using (1.4, 2.3) MeV and (1.4, 2) MeV for the proton and $^4$He beams, respectively. Three detectors were used. One located at a scattering angle of 140º and two pin-diode detectors located symmetrically to each other, both at 165º. Measurements were made for two sample tilt angles, 0º and 30º. Composition profiles for the as-deposited samples were determined using the NDF software [53]. For the $^{14}$N, $^{16}$O and $^{28}$Si data, the cross-sections given by Gurbich were used [54]. The area analysed was about 0.5×0.5 $mm^2$. The uncertainty in the N concentrations is around 5 at. %.

The adhesion of the Ag:TiN films to the polyurethane substrates (untreated and plasma treated) was assessed by performing the cross-cut tape test, according to the ASTM D3359-B standard. The SEM/EDS analysis was carried out in a FEI Quanta 400FEG ESEM/EDAX Genesis microscope equipped with X-Ray Microanalysis operating at 15 keV.

### *2.3. EEG monitoring*

In the EEG monitoring tests a conventional wet Ag/AgCl ring electrode (B10, EASYCAP GmbH, Germany) was placed at frontal position Fp2, while a multipin (MP) test electrode and another wet Ag/AgCl electrode were placed next to each other at occipital position O2. Furthermore, a reference test using two Ag/AgCl electrodes at position O2 was performed. Prior to electrode placement the skin at each electrode position was cleaned using ethanol and a soft cloth. The Ag/AgCl electrodes were applied in combination with electrolyte gel (Electrogel, EGI Inc., USA), while the MP electrodes (from each plasma activation condition) were used in dry conditions only. Both occipital electrodes were connected to independent bipolar channels of a commercial EEG amplifier (Refa Ext, Advanced Neuro Technologies B.V., The Netherlands), while both channel references were connected to the same frontal electrode at position Fp2. Electrode fixation and adduction was provided by a custom-made silicone cap. The MP electrodes were contacted using custom brass mountings. The measurement setup enables simultaneous recording of independent EEG signals. Hence, a direct comparison of the acquired signals using conventional and MP electrodes is possible. Resting-state EEG, alpha activity and eye-blinking artifacts were monitored during the in-vivo tests. Also, a pattern reversal visual evoked potential (VEP) was recorded according to ISCEV standards consisting of 300 trials. The three different MP electrodes (activated with argon, nitrogen and oxygen) and the reference Ag/AgCl electrode were tested in three individual tests per material on three volunteers (two male, one female), resulting in an overall number of 12 test sequences per volunteer. Finally, the simultaneously recorded signals of the wet (w) and dry (d) electrodes were compared by means of the Root Mean Square Deviation (RMSD), the Spearman's rank correlation (CORR) as well as the Welch estimation of the Power Spectral Density (PSD). Therefore, the signals were filtered using a bandpass with cut-off frequencies at 1-40 Hz and automatically selected data sequences of 10 s were analyzed. Further details about the EEG monitoring and analysis procedures can be found in reference [18].

## 3. RESULTS AND DISCUSSION

### *3.1. Wettability evaluation of the plasma treated PU surfaces*

The hydrophilicity of the untreated and Ar, $O_2$ and $N_2$ plasma treated polyurethane samples was evaluated as a function of the treatment parameters that were used, since it is a reliable indicator for the formation of reactive groups and surface roughness promotion, which is expected to promote the desired thin film adhesion levels [55].

Fig. 1 a) and b) represent the water contact angle (C.A.) evolution with increasing plasma treatment times and powers for the three used gases, respectively. Regarding the plasma treatment time parameter, Fig. 1 a), all treatments were performed with a fixed power of 100 W (equipment maximum) and increasing exposure times from 2 to 20 minutes.

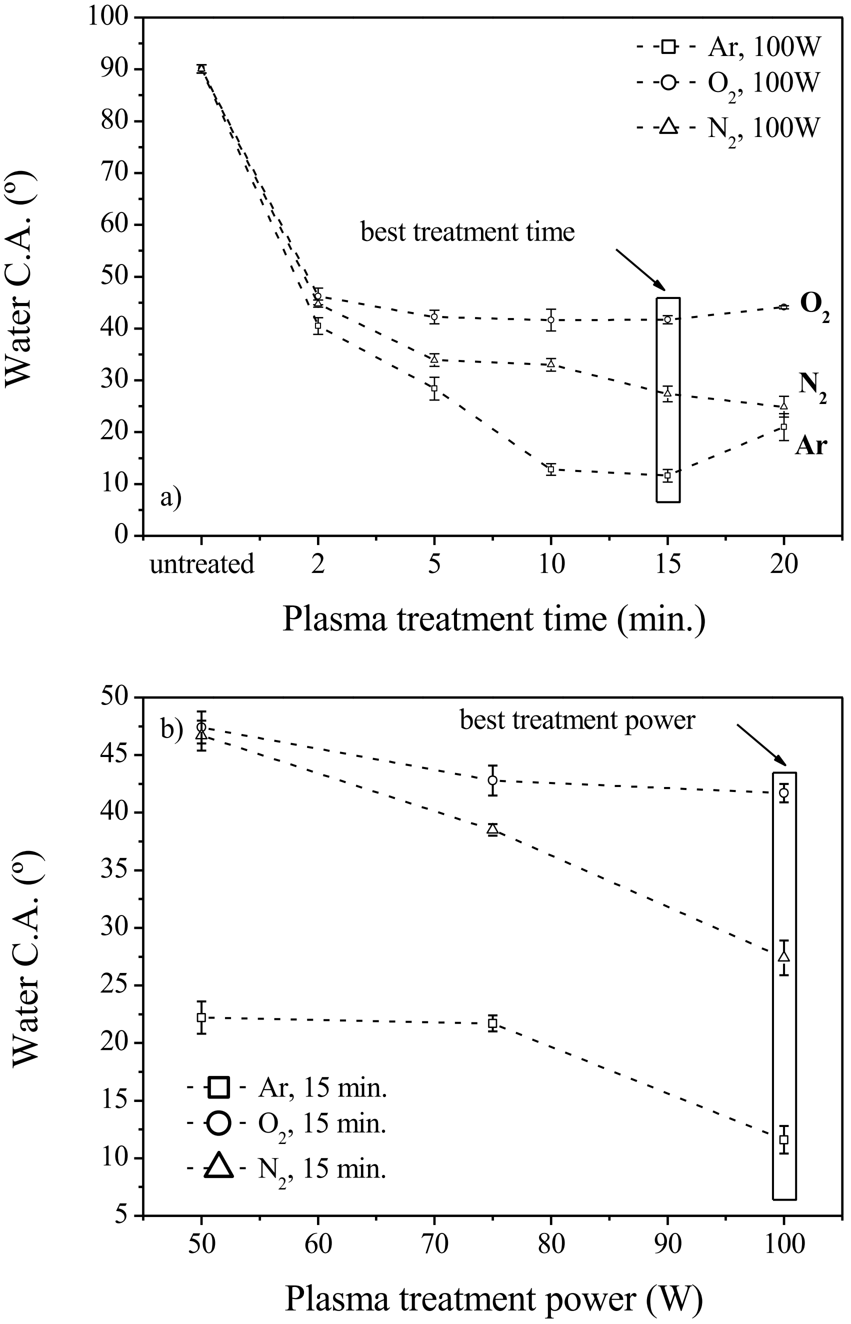

**Fig. 1.** Water contact angle evolution with (a) increasing plasma treatment times and with (b) decreasing plasma treatment power.

Fig. 1 shows that it is possible to reduce the water C.A. from 90º (untreated) to 40º-45º after only 2 minutes of activation (valid for all gases). Subsequently, with further increase of the plasma treatment time, a clear differentiation of the C.A. behaviour is patent, taking into account the different gases used. The most pronounced reduction of the C.A. is achieved using Ar, with a minimum of 12º after 15 minutes of exposure, corresponding to a hydrophilicity increase of 87%, comparing to the untreated value. When a 20 minutes treatment is performed, the water C.A. values suffer a slight increase until 21º. Regarding the nitrogen series, a constant decrease of the C.A. values can be seen up to 20 minutes of treatment time (minimum of 25º, 72% hydrophilicity increase). As for the oxygen treatments, a minimum C.A. of 42º is achieved after 5 minutes (53 % hydrophilicity increase), with the values remaining rather constant with increasing activation times.

Taking into account the results of the exposure time variation in the water C.A., the 15 minutes plasma activation treatment was selected as the best treatment time, since all surfaces activated with the three used gases displayed the lowest C.A. value. In the case of the nitrogen activation, the slight decrease of the C.A. observed from 15 to 20 minutes was not considered as significant, taking into account that the error bars of both experimental data are overlaid. Hence, after selecting the most appropriate treatment time (15 minutes), the effect of the plasma power was also investigated by decreasing the values from 100 W (maximum power output allowed by the equipment used) to 50 W, Fig. 1 b). With the exception of the oxygen treatments (which display roughly the same C.A. with 100 W and 75 W), the argon and nitrogen plasma ones exhibit increasing C.A. values with decreasing plasma powers. Consequently, regarding the water C.A. evolution, the plasma treatments that were found to be more effective in increasing the wettability/hydrophilicity of the PU surface were the ones performed with 100 W for 15 minutes, regardless of the used gas.

The water C.A. behaviour of the plasma activated PU surfaces, consistent with results obtained by other authors [29,35,39,48], may be explained by considering the Wenzel's equation [55,56]:

$$\cos(\theta_W) = r \cos(\theta_Y) \qquad (1)$$

Equation (1) describes the relation between the apparent C.A. on a rough surface ($\theta_W$), the surface average roughness ratio (r, ratio between the real and geometric area) and the C.A. on a chemically similar smooth surface ($\theta_Y$). Hence, taking into account this relation, it is possible to claim that the wettability evolution is strongly related with the chemical and topographic changes promoted by the plasma activation treatments. Therefore, an extensive surface chemical and topographical analysis will be performed in the subsequent sections of this work (3.2. and 3.3.), in order to draw correlations regarding the observed water C.A. behaviour.

## ***3.2. Chemical analysis of the plasma activated PU surfaces***

### *3.2.1. FTIR-ATR analysis*

The FTIR-ATR analysis was again performed on PU surfaces activated with different gases, exposure times and plasma powers (same conditions as in the previous section) in order to validate the selection of the best plasma parameters (time and power) that were performed, taking into account the water C.A. behaviour.

The results of the overall chemical bonding changes promoted are patent in Fig. 2 $a_{1\text{-}3}$) and $b_{1\text{-}3}$).

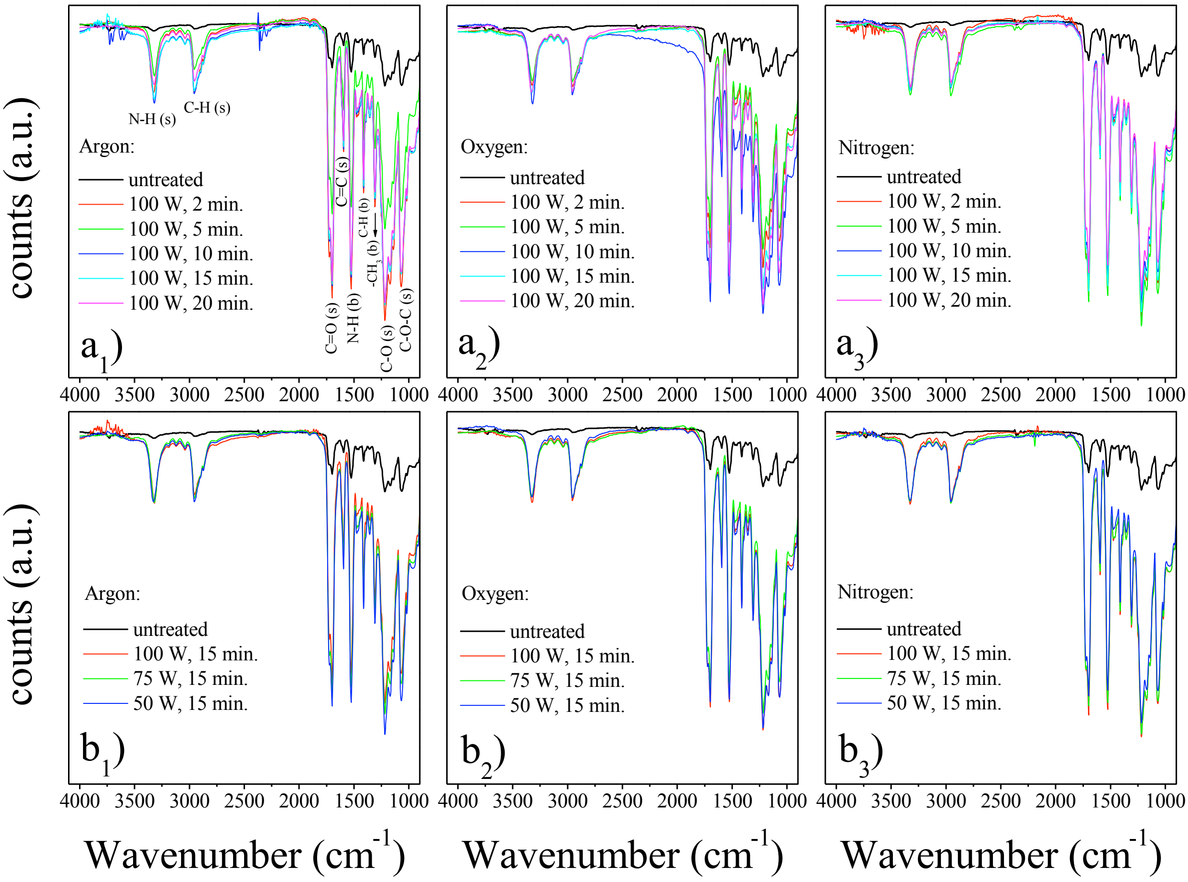

**Fig. 2.** FTIR spectra of the polyurethane samples with increasing plasma treatment times ($a_{1-3}$) and with decreasing plasma treatment power ($b_{1-3}$).

The bands at 3320 and 2956 cm$^{-1}$ refer to N-H and C-H stretching (s), respectively. As for the peaks detected between 2000 and 1500 cm$^{-1}$, that may be indexed to C=O (s) at 1700 cm$^{-1}$, C=C (s) at 1600 cm$^{-1}$ and N-H bending (b) at 1528 cm$^{-1}$. From 1500 to 1000 cm$^{-1}$, the C-H (b) at 1414 cm$^{-1}$, -CH3 (b) at 1312 cm$^{-1}$, C-O (s) at 1216 cm$^{-1}$ and C-O-C (s) at 1067 cm$^{-1}$ bonds were observed. All the FTIR spectra were indexed according to references [57,58].

Major changes regarding the intensity of the indexed bands can be seen on the FTIR spectra of the activated surfaces when comparing to the untreated sample, meaning that the performed plasma treatments effectively changed the chemical surface of the PU samples, by increasing its reactivity (higher intensity of the reactive oxygen-containing groups can be seen). However, no new species were detected, regardless of the used gas, exposure time and plasma power, which was somewhat expected since FTIR is known for not being particularly sensitive to small amounts of chemical species [55]. In addition, and unlike what was observed from C.A. measurements, no significant changes can be seen when focusing on the exposure time and plasma power, with the respective spectra appearing overlaid. This is particularly evident taking a closer look at the reactive C=O oxygen-containing group band, Fig. 3, where no specific trend regarding the exposure time and used power can be observed. Hence, due to the lower water C.A. values observed in section 3.1., the Ar 100 W 15 min., $O_2$ 100 W 15 min. and $N_2$ 100 W 15 min. plasma treatments were selected to be further investigated.

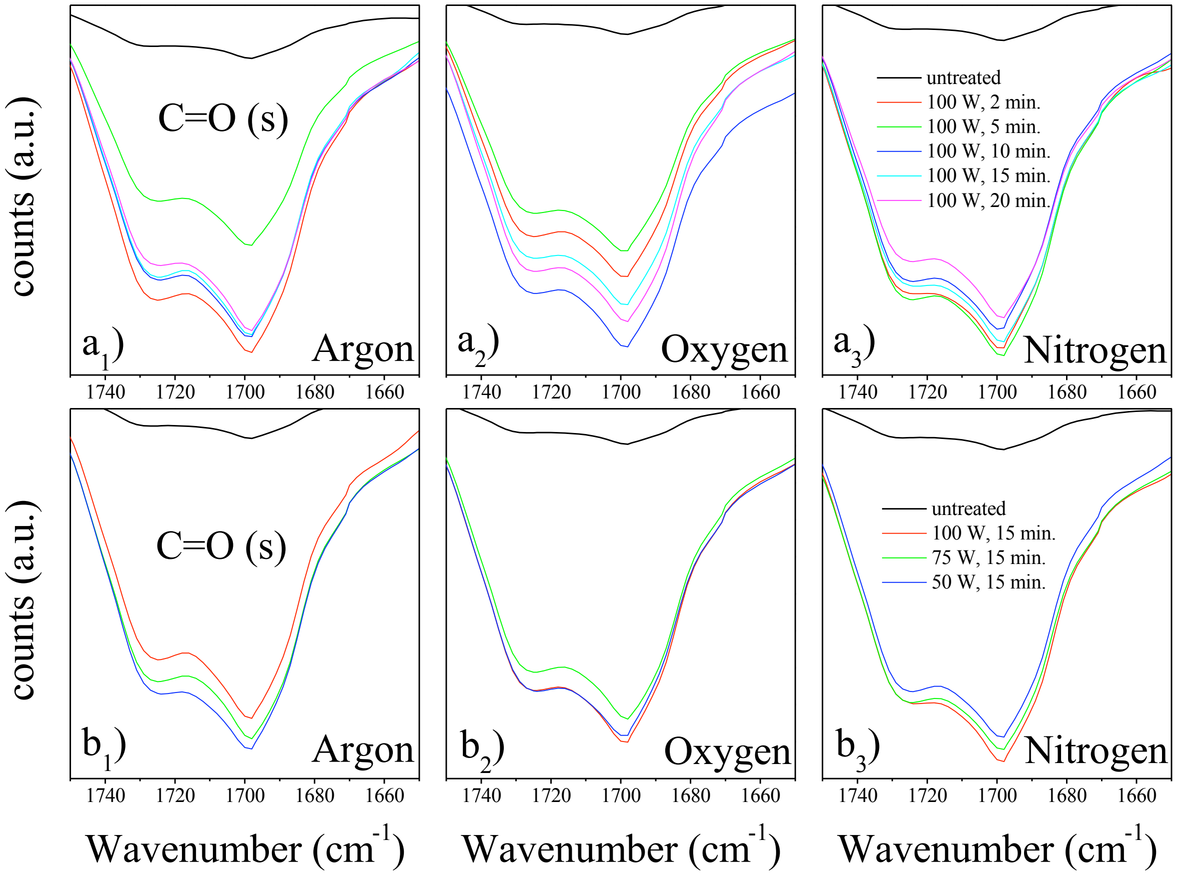

**Fig. 3.** Effects of the activation treatments on the C=O bond with increasing plasma treatment times ($a_{1-3}$) and with decreasing plasma treatment power ($b_{1-3}$).

The FTIR spectra of the plasma activation treatments performed with the previously selected parameters are plotted in Fig. 4 $_{a-c)}$. Since the inclusion of reactive species is an important indicator of good polymer/thin film interfacial adhesion levels and may also explain the water C.A. evolution (bearing in mind the Wenzel's equation), the effect of the performed surface activation on the promotion of C=O, C-O and C-O-C bonds is depicted on Fig. 4 b) and c). Despite the small intensity differences that are, once more, perceivable, the same behaviour is patent when taking into account the changes promoted by the three gases. As expected, the Ar 100 W 15 min. treatment consistently gives rise to lower amounts of oxygen-containing reactive species, due to the fact that argon is a non-reactive, ideal gas.

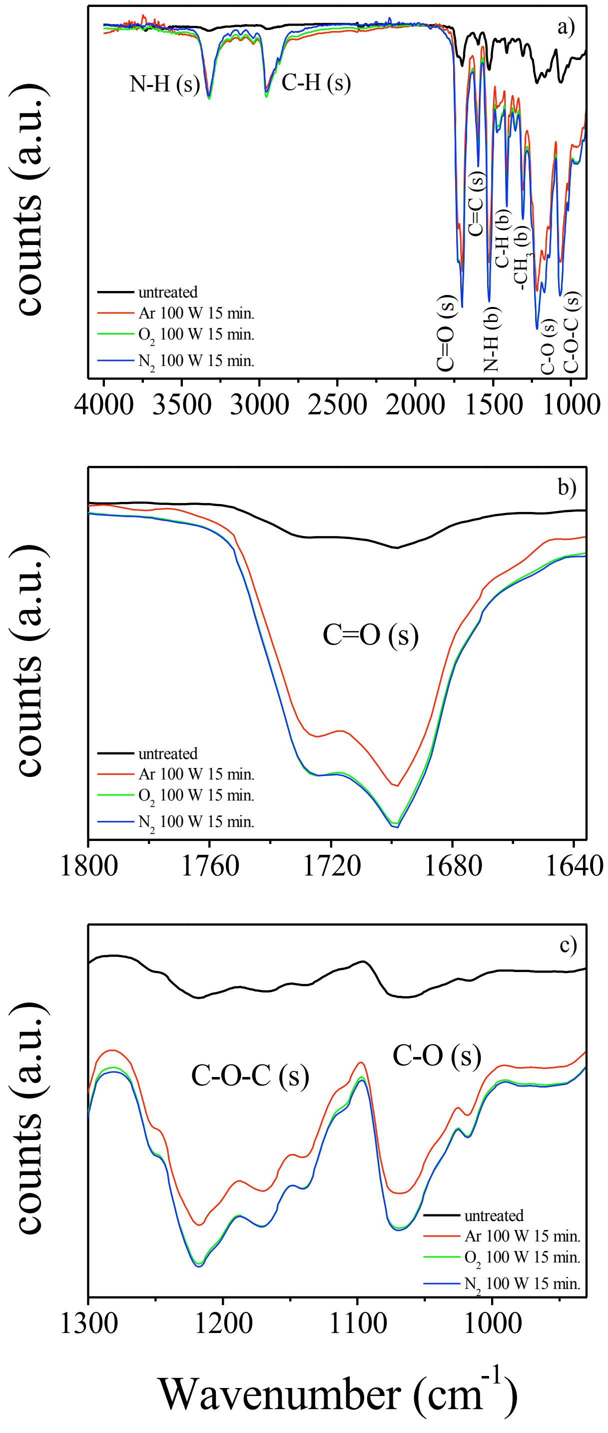

**Fig. 4.** FTIR spectra of the polyurethane samples (a) treated with the best treatment time and power for the three used gases. (b) and (c) represent magnifications of the reactive oxygen containing bonds.

Hence, argon should mainly promote the formation of free radicals (dangling bonds) that may later recombine with oxygen and other elements (including water) when exposed to ambient air [35,55]. It is important to note that the activated PU samples were analysed shortly after the plasma treatments, thus only a brief exposure to ambient air occurred. In opposition, the treatments performed with nitrogen and, especially, oxygen are more effective in creating further amounts of reactive groups. Nitrogen, despite not being a noble gas, acts in a similar way to argon, by promoting the formation of free radicals due to the occurrence of extensive polymer chain scission [29,30]. The reactive groups are then formed by combination with ambient oxygen. When using oxygen as working gas, the reactive oxygen-containing functionalities are obtained during the plasma treatment itself [35]. Furthermore, some free radicals may also be formed and later recombine with the elements present in ambient air.

### *3.2.2. XPS analysis*

Since the FTIR investigation was not sufficient to clearly differentiate the chemical effects of the used working gases, an extensive XPS analysis was performed on the PU surfaces activated with the previously optimized plasma conditions, Fig. 5. The identification of the peaks was performed using references [30,59].

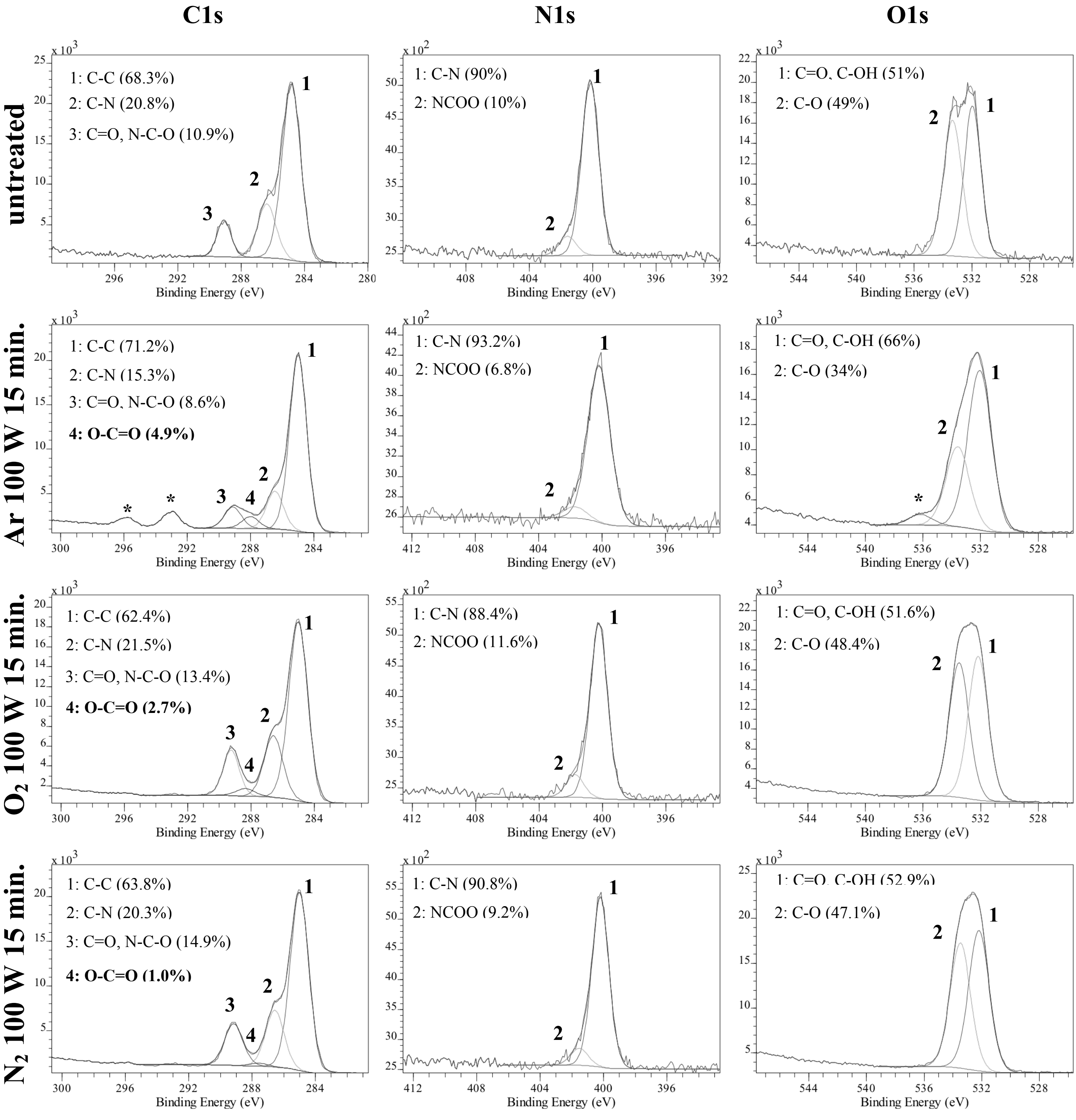

**Fig. 5.** XPS spectra of the untreated and plasma treated polyurethane substrates.

From the XPS spectra analysis it is possible to see significant changes when comparing the untreated and plasma treated samples, namely regarding the C1s signal. It is important to note that some contaminations (F, Na, S, Cl, K and Ca) were detected (peaks identified as * in Fig. 5). These contaminations were probably introduced in the manufacturing of the PU samples, since the related peaks were not reduced after ionic etching. This should mean that the impurities are part of the bulk polymer and not promoted by the plasma treatments.

All plasma treatments promoted the increase of the oxygen-containing functionalities (13.5 %, 16.1 % and 15.9 % for the Ar, $O_2$ and $N_2$ treatments, respectively), when comparing to the untreated PU sample (10.9 %) in the C1s spectra. These results are consistent with the FTIR analysis performed in the previous section. Moreover, the insertion of a new chemical functionality at around 288 eV is perceivable due to the formation of C=O or N-C-O bonds at the surface of all activated PU samples. Note that in the FTIR analysis no new reactive groups were detected after the performed plasma treatments. Despite not being reactive gases, the XPS analysis proves that argon and nitrogen are effective (although not in the same extent as oxygen) in promoting the desired chemical changes, including the creation of new functionalities, which should be mainly due to the higher ability to induce the formation of free radicals that later act as anchoring points for the oxygen species present in the ambient air. Oxygen is then the most effective working gas regarding the production of reactive groups. The grafting of such reactive oxygen-containing groups should, in fact, be responsible for the increased hydrophilicity of the activated samples.

Nevertheless, this set of results seem to indicate that the chemical alterations studied by FTIR and XPS do not provide a clear explanation for the wettability differences that were promoted by the different working gases. As seen in section 3.1., the Ar 100W 15 min. plasma treatment promoted lower water C.A. values (12º) than the $N_2$ 100 W 15 min. (25º) and $O_2$ 100 W 15 min. (42º) ones, despite being less effective in the chemical functionalization of the PU surfaces. It is also important to note that the argon treatment promoted the least amount of oxygen-containing groups (13.5 %), followed by nitrogen (15.9 %) and finally oxygen (16.1 %). Hence, considering only the surface chemical chances, no definitive explanations can be found regarding the water C.A. behaviour observed in section 3.1. Consequently, taking into account equation (1), the wettability behaviour should be further explained by investigating the topography changes induced on the activated PU surfaces.

### *3.3. Topographic features of the plasma treated PU samples*

Wenzel's equation shows that for a hydrophilic surface ($\theta_Y < 90^o$) the roughness should turn the surface more hydrophilic and a hydrophobic surface ($\theta_Y > 90^o$) more hydrophobic. However, for water C.A. close to 90º this parameter is insensitive to roughness variations. In addition, the more hydrophilic the surface is, the higher the effect of the roughness on the water C.A. In section 3.1., it was seen that the water C.A. of the PU substrates decreased from 90º (untreated) to a minimum of 42º, 25º and 12º for the $O_2$ 100 W 15 min., $N_2$ 100 W 15 min. and Ar 100 W 15 min. plasma treatments, respectively. These wettability variations from the untreated to the plasma treated polymer can be explained, in part, by the significant grafting of oxygen-containing species in the surface of the activated PU samples. However, as seen in section 3.2., the chemical changes are not able to explain the hydrophilicity changes observed for the different working gases, since the sample treated with the gas that promoted the formation of higher amounts of reactive oxygen-containing groups (oxygen, 16.1 %) displayed the higher water C.A. (42º). In opposition, the Ar treatment exhibited the lowest water C.A. (12º) despite promoting the formation of less amounts of reactive species (13.5 %).

Hence, the wettability behaviour should be further explained by the topographic changes promoted by the different plasma treatments, Fig. 6. In order to take account of potential irreproducibility in the fabrication of the PU samples that may derive from the manufacturing process (compression moulding), three untreated samples were selected, suitably identified and then, activated with the selected conditions and working gases.

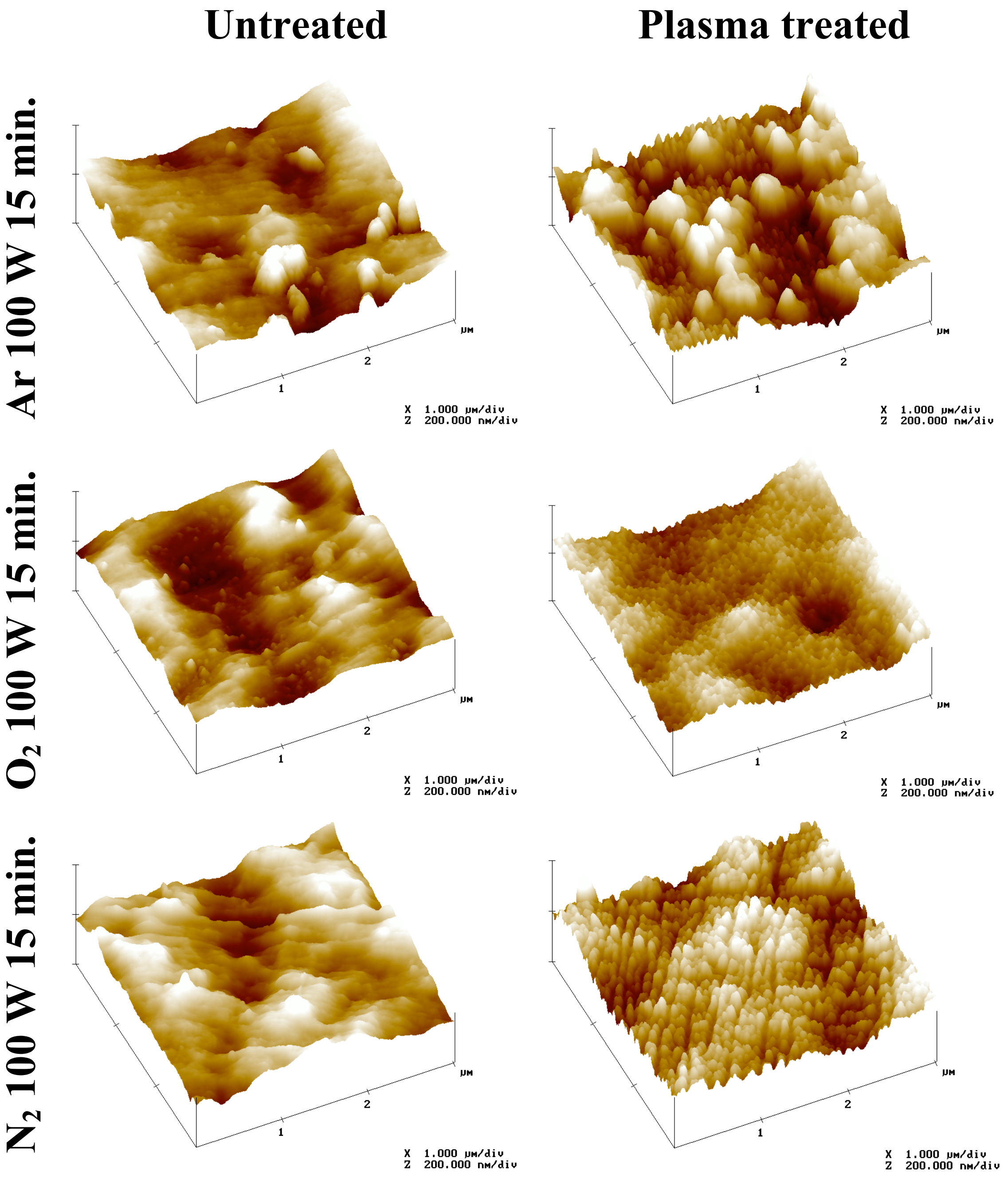

**Fig. 6.** AFM micrographs of the untreated and plasma treated polyurethane samples.

Once more, clear topographic differences can be seen when comparing the plasma treated PU surfaces to their untreated counterparts. Furthermore, the different topographic effects promoted by each of the working gases are also clear. Finer topographic features seem to be introduced by the nitrogen and oxygen treatments, while argon promotes the formation of a coarser topography. Looking at Table III, it is possible to see that the Ar 100 W 15 min.

treatment gives rise to the highest increase of the average roughness of the PU surfaces, increasing from 19.3 nm (untreated) to 37.8 nm.

**Table III.** Roughness variation promoted by the performed plasma treatments.

| Plasma treatment | untreated | | plasma treated | | $\Delta R_a$ |
|---|---|---|---|---|---|
| | $R_a$ (nm) | RMS (nm) | $R_a$ (nm) | RMS (nm) | |
| **Ar 100 W 15 min.** | 19.3±1.1 | 24.5±1.4 | 37.8±1.1 | 46.6±2.3 | +96% |
| **$O_2$ 100 W 15 min.** | 16.4±1.3 | 20.9±0.8 | 21.6±1.4 | 27.2±1.7 | +31% |
| **$N_2$ 100 W 15 min.** | 19.5±1.6 | 24.6±1.7 | 28.9±2.7 | 35.2±3.3 | +48% |

The average roughness of the untreated sample was then almost doubled (96 % increase) when using argon as working gas. In opposition, the oxygen treatment promotes the least amount of topographic changes, with the average roughness increasing from 16.4 nm (untreated sample) to 21.6 nm, meaning that only a 31 % increase of the surface roughness was achieved. The $N_2$ 100 W 15 min. activation originates intermediate changes of the surface topography, with the roughness suffering a 48 % increase, from 19.5 nm to 28.9 nm. It is interesting to note that all plasma treatments gave rise to increased surface roughness of the PU samples. These results are not consistent with the work of other authors [35], where a softening of the surface was observed, which must be due to the lower activation times that were used (3 min. vs. 15 min.). Hence, it is possible to say that higher plasma activation times are beneficial for the promotion of increased surface roughness on PU samples.

To summarize, regarding the influence of the chemical changes and surface roughness promotion on the wettability behaviour of the PU samples, a clear relation is perceivable. The samples treated with argon, which display the highest roughness increase (96 %), are also more hydrophilic (lower water C.A., 12º), despite also exhibiting the lowest amount of reactive oxygen-containing groups (13.5 %). In turn, the PU samples activated using oxygen as working gas, which present the most chemically active surface (grafting of 16.1 % of reactive species), display the least amount of topographic changes (31 % roughness increase) and the highest water C.A. value (42º). The samples activated with the $N_2$ 100 W 15 min. plasma treatment exhibit intermediate water C.A. values (25º), which should be due to the also intermediate roughness increase (48 %) and grafting of oxygen reactive groups (15.9 %).

In conclusion, all plasma treatments performed with the optimized conditions (100 W, 15 min.) are effective in producing the desired wettability changes, through the grafting of reactive oxygen-containing species and roughness promotion on the surface of the PU samples. The extent of the aforementioned surface alterations is dependent on the used working gas and the hydrophilicity behaviour is effectively explained by taking into consideration the relation between chemical and topographic changes patent in the Wenzel's equation (1).

### *3.4. PU/Ag:TiN adhesion assessment*

In order to investigate if the performed plasma treatments promote, in fact, an enhancement of the PU/thin film interfacial adhesion, a Ag:TiN coating (with N/Ti atomic ratio of 0.7 and 6 at.% Ag) was deposited on the untreated and plasma treated PU substrates. The adhesion was studied using the cross-cut tape test, according to the ASTM D3359-B standard (which provides a decreasing adhesion classification between 5B and 0B) and the results are patent in Fig. 7.

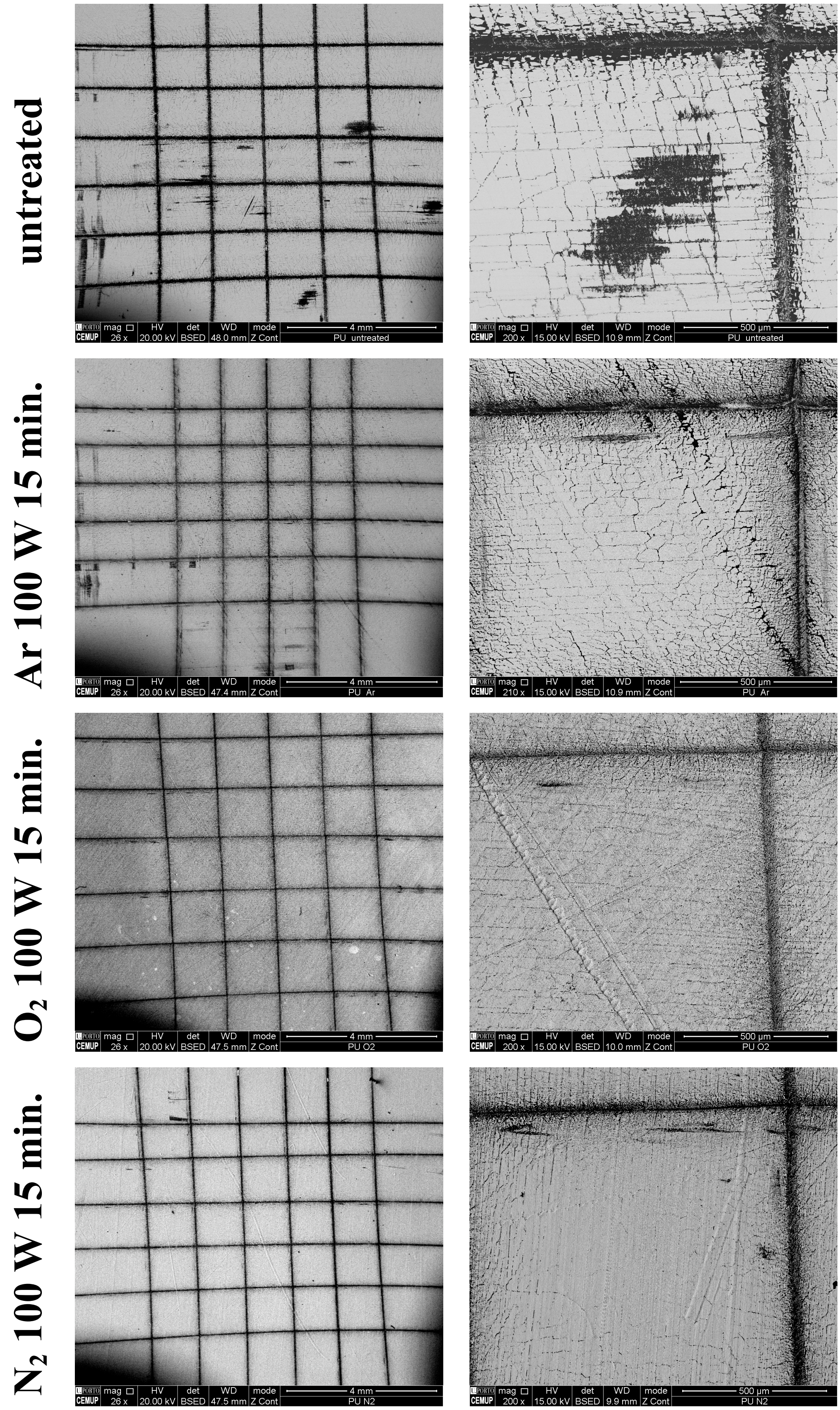

**Fig. 7.** SEM imaging of the cross-cut tape tests performed on the untreated and plasma treated Ag:TiN-coated polyurethane substrates.

As expected, due to the significant chemical and topographic changes underwent by the plasma treated PU surfaces (grafting of reactive oxygen-containing species and increase of the surface roughness), the untreated sample exhibits the lowest adhesion to the Ag:TiN film. As it can be seen from the backscattered images, extensive delamination can be seen not only along the cuts, but also inside some of the squares (although in a smaller extent). According to the aforementioned standard, the appropriate adhesion classification seems to be 3B: small flakes of the coating are detached along the edges and at the intersections of the cuts; the area affected is 5 to 15 % of the lattice. In opposition, no definitive differences can be found among the plasma treated samples. However, the argon treated sample seems to exhibit slightly higher amounts of cracks, which may be an indication of the importance of the grafting of reactive oxygen-containing groups. Note that the argon treatment promoted the formation of smaller amounts of reactive species (13.5 %). All plasma treatments, Ar 100 W 15 min., $O_2$ 100 W 15 min. and $N_2$ 100 W 15 min., translate into excellent levels of interfacial adhesion (rated as 5B), since no delamination of the edges of the cuts or inside the squares of the lattice is perceivable.

Hence, it is possible to conclude that the performed plasma treatments produced the desired increase of the PU/Ag:TiN interfacial adhesion by effectively activating the PU surface chemically and by increasing the surface roughness. Both parameters should lead to an increase of anchoring and interlocking points to the sputtered Ag:TiN film [55].

### *3.5. EEG trials*

With the objective of investigating further differences between the performed plasma treatments, three sets of PU MP electrodes were activated using the previously optimized plasma conditions and subsequently coated with the same Ag:TiN coating used in the previous section, Fig. 8.

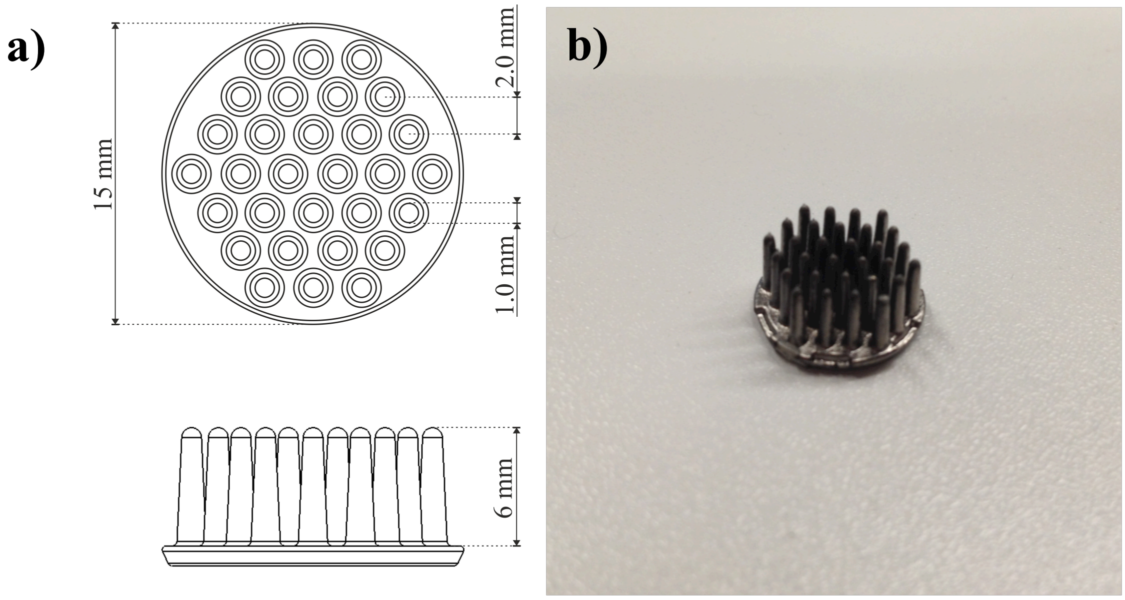

**Fig. 8.** PU multipin electrode used for the EEG tests. (a) electrode design and (b) Ag:TiN-coated electrode.

Subsequently, the dry MP electrodes were used in parallel with the commercial wet Ag/AgCl electrodes in several EEG monitoring tests, in order to assess their characteristics in a realistic EEG acquisition scenario and to evaluate if considerable signal differences could be found among the electrodes. As it is possible to see from Table IV, the magnitude of the calculated RMSDs of the plasma activated and Ag:TiN-coated polyurethane MP dry electrodes is only marginally lower (maximum difference of 2.4 µV) than the RMSD of the wet Ag/AgCl reference test.

**Table IV.** Signal differences between the plasma treated Ag:TiN-coated polyurethane MP dry electrodes vs. Ag/AgCl reference wet electrodes calculated for the VEP, as well as for 10 s long sequences of resting state EEG, alpha activity, and EEG containing eye blink artefacts.

| Plasma treatment | RMSD (µV) | | | | CORR | | | |
|---|---|---|---|---|---|---|---|---|
| | Resting | Alpha | Eye blink | VEP | Resting | Alpha | Eye blink | VEP |
| **Ar 100 W 15 min.** | 8.3 ±2.9 | 7.5 ±2.6 | 7.9 ±1.9 | 0.5 ±0.08 | 0.85 ±0.15 | 0.86 ±0.18 | 0.94 ±0.06 | 0.97 ±0.01 |
| **$O_2$ 100 W 15 min.** | 6.9 ±3.7 | 6.5 ±2.5 | 6.5 ±1.6 | 0.6 ±0.06 | 0.81 ±0.20 | 0.82 ±0.17 | 0.97 ±0.07 | 0.97 ±0.01 |
| **$N_2$ 100 W 15 min.** | 7.4 ±2.6 | 7.3 ±2.0 | 7.4 ±1.3 | 0.9 ±0.09 | 0.83 ±0.12 | 0.86 ±0.13 | 0.96 ±0.08 | 0.97 ±0.01 |
| **Ag/AgC reference** | 5.9 ±2.0 | 6.0 ±1.6 | 6.2 ±0.9 | 0.5 ±0.1 | 0.88 ±0.12 | 0.89 ±0.09 | 0.98 ±0.04 | 0.97 ±0.01 |

Similar trends are visible for the VEP results (maximum difference of 0.9 µV) and the Spearman’s rank correlation. These negligible differences between the monitored EEG signals are likely caused by the spatial distance of the two occipital electrode positions, as well as environmental noise or even due to inevitable experimental differences that derive from the manual positioning and preparation of the electrodes [15,17,18]. Moreover, taking into account the high correlation values (> 0.8) as well as the standard deviations (for both RMSD and CORR), no considerable differences in terms of signal quality can be identified: neither (i) between dry MP and wet electrodes, nor (ii) among the different dry MP electrodes. Furthermore, no considerable alterations of the shape and amplitude of the EEG signals can be seen, regardless of the used electrode, Figs. 9 and 10.

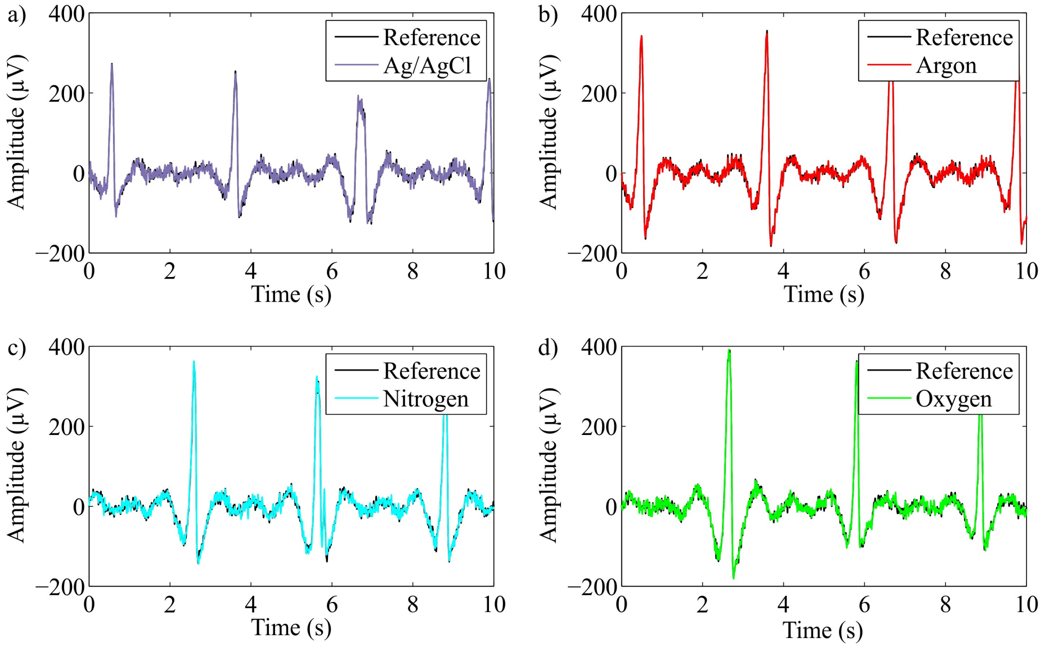

**Fig. 9.** Overlay plot of 10 seconds of EEG signal containing eye-blinking artefacts recorded with (a) two independent wet Ag/AgCl reference electrodes, (b) Ag/AgCl reference & Ar treated MP dry electrode, (c) Ag/AgCl reference & $N_2$ treated MP dry electrode, and (d) Ag/AgCl reference & $O_2$ treated MP dry electrode pairs.

Hence, data from Table IV, Fig. 9 and Fig. 10 indicate that the relevant EEG signal information can be recorded with both the proposed plasma activated and Ag:TiN-coated polyurethane MP dry electrodes and the reference conventional wet Ag/AgCl electrodes.

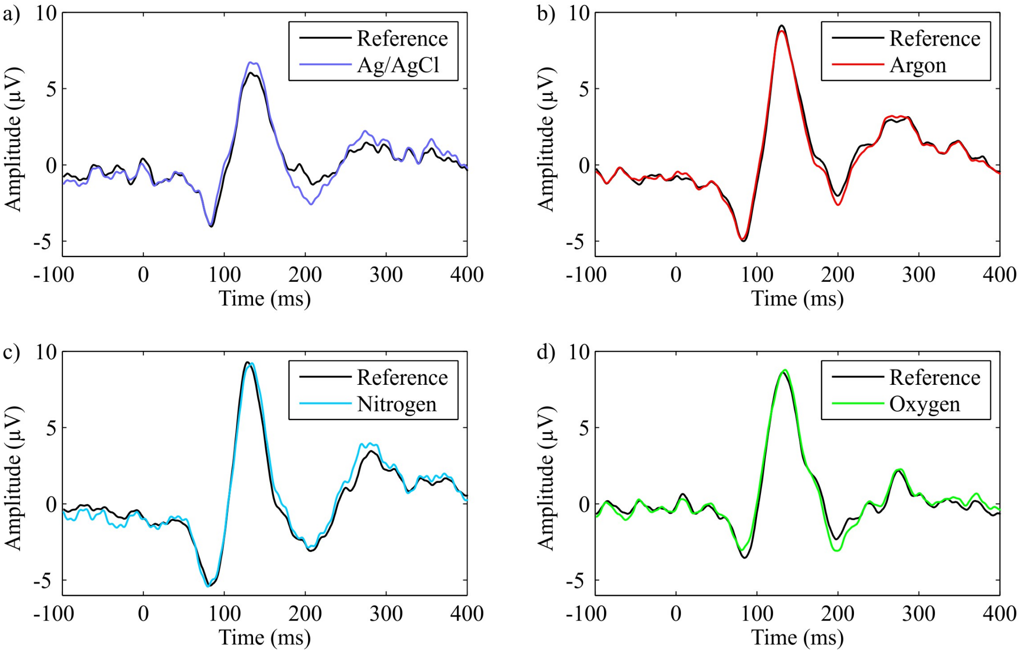

**Fig. 10.** Overlay plot of the VEP results 100 ms pre- and 400 ms post-stimulus acquired with (a) two independent wet Ag/AgCl reference electrodes, (b) Ag/AgCl reference & Ar treated MP dry electrode, (c) Ag/AgCl reference & $N_2$ treated MP dry electrode, and (d) Ag/AgCl reference & $O_2$ treated MP dry electrode pairs.

In order to analyse frequency-dependent signal differences, the power spectral density (PSD) of the EEG signals monitored with dry and wet electrodes is shown in Fig. 11. Resting state EEG and alpha activity (Fig. 11 a) and b), respectively) show similar trends. The power increases for lower frequencies for all electrodes. For frequencies below 3 Hz, an increase towards higher values is perceivable in the plasma treated dry MP electrodes, which should be attributed to slightly increased drift behaviour, which was already observed in previous studies [17].

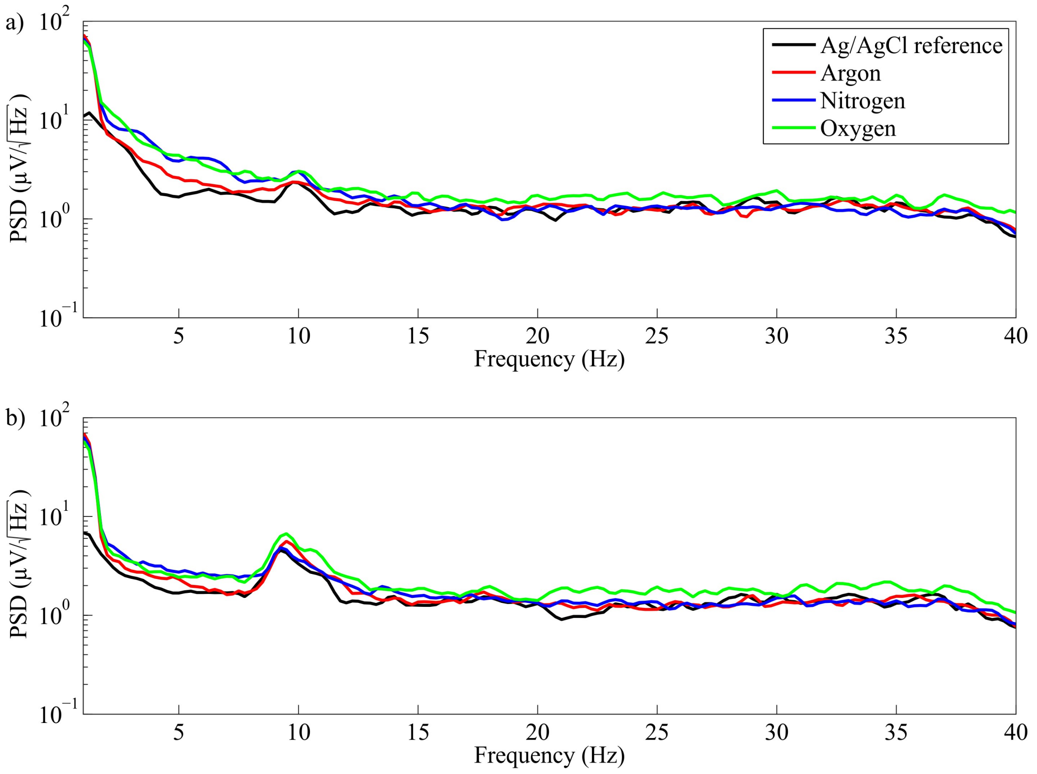

**Fig. 11.** Characteristic EEG signals acquired with the proposed plasma treated Ag:TiN-coated polyurethane MP dry electrodes and conventional Ag/AgCl electrodes: Welch estimation of the power spectral density of 10 seconds of (a) resting state EEG and (b) EEG exhibiting alpha activity.

To summarize, the small differences found in terms of EEG signal characteristics, shape and amplitude indicate that the proposed dry MP electrodes are promising candidates to replace the standard wet Ag/AgCl ones, which should translate into faster and simple montages, beneficial for many clinical or ambulatory procedures.

## 4. CONCLUSIONS

The present study focused on the optimization of the plasma treatment conditions with the objective of enhancing the PU/Ag:TiN system interfacial adhesion so that it may be later used as dry EEG electrodes. The optimal treatment conditions were selected taking into account the influence of the exposure time and plasma power on the wettability of the PU surfaces. Minimum water C.A. values (42º, 25º and 12º for oxygen, nitrogen and argon, respectively) were obtained using 100 W and 15 min., regardless of the used working gas. The steep reduction from 90º (untreated PU) was attained due to significant chemical and topographic changes of the PU surface. After FTIR and XPS analysis it was found that the plasma activation promoted the grafting of reactive oxygen-containing groups at the PU surface. Oxygen was the most effective gas, inducing the formation of higher amounts of the referred species (16.1 %), followed by nitrogen (15.9 %) and argon (13.5 %). Furthermore, the Wenzel's equation predicted that also topography changes should play an important role on the hydrophilicity evolution, thus from the AFM studies it was found that a 96 %, 48 % and 31 % roughness increase was promoted by the argon, nitrogen and oxygen, respectively. As expected, the promoted chemical and topographic changes translated into an excellent PU/Ag:TiN interfacial adhesion, being rated with the maximum classification of 5B. The untreated PU sample exhibited extensive delamination along the edges of the cuts and in some areas inside the squares defined by the cross-cut tape test.

The results obtained from the EEG trials allowed to conclude that no considerable differences in terms of shape, amplitude and spectral characteristics were found when comparing signals acquired by conventional wet reference Ag/AgCl electrodes and the proposed plasma activated and Ag:TiN-coated polyurethane dry MP electrode, regardless of the used plasma working gas. No differences between the dry electrodes themselves could also be found. Consequently, since most of the EEG signal information is maintained when the dry electrode system proposed in the present work is used, it is possible to conclude that the PU/Ag:TiN dry electrodes are promising candidates to substitute the standard Ag/AgCl ones in specific clinical and ambulatory procedures.

## ACKNOWLEDGEMENTS

This research is partially sponsored by FEDER funds through the program COMPETE – Programa Operacional Factores de Competitividade and by national funds through FCT – Fundação para a Ciência e a Tecnologia, under the projects PEst-C/EME/UI0285/2011, PTDC/SAU-ENB/116850/2010, PTDC/CTM-NAN/112574/2009 and Programa Pessoa 2012/2013 Cooperação Portugal/França, Project no. 27306UA Porous architectures in GRAded CERamic thin films for biosensors - GRACER. The authors would also like to acknowledge CEMUP for SEM analysis and Yantai Wanhua Polyurethanes Co., Ltd for providing the thermoplastic polyurethane pellets. P. Pedrosa acknowledges FCT for the Ph.D. grant SFRH/BD/70035/2010. P. Fiedler acknowledges the German Federal Ministry of Education and Research project – 03IPT605A. P. Pedrosa and P. Fiedler both acknowledge FP7-People Marie Curie IAPP project 610950 (ANDREA) and German Academic Exchange Services for the Germany/Portugal bi-lateral project – D/57036536.

## REFERENCES

1. M. Teplan, “Fundamentals of EEG measurement”, Meas. Sci. Rev., 2 (2) (2002) 1-11.
2. E. McAdams, “Bioelectrodes”, in Encyclopaedia of Medical Devices and Instrumentation, Webster J. G. Ed., New York, Wiley, (1988) 120-166. DOI: 10.1002/ 0471732877.
3. A. Searle, L. Kirkup, “A direct comparison of wet, dry and insulating bioelectric recording electrodes”, Physiol. Meas. 22 (2000) 271-283. DOI: 10.1088/0967-3334/21/2/307.
4. T. H. Sander, T.R. Knösche, A. Schlögl, F. Kohl, C.H. Wolters, J. Haueisen, L. Trahms, “Recent advances in modeling and analysis of bioelectric and biomagnetic sources”, Biomed. Tech., 55 (2010) 65-76. DOI: 10.1515/bmt.2010.027.
5. P. Fiedler, S. Griebel, P. Pedrosa, C. Fonseca, F. Vaz, L. Zentner, F. Zanow, J. Haueisen, “Multichannel Eeg With Novel Ti/Tin Dry Electrodes”, Sensors and Actuators: A Physical (2014), DOI: 10.1016/j.sna.2014.10.010.
6. Z. Iscan, Z. Dokur, “A novel steady-state visually evoked potential-based brain–computer interface design: Character Plotter”, Biomed. Signal Proces., 10 (2014) 145-152. DOI: 10.1016/j.bspc.2013.11.009.
7. F. Akram, H.-S. Han, T.-S. Kim, “A P300-based brain computer interface system for words typing”, Comput. Biol. Med., 45 (2014) 118-125. DOI: 10.1016/j.compbiomed.2013.12.001.
8. L. Lun-De, L. Chin-Teng, K. McDowell et al., “Biosensor Technologies for Augmented Brain-Computer Interfaces in the Next Decades”, Pr. Inst. Electr. Elect., 100 (2012) 1553-1566. DOI: 10.1109/JPROC.2012.2184829.
9. B.A.-Taheri, R.T Knight, R.L Smith, “A dry electrode for EEG recording”, Electroen. Clin. Neuro, 90 (1994) 376-383. DOI: 10.1016/0013-4694(94)90053-1.
10. P. Brunner, L. Bianchi, C. Guger, F. Cincotti, G. Schalk, “Current trends in hardware and software for brain–computer interfaces (BCIs)”, J. Neural Eng., 8 (2011) 025001. DOI: 10.1088/1741-2560/8/2/025001.
11. E.S. Valchinov, N.E. Pallikarakis, “An active electrode for biopotential recording from small localized bio-sources”, Biomed. Eng. OnLine 3 (2004) 25-39. DOI: 10.1186/1475-925X-3-25.
12. C. Fonseca, J.P. Silva Cunha, R.E. Martins, V. Ferreira, J.P. Marques de Sá, M.A. Barbosa, A. Martins Silva, “A novel dry active electrode for EEG recording”, IEEE Trans. Biomed. Eng. 54 (1) (2007) 162–165. DOI: 10.1109/TBME.2006.884649.

13. B.A.-Taheri, R.T. Knight, R.L. Smith, “An active, microfabricated, scalp electrode array for EEG recording”, Sens. Actuat. A, 54 (1996) 606-611. DOI: 10.1016/S0924-4247(97)80023-4.
14. N.S. Dias, J.P. Carmo, A.F. da Silva, P.M. Mendes, J.H. Correia, “New dry electrodes based on iridium oxide (IrO) for non-invasive biopotential recordings and stimulation”, Sens. Actuat. A, 164 (2010) 28-34. DOI: 10.1016/j.sna.2010.09.016.
15. P. Fiedler, L.T. Cunha, P. Pedrosa, S. Brodkorb, C. Fonseca, F. Vaz, J. Haueisen, “Novel $TiN_x$-based biosignal electrodes for electroencephalography”, Meas. Sci. Technol., 22 (2011) 124007. DOI: 10.1088/0957-0233/22/12/124007.
16. P. Pedrosa, E. Alves, N.P. Barradas, P. Fiedler, J. Haueisen, F. Vaz, C. Fonseca, “$TiN_x$ coated polycarbonate for bio-electrode applications”, Corros. Sci. 56 (2012) 49–57. DOI: 10.1016/j.corsci.2011.11.008.
17. P. Fiedler, P. Pedrosa, S. Griebel, C. Fonseca, F. Vaz, F. Zanow, J. Haueisen, “Novel Flexible Dry PU/TiN-Multipin Electrodes: First Application in EEG Measurements”, Proceedings of the 33rd Annual International Conference of the IEEE EMBS (2011) 55-58. DOI: 0.1109/IEMBS.2011.6089895.
18. P. Fiedler, C. Fonseca, P. Pedrosa, A. Martins, F. Vaz, S. Griebel, J. Haueisen, “Novel Flexible Dry Multipin Electrodes for EEG: Signal Quality and Interfacial Impedance of the Ti and TiN Coatings” Proceedings of the 35th Annual Conference of the IEEE EMBS (2013) 547-550. DOI: 10.1109/EMBC.2013.6609558.
19. Y. M. Chi, Y.-T. Wang, Y. Wang, C. Maier, T.-P. Jung, G. Cauwenberghs, “Dry and Noncontact EEG Sensors for Mobile Brain-Computer Interfaces,” IEEE Transactions on Neural Systems and Rehabilitation Engineering 20 (2012) 228-235. DOI: 10.1109/TNSRE.2011.2174652.
20. P. Fiedler, J. Haueisen, D. Jannek, S. Griebel, L. Zentner, F. Vaz, C. Fonseca, “Comparison of three types of dry electrodes for electroencephalography”, Acta IMEKO 3 (2014) 33-37. DOI: IMEKO-ACTA-03 (2014)-03-08.
21. V. Marozas, A. Petrenas, S. Daukantas, A Lukosevicius, “A comparison of conductive textile-based and silver/silver chloride gel electrodes in exercise electrocardiogram recordings”, J. Electrocardiology 44 (2011) 189–194. DOI: 10.1016/j.jelectrocard.2010.12.004.
22. G. Gargiulo, R.A. Calvo, P. Bifulco, M. Cesarelli, C. Jin, A. Mohamed, A. van Schaik, “A new EEG recording system for passive dry electrodes”, Clin. Neurophysiol. 121 (5) (2010) 686–693. DOI: 10.1016/j.clinph.2009.12.025.

23. K.-P. Hoffmann and R. Ruff, “Flexible Dry Surface-electrodes for ECG Long-term Monitoring”, Proceedings of the 29th Annual International Conference of the IEEE EMBS, Lyon, France, August, (2007) 23-26. DOI: 10.1109/IEMBS.2007.4353650.

24. J. Baek, J. An, J. Choi, K. Park, S. Lee, “Flexible polymeric dry electrodes for the long-term monitoring of ECG”, Sens. Actuators A 143 (2008) 423–429. DOI: 10.1016/j.sna.2007.11.019.

25. A. Gruetzmann, S. Hansen, J. Muller, “Novel dry electrodes for ECG monitoring”, Physiol. Meas. 28 (2007) 1375–1390. DOI: 10.1088/0967-3334/28/11/005.

26. R.J. Zdrahala, I.J. Zdrahala, “Biomedical applications of polyurethanes: a review of past promises, present realities, and a vibrant future”, J. Biomater. Appl., 14 (1999) 67–90. DOI: 0.1177/088532829901400104.

27. K. Stokes, A. Coury, P. Urbanski, “Autooxidative degradation of implanted polyether polyurethane devices”, J. Biomater. Appl., 1 (1986), 411–448.

28. A. Tiwari, H. Salacinski, A.M. Seifalian, G. Hamilton, “New prostheses for use in bypass grafts with special emphasis on polyurethanes”, Cardiovasc. Surg., 10 (2002), 191–197. DOI: 10.1177/096721090201000301.

29. M.R. Sanchis, O. Calvo, O. Fenollar, D. Garcia, R. Balart, “Characterization of the surface changes and the aging effects of low-pressure nitrogen plasma treatment in a polyurethane film”, Polymer Testing 27 (2008) 75–83. DOI: 10.1016/j.polymertesting.2007.09.002.

30. C. Zandén, M. Voinova, J. Gold, D. Mörsdorf, I. Bernhardt, J. Liu, “Surface characterisation of oxygen plasma treated electrospun polyurethane fibres and their interaction with red blood cells”, European Polymer Journal 48 (2012) 472–482. DOI: 10.1016/j.eurpolymj.2012.01.004

31. P. Pedrosa, D. Machado, C. Lopes, E. Alves, N.P. Barradas, N. Martin, F. Macedo, C. Fonseca, F. Vaz, “Nanocomposite Ag:TiN thin films for dry biopotential electrodes”, Appl. Surf. Sci. 285P (2013) 40-48. DOI: 10.1016/j.apsusc.2013.07.154.

32. P. Pedrosa, E. Alves, N.P. Barradas, N. Martin, P. Fiedler, J. Haueisen, F. Vaz, C. Fonseca, “Electrochemical behaviour of nanocomposite $Ag_x$:TiN thin films for dry biopotential electrodes”, Electrochim. Acta 125 (2014) 48-57. DOI: 10.1016/j.electacta.2014.01.082.

33. P. Pedrosa, D. Machado, M. Evaristo, A. Cavaleiro, C. Fonseca, F. Vaz, “Ag:TiN nanocomposite thin films for bioelectrodes: The effect of annealing treatments on the

electrical and mechanical behavior", J. Vac. Sci. Technol. A, 32 (2014), 031515. DOI: 10.1116/1.4873555.

34. P. Pedrosa, C. Lopes, N. Martin, C. Fonseca, F. Vaz, "Electrical characterization of Ag:TiN thin films produced by glancing angle deposition", Materials Letters 115 (2014) 136–139. DOI: 10.1016/j.matlet.2013.10.044.
35. P. Alves, S. Pinto, H.C. de Sousa, M.H. Gil, "Surface modification of a thermoplastic polyurethane by low-pressure plasma treatment to improve hydrophilicity", J. Appl. Polym. Sci., 122 (2011), 2302–2308. DOI: 10.1002/app.34348.
36. N. Gomathi, A. Sureshkumar, S. Neogi, "RF plasma-treated polymers for biomedical applications", Curr. Sci., 94 (2008), 1478–1486.
37. P. Chu, J. Chen, L. Wang, N. Huang, "Plasma-surface modification of biomaterials", Mater. Sci. Eng. R, 36 (2002), 143–206. DOI: 10.1016/S0927-796X(02)00004-9.
38. M. Noeske, J. Degenhardt, S. Strudthoff, U. Lommatzsch, "Plasma jet treatment of five polymers at atmospheric pressure: surface modifications and the relevance for adhesion", Int. J. Adhes., 24 (2004), p. 171-177. DOI: 10.1016/j.ijadhadh.2003.09.006.
39. Y. Ozdemir, N. Hasirci, K. Serbetci, "Oxygen plasma modification of polyurethane membranes", J. Mater. Sci. – Mater. Med., 13 (2002), 1147-1152. DOI: 10.1023/A:1021185803716.
40. T. Yamamoto, J.R. Newsome, D.S. Ensor, "Modification of surface-energy, dry-etching, and organic film removal using atmospheric-pressure pulsed-corona plasma", IEEE Trans. Ind. Appl., 31 (1995), 494-499. DOI: 10.1109/28.382108.
41. Y. Zhao, S. Tang, S.-W. Myung, N. Lu, H.-S. Choi, "Effect of washing on surface free energy of polystyrene plate treated by RF atmospheric pressure plasma", Polym. Test., 25 (2006), 327-332. DOI: 10.1016/j.polymertesting.2005.12.007.
42. I. Gancarz, G. Pozniak, M. Bryjak, "Modification of polysulfone membranes: 3. Effect of nitrogen plasma", Eur. Polym. J., 36 (2000), 1563-1569. DOI: 10.1016/S0014-3057(99)00240-2.
43. C. Oehr, "Plasma surface modification of polymers for biomedical use", Nucl. Instr. and Meth. in Phys. Res. B, 208 (2003), 40–47. DOI: 10.1016/S0168-583X(03)00650-5.
44. D. Hegemann, H. Brunner, C. Oehr, "Plasma treatment of polymers for surface and adhesion improvement", Nucl. Instr. and Meth. B, 208 (2003), 281-286. DOI: 10.1016/S0168-583X(03)00644-X.

45. E.M. Liston, L. Martinu, M.R. Wertheimer, “Plasma surface modification of polymers for improved adhesion: a critical review”, J. Adhes. Sci, 7 (1993), 1091-1127. DOI: 10.1163/156856193X00600.
46. R. Molina, P. Erra, L. Julia, E. Bertran, “Free radical formation in wool fibers treated by low temperature plasma”, Text. Res. J., 73 (2003), 955-959. DOI: 10.1177/004051750307301104.
47. Y.M. Chung, M.J. Jung, J.G. Han, M.W. Lee, Y.M. Kim, “Atmospheric RF plasma effects on the film adhesion property”, Thin Solid Films 447 (2004), 354-358. DOI: 10.1016/S0040-6090(03)01080-0.
48. Y.-H. Li, Y.-D. Huang, “The study of collagen immobilization on polyurethane by oxygen plasma treatment to enhance cell adhesion and growth”, Surf. Coat. Technol., 201 (2007), 5124–5127. DOI: 10.1016/j.surfcoat.2006.07.128.
49. Y. Zhang, S. Myung, H. Choi, I. Kim, J. Choi, “Optimum conditions for the surface modification of polyurethane by oxygen plasma treatment”, J. Ind. Eng. Chem., 8 (2002), 236–240.
50. N.T. Correia, J.J.M. Ramos, B.J.V. Saramago, J.C.G. Calado, “Estimation of the surface tension of a solid: application to a liquid crystalline polymer”, J. Colloid. Interf. Sci. 189 (1997), 361-369. DOI: 10.1006/jcis.1997.4857.
51. E. Chibowski, “Surface Free Energy of a Solid from Contact Angle Hysteresis”, Adv. Colloid. Interf. Sci. 103 (2003), 149-172. DOI: 10.1016/S0001-8686(02)00093-3.
52. K. Rokosz, T. Hryniewicz, “Cr/Fe ration by XPS spectra of Magnetoelectropolished AISI 316L SS using linear, Shirley and Tougaard methods of background subtraction”, Adv. Mat. Sci., (2013), 13-35.
53. N.P. Barradas, C. Jeynes, R.P. Webb, “Simulated annealing analysis of Rutherford backscattering data”, Appl. Phys. Lett., 71 (1997) 291-293. DOI: 10.1063/1.119524.
54. A.F. Gurbich, “Evaluated differential cross-sections for IBA”, Nuclear Instruments and Methods in Physics Research Section B: Beam Interactions with Materials and Atoms, 268 (2010) 1703-1710. DOI: 10.1016/j.nimb.2010.02.011.
55. P. Pedrosa, J.-M. Chappé, C. Fonseca, A.V. Machado, J.M. Nóbrega, F. Vaz, “Plasma Surface Modification of Polycarbonate and Poly(propylene) Substrates for Biomedical Electrodes”, Plasma Process. Polym. 7 (2010) 676-686. DOI: 10.1002/ppap.200900176.
56. G. Wolansky, A. Marmur, “Apparent contact angles on rough surfaces: the Wenzel equation revisited”, Colloids Surf. A, 156 (1999) 381-388. DOI: 10.1016/S0927-7757(99)00098-9.

57. L. Jiao, H. Xiao, Q. Wang, J. Sun, “Thermal degradation characteristics of rigid polyurethane foam and the volatile products analysis with TG-FTIR-MS”, Polym. Degrad. Stab. 98 (2013) 2687-2696, DOI: 10.1016/j.polymdegradstab.2013.09.032.

58. Y. Zhang, J. Maxted, A. Barber, C. Lowe, R. Smith, “The durability of clear polyurethane coil coatings studied by FTIR peak fitting”, Polym. Degrad. Stab. 98 (2013) 527-534. DOI: 10.1016/j.polymdegradstab.2012.12.003.

59. X. Fu, M.J. Jenkins, G. Sun, I. Bertoti, H. Dong, “Characterization of active screen plasma modified polyurethane surfaces”, Surf. Coat. Technol. 206 (2012) 4799–4807. DOI: 10.1016/j.surfcoat.2012.04.051.

## TABLE OF CONTENTS

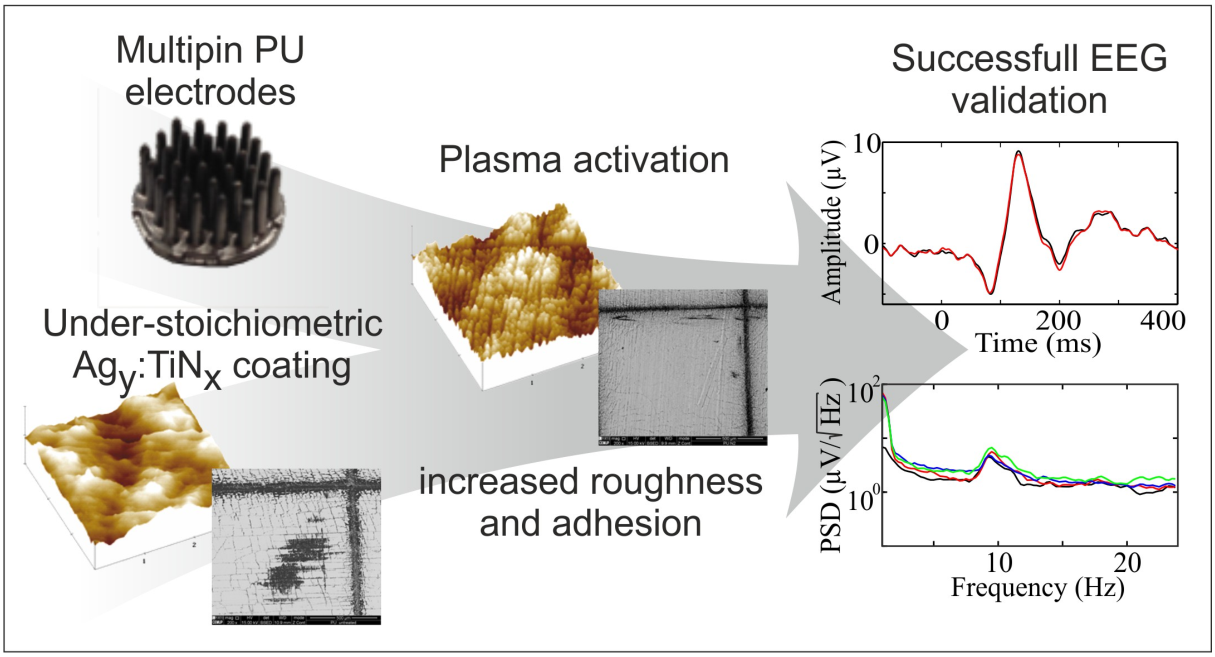

# CHAPTER 7

## CONCLUSIONS

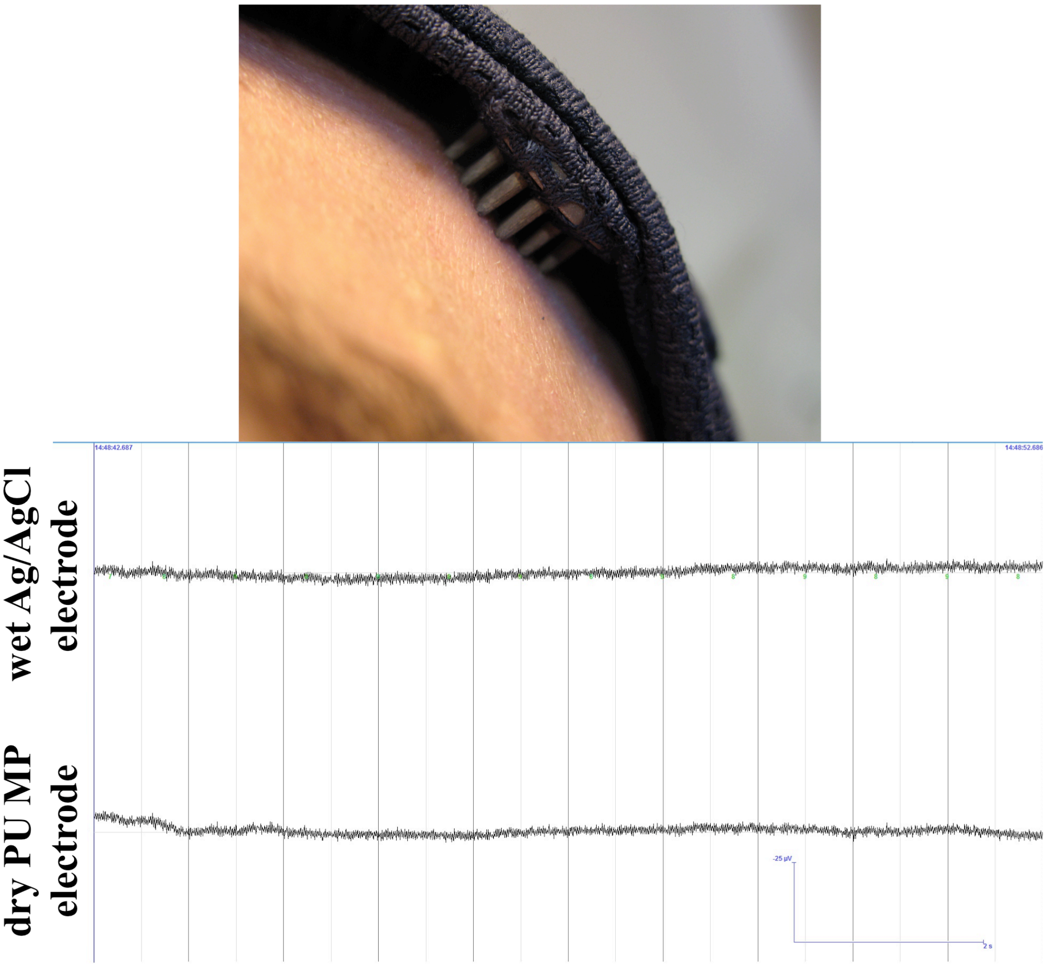

***top:*** *Ag:TiN-coated PU MP dry electrode placed on the forehead.*

***bottom:*** *10 seconds, all working channels, no filtering, resting state EEG without considerable artefacts.*

## 7.1. General discussion and main conclusions

The present section has the purpose of bringing together all major results that were obtained in the individual chapters, according to the different publications.

In chapter 2, a step forward on the investigation of the $TiN_x$ coatings was taken by sputtering the referred thin film system onto polycarbonate (PC) substrates. Since encouraging results were already achieved using this system in titanium disks for bioelectrical signal monitoring,, the next valid step should, in fact, be the assessment of the $TiN_x$ sputtering viability onto polymeric substrates, which has to be performed at low temperatures. Hence, a set of PC disks were coated with the $TiN_x$ thin film system in a wide range of compositions (increasing N contents) with the ultimate goal of selecting the best stoichiometry (N/Ti atomic ratio) to be used in dry electrode application. Accordingly, an extensive morphological, structural and electrochemical characterization was performed. The sputtered films could be divided into three zones. Zone I comprised the strongly under-stoichiometric coatings ($N/Ti < 0.24$) and, due to the low N incorporation were morphologically compact and mainly composed of a distorted α-Ti lattice. Then, for high N contents ($N/Ti > 0.85$) the close-stoichiometric and stoichiometric $TiN_x$ coatings were indexed to zone II. In this zone, a highly porous (disaggregated pyramid-like columns) and well-crystallized δ-TiN structure could be seen. The samples with $0.24 < N/Ti < 0.85$ comprise a transition zone (zone T) between under-stoichiometric and stoichiometric $TiN_x$ conditions. Regarding the application-oriented electrochemical characterization, it was found that all compositions exhibited a good chemical resistance in chloride-containing solutions, displaying passive dissolution currents below 1 $\mu A/cm^2$. However, lower passive dissolution currents, as well as lower impedance values and electrochemical noise and drift values comparable to those exhibited by the wet Ag/AgCl commercial electrodes, were found for zone II (stoichiometric) films. Moreover, due to a more stable and stress-free lattice, the zone II coatings showed the best adhesion to the

PC disk substrates. Consequently, the stoichiometric zone II $TiN_x$ coatings were considered the most suitable ones to be used as dry biopotential electrodes.

However, despite the promising results of the $PC/TiN_x$ system, it was found in preliminary EEG tests that the planar disk design was not suitable to effectively interfuse the hairline, which gave rise to high electrode/skin impedances and unreliable electrode/skin contact in dry conditions. Moreover, the high hardness of the PC disks meant that this initial electrode design was not comfortable to long-term patient use. Hence, the polyurethane multipin electrode design (allows an effective hair interfusion and superior patient comfort due to the tailorable hardness) was then tested using the optimized stoichiometric $TiN_x$ film. The results were encouraging in terms of signal reproducibility (comparing to the wet Ag/AgCl electrodes), but often delaminated after only one EEG trial. This mechanical failure was attributed to the low elasticity of the stoichiometric $TiN_x$ system, thus the decision to add Ag to the nitride matrix was made, in order to tailor most of the properties of the proposed $Ag_x$:TiN system. Beyond that, the presence of Ag, when combined with a top layer of AgCl, also helps stabilizing the material electrochemical potential.

Therefore, the $Ag_x$:TiN thin film system with Ag contents varying from 0.1 to ~50 at.% was extensively studied in terms of morphology, structure stability and electrochemical behaviour throughout chapter 3. As a result, the sputtered films were indexed to three distinct behavioural zones, according to the Ag incorporation in the TiN matrix. Zone I comprised the crystalline nitride-like films with $0.1 < \text{Ag at.\%} < 4.3$, which displayed a rather porous morphology (similar to pure TiN) and the lowest conductivity values. The coatings with intermediate Ag contents, $4.3 \leq \text{Ag at.\%} \leq 33.2$, were indexed to the transition zone II. The films belonging to this composition zone exhibited a less crystalline matrix and lower resistivity values. These changes were ascribed to the formation of highly conductive Ag aggregates present on top and among the disaggregated stoichiometric TiN matrix columns. Finally, the metallic-like zone III was comprised of the coatings with high Ag contents, 33.2 ≤

Ag at.% ≤ 47.5. The resistivity values fell below those of the pure Ti due to increased densification and occurrence of Ag aggregates on top of the TiN matrix, although in smaller dimensions than those observed in zone II samples. An important result was the fact that some films from zone II and zone III (with Ag contents above 20 at.%) did not exhibit such extensive Ag segregation phenomenon, which could be ascribed to a possible formation of $Ti_xAg$ intermetallics due to the combined effect of a slightly under-stoichiometric TiN matrix and moderate Ag incorporation. Consequently, the $Ag_x$:TiN films from late zone II and zone III were considered the most suitable ones to be used as dry biopotential electrodes.

However, only two months after the sputtering and characterization of the samples, extensive grey areas could be seen in the surface of the coatings, which replaced the rather uniform original golden-brown colour, which was observed in the as-deposited films. These surface alterations were due to the presence of large amounts of Ag aggregated particles, indicating that the Ag-alloyed stoichiometric TiN films are not morphologically and structurally stable, thus also not suitable to be used as biopotential electrodes.

In order to investigate the reasons and mechanisms for the occurrence of such extensive Ag segregation, the $Ag_x$:TiN films were subjected to a set of annealing treatments with temperatures ranging from 200 to 500 ºC. It was found that Ag diffusion was favoured by highly disaggregated and porous structures, forming Ag diffusion paths. As already stated, most of the $Ag_x$:TiN films displayed disaggregated columns, hence Ag segregation was facilitated. Nevertheless, regarding the envisaged application, extensive Ag segregation promotes an effective increase of the elasticity of the films due to the presence of soft Ag particles within the TiN matrix.

Subsequently, the electrochemical behaviour of the $Ag_x$:TiN system in synthetic sweat was investigated, thus simulating the electrode/hydrated skin interface present during the EEG monitoring procedure. The open circuit potential (OCP) behaviour was found to be closely related to the grain size of the Ag phases present in the films, which varied from a maximum of 28 nm to a minimum of 10 nm. The coatings with the more crystalline and loosely attached Ag phases (0.1 and 12.1 at.% Ag) exhibited OCP values close to that of the pure Ag film (~40 mV), while the polycrystalline ones (20.2, 36.3 and 47.5 at.% Ag) presented much less nobler values (~ -160 mV). The steep reduction of the OCP values was then ascribed to the increased reactivity of the well-adhered nanosized Ag phases. A continuous densification of the films with increasing Ag contents was confirmed by the voltammetric experiments, as well as a maximum Ag area ratio for the sample with 20.2 at.% Ag. The electrochemical noise values were comparable to those exhibited by the wet Ag/AgCl commercial electrodes, thus the coatings with Ag contents above 20.2 at.% were considered (although with some reserves) the best ones to be used as biopotential electrodes. It is important to note that this conclusion was drawn before the occurrence of the aforementioned Ag segregation, which happened approximately two months after the sputtering and characterization of the $Ag_x$:TiN system.

Therefore, since the observed Ag segregation phenomenon should translate into unstable electrode behaviour and based on the observed results, a new set of $Ag_y$:$TiN_x$ films were sputtered with decreasing N contents (towards under-stoichiometric TiN conditions) and Ag contents. This thin film system was produced and characterized as described in chapter 4 in order to explore the possibility of using a dense under-stoichiometric TiN matrix as a Ag segregation inhibitor through the formation of $Ti_xAg$ intermetallics. Once more, the $Ag_y$:$TiN_x$ films could be divided into three zones, according to the exhibited N/Ti atomic ratio. Zone I films (with N/Ti atomic ratios of 0.1 and 0.2 and correspondent Ag contents of 10 and 8 at.%, respectively) were obtained with low target potentials and deposition rates, which translated into dense N-doped hcp-Ti structures with high resistivity values and low hardness and reduced modulus. The coatings with N/Ti atomic ratios of 0.3 (15 at.% Ag) and 0.7 (32 at.% Ag) were indexed to a transition zone, zone II, and were obtained with higher target potentials due to the TiN poisoning phenomenon that occurs in the Ti fraction of the Ti/Ag target with increasing nitrogen flow rates. The steep increase of the Ag incorporation (from 8-10 to 32 at.%) was attributed to the increasing coverage of the target with a thin TiN layer. The films from this transition zone exhibited higher hardness and reduced modulus values. Zone III was comprised of the stoichiometric $Ag_y$:$TiN_x$ film with a N/Ti atomic ratio of 1 and 20 at.% Ag and served as comparison between the present thin film system and the $Ag_x$:TiN system studied in chapter 3. This stoichiometric sample was the only one exhibiting extensive Ag segregation, since it was found a probable occurrence of $Ti_xAg$ intermetallics in the under-stoichiometric samples. Due to presence of soft and highly conductive Ag phases, the resistivity and hardness values suffered a steep decrease. In addition, this sample was obtained with high target potentials and low deposition rates due to the aforementioned target poisoning phenomenon.

Regarding the electrochemical behaviour of the $Ag_y$:$TiN_x$ films it was found that the under-stoichiometric films, which avoid metallic Ag segregation, exhibit considerably nobler OCP values (close to those of pure Ag) than that of the stoichiometric film. Moreover, due to the increased porosity and Ag availability of the under-stoichiometric coatings, lower impedance, noise and potential drift rate values (similar to the wet Ag/AgCl electrodes) were attained. Hence, the TiN0.3Ag15 and TiN0.7Ag32 $Ag_y$:$TiN_x$ films were structurally, mechanically and electrochemically considered the most promising samples to be used as biopotential electrodes.

Following the optimization of a set of N/Ti atomic ratios and Ag contents, and since it was found that the porosity of the samples played a major role on the electrochemical behaviour of the films, the GLAD technique was used to tailor the architecture of the coatings. The architecture optimization and characterization of the GLAD sputtered Ag:TiN films with a fixed N/Ti ratio of 0.7 and 10 at.% Ag was performed as described in chapter 5.

In a first approach, several Ag:TiN coatings were produced with incidence angles (α) of 0º (typical columnar films), 40º, 60º and 80º, as well as with different column architectures (zigzag and spiral features with 4 and 8 periods, both with α = 80º). It was concluded that the morphology and porosity of the films could be tailored without significantly compromising the exhibited resistivity, whose values remained compatible with the envisaged application. Nevertheless, it was also found that more than four zigzag or spiral periods translated into an inversion of the porosity and resistivity evolution of the coatings, with more compact films being obtained.

Consequently, the Ag:TiN film architectures chosen to be sputtered onto flexible polyurethane substrates were the ones with α = 0º (comparison), 40º and 80º with 2 and 4 zigzag periods. These GLAD sputtered samples were characterized regarding their morphology, structure, resistivity and electrochemical behaviour. Once more, no Ag segregation was visible in the sputtered samples (even several months after deposition), which was again attributed to the possible formation of $Ti_xAg$ intermetallics. Due to the porosity and Ag surface content observed when α increases from 40º to 80º, the Ag:TiN 80º, Ag:TiN 80º 2Z and Ag:TiN 80º 4Z porous films exhibited lower impedance and electrochemical noise values, as well as more stable potentials (low drift rates), comparable to those of the wet Ag/AgCl commercial electrodes, than the Ag:TiN 0º and Ag:TiN 40º dense ones. Therefore, the porous GLAD coatings presented the most promising set of properties for the envisaged application as dry biopotential electrodes.

Finally, the PU/Ag:TiN interfacial adhesion and in-service EEG monitoring validation of the optimized films, plasma conditions and electrode design was performed in chapter 6. The plasma conditions for three different working gases (argon, nitrogen and oxygen) were optimized in a first stage, by studying the influence of several plasma parameters, such as exposure time and plasma power, in the wettability of the PU surfaces. Comparing to the untreated PU sample, the plasma activated surfaces showed signs of improved wettability, since the water C.A. values decreased from 90º (untreated) to 42º, 25º and 12º for the $O_2$ 100 W 15 min., $N_2$ 100 W 15 min. and Ar 100 W 15 min. treatments, respectively. Hence, a plasma power of 100 W and an exposure time of 15 min. were selected as the best plasma conditions, regardless of the used gas.

Taking into account the Wenzel's equation, the chemical and topographic features introduced by the activation treatments were studied, since they should explain the PU hydrophilicity behaviour. It was found that different amounts of reactive oxygen-containing species were grafted in the PU surfaces, depending on the used gas (16.1 % for oxygen, 15.9 % for nitrogen and 13.5 % for argon). The topographic changes were also strongly dependent on the used working gas, with a 96 %, 48 % and 31 % roughness increase promoted by the argon, nitrogen and oxygen, respectively. Consequently, since the activated PU surfaces benefited from the combined effects of increased roughness and grafting of reactive species, the subsequent adhesion levels of such samples were much higher than those of the untreated ones. In the case of the activated samples, no significant film detachment was found, while on the untreated one, extensive delamination (5-15 % of the area) could be seen.

Regarding the EEG trials that were performed, no significant differences were found in terms of EEG signal quality, shape and amplitude. Hence, since most of the EEG signal information is maintained when the proposed dry electrode system is used, it may be possible to conclude that the plasma activated and Ag:TiN-coated polyurethane dry MP electrodes are promising candidates to replace the standard wet Ag/AgCl ones. The use of such electrodes should translate into faster and simple montages, beneficial for many clinical or ambulatory procedures.

To conclude, after the discussion of the obtained results, it is possible to say that the Ag:TiN GLAD sputtered films display the most appropriate set of properties to be successfully used as biopotential electrodes, in comparison with the other thin film systems studied in the present thesis. However, further studies should be conducted regarding this thin film system in a more application-oriented basis.

## 7.2. Future work

The present thesis focused on several approaches to optimize and tailor a set of Ag-alloyed TiN thin film systems to be used as biopotential electrodes, always taking into account the different technical specifications of the envisaged application. Regarding the general discussion and main conclusions of the performed work, some concerns may still be addressed.

One of the main conclusions from chapters 4 and 5 was the probable formation of $Ti_xAg$ intermetallics when the TiN matrix attained under-stoichiometric conditions, which translated to a depletion of the Ag segregation phenomenon reported in chapter 3. Although the phases cannot be clearly differentiated in the XRD diffractograms and since no metallic Ag grains could be seen during SEM analysis, it is possible to claim that the occurrence of $Ti_xAg$ intermetallics is likely taking into account the combined results from SEM and XRD. Moreover, this claim was supported by similar results obtained in the group in the Ag:Ti thin film system. However, no definitive proof of the presence of such intermetallic compounds was provided during the performed characterization. Hence, the Transmission Electron Microscopy (TEM) technique could be used in order to eliminate any potential reserves about the formation of $Ti_xAg$ intermetallics.

In chapter 6, the interfacial adhesion of the Ag:TiN films to the polyurethane substrates was investigated with the cross-cut tape test. Despite the comparative differences that were found using different plasma activation treatments, the used test is above all a comparative/qualitative adhesion test. In order to provide a quantitative measurement of the thin film/substrate adhesion, other techniques such as scratch and abrasion test could be employed as future work. It is important to note that the referred tests are easily available for coatings deposited on traditional substrates like glass, silicon and steel due to the higher adhesive strengths (and loads) involved. However, in order to be suitably applied to thin film-coated polymers (lower adhesive strengths), the involved loads should be significantly lower, thus more expensive load cells are required.

The mechanical behaviour of the films was tested (also in chapter 6) using in-service conditions, this is, by performing several EEG trials using a limited number of Ag:TiN-coated multipin electrodes and assessing if and/or how many pins delaminated in the process. However, a more academic approach could be made by performing conductivity measurements as a function of the mechanical deformation of the coated substrates. Using this modified stress-strain test, it should be possible to obtain a maximum deformation value for which the coating looses conductivity, thus not meeting one of the main requirements for the envisaged application.

Regarding the EEG application of the optimized Ag:TiN-coated multipin electrodes, a further extensive characterization may be proposed. The EEG tests present on the current study (chapter 6) were performed on three subjects. However, the skin preparation, inter-individual, as well as intra-individual variations of skin and hair constitution will have a considerable impact on the overall performance of the proposed biopotential electrodes. Future studies should then be conducted on an increased number of volunteers in order to provide a more solid dataset for statistical analysis and interpretation. Current trends in neurosciences include multichannel setups with a dense biosensor array of more than 128 electrodes. Within such setups, the variation of the open circuit potential and the electrode/skin interfacial impedance determine the requirements for input stage impedance, as well as dynamic range of subsequent amplification electronics. Hence, complete multichannel caps should be manufactured and tested in multiple subjects and application scenarios in order to assess the level of variation and derive electronics compatibility requirements. Furthermore, the long-term stability of the noise and impedance levels of the optimized Ag:TiN coatings should be investigated.

Finally, since the Ag:TiN GLAD coatings exhibited the best set of properties when comparing to the other investigated systems, further studies should be conducted in order to validate a future PU multipin/GLAD Ag:TiN dry electrode system. With this intent (among others), the author of the present thesis submitted a post-doc proposal (SFRH/BPD/100054/2014) to the Portuguese Science Foundation (FCT).